8-5-2016 12:00 AM

Mechanism of ethanol partial oxidation over titania supported vanadia catalysts: geometric and electronic structure consequences on reaction kinetics

Dongmin Yun
The University of Western Ontario

Supervisor
Jose Herrera
The University of Western Ontario

Graduate Program in Chemical and Biochemical Engineering
A thesis submitted in partial fulfillment of the requirements for the degree in Doctor of Philosophy
© Dongmin Yun 2016

Abstract

Supported vanadium oxide catalysts (VO_x) are used for a wide range of industrial processes. A significant amount of research has been carried on this specific system with the aim to identify the critical parameters involved in catalytic activity. The results on this relative large body of research indicate that the catalyst support plays a critical role in determining the catalytic activity of vanadia and the use of titanium dioxide as support renders a catalyst with superior activity. Studies on supported vanadia on titanium oxide (VO_x/TiO_2) have provided an understanding on support interactions that result in tuning of not only the vanadia cluster size but also on its electronic structure. These modifications result in changes in catalytic activity.

This dissertation focuses on the controlled synthesis and the characterization of the electronic structure of VO_x/TiO_2 catalysts and the consequences of synthesis parameters on catalytic activity using ethanol partial oxidation as a probe reaction. A battery of analytic techniques such as nitrogen physisorption, X-ray diffraction, *in situ* diffuse reflectance ultra violet visible spectroscopy, *in situ* Fourier transform infrared spectroscopy, *in situ* Raman spectroscopy, X-ray photoelectron spectroscopy and temperature programmed techniques were used to characterize the catalyst. Computational simulations were also carried out to evaluate the electronic structures of the VO_x/TiO_2 catalysts. The results of these combined approaches (experimental and theoretical) indicate the vanadium oxide is heterogeneously distributed on the TiO_2 surface as mainly isolated and polymerized VO_x. We also found that the domain size of VO_x correlates with its reducibility and that polymerized VO_x species present in the catalyst do not anticipate in the catalytic turnovers. A novel methodology for the quantification of redox active sites is also presented.

Keywords

Acknowledgments

I am always grateful to my supervisor Prof. José Herrera for giving me the opportunity to study at Western and supporting me in my quest to gain a lot of academic achievement. I really enjoyed his valuable advice, criticism, instruction and ideas to my research. I also want to express my appreciation to Prof. Song in Department of Chemistry at Western for granting me access to use a fantabulous Raman spectroscopy system in his lab, which was of great help in improving my research. I thank Prof. Rohani for helping me on automatic system development. I am also thankful to Prof. Chin in University of Toronto to examine my thesis and for her insightful advise me from time to time.

I thank all my friends at Western and at University of Toronto for their friendship and for making it such a great place to work and many valuable discussions.

She is at the bottom of this list, but tops in my heart, thanks to my wife. So Mi

Dongmin Yun

July 2016

Table of Contents

List of Tables

List of Figures

Chapter 1

1 Introduction

1.1 Background

With increased demands for energy, stricter environmental regulations, and depleting fossil fuel supplies, developing alternative renewable energy resources becomes essential in the field of research as well as for industry[1]. According to the Renewable Fuels Association (RFA), the annual bioethanol production from 29 states in USA corresponded to 14.7 billion gallons in 2015[2]. Driven by the latest innovation and technology, it is anticipated that the excess ethanol will be available for the production of value chemicals in the near future. For example, ethanol can be successfully converted to acetaldehyde, ethyl acetate, acetic acid, ethylene, diethyl ether, etc. Among them, if a cheap ethanol source is available together with a new catalyst with high activity and selectivit[3], acetaldehyde production via oxidative dehydrogenation of ethanol becomes an alternative to the production of acetaldehyde via Wacker process, which generates chlorinated waste.

Among possible catalytic materials for this process, transition metal oxides are of interest. They have been applied to a variety of fields, from heterogeneous catalysis, photocatalysis, solar cells, gas sensors, pigments, corrosion-protective coatings, electronic devices, etc[4–7]. Nowadays, metal oxides as catalysts play a prominent role in our society. They are used to produce commodity chemicals and fuels. Besides, metal based catalytic processes have become indispensable in controlling environmental pollution as well. For example, selective catalytic routes replaced stoichiometric processes that typically generate waste problems. In the field of catalysis, metal oxides are playing a crucial role also as support materials. In fact, most of the commercial catalysts are dispersed on oxide powders such as SiO_2, Al_2O_3, and TiO_2.

Among these metal oxides, the transition metal vanadium is attractive, as it presents itself in different vanadium oxide structures with diverse physicochemical properties. As

catalyst, however, bulk unsupported vanadium pentoxide originally exhibits poor thermal stability and mechanical strength. However, once vanadia is incorporated in an appropriate support, the catalytic performance of vanadium oxide is significantly improved. For these reasons, supported vanadia is widely used in the field of catalysis, being particularly active and selective in the oxidative dehydrogenation of ethanol to acetaldehyde. Although, this process has been heavily investigated, its kinetic and mechanistic details have yet to be established. In fact, many aspects of this process still remain unclear. Therefore, an in depth understanding of the electronic structure, as well as a mechanistic elucidation of partial oxidation processes over vanadium oxide will facilitate the design of better catalysts.

1.2   General review

1.2.1   Oxidative dehydrogenation and partial oxidation

Oxidative dehydrogenation (ODH) refers to a process that occurs formally without any participation of hydrogen (i.e. consumption or formation) and leads to the removal of two hydrogen atoms from the original molecule as water in the presence of oxygen. The original molecule is converted into an unsaturated one. The ODH of alkanes leading to the formation of alkenes has been proposed as an alternative method to overcome the drawbacks of traditional methods due to its favorable thermodynamics and negligible coke formation[8]. ODH processes can be conducted at relatively lower temperature than alternative thermal or the non-oxidative catalytic process. Moreover, ODH reactions typically have large equilibrium constants, which decrease at higher temperatures. Most importantly, the presence oxygen prevents the formation of coke and in turn prolongs the catalyst usage.

ODH processes for alcohols conversion to aldehydes are known as partial oxidation of alcohols. The formation of formaldehyde via methanol partial oxidation is a typical example. Partial oxidation reactions are highly exothermic ($\Delta H = -156 \; kJ \cdot mol^{-1}$ for the case of methanol partial oxidation to formaldehyde)[9]. In the case of alcohols, the

formation of combustion products is thermodynamically favorable (i.e. $CH_3OH + O_2 \rightarrow CO + 2H_2O$, $\Delta G°_{298K} = -455.2\ kJ \cdot mol^{-1}$ at 25 °C), thus, tuning of the reaction selectivity through the selection of an adequate catalyst is key to successful operation.

1.2.2   Reactions and reactants stoichiometry

This section provides background information about partial oxidation of ethanol and the pathways that the reaction can follow. A comprehensive literature review is presented for these processes.

1.2.2.1   Desired main reactions

Oxidative dehydrogenation of ethanol to acetaldehyde (ethanol partial oxidation) is usually conducted at low temperatures (100 – 300 °C) under atmospheric pressure (eq1.1). This process is thermodynamically favored (ΔG = -184.8 kJ·mol^{-1}) at 200 °C:

$$CH_3CH_2OH(g) + 0.5O_2(g) \rightarrow CH_3CHO(g) + H_2O(g) \qquad \text{eq.(1.1)}$$
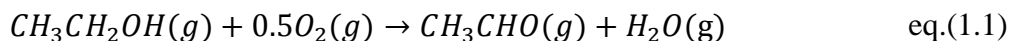
$$\Delta H° = -200.4\ kJ \cdot mol^{-1}, \quad \Delta G°_{298K} = -190.6\ kJ \cdot mol^{-1}$$

1.2.2.2   Side reactions

During ethanol partial oxidation the main side unimolecular reactions are three: dehydration of ethanol to ethylene (eq.1.2), direct dehydrogenation of ethanol to acetaldehyde (eq.1.3), and acetaldehyde oxidation to acetic acid (eq.1.4). The selective oxidation to acetic acid is thermodynamically favorable at ambient temperature and the dehydration of ethanol to ethylene thermodynamically favored at temperatures near 70 °C. On the other hand, direct dehydrogenation of ethanol to acetaldehyde has a positive Gibbs free energy value at temperatures below 380 °C, indicating that this process can be ruled out at lower temperatures (< 300 °C).

$$CH_3CH_2OH(g) \rightarrow C_2H_4(g) + H_2O(g)$$ eq.(1.2)
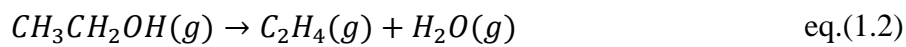
$$\Delta H° = 44.1 \ kJ \cdot mol^{-1}, \quad \Delta G°_{298K} = 5.7 \ kJ \cdot mol^{-1}$$

$$CH_3CH_2OH(g) \rightarrow CH_3CHO(g) + H_2(g)$$ eq.(1.3)
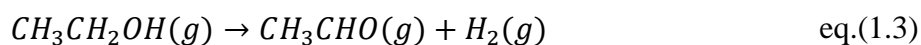
$$\Delta H° = 68.45 \ kJ \cdot mol^{-1}, \quad \Delta G°_{298K} = 34.98 \ kJ \cdot mol^{-1}$$

$$CH_3CHO(g) + 0.5O_2(g) \rightarrow CH_3COOH(g)$$ eq.(1.4)

$$\Delta H° = -292.2 \ kJ \cdot mol^{-1}, \quad \Delta G°_{298K} = -261.5 \ kJ \cdot mol^{-1}$$

Undesired products through bimolecular process can be formed either by bimolecular dehydrogenation leading to the formation of ethyl acetate (eq.1.5) or the formation of diethyl ether through dehydration (eq.1.6). Compared to the direct dehydrogenation these processes are thermodynamically favorable, so the selection of an adequate catalysts and reaction conditions (temperature, reactants rations and residence time) is critical to minimize the likelihood of these two pathways.

$$\text{CH}_3CH_2OH(g) + CH_3CHO(g) \rightarrow C_4H_8O_2(g) + H_2(g)$$ eq.(1.5)
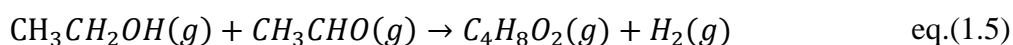
$$\Delta H° = -9.0 \ kJ \cdot mol^{-1}, \quad \Delta G°_{298K} = -29.6 \ kJ \cdot mol^{-1}$$

$$2\text{CH}_3CH_2OH(g) \rightarrow C_4H_8O_2(g) + H_2O(g)$$ eq.(1.6)
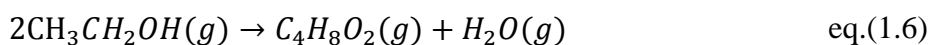
$$\Delta H° = 16.9 \ kJ \cdot mol^{-1}, \quad \Delta G°_{298K} = -9.92 \ kJ \cdot mol^{-1}$$

1.2.3   Catalytic support effect

1.2.3.1   General trends

Supporting a metal oxide on the surface of another oxide, such as SiO_2, Al_2O_3, TiO_2, and ZrO_2 was initially proposed to improve the activity of transition metal oxide catalysts[10–12]. When the metal oxide is supported in another oxide, the system potentially increases

its surface area and gains thermal, chemical and mechanical stability through mixed oxide formation at the metal oxides interface[10]. For example, bulk V_2O_5 exhibits poor thermal stability and mechanical strength. However the catalytic property of vanadia can be improved by incorporating it on an appropriate support. Therefore, supported metal oxide systems are important materials and at the same time important tools for the design and development of heterogeneous catalysts. During the main part of the past century, the support was only considered as inert material that provided a high surface area to carry the active metal oxide component or to improve the mechanical strength of the catalytic material[11,12]. However, during the last decade it has been unambiguously reported that the activity and selectivity of supported metal oxide catalysts are significantly affected by the properties of the support metal oxide[13,14]. This is generally known now in the catalyst field as the metal oxide-support effect although its exact mechanism of operation is still unclear.

In addition to support effects, for the specific case of vanadium oxide there is a particular aspect that is relevant to its catalytic behavior[15]. That is its ability to alternate between different oxidation states. The ability of supported vanadia (denoted as VO_x, which indicates a vanadium oxide cluster formed by adding x number of oxygen atoms to a vanadium atom[16]) to switch between different redox states is intrinsically linked to its catalytic activity in catalytic redox processes. The reducibility of vanadium oxide thus has been used as a descriptor for catalytic activity. This reducibility has been linked to the temperature (T_{max}) at which the reduction of supported VO_x by hydrogen reaches a maximum using temperature programmed reduction techniques (TPR). Even though the reduction characteristics and the T_{max} value seem to vary depending of experimental conditions, certain trends do stand out. The reducibility of supported VO_x changes depending of the support and decreases in the following order: $TiO_2 > ZrO_2 > Al_2O_3 > SiO_2 > MgO$. Therefore, regardless of the chemical factors at work, the choice of TiO_2 as a support for VO_x is at least partly based on the greater ease of reduction that it provides to vanadium oxide.

For more than 40 years, a relative large number of different attempts were made to correlate the catalytic reactivity of supported VO_x catalysts with a single global descriptor.

Among these, reports indicating the Sanderson electronegativity of the metal atom on the catalyst support was chosen as descriptor of catalytic activity since a strong dependence of catalytic activity on the chemical identity of the catalyst supports was observed. This indirectly suggested that the bridging V-O-M (where M represents the support metal atom) plays a critical role on activity, and perhaps on the rate limiting step of these processes[17–19]. Indeed, the observed steady state catalytic turnover frequency (TOF) values for probing oxidative dehydrogenation reactions carried over VO_x bearing catalysts increased by a factor of 10^3 in the following order: $SiO_2 < Al_2O_3 < Nb_2O_5 < CeO_2 < ZrO_2 < TiO_2$[20]. By taking the Sanderson electronegativity of the support cation, a general trend is obtained where there is an inverse correlation between TOF values and metal support electronegativity.

The reducibility of VO_x, defined as the ability of the fully oxidized V(+5) species to gain electrons, has also been proposed as a reactivity descriptor[21,22]. More recently, Schomäcker and coworkers suggested the reducibility of VO_x can be used as a relevant descriptor through the oxygen defect formation enthalpies of vanadia. The authors calculated these oxygen defect formation energies for the cases where vanadia was supported on of ceria (CeO_2) and alumina (Al_2O_3) using a computational approach (Density Functional Theory, DFT). The results showed that the oxygen defect formation energy for VO_x/CeO_2 ($76\ kJ \cdot mol^{-1}$) is much smaller than that for VO_x/Al_2O_3 ($388\ kJ \cdot mol^{-1}$), which is a much less active catalyst. This observation suggests the catalytic activity of supported VO_x linked to oxygen defect formation energy as well as its reducibility.

1.2.3.2 TiO_2 as support

Titanium dioxide (TiO_2) is one of the most investigated materials in the science of metal oxides[6]. TiO_2 is used in heterogeneous catalysis, photocatalysis, gas sensors, corrosion protective coatings, pigments etc. In the field of catalysis, TiO_2 –based systems were used to model strong metal support interactions (SMSI)[23].

The physicochemical properties of metal oxides are of critical importance in heterogeneous catalysis since it serves as platform for the interactions between reactants and adsorbed species[24]. In general, surfaces of most metal oxides like silica (SiO_2), alumina (Al_2O_3), and titania (TiO_2) etc, are hydroxylated (OH) or become hydroxylated upon contact with liquid water or water vapor[25]. Many attempts have been made to identify the presence of the surface hydroxyl functional groups, mainly using infra-red (IR) spectroscopy. This technique revealed that different types of surface hydroxyl exist in the OH stretching region of most oxides[26,27]. These surface hydroxyl groups have a general Brønsted acidic behavior. A general trend in acidic strength is general observed: a lower OH infrared stretching frequency indicates a more acidic character of the attached proton[28].

Surface hydroxyl groups on TiO_2 have been investigated using spectroscopic techniques. These results suggested that TiO_2 particle size and its morphology greatly influences OH stretching frequencies and consequently their acid strength[29]. It is generally accepted that infrared OH stretching frequencies appearing in the $3715 - 3675$ cm^{-1} range are linked to the presence of isolated OH moieties[30]. These isolated hydroxyls can in turn be classified as terminal and bridged species. Schematic drawings of these two types of hydroxyls are depicted in Figure 1.1.
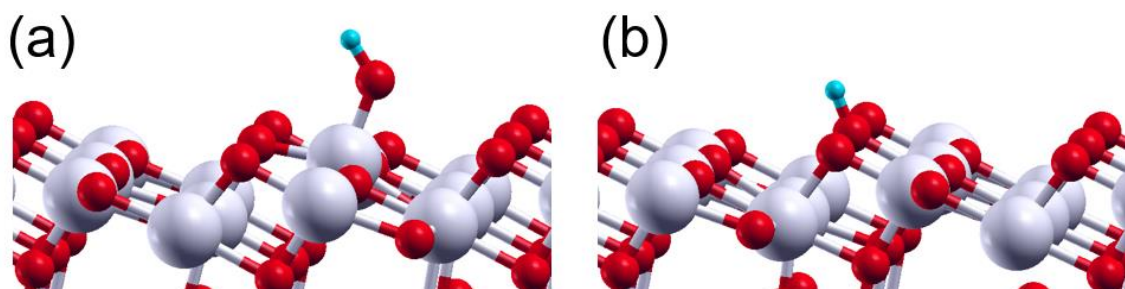
Figure 1.1. Schematic view of surface hydroxyl on TiO_2 (anatase 101). (a) Terminal hydroxyl and (b) bridged hydroxyl species.

Thermal treatment of TiO_2 in an oxygen depleted environment above 400 °C (He, N_2, Ar or vacuum) creates oxygen vacancies[31]. If dehydration takes place, the amount of

terminal OH decreases significantly compared to that of bridged OH groups. Dehydration takes place via desorption of terminal OH and hydrogen atoms from bridging OH (as water). Leaving the bridging oxygen moities behind. The removal of a terminal hydroxyl by high-temperature treatment leads to the formation of a fivefold-coordinated Ti atom (5c-Ti), which is stabilized by an adjacent oxygen vacancy. The proposed dehydroxylation mechanism is depicted in Fig.1.2[28]. It has been recently proposed that this dehydroxylation process takes place even at room temperature[32].
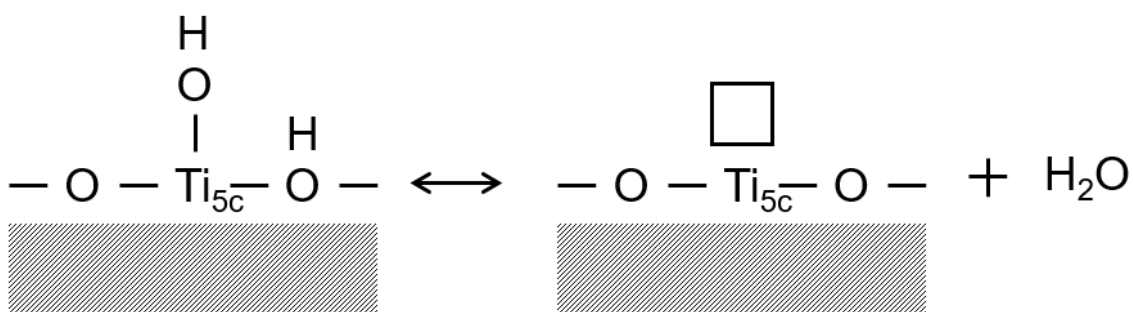
Figure 1.2. The formation process of oxygen vacancies on TiO₂ surface via dehydroxylation mechanism.

1.2.3.3   Nitrogen doped TiO$_2$

As mentioned in section 1.2.3.1, TiO$_2$ is the preferred choice for supporting VO$_x$ for catalytic oxidation reactions. In the field of environmental science and engineering, TiO$_2$ has been widely used in photochemistry. In spite of its intrinsic advantages such as chemical stability, biocompatibility and availability, the main drawback of TiO$_2$ is its wide band gap, 3.0 – 3.2 eV, absorbing light only in the UV region. Hence, a large effort has been put in preparing doped TiO$_2$ systems that absorb in the visible region. One of these modifications involves doping N atoms in the TiO$_2$ matrix. While this modification improves photocatalytic activity, two aspects of related to the chemical structure of the doped material still remain unknown. One is the chemical state and local environment of the doping nitrogen atoms. There are large numbers of reports on the preparation of N-TiO$_2$ materials using different routes and N precursors and on the identification of N

species doped in TiO_2 using X-ray photoelectron spectroscopy (XPS), solid-state nuclear magnetic resonance (SSNMR), electron paramagnetic resonance (EPR)[33,34], near-edge x-ray absorption fine structure spectroscopy (NEXAFS) and density functional theory (DFT)[35]. Zhang et al. reviewed almost all characterization results and suggested that the doped N is present as N^{2-} and N^{3-} species, coexisting in TiO_2, depending on the method used for nitrogen incorporation on the titania matrix[36]. The effect of electronegativity differences between N and O on the electronic properties of N doped TiO_2 has been studied using standard density functional theory (DFT) calculations as well[37]. These indicate that when nitrogen is introduced in the TiO_2 system, the titanium atoms increase their electronic density becoming less positive, while the adjacent O ions become more electron rich. For comparison, the electron density difference before and after N doping is presented in Fig.1.3. The charge on Ti, bonded to the N is +1.29 while that in pure TiO_2 arrive up to +1.33, indicating that the Ti atom bonded to the N is less positive. Even though the precise position of doped N is still unknown, the electronegative deference between nitrogen and oxygen significantly influence on electronic properties of N-doped TiO_2.
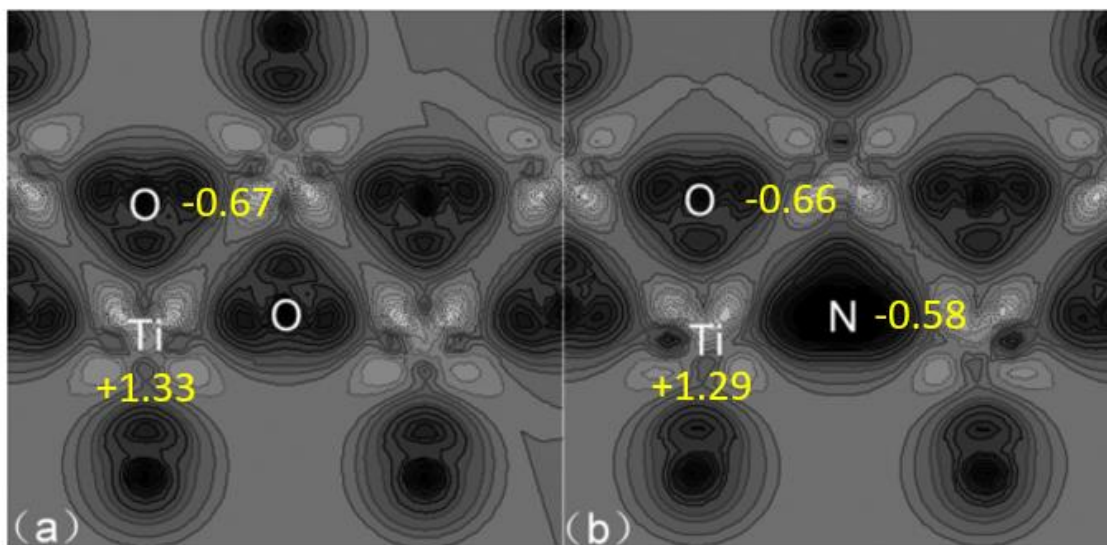
Figure 1.3. The electronic density difference of (a) N free TiO_2 and (b) N-doped TiO_2. The dark regions and light regions stand for the decreasing and increasing of the electron densities, respectively. Numbers indicate electronic charges on various atoms. Reproduced with permission from [37].

1.2.4　TiO$_2$ supported vanadium oxide catalyst

1.2.4.1　History of supported vanadium oxide

Vanadium oxide is one of the most important transition metal oxide catalysts used in the manufacture of chemicals (such as sulfuric acid and phthalic anhydride) and in the abatement of environmental pollution (nitrogen oxides from flue gas in power plants)[15,38]. Among these, the oxidation for sulfur dioxide to sulfur trioxide by vanadium oxide catalyst in the production of sulfuric acid, discovered in 1899, has become the most economically significant catalytic oxidation process[39]. In 1916 it was commercialized for the oxidation of naphthalene, to produce phthalic anhydride. Later the discovery of supported vanadium oxide over other metal oxide acting as support, consisting of a surface vanadium oxide phase strongly interacting with the metal oxide support culminated in new class of catalytic materials. Table 1.1 summarizes the main industrial applications of vanadium oxide as catalyst.

Table 1.1 Industrial catalytic process using vanadium oxide. Reproduced with permission from [10].

Industrial process	Catalyst material
Oxidation of SO$_2$ to SO$_3$ in the production of sulfuric acid	V$_2$O$_5$
Oxidation of benzene to maleic anhydride	V$_2$O$_5$
Oxidation of naphthalene to phthalic anhydride	V, Mo oxides
Oxidation of butene to phthalic anhydride V, P oxides	V, P oxides
Oxidation of o-xylene to phthalic anhydride V, Ti oxides	V, Ti oxides
Selective catalytic reduction of NO$_x$ with NH$_3$	V$_2$O$_5$/WO$_3$/TiO$_2$
Oxidation of mercury to mercury oxides	VO$_x$/WO$_x$/TiO$_2$

As shown in Table 1.1 titania-supports are the preferred choice for vanadia catalysts. Accordingly, the molecular structures of the surface VO_x species present over titania surfaces have been extensively investigated using a wide range of techniques including X-ray photoelectron spectroscopy (XPS), Raman spectroscopy, infrared (IR) spectroscopy, X-ray absorption near edge structure and Extended X-ray absorption fine structure (XANES/EXAFS), Solid state magic angle spinning nuclear magnetic resonance spectroscopy (MAS NMR), Ultraviolet visible spectroscopy (UV-vis), and Electron paramagnetic resonance spectroscopy (EPR). These studies revealed that the vanadia clusters present in different forms over titania surfaces and that their electronic state and size depend of a wide range of variables including the degree of hydration, temperature and whether there are immersed in an oxidative or reductive atmosphere[40]. In the following sections, we briefly review the most relevant results obtained using these spectroscopic techniques.

1.2.5 Structure of titania supported VO_x catalyst

Most of the information gained to date on the structure of vanadia cluster supported on titania has been mainly elucidated using studies based on Raman, IR, and UV-vis spectroscopy. Extended X-ray absorption fine structure (EXAFS)[41] has also provided additional information in this respect. Based on distinguishable features such as V=O stretching from Raman spectroscopy and bond distances and coordination numbers obtained from EXAFS, tetrahedral VO_x has been widely proposed for the structure of supported VO_x over titania[42,43]. Over the last 15 years, computational tools for evaluating molecular structure have gained ground as alternative tools. Among these, Density Functional Theory (DFT) became one of the most successful and important methods used to achieve much needed atomic detail as it can potentially provide the geometry, electronic structure as well as the reaction pathways of heterogeneous catalytic processes[44]. Thus, in this section, the previously proposed structures of VO_x/TiO_2 calculated by DFT are presented for the case of supported VOx on anatase (001) and (101).

Selloni and coworkers established slab models to describe VO_x moieties anchored at the (001) surface[45]. The (001) surface was expected to be more prevalent for the formation of supported VO_x, rather than (101) surface on the assumption that the (001) surface has higher ability to dissociatively adsorb water and thus a superior ability to anchor vanadia through the formation of V-O-Ti moities. On the contrary, water can be absorbed dissociatively onto (101) surface only at oxygen vacancy sites. A comparison of formation energies (E_f) for model species with monomeric VO_x cluster, tetrahedral coordinated = VO(OH) with a preferred orientation is quite favorable, as depicted in Fig.1.4. ($E_f = -0.07$eV per 1 ×1 slab).
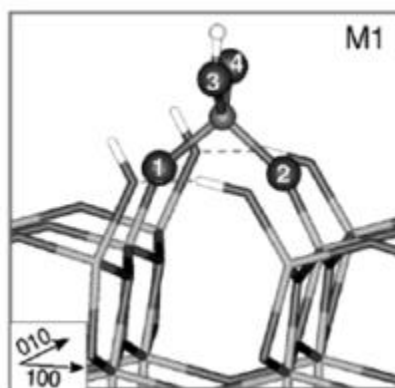
Figure 1.4. Most stable relaxed structure for monomeric VO_x cluster onto hydroxylated anatase (001) surface proposed by Selloni group. Reproduced with permission from [45].

As mentioned before, monomeric VO_x tends to form large domain species such as dimeric and polymeric VO_x, upon increasing the VO_x loading on the titania surface. The most stable dimeric species formed over anatase (001) surfaces was found to have an orientation similar to that of monomeric VO_x ($E_f = -0.08$eV per 1 ×1 slab), as depicted in Fig.1.5. This identical orientation suggested that tetrahedrically coordinated vanadia clusters preferentially polymerize along the (010) direction irrespective of the differences in computational and modeling approaches.
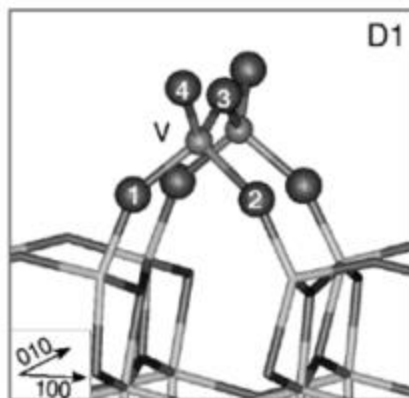
Figure 1.5. Most stable relaxed structure for dimeric VO_x cluster, formed by dimerizing two monomeric =VO(OH) units onto hydroxylated anatase (001) surface. Reproduced with permission from [45].

Although a large number of different crystallographic surfaces could be present in powder form, it is well known that the anatase (101) surface is by far the most stable[35]. Similar theoretical calculations on supported VO_x structures over anatase (101) were also carried out by Bell and coworkers[46]. Based on their comparison of formation energies for different types of VO_x species, the authors concluded that a tetrahedrically coordinated vanadium atom is the most abundant form of isolated monomeric VO_x species in the system under an oxidizing environment. In this structure, one of the oxygen atoms surrounding the vanadium came originally from the titania support, one of the oxygen atoms is forming a double bond with vanadia, and the two remaining are shared between vanadium and titania forming V-O-Ti moities (Fig.1.6).
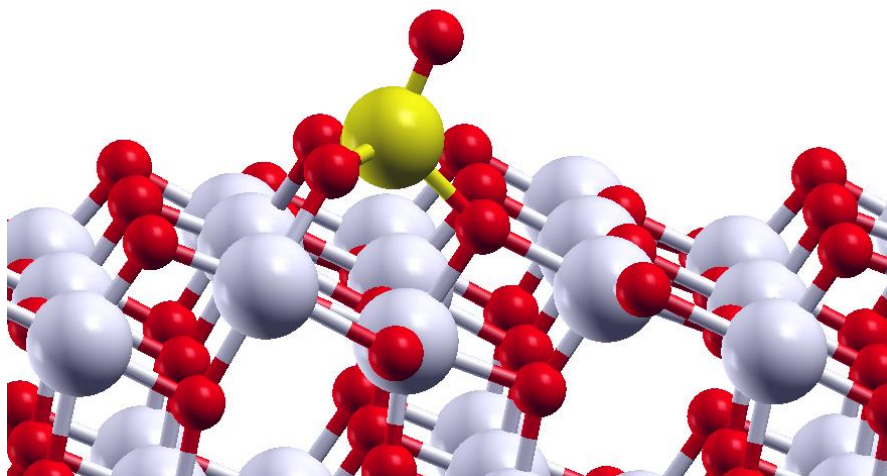
Figure 1.6. Most stable relaxed structure for monomeric VO$_x$ cluster on anatase (101) surface. The titanium, oxygen and vanadium atoms are represented in white, red and yellow respectively.

1.2.6   Characterization of titania supported VO$_x$ catalyst

1.2.6.1   *In situ* UV-vis spectroscopy

Ultraviolet visible spectroscopy (UV-vis) is an excellent spectroscopic tool to characterize the individual oxidation state of a transition metal oxide catalysts and its coordination environment. As mentioned in section 1.2.1, the structure of supported VO$_x$ catalyst is highly dependent on reaction conditions. Therefore, experiments aimed at elucidating relevant chemical structure of these materials need to be performed *in situ*. UV-vis spectroscopy can thus be applied to investigate the structures of pentavalent vanadium (V^{+5})-containing materials due to the ligand-to-metal charge transfer (LMCT) transitions of V in the UV-vis (208 - 500 nm, 20000 - 48000 cm^{-1}) range. In the case where VO$_x$ catalyst are supported on SiO$_2$ or Al$_2$O$_3$, the electronic transitions from the supports are negligible as compared to the strong absorption of V^{+5} [47–49]. However, in the case of the VO$_x$/TiO$_2$ catalysts, the LMCT from TiO$_2$ overlaps with that from V cations. Scientists tried to overcome this difficulty by mathematically subtracting the TiO$_2$

absorption band from the DRS spectra of the VO_x/TiO_2 catalysts based on the expectation that only adsorption by V^{+5} was displayed[50–52].

Gao and Wachs extensively used UV-vis spectroscopy to provide the structural characteristic of supported VO_x species on various metal oxide supports under different environmental conditions[53]. They observed that the band gap (E_g) of VO_x/TiO_2 catalysts with different vanadia loadings (1% and 5%) showed at 2.77 and 2.65 eV, respectively. The authors pointed out that the slight change in band gap between the two catalysts resulted likely from the strong TiO_2 support absorption in the higher energy region (200 – 300 nm) that overlaps the weak absorption from a small amount of V^{+5} in the same region[51,53]. Because the E_g values for reducible metal oxide supports such as TiO_2, and CeO_2 are so close to that of VO_x, they, thus, suggested that the investigation of structures of VO_x/TiO_2 catalysts may not be reliable, especially for catalysts with low VO_x loadings.

Nonetheless, correlations between the edge energy (E_g) and the number of covalent V-O-V bonds (CVB) has been empirically well-established, as shown in Fig.1.7. This correlation was based on the edge energy (E_g) values obtained for several crystalline pentavalent vanadium (V^{+5})-containing compounds and oxides (V_2O_5, MgV_2O_6, NH_4VO_3, $Mg_2V_2O_7$, and $Mg_3V_2O_8$). The obtained E_g values are inversely proportional to the CVB number. The equation of the correlation line can be expressed by CVB = 14.03 - 3.95·$E_{g\ (eV)}$[53]. It is well known that the E_g of nanosized particles shifted to higher energies as the particle size decreases. This is due to the valence and conduction bands in nanosized particles comprising discrete electronic levels as opposed to continuous energy bands present in large particles. Moreover, Weber previously proposed that the energy band gap values of molecularly sized clusters associates with the degree of spatial delocalization of the molecular orbitals involved in the electronic transitions of these materials[54].
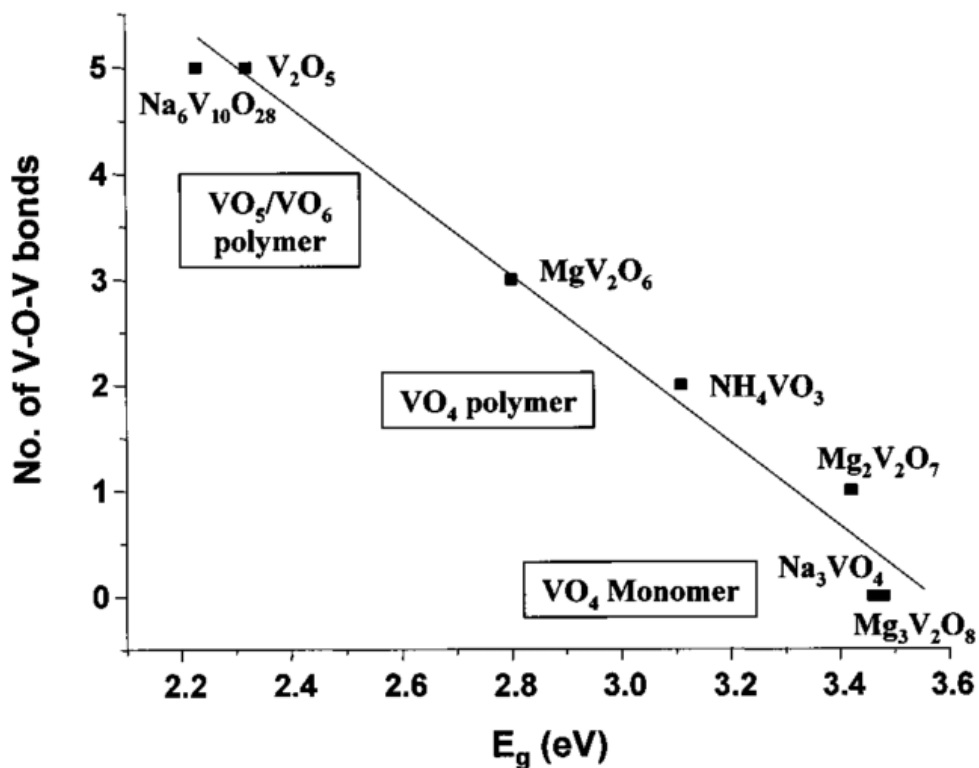
Figure 1.7. Edge energies of V^{5+}-containing reference oxides/compounds as a function of number of covalently bonded V-O-V bonds in the coordination sphere of central V^{+5} cation. Reproduced with permission from [53].

UV-vis spectroscopy is also a powerful technique to characterize the reduced species present in the catalyst. This can be accomplished by defining "the extent of reduction" of the supported VO_x catalysts as the number of transferred electrons to vanadia per vanadium atom ($\Delta e^- / V\ atom$). Argyle and coworkers extensively analyzed various optical spectral features of oxidized and reduced supported VO_x species on alumina, in particular, the pre-edge spectral features caused by the reduction[47,48]. The values that represent the extent of reduction were obtained by the authors from a series of experiments: first, the catalysts (VO_x/Al_2O_3) were reduced in flowing H_2. Then, the catalyst was exposed to oxygen and the amount of O_2 consumed by the catalyst was measured while the UV-Vis absorption spectra were obtained, this continued until the catalysts returned back to its fully oxidized state (V^{+5}). The extent of reduction ($\Delta e^- /$

$V\ atom$) was calculated by assuming that each O atom accepts two electrons. The results showed a linear correlation between the calculated extent of reduction and the pre-edge absorption intensities measured by UV-vis spectroscopy. This analysis was applied during propane oxidative dehydrogenation reaction carried over alumina supported catalyst with different vanadia loadings. The results of such analysis indicate that the extent of reduction per surface vanadium ($\Delta e^-/V\ atom$) atom increase with increasing propane to O_2 ratio in the influent stream and also with increasing VO_x loading in the catalysts (Fig.1.8). A low extent of reduction (i.e. 0.11 $\Delta e^-/V\ atom$ at global maximum in Fig.1.8) was observed regardless of VO_x loading, and turnover rate values increased with vanadium loading. The significant differences in the extent of reduction that resulted from the use of catalyst with different VO_x loadings and the low values of the extent of reduction observed for all catalysts tested indicated that the absolute number of reduced vanadium atoms present during catalytic turnovers is unrelated to catalytic activity.
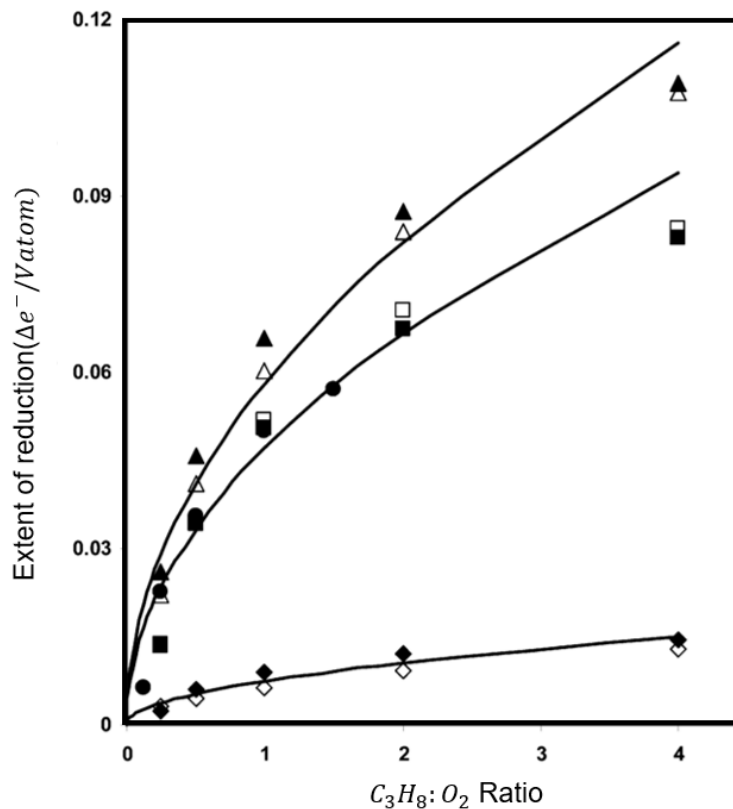
Figure 1.8. Dependence of the extent of catalytically relevant reduction per surface V-atom on the C_3H_8/O_2 ratio for VO_x/Al_2O_3 catalysts during propane oxidative dehydrogenation [filled symbols: C_3H_8 dependence (1.0-16 kPa C_3H_8, 4.0 kPa O_2, balance Ar, 603 K); open symbols: O_2 dependence (4.0 kPa C_3H_8, 1.0-16 kPa O_2, balance Ar, 603 K); diamonds: 3.5 wt % V_2O_5/Al_2O_3 (2.3 V/nm^2); squares: 10 wt % V_2O_5/Al_2O_3 (8.0 V/nm^2); triangles: 30 wt % V_2O_5/Al_2O_3 (34 V/nm^2); filled circles are C_3H_8 dependence (8.0 kPa O_2, 1.0-12 kPa O_2, balance Ar, 603 K) for 10wt.%V_2O_5/Al_2O_3 (8.0 V/nm2)]. Reproduced with permission from [47].

1.2.7 *In situ* Raman spectroscopy

As previously discussed, vibrational spectroscopy is a sensitive probe of the atomic structure and chemical bonding and thus of electronic structure. Most frequently used vibrational techniques are Infrared, and Raman spectroscopy. Raman spectroscopy, based on inelastic scattering effects, has become a powerful tool for studying the structure of catalysts and identifying catalytic active sites[21,51,55–59]. For the specific case of vanadia, this technique is considered the gold standard for the identification of the specific type surface vanadium-oxygen bonds present in the catalyst[57].

Here, bulk vanadium oxide (V_2O_5) typically exhibits Raman peaks at 990, 700, and 483 cm^{-1} [15,51]. The strong peak at 990 cm^{-1} is typically assigned to the characteristic symmetric stretching of the terminal vanadyl bond (V=O) and is characteristic of large vanadium oxide clusters. On the contrary, supported well-dispersed VO_x structures do not exhibit this characteristic sharp Raman band found in bulk V_2O_5. In the case of supported VO_x, instead, other characteristic peaks appear depending on the degree of agglomeration of the vanadium oxide clusters (referred as polymerization). Under fully oxidizing dehydrated conditions the Raman bands of oxidized supported vanadium oxide appear at ~1030 and ~920-950 cm^{-1}, as depicted in Fig.1.9. The strong and intense peak at ~1030 cm^{-1} is assigned to the characteristic symmetric stretching of a mono-oxo terminal vanadyl species and the broad Raman band at ~920-950 cm^{-1}, assigned to bridging V-O-V moities. In contrast to these V=O and V-O-V bonds, which are easily identified through Raman signals it is difficult to detect Raman bands from V-O-M (M describing the metal atom of the support) moieties, since these bonds have very weak Raman scattering cross-section, resulting in the inability to direct detect these type of vibrations[60].
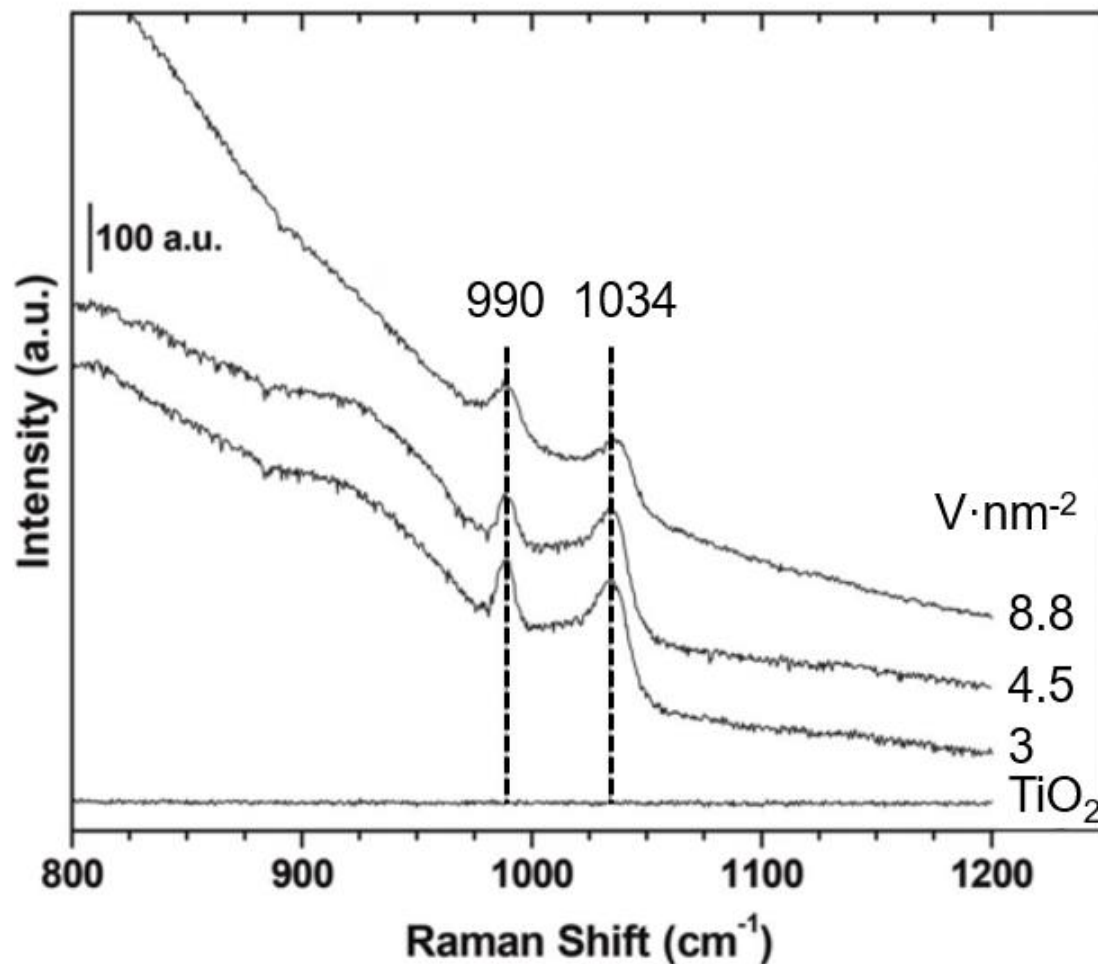
Figure 1.9. *In situ* **Raman spectroscopy (532 nm) of dehydrated (500 °C) VO$_x$/TiO$_2$ catalysts as a function of surface vanadium density (V atoms per nm^2) prepared by impregnation of ammonium metavanadate precursor in aqueous oxalic acid. Reproduced by permission from ref [61].**

Jehng et al. reported that sample temperature and presence of water vapor on the surface of vanadia supported over TiO$_2$ sometimes influences the position of Raman bands of the vanadium oxygen bonds, specifically the frequency of the symmetric stretching mode of the terminal V=O Raman band[62]. In their study they observed that for the case of samples with a low vanadia loading (such as 1wt.% as V$_2$O$_5$), the terminal Raman band shifts from 1024 cm^{-1} at 450 °C to 1006 cm^{-1} at 120 °C and becomes broad in the

presence of water vapor. They reported as well that, for high loading VO_x/TiO_2, samples a red shift of terminal V=O Raman band is observed from 1029 to 1018 cm^{-1} when the temperature is decreased from 450 ^oC to 120 ^oC. Similarly, the characteristic band appearing at ~920-950 cm^{-1} commonly assigned to bridging V-O-V moieties was affected by the introduction of water vapor. On the other hand, the Raman bands of terminal V=O bonds at 990 cm^{-1} in large crystalline VO_x species were not affected by the presence of water[62].

Raman studies in combination with $^{18}O/^{16}O$ isotope oxygen exchange measurements have also provided critical insights into the behavior of supported vanadia during redox catalysis. For instance, an isothermal isotopic exchange of $^{18}O_2$ with $^{16}O_2$ taking place over VO_x/ZrO_2 at relatively high temperatures (450^oC) was conducted by Weckhuysen and coworkers[63]. After successive reduction-reoxidation cycles, a single new Raman band ($^{18}O=V$), red-shifted by ~50 cm^{-1} from the original Raman band previously observed for the equivalent bond ($^{16}O=V$), was generated at the expense of the original V=O band ($^{16}O=V$). Therefore, it could be concluded that in this system, the terminal oxygens (^{16}O) can be completely exchanged to ^{18}O to form $V=^{18}O$ bonds[63].

Moreover, isotopic Raman studies can also provide critical information regarding the elementary steps of catalyst reoxidation that takes place during redox catalysts. Though, to the best of our knowledge this has not been accomplished yet on the VO_x/TiO_2 system. However a study of this type was carried over a similar redox catalytic system (MoO_x/TiO_2)[59]. The results reported are applicable to vanadia since in the molybdena/titania system molybdenum is present in a mono-oxo tetrahedral configuration $O=Mo(-O-Ti)_3$, analogous to vanadia in the VO_x/TiO_2 system. Mo can also shift between several redox states, in a similar way as vanadium. The authors carried isotopic oxygen exchange at the same time that Raman spectra was acquired. They reported that a gradual red-shift in the terminal ($^{16}O=Mo(-^{16}O-Ti)_3$) band at 994 cm^{-1} to 988 cm^{-1} ($^{16}O=Mo(-^{18}O-Ti)_3$) and to ($^{18}O=Mo$ ($-^{18}O-Ti)_3$) 944 cm^{-1}after repetitive reduction-reoxidation cycles was observed. It was then suggested that this Raman shift in terminal oxygen band is due to a sequential process where $^{18}O/^{16}O$ exchange takes place first at oxygen sites in the titania support followed by exchange at the terminal oxygen of

the O=Mo functionality. On the basis of these observation, they also suggested that the most favorable sites for exchange could be the bridging Mo-O-Ti species or the Mo-O-Mo sites to a less extent. Summarizing these results, the $^{18}O/^{16}O$ isotopic exchange sequentially occurs as follow:

$$^{16}O = \text{Mo}\left(-^{16}O - \text{Ti}\right)_3 \xrightarrow{\frac{^{18}O}{^{16}O}} {}^{16}O = \text{Mo}\left(-^{18}O - \text{Ti}\right)_3 \xrightarrow{\frac{^{18}O}{^{16}O}} {}^{18}O = \text{Mo}\left(-^{18}O - \text{Ti}\right)_3$$
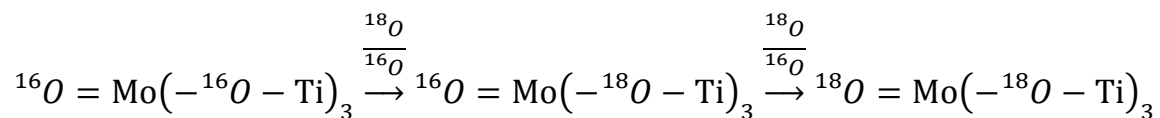
Such an isotopic substitution then takes place selectively before the substitution of the terminal ^{16}O of the terminal Mo=O site. They also pointed that unsaturated Ti-O-Ti sites are easier to be substituted during isotopic exchange process. Thus, ^{18}O substitution take place on the unsaturated surface Ti-O-Ti sites followed by a surface diffusion/spillover of dissociated ^{18}O toward Mo-O-Ti sites. Although direct extrapolation of these results to the VO_x/TiO_2 system needs to be carefully considered, a viewpoint where the V-O-M (M: metal support atom) moieties in the catalyst play a similar role could be proposed for the case of reducible metal oxides supports such as TiO_2, and CeO_2.

1.2.8   *In situ* FTIR spectroscopy

Infrared (IR) absorption spectroscopy was one of the first techniques used for the characterization of catalysis, and it is still one of the most favored. Common setups can be divided in four categories: (a) transmittance (TIR), (b) Diffuse reflectance (DRIFTS), (c) Attenuated total reflectance (ATR), and (d) Reflection absorption (RAIRS). Among them, DRIFTS mode has been one of the most popular methods for characterization of catalysts due to the ease of sample loading procedure[64] and its suitability for the characterization of powdered samples. In contrast to silica, and zirconia supported VO_x catalysts, whose vibrational spectroscopic absorbance cutoff is ~1050 cm^{-1}, the cutoff for VO_x/TiO_2 occurs below 900 cm^{-1}. Because of such low cutoff frequencies, spectral information such as V-O vibrational modes (900-1000 cm^{-1} region) can be obtained from IR spectroscopy. Similar to titania, IR spectroscopy is formally applicable for alumina and ceria supports. For instance, the IR spectra of the VO_x/TiO_2 system during catalysis

was widely studied by Burcham and coworkers[51], aiming to identify the VO_x active sites during methanol oxidation. Their results are described below.

Typical IR spectrum of VO_x/TiO_2 in the fundamental region is shown in Fig.1.10. A characteristic[18,51,65] band at ~1030 cm^{-1} was observed in the spectra of dehydrated 5%VO_x/TiO_2 in oxygen-rich environment and essentially consistent with frequencies observed in Raman spectra for the same vibrational mode. The shoulder peak at 1017 cm^{-1} was assigned to terminal V=O bonds in polymerized surface VO_x species due to the different local symmetry of these species. However, there is a conflicting interpretation of this feature in the literature. Freund and coworkers[66,67] reported that the V=O band at lower wavenumber (<1020 cm^{-1}) corresponds highly dispersed VO_x species (mainly monomeric VO_x) normally present at low vanadium loadings (0.5 V nm^{-2}). The band at higher wavenumbers (1030 cm^{-1}) can then be assigned to V=O present on trimeric VO_x moieties, anchored flat on the support surface, as revealed by the combined results of scanning tunneling microscopy, IR absorption spectroscopy, and X-ray photoelectron spectroscopy. Besides, the analysis of the spectral overtone region of infrared spectra can also potentially provide additional information for a series of VO_x/TiO_2 catalysts. A broad V=O 1st overtone band at 2035 cm^{-1} is observed in this region for oxidized vanadia, reported by early studies, once more strongly suggesting the presence of V=O[68–70].
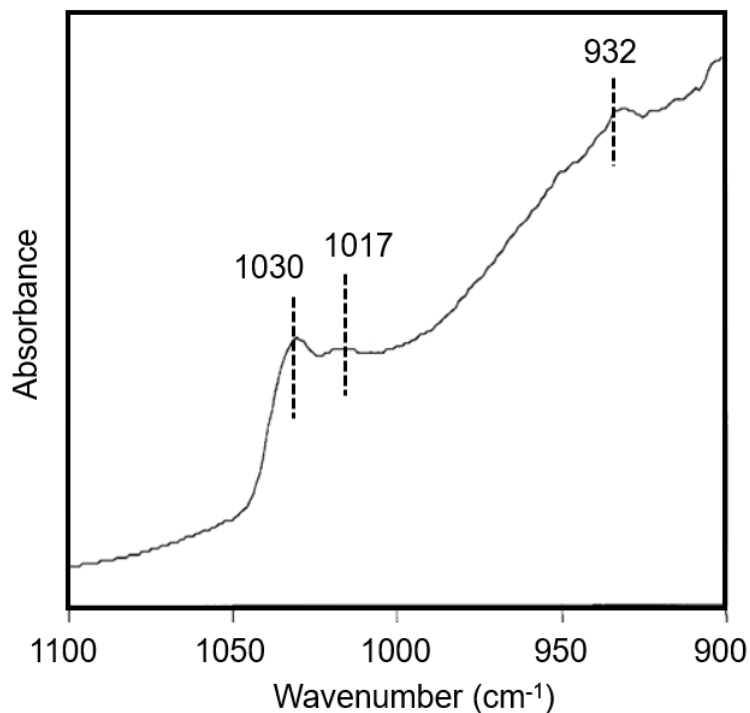
Figure 1.10. *In situ* **IR spectra in fundamental stretching region and 5 wt.%VO$_x$/TiO$_2$ catalysts in oxygen-rich environment (fully-oxidized at 350 ^{o}C) Reproduced with permission from [51].**

The formation of adsorbed alcohol species such as methoxy (M-OCH$_3$, M represents a metal atom) and ethoxy (M-OCH$_2$CH$_3$) can be also easily monitored by *in situ* FTIR spectroscopy. Alcohol adsorbed species formed over TiO$_2$ have been reported by many research groups[30,71,72]. Figures 1.11, 1.12 and 1.13 show some of these previous results. The IR spectra obtained on these systems after ethanol adsorption followed by evacuation of ethanol vapor at ambient temperature show characteristic C-H stretching bands at 2870, 2931, and 2971 cm^{-1} (Fig.1.11), C-H bending in the 1280-1500 cm^{-1} region as well as C-O and C-C stretching bands at 1000-1200 cm^{-1} (Fig.1.12) and O-H bending modes at 1264 cm^{-1} and 1635 cm^{-1} (Fig.1.13). The vibrational assignment of C-H stretching can be divided into three categories in terms of the carbon geometry: CH$_3$ asymmetric stretching (~2970 cm^{-1}), CH$_2$ asymmetric stretching (~2930 cm^{-1}) and CH$_3$ stretching (~2870 cm^{-1}), as shown in Fig.1.11[12,71,72].

Identification of the C-C and C-O bands resulting from ethanol adsorption over titania was accomplished by comparing the position of these IR bands to that obtained for the bands of methanol adsorbed over the same system. In this way, the broad peaks observed at 1042, 1118, and 1144 cm^{-1} are assigned to C-O stretching while sharp peaks at 1064, 1074, and 1093 cm^{-1} are assigned to C-C stretching modes (Fig.1.12). C-O bands can be differentiated in terms of adsorption geometry. A monodentate coordination can result from the dissociative adsorption of ethanol over an oxygen vacancy on a coordinately unsaturated single titanium atom through O-H bond cleavage. On the other hand, a bidentate coordination can result from two different scenarios. In the first one, ethanol adsorbs through C-O bond cleavage resulting in the CH$_3$CH$_2$ group bonded to a bridging oxygen (Ti-O-Ti) of the titania the surface. The second scenario takes place when a CH$_3$CH$_2$O group is bonded to an oxygen vacancy site located between two coordinately unsaturated titanium atoms, resulting in a bidentate coordination. The bands observed at higher wavenumbers (1118 and 1144 cm^{-1}) correspond to monodentate CH$_3$CH$_2$O(a) species and the band at 1042 cm^{-1} result from the formation of bidentate species. Fig.1.13 shows difference IR spectrum of adsorbed ethanol on TiO$_2$ at 200°C in the C-H and C-O vibrational regions, referenced to TiO$_2$. Table 1.2 lists the frequencies of adsorbed species observed in the ethanol adsorption studies over titania.

Alcohol adsorption over vanadium oxide has been also the subject of intense study, in the context of methanol oxidation[18,51,69]. However, relatively few studies have been conducted on ethanol adsorption over VO$_x$/TiO$_2$ catalysts[12]. On the basis of these literature reports, the vibrational modes of molecularly adsorbed ethoxide species over TiO$_2$ supported vanadia are shown in Table 1.2. For comparison, an analogous result for VO$_x$/Al$_2$O$_3$ is also listed[73,74]. Compared to ethanol adsorption on bare TiO$_2$, new bands appear at ~1550, ~1470, ~1730 and ~1680 cm^{-1} for VO$_x$/TiO$_2$ case. The bands at 1730 and 1664 can be assigned to C=O vibrations of adsorbed acetaldehyde, the main product of ethanol oxidation over VO$_x$/TiO$_2$ surfaces[12]. The bands at 1532 and 1444 cm^{-1} could be assigned to adsorbed acetate (COO) vibrations[12,73]. Although a variety of species can be simultaneously present on the VO$_x$/TiO$_2$ surface, the thermal stability of each species is quite different. As shown in Figure 1.13, C=O bands from the CH$_3$CHO(a) appeared at 100 $^\circ$C and decreased in intensity with rising temperature up to 200 $^\circ$C. While the acetate

bands (COO) were observed at 130 ºC increasing in intensity with heating up to 200 ºC and then then nearly disappeared as heating reached 250 ºC. The authors thus, identified the surface intermediates for ethanol partial oxidation as ethoxide species, adsorbed acetaldehyde, and acetate species.

Table 1.2. Vibrational mode assignments for adsorbed surface species on TiO$_2$ and VO$_x$/TiO$_2$.

Mode	Surface species	Wavelength (cm^{-1})			
		TiO$_2$ [71]	TiO$_2$ [72]	VO$_x$/TiO$_2$ [30]	VO$_x$/Al$_2$O$_3$ [74]
ν_{as}(CH$_3$)	CH$_3$CH$_2$O(a)	2971	2971	2977	2974
ν_{as}(CH$_2$)	CH$_3$CH$_2$O(a)	2931	2931	2934	2931
ν_s(CH$_3$)	CH$_3$CH$_2$O(a)	2872, 2869	2870	2877	2870
ν(C=O)	CH$_3$CHO(a)	-	-	1730, 1680	-
ν_{as}(COO)	CH$_3$COO(a)	-	-	1532	~ 1550
ν_s(COO)	CH$_3$COO(a)	-	-	1444	1468
ν(C-O) monodentate	CH$_3$CH$_2$O(a)	1147, 1113	1119	1144, 1090	-
ν(C-C)	CH$_3$CH$_2$O(a)	-	1074	-	-
ν(C-O) bidentate	CH$_3$CH$_2$O(a)	1052	1042	1040	-
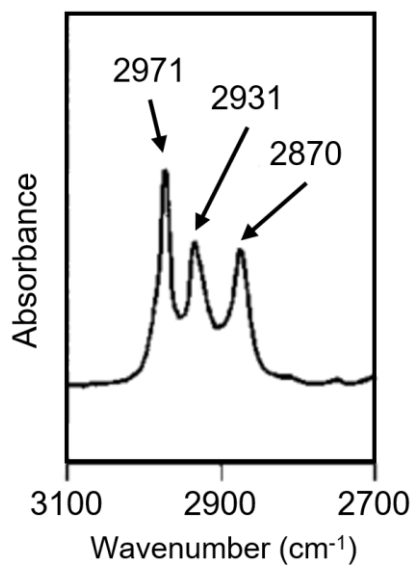
Figure 1.11. IR spectrum of TiO$_2$ exposed to ethanol and then evacuated at 200 ºC in C-O vibrational region. Reproduced with permission from [71].
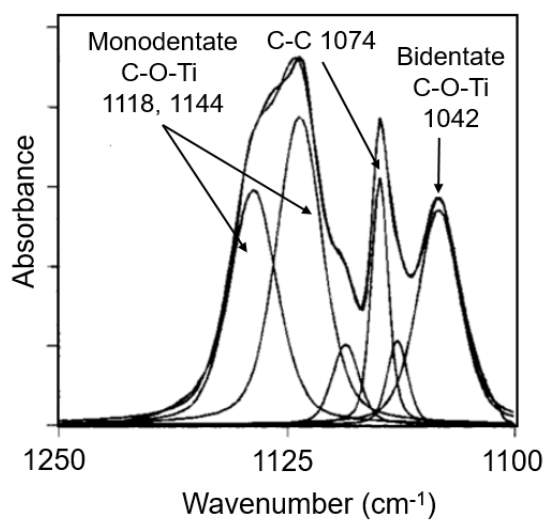
Figure 1.12. IR spectrum and curve fittings of CH$_3$CH$_2$O(a) on TiO$_2$ at 200 ºC in C-O vibrational region. Reproduced with permission from [71].
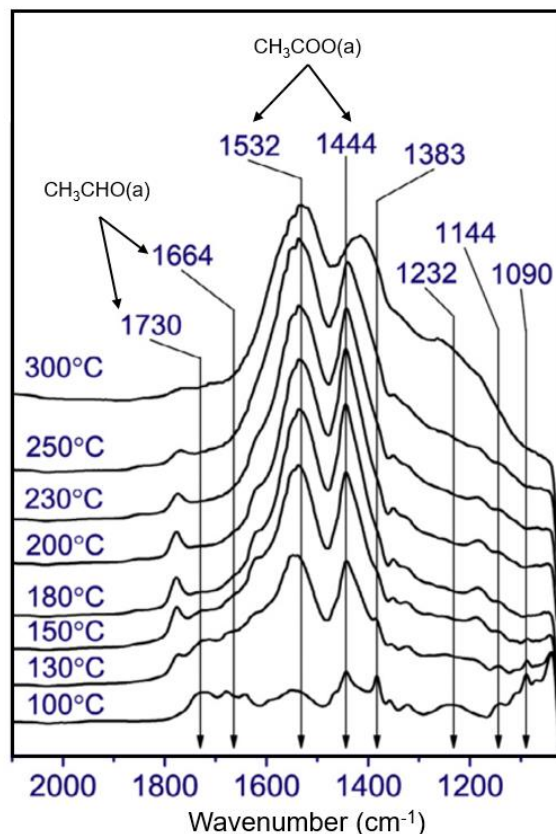
Figure 1.13 IR spectra of the VOₓ/TiO₂ catalyst obtained in flowing of ethanol/helium mixture with rising temperature. Reproduced with permission from [12].

1.2.9 *In situ* MAS NMR spectroscopy

Solid state magic angle spinning (MAS) NMR is a powerful technique for the study of supported VO_x/TiO_2 catalyst system. ^{51}V is naturally abundant (99.75%) and has quantum spin 7/2, and thus, a nuclear electric quadrupole moment. When it comes to conventional NMR, however, due to the complexity of quadrupolar and dipole interactions as well as chemical shift anisotropy interactions a dramatic broadening of NMR signals for the various VO_x species present is observed. To overcome such drawbacks, the use of MAS NMR helps in improving spectral resolution, but even using this technique NMR results on VO_x/TiO_2 catalysts are difficult to interpret[75,76]. Recently

however, Peden and coworkers successfully established ^{51}V NMR peak assignments with the aid of computational calculations[77]. At low VO_x loadings, it was found that only monomeric VO_x clusters predominantly exists, showing two ^{51}V NMR peaks at about -502 and -529 ppm, with respect to the common reference of $VOCl_3$ (0 ppm). Linear dimeric VO_x was found to have a peak at -555 and -630 ppm, assigned to bridging oxygens from V-O-Ti, and V-O-V, respectively. Lastly, linearly structured polymeric VO_x with only one bridging oxygen atom between adjacent V atoms (V-O-V) present a NMR peak at -630 ppm.

Since for the case of redox catalysis, and for partial oxidation processes in particular, oxygen exchange sites are particularly relevant, determination of the site location where oxygen exchange process occur is critical. For this purpose, ^{17}O MAS NMR were carried by Wachs and coworkers[78]. These investigations on, oxygen exchange rates for VO_x-free supports, indicated that degree of oxygen exchange capacity increases in the order of $TiO_2 > Al_2O_3 > SiO_2$.

The comparison of NMR shifts for $^{17}O_2$-exchanged references such as bulk V_2O_5 and KVO_3 enabled to identify distinct oxygen sites. They are a vanadyl (V=O, atomic distance, $d_{V=O} = 1.58\text{Å}$), and a bridging V-O-V ($double\ d_{V-O} = 1.78\text{Å}$). Obtained chemical shifts for those components, thus, correspond to 900-1400 ppm for V=O, 400-900 ppm for V-O-V, respectively. Moreover, on the basis of the ^{17}O NMR spectra obtained on a monolayer covered VO_x/TiO_2 catalysts (corresponding to about 5%wt. V_2O_5) results indicated that less lattice oxygen was exchanged in this case than when bare TiO_2 was used. This suggests that the formation of supported VO_x prevents the oxygen exchange on the TiO_2 lattice.

1.2.10 *In situ* EPR spectroscopy

Electron paramagnetic resonance (EPR) spectroscopy has been utilized to characterize catalysts from very early on in a wide range of applications from heterogeneous to homogeneous catalysts. EPR is extremely useful for the characterization of paramagnetic

species. Detailed information on paramagnetic electron environment such as its geometry, structure as well as their chemical environment can be obtained through this technique[79]. Paramagnetic species can be present as intermediates during heterogeneous catalytic reaction as well, in particular, on catalytic redox process in which electrons can be transferred between catalysts and reactants. For the case of supported VO_x catalysts, paramagnetic vanadium oxidation states such as V^{+4} and V^{+3} have been identified by EPR[77,80–82]. Dinse and coworkers extensively studied VO_x on various supports system (Al_2O_3, SiO_2, and TiO_2) and quantified paramagnetic sites before and after oxidative dehydrogenation of propane (ODP) at 450 °C[80,81,83]. The results pointed out that, in the case of VO_x over inert supports (Al_2O_3 and SiO_2), V^{+4} sites were found to be the most abundant paramagnetic species while for the case of TiO_2 supported catalysts Ti^{+3} was predominantly present instead of V^{+4}. Moreover, recent research on TiO_2 supported VO_x in combination with MAS NMR and EPR suggests the presence of both V^{+4} and Ti^{+3} species during catalytic turnovers.

1.2.11   Impedance spectroscopy

Electrochemical impedance spectroscopy (EIS) is a method to study dynamic processes of charged particles and their conductivity, carrier mobility and dielectric properties. EIS was originally developed in the field of wet electrochemistry[84]. Later on, the use of frequencies with broad bandwidth (mHz to MHz) allowed to resolve the electronic charge transport in solid materials. This technique has been employed less frequently than other spectroscopic techniques. Nevertheless, for the field of supported vanadium oxide catalysts, Görke and coworkers applied EIS to extensively investigate the redox properties of vanadium oxide on different oxide supports and to correlate defect formation with catalytic activity[85,86]. Using their results they reported oxygen defect formation enthalpies (ΔH^o_{def}) for supported VO_x catalysts. Different ΔH^o_{def} values were found depending on the support in the following order: VO_x/TiO_2 < VO_x/ZrO_2 < VO_x/SiO_2 < V_2O_5 < VO_x/MgO < VO_x/Al_2O_3. The corresponding enthalpies are summarized in Table 1.4. They also proposed the occurrence of ionic and electronic

transport during redox catalytic cycles, proposing that the reoxidation of the reduced VO_x can occur via lattice oxygen diffused from at a different site than the original site reduced during the first stage of the catalytic cycle.

Table 1.3. Defect formation enthalpies (ΔH^o_{def}) of supported VO_x catalysts.

Catalysts	VO_x/TiO_2	VO_x/ZrO_2	VO_x/SiO_2	V_2O_5	VO_x/MgO	VO_x/Al_2O_3
ΔH^o_{def} (eV)	0.55	0.85	1.11	1.3	1.62	2.8

1.2.12   Temperature programmed techniques

A large variety of temperature-programmed experiments has been implemented in heterogeneous catalysis to characterize the activation and reactivity of catalytic materials[15,60,87,88]. Temperature programmed desorption (TPD), reduction (TPR), reaction spectroscopy (TPRS) and oxidation (TPO) are thus widely used. Among these thermo-analytical techniques, TPD and TPR are the most commonly used tools for characterizing heterogeneous catalysts. In TPD studies a solid (adsorbent) is first equilibrated with an adsorbing gas (adsorptive) to form adsorbate species. After this process then temperature increases gradually, leading to desorption of gas molecules which are monitored normally by mass spectrometry. The concentration and identity of this desorbed species is then plotted against desorption temperature to obtain information on the solid materials such as, surface acidity, temperature range of adsorbate desorption, temperature of maximum desorption rate, total adsorption capacity, surface heterogeneity, in some cases the mechanism and kinetics of adsorption and desorption.

In an analogous manner, in TPR the solid catalyst is exposed to a reducing gas mixture (commonly hydrogen gas) at the same time that its temperature is linearly risen. Then the consumption of the reducing agent or the generation of reduction products in the gas phase is monitored as function of temperature. Thus TPR provides information on the

distribution of reducible sites in the catalyst and provides information on the oxidation states of supported metal oxide materials. Thus a redox, 'fingerprint' profile of the material can be obtained together with the temperature range of consumption of the reducing agent, and the total consumption of reducing agent. Comparison between TPR profiles can also provide information on the interaction between the metal oxide and its support as well as identify different valence states of metal atoms and details on the mechanism and kinetics of metal oxide reduction.

For the specific case of supported VO_x catalysts on metal oxide catalysts, TPR has widely used to determine the reducibility of VO_x on different supports. Comparison of the peak maxima when using H_2 as reductant gives the following order for the reducibility of VO_x: VO_x/ZrO_2 (357 ^oC) > VO_x/TiO_2 (399 ^oC) > VO_x/Al_2O_3 (425 ^oC) > VO_x/CeO_2 (437 ^oC) > VO_x/SiO_2 (550 ^oC)[89,90]. In particular, for the case of VO_x/TiO_2 catalysts, this technique has also been used to determine the distribution of vanadia species. Bell and coworkers extensively conducted TPR as well as isothermal oxygen chemisorption followed by reduction in a flow of hydrogen[91]. Figure 1.14 shows typical TPR profiles obtained by this group. TPR profiles of various VO_x/TiO_2 catalysts show only one predominant peak maxima for all cases. However, the reduction peak position (T_{max}) increases from 454 ^oC to 469 ^oC with an increase in VO_x loading. They also reported that T_{max} does not change beyond 6.0wt.% VO_x loading as V_2O_5, suggesting that the presence of the same kind of VO_x species at loadings beyond 6.0wt.%, probably due to formation of crystalline vanadium oxide. Lower T_{max} value observed at low VO_x loadings indicates isolated species with stronger interactions with the TiO_2 support.

Bell and coworkers carried out successive TPR/TPO cycles on VO_x/TiO_2 catalysts with different VO_x loadings (1.3wt.% to 9.8 wt.% VO_x as V_2O_5)[92]. They found out that reoxidation of monomeric vanadia species is likely to occur at lower temperatures than that of polymeric VO_x, suggesting that the catalytic turnover for monomeric species could be much faster than that for polymeric species.
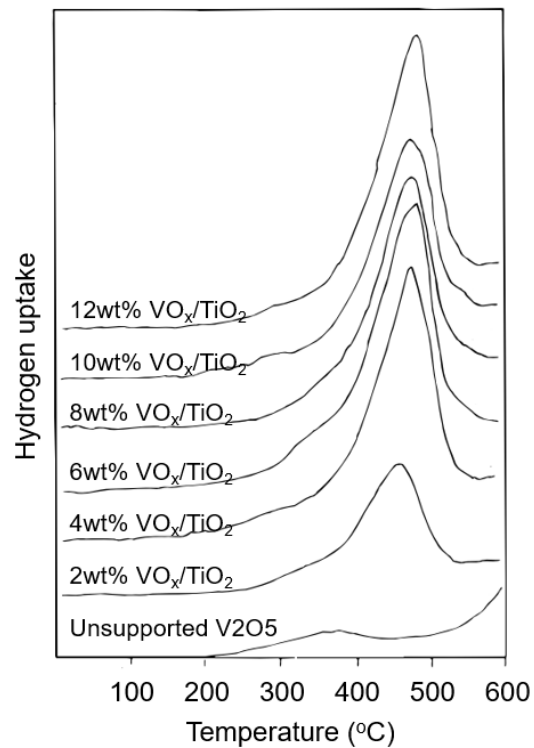
Figure 1.14. Temperature programmed reduction (TPR) profiles of VO$_x$/TiO$_2$ (anatase) catalysts. Reproduced with permission from [91].

1.2.13   Active VO$_x$ sites on titania supported vanadia catalysts

As described above, a variety of different supported vanadia structures form once these material is dispersed on a support. The common factor on all these species is the presence three types of oxygen-vanadium bonds: terminal V=O (referred in the literature as vanadyl bond), bridging V-O-V bonds and bridging V-O-M (M represents the support). After more than 20 years of intense study and debates it is commonly agreed now that the bridging V-O-V bond do not play a significant role in the redox catalytic cycle. Between the remaining two species, the determination of the real active sites that govern the catalytic performance are still under debate. In the past, a higher catalytic activity was thought to be the result of an increase on the number of V=O terminal species in the catalyst surface[15,93]. This conventional idea has been contested by Wachs and coworkers later, suggesting that the bridged V-O-M are the active sites for the oxidation reaction[40]. The role of each of these three different vanadium oxygen bonds is briefly described below.

1.2.13.1   Role of the terminal V=O bonds

Initially, the V=O terminal bond was proposed as the active surface site containing the oxygen essential for catalytic redox processes to take place[15]. However, based on *in situ* Raman spectroscopy in combination with catalytic measurements, it has been reported that there is no direct relation between the number of terminal V=O bonds and the catalytic performance of supported VO$_x$ in partial oxidation reactions. In addition to this fact, it has been also revealed that the terminal V=O bond is very stable and shows a slower isotopic exchange rate than the effective reaction rate as probed using *in situ* Raman spectroscopy experiments[10]. Consequently, it has been proposed that the terminal V=O bonds do not contain the critical oxygen atom that may affect the reactivity of supported vanadia catalyst during oxidation reactions.

1.2.13.2   Role of terminal V-O-V bonds

Generally, the surface concentration of bridging V-O-V bonds increases with VO$_x$ coverage because of the increase in the ratio of polymerized to isolated VO$_x$ monomers.

Iglesia and coworkers[73] clearly established that intrinsic catalytic activities in terms of turnover frequencies are independent of the amount of VO_x coverage in the catalyst surface, this indicated that the oxygen associated with the bridging functionality does not critically participate in the catalytic reaction during partial oxidation processes.

1.2.13.3   Role of terminal V-O-Support bonds

The role of the V-O-support bonds can be in principle evaluated by attempting to change the specific oxide support without affecting the structure of the VO_x species. This is extremely challenging since the geometry and size of the vanadium oxide clusters formed depend on the chemical identity of the support. Indirect evidence for the role of the V-O-M bond strongly suggests that the oxygen atom present in this bond is critical for the catalytic activity in partial and total oxidation reactions. This would also explain why the specific support oxide composition dramatically influences turnover frequencies values obtained after normalization by surface area and surface loading[61,94]. The inverse correlation observed between catalytic activity and the electronegativity of the different support cations confirms the role of V-O-supports bonds as critical for catalytic activity, as discussed in section 1.2.3.1[19,39]. The trend is caused by the fact that the electron density of vanadium increases and the bridging oxygen in V-O-support bonds are more electronegative when the electronegativity of the support cation decreases. Therefore, it was proposed that a higher electronic density of the vanadium atom facilitates the rate-determining step (H abstraction) leading to the formation of $V-O-CHCH_3$ bond in the case of ethanol partial oxidation. It should be consequently noted that is the oxygen in the V-O-support bond rather than the terminal V=O and V-O-V bonds the one that plays a critical role in catalytic oxidation reaction.

1.2.14   Titration of active Redox sites in catalytic materials

Identifying and quantifying the active sites in metal oxide catalysis is indispensable to determine precise turnover frequencies. For acid catalysts such as zeolites and heteropolyacid clusters (i.e. Keggin structure), the titration method for Brønsted and

Lewis acid sites is well established. Bases such as NH_3 and pyridine are frequently used to titrate and identify acid sites. Moreover, nowadays Iglesia's method for the selective titration of protons (Brønsted acid sites) with organic bases (2,6-di-tert-butylpyridine) during catalysis is used in the field of zeolitic materials[95,96] and acidic catalysts[97–99]. On the contrary, a successful methodology for titrating Redox sites has not yet been finalized for supported metal oxide catalysts. Several methods have been proposed all with accompanying advantages and drawbacks. For the case of vanadium supported catalysts, reporting the turnover rates as obtained by normalizing reaction rates by the number of metal atoms present in the catalyst (assuming all metal atoms participate in the catalytic cycle) is still widely used. In this manner, such factors as local structure and site distribution are overlooked. An alternative has been proposed where the measurement of the number of terminal vanadyl species (V=O) present in the catalysts by using ^{18}O exchange, but this method is applicable only for cases where the active site is associated with a terminal vanadyl oxygen. Oxygen chemisorption after prereduction in H_2 stream has also been attempted, but this method led to incorrect estimates at low-temperatures due to physisorbed oxygen[100]. Recently Baertsch and collaborators proposed isothermal anaerobic titration as an accurate technique to quantify active redox sites densities in supported metal oxide catalysts[74], however, this method overestimates the number active sites for the case of reducible metal oxide supports such as TiO_2 or ZrO_2, whose lattice oxygens are likely involved during catalysis.

1.2.15   Kinetics and reaction mechanism of ethanol ODH

1.2.15.1   Mars-van Krevelen mechanism

Most of the oxidation reactions carried over supported VO_x catalysts proceed via a Mars-van Krevelen redox mechanism. This mechanism was suggested in 1954 by P. Mars and D.W. van Krevelen[101]. According to the Mars-van Krevelen redox mechanism, the surface itself is an active part in the reaction. In this mechanism, the oxidation of reactants occurs by two sequential steps. The reactant molecule initially reduces an oxidized oxide surface site and then the reduced surface site is subsequently reoxidized with oxygen that comes from the catalyst itself, the lattice oxygen in this case, and not

from gas phase molecular O_2 (Langmuir-Hinshelwood mechanism). When the reaction product desorbs, a vacancy is left behind in the surface. The vacancy is now filled again by a reactant atom from the bulk, rather than directly by the gas phase. As a matter of fact, whether the vacancies are filled by the bulk or the gas phase is still a subject of intense debate in the catalysis community, even though this difference does not influence the relevant processes within the reaction mechanism[102] itself. In Fig.1.15 the Mars-van Krevelen redox mechanism is depicted.

Several kinetics and isotopic tracer studies have been conducted, demonstrating that the oxidation on VO_x domains occurs via a Mar-van Krevelen redox mechanism[10,89,101,103]. In the following section isotopic tracer studies and detailed kinetics on VO_x/TiO_2 catalyst for the oxidation are described in detail.
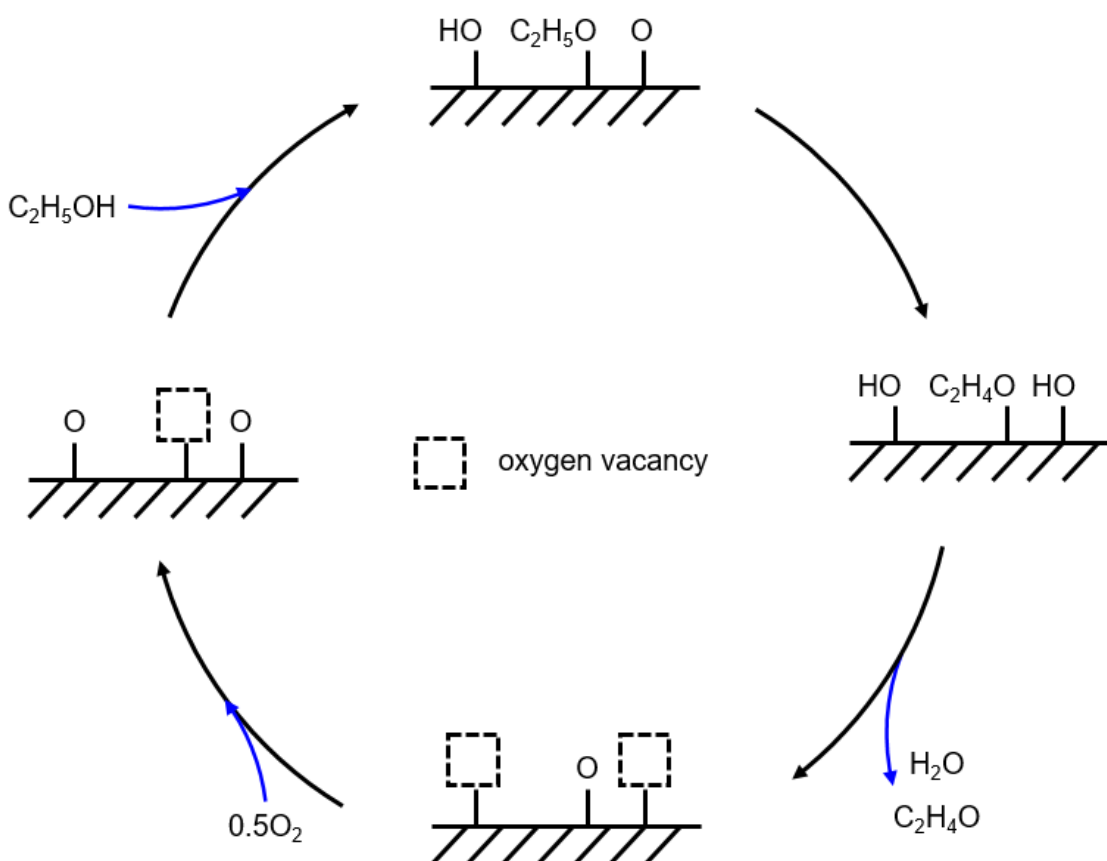
Figure 1.15. Mars−van Krevelen mechanism of ethanol partial oxidation.

1.2.16   Isotopic studies

Isotopic transient exchange experiments have been done with the purpose of proving the identity of elementary steps and the reversibility of each elementary step during catalysis. For studies on partial oxidation of ethanol over supported VO_x catalysts, Iglesia, in the recent past, identified the rate-limiting step of the reaction and the reversibility of each elementary step for ethanol partial oxidation. His group conducted isotopic studies with deuterium labeled ethanol (CH_3CH_2OD and CD_3CD_2OD) on VO_x/Al_2O_3 catalyst to confirm their mechanistic hypotheses, which assigns the rate-limiting step to the H-abstraction from the ethoxide intermediate[73]. The obtained kinetic isotopic effects (KIE) value for CH_3CH_2OD ($r_{CH_3CH_2OH}/r_{CH_3CH_2OD}$) was 1.02 indicating that ethanol adsorption (activation of O-H bonds) is quasi-equilibrated. In contrast, the KIE value for CD_3CD_2OD ($r_{CH_3CH_2OH}/r_{CD_3CD_2OD}$) was found to be ~5, undoubtedly indicating that the activation of C-H bonds is involved in the kinetically relevant step for ethanol oxidation on supported VO_x catalysts. Consistent behavior has been observed for supported MoO_x, and WO_x catalysts during ethanol oxidation reaction as well by other authors (Nair et al. 2011)[105]. The comparison of KIE values for between CH_3CD_2OH and CD_3CH_2OH also supports the fact that the activation of C-H bonds is the kinetically relevant step. Replacement of an α-H atom with D-atom (CH_3CD_2OH) in ethanol resulted in a decrease in the product formation rate, whereas that of $β$-H (CD_3CH_2OH) led to no isotope effect. This indicated that the activation of C-H bonds in the alpha CH_2 group of ethanol is the rate-limiting step for ethanol oxidation.

Indeed, transient isotopic exchange experiments confirmed the reversibility of the vanadia reoxidation step, which is the last step of ethanol partial oxidation cycle over VO_x bearing catalysts. These experiments were conducted by switching from $^{16}O_2$ to $^{18}O_2$ during ethanol oxidation[106,107]. The possible mechanisms for oxygen exchange are:

- R^0 mechanism: The oxygen molecule exchanges one of its atoms with an atom of another oxygen molecular from the gas phase, without the participation of the oxygen in the oxide, described as follows

$$^{18}O_{2(g)} + {}^{16}O_{2(g)} \rightarrow 2\,{}^{18}O\,{}^{16}O_{(g)} \qquad \text{eq.(1.7)}$$
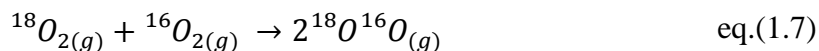
- R^1 mechanism: The oxygen molecule exchanges one of its two atoms with the surface oxygen of the solid metal oxide ($O_{(s)}$)

$$^{18}O_{2(g)} + {}^{16}O_{(s)} \rightarrow {}^{18}O\,{}^{16}O_{(g)} + {}^{18}O_{(s)} \qquad \text{eq.(1.8)}$$
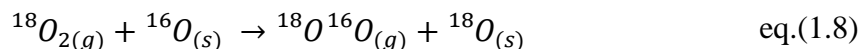
- R^2 mechanism: The oxygen molecule exchanges both its atoms with the surface oxygen of the solid metal oxide

$$^{18}O_{2(g)} + 2\,{}^{16}O_{(s)} \rightarrow {}^{16}O_{2(g)} + 2\,{}^{18}O_{(s)} \qquad \text{eq.(1.9)}$$
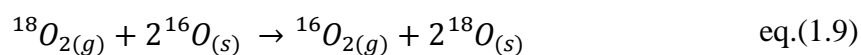
The study of isotopic oxygen exchange for VO_x/TiO_2, conducted by Sadivskaya and colleagues[106], indicated that the injection of $^{18}O_2$ into dehydrated VO_x/TiO_2 together with dry $^{16}O_2$ below 400 °C did not lead to formation of $^{16}O^{18}O$. This observation directly indicates that the dioxygen homoexchange (R^0 mechanism) and R^1 mechanisms are negligible. A similar trend was observed for experiments of propane oxidative dehydrogenation over VO_x/ZrO_2 catalysts[107]. The reversibility of the dissociative O_2 chemisorption was determined using an $^{18}O_2$-$^{16}O_2$-propane influent stream and measuring the rate of appearance of $^{16}O^{18}O$ in the product stream. Formation of $^{16}O^{18}O$ in the effluent stream below 500 °C was not observed. Therefore the authors proposed a mechanism where $^{16}O_2$ is removed from the lattice and it is replaced in equivalent amounts of either $^{16}O_2$ or $^{18}O_2$: the R^2 mechanism[107].

1.2.17   Kinetic models for ethanol partial oxidation

All of the results discussed in the previous sections can be summarized for a simplified reaction mechanism describing the partial oxidation of ethanol to acetaldehyde over vanadia supported catalysts, as depicted in Fig.1.16.
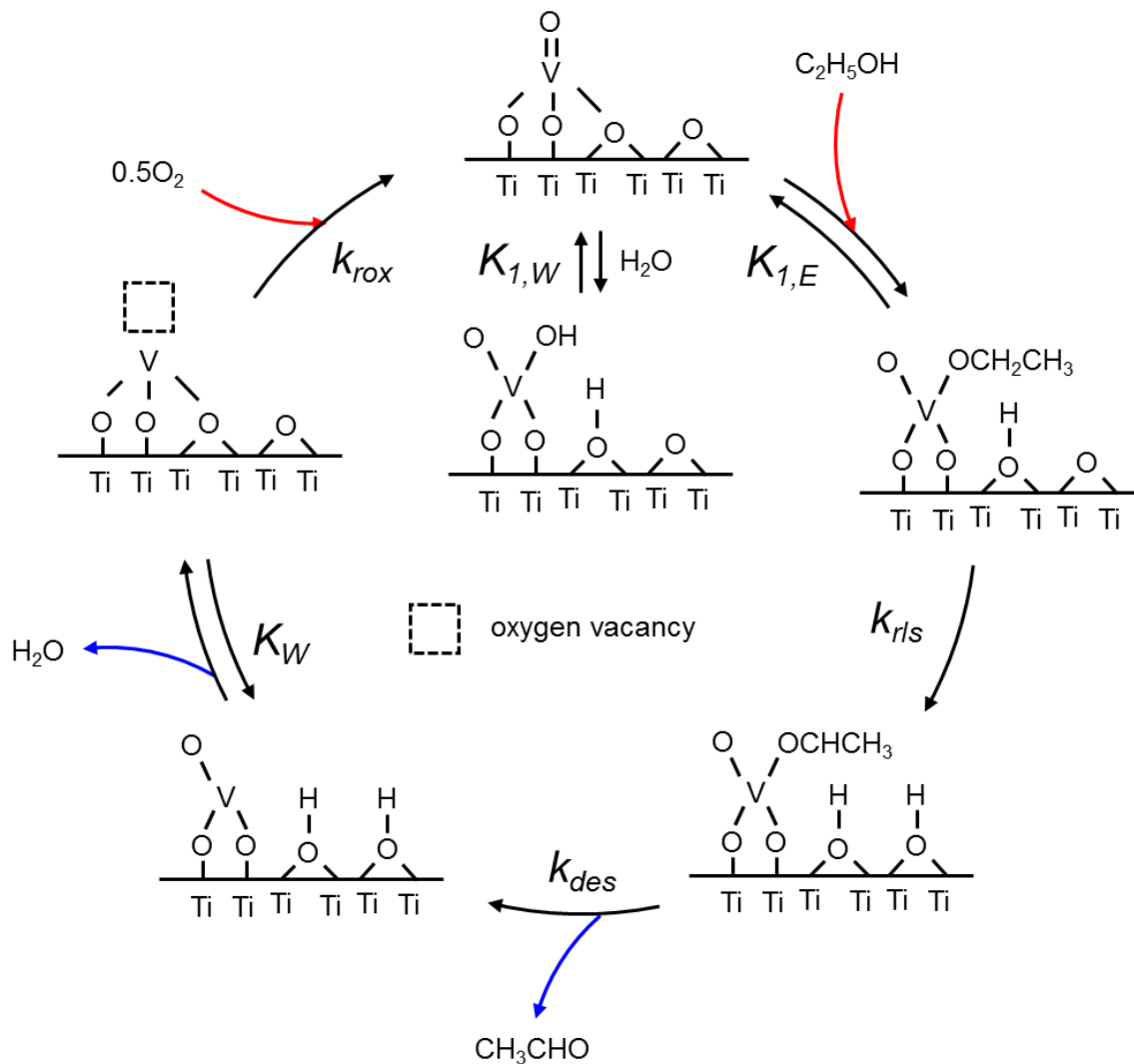
Figure 1.16 A schematic diagram for ethanol partial oxidation over VO$_x$/TiO$_2$ catalysts.

For acetaldehyde formation, the first step is the dissociative adsorption of ethanol as an ethoxy species at V-O-Ti site to form V-O-CH$_2$CH$_3$ and Ti-O-H, as widely observed by *in situ* infra-red spectroscopy studies[74] (see section 1.2.8). This step is quasi-equilibrated, as proven by kinetic isotope experiments $(r_{CH_3CH_2OH}/r_{CD_3CD_2OD} = 1.02)$[73]. This step is shown in eq.1.10:

$$CH_3CH_2OH + OV - O - Ti/O - Ti \overset{K_{1,E}}{\longleftrightarrow} CH_3CH_2O - VO/HO - Ti/O - Ti \qquad \text{eq.(1.10)}$$
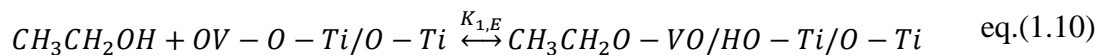
The next step is considered to be the rate-limiting step[89,108]. The α-H atom from the CH_2 group in the adsorbed ethoxy species irreversibly transfers to the adjacent O atom contained in either a V-O-Ti, or a Ti-O-Ti group. Although the majority of experimental evidence seems to indicate is the Ti-O-Ti group the one involved in this step[46]. This process is described in eq.1.11. The H abstraction concurrently results in the chemical reduction of the catalyst surface due to the removal of a redox-active species such as the bridging lattice oxygen (O in Ti-O-Ti).

$$OV - OCH_2CH_3/HO - Ti/O - Ti \xrightarrow{k_{rls}} OV - OCHCH_3/HO - Ti/HO - Ti \qquad \text{eq.(1.11)}$$
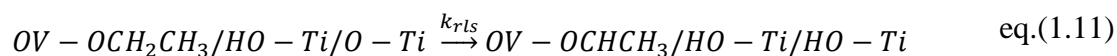
After this step the main reactions products (acetaldehyde and water) desorb. Acetaldehyde is produced from CH_3CHO-V species and the two hydroxyl pairs linked to titania can recombine to form gaseous H_2O together with a O-vacancy site. The hydroxyl recombination has been found to be reversible and almost quasi-equilibrated, based on the observed inhibition by H_2O[99,107]. These two processes are described in eq.1.12 and eq.1.13:

$$OV - OCHCH_3/HO - Ti/HO - Ti \xrightarrow{k_{des}} CH_3CHO + VO/HO - Ti/HO - Ti \qquad \text{eq.(1.12)}$$

$$VO/OH - Ti/HO - Ti \xleftrightarrow{K_w} H_2O + V - O - Ti/O - Ti \qquad \text{eq.(1.13)}$$
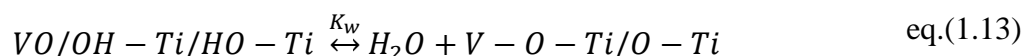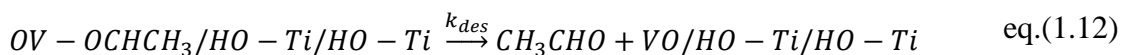
Besides, the gaseous H_2O produced also inhibits the first elementary step (eq.1.10). Because water directly interacts with the surface active sites[57,106] generating an extra elementary step which is analogous to the ethanol adsorption, as described in eq.1.14:

$$OV - O - Ti/O - Ti + H_2O \xleftrightarrow{K_{1,W}} OV - OH/HO - Ti/O - Ti \qquad \text{eq.(1.14)}$$
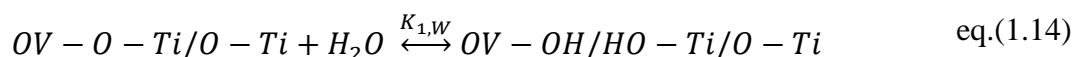
Lastly, irreversible reoxidation is typically assumed to occur via dissociative chemisorption of O_2 at oxygen vacant sites as described in sections 1.2.7 and 1.2.16. Most studies agree on the reoxidation step of VO_x bearing catalysts following a R^2 mechanism that is independent to oxygen partial pressure (see section 1.2.16). This reoxidation step is considered to be very fast as observed from microkinetic simulations and the lack of O_2 pressure effects on turnover rates[107,109]. However, there is still

disagreement on the exact surface site where reoxidation take place, although some results indicate that the reduced V atom could be the appropriate place[108]. If the reduced vanadium atom is the place of reoxidation, the irreversible reoxidation step take would take place in an oxygen vacant vanadium site through the formation of a peroxide species (eq.1.15)[110,111], followed by the adsorption of O_2. And then one O atom participates in reoxidizing the V atom (eq.1.16) and the remaining O atom (O_m) then migrates through the support until another V atom in a different catalytic site is reoxidized to regenerate the original V^{+5} species (eq.1.17). Additionally, on the basis of theoretical calculations[109], the largest activation barrier in this reoxidation pathway is found to be 68.04 $kJ \cdot mol^{-1}$, which is smaller barrier than that for H abstraction (161.7 $kJ \cdot mol^{-1}$). Thus, this step is considered to be faster and thus kinetically-irrelevant. The elementary steps for the reoxidation can therefore be described as:

$$V - O - Ti/O - Ti + O_2 \xrightarrow{k_{rox,1}} OOV - O - Ti/O - Ti \qquad \text{eq.(1.15)}$$

$$OOV - O - Ti/O - Ti \xrightarrow{k_{rox,2}} OV - O - Ti/O - Ti + O_m \qquad \text{eq.(1.16)}$$

$$V - O - Ti/O - Ti + O_m \xrightarrow{k_{rox,3}} OV - O - Ti/O - Ti \qquad \text{eq.(1.17)}$$
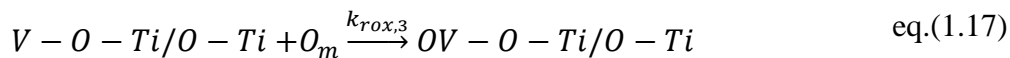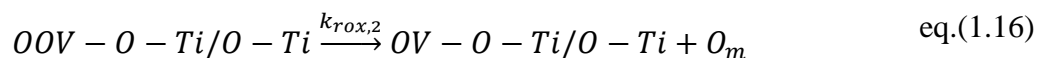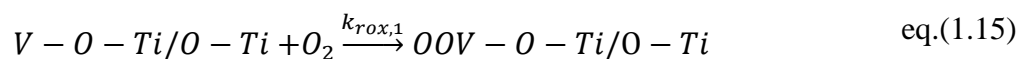
Tsilomelekis and Boghosian, have proposed a different scenario where the site for oxygen adsorption is not the reduced vanadium atom but an oxygen vacancy present on titania instead. This was based on *in situ* Raman spectroscopy in combination with $^{18}O/^{16}O$ isotope exchange observations[59]. An independent study, reporting a significant decrease observed for isotope oxygen exchange rates for VO_x/TiO_2 system at increasing VO_x coverage, supports this proposal[78]. In this particular scenario, the reoxidation step can be described as:

$$O_V + \frac{1}{2}O_2 \xrightarrow{k_{rox,4}} O \qquad \text{eq.(1.18)}$$

$$O + V - O - Ti/O - Ti \xrightarrow{k_{rox,5}} OV - O - Ti/O - Ti \qquad \text{eq.(1.19)}$$
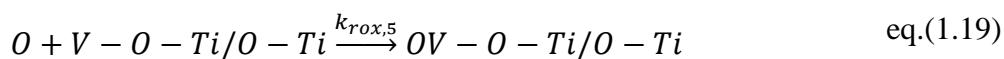
1.2.18   Summary

In this chapter, we have briefly reviewed the oxidative dehydrogenation reaction (ODH) in particular partial oxidation of alcohols over vanadia catalysts and the role of the support on the activity of the VO_x/TiO_2 system. The characterization techniques commonly used to evaluate the structure of this system were briefly discussed. In most studies, it is observed that the VO_x are heterogeneously distributed as a variety of structures, these mainly depend on vanadia loading.

In terms of catalytic activity the electronegativity of the cation in metal oxide supports seems to play a critical role. The descriptors for activity are related to redox behavior of the vanadia clusters (reducibility, oxygen defect formation energy, and the extent of reduction of VO_x) and are each of them have been proposed as single global descriptor that determines the catalytic behavior of vanadia as a redox catalyst.

Kinetic isotopic experiments conducted together with *in situ* spectroscopies have facilitated the proposal of kinetic mechanisms of partial oxidation of ethanol over VO_x/TiO_2 catalysts. The kinetic relevant steps were summarized and categorized. As discussed, H abstraction from CH_2 in the adsorbed ethoxide ($V-OCH_2CH_3$) to the lattice bridging oxygen on TiO_2 support (Ti-O-Ti) has been proposed as the rate limiting step for this process. The conflicting perspectives on the surface sites where reoxidation step takes place after surface reduction concomitantly with ethanol oxidation were discussed. These published results and discussions herewith will help to guide the discussion and rationalization of experimental data presented in the following chapters of this thesis.

1.3 Objectives

This main objectives of this dissertation are 1) to develop a kinetic and electronic model to describe the geometry, electronic structure and catalytic behavior of supported vanadia (VO_x) on both bare TiO_2 (VO_x/TiO_2) and modified TiO_2 ($VO_x/N\text{-}TiO_2$), 2) to explore the use of nitrogen-doped TiO_2 as a support for vanadia catalyst to improve its catalytic oxidative dehydrogenation activity and 3) to elucidate the role of doping nitrogen in the catalytic cycle. In order to achieve these objectives a wide range of VO_x/TiO_2 and $VO_x/N\text{-}TiO_2$ materials with different compositions and properties were prepared and tested. In particular, for the case of the nitrogen doped $VO_x/N\text{-}TiO_2$ catalytic system, both interstitial N doping (N_i) and substitutional N doping (N_s) were evaluated. The obtained materials were comprehensively characterized to confirm the presence of N in the TiO_2 matrix. The upper electronic states of all N-doped and undoped samples were probed using a battery of spectroscopic techniques. The influence of the doping N on the behavior ethanol adsorption over the prepared catalysts was evaluated using temperature programmed techniques. *In situ* UV-vis and Raman spectroscopic studies were conducted to monitor the changes in electronic structure and geometry around the vanadium atom during catalysis. To evaluate catalytic activity partial oxidation of ethanol was carried over all these materials as probe reaction. To understand the changes in electronic structure originated by nitrogen doping and taking places during catalysis, periodic density functional theory calculations were carried. Lastly, a new titration method for quantifying redox sites during catalysis was developed to get a quantitative description of real catalytic turnover rates over these materials.

1.4 Thesis outline

This dissertation is organized as follows. Chapter one presents the general background, research objectives, and a literature review of previous work on characterization, reaction mechanism, and structure of supported vanadium oxide on TiO_2. Chapter two focuses primarily on the assessment of the electronic structure of a series of VO_x/TiO_2 catalysts and its consequences for catalytic activity. Catalyst preparation and a comprehensive spectroscopic characterization and electronic structure modeling of the nitrogen doped $VO_x/N\text{-}TiO_2$ system are discussed in chapter three. Chapter four addresses the chemical identity of the VO_x structure anchored on TiO_2 structure that primarily participates on partial oxidation catalytic turnovers. Chapter five describes a newly developed method used for quantification of active catalytic redox sites in vanadia supported on titania. Finally, the overall conclusions and recommendations for future work are presented in chapter six.

References

(1)   Sun, J.; Wang, Y. *ACS Catal.* **2014**, *4* (4), 1078–1090.

(2)   Renwable fuels association. **2015**.

(3)   Tesser, R.; Maradei, V.; Di Serio, M.; Santacesaria, E. *Ind. Eng. Chem. Res.* **2004**, *43* (7), 1623–1633.

(4)   Asahi, R.; Morikawa, T.; Ohwaki, T.; Aoki, K.; Taga, Y. *Science* **2001**, *293* (5528), 269–271.

(5)   Thomas, A. G.; Syres, K. L. *Chem. Soc. Rev.* **2012**, *41* (11), 4207–4217.

(6)   Diebold, U. *Surf. Sci. Rep.* **2003**, *48* (5-8), 53–229.

(7)   Setvin, M.; Aschauer, U.; Scheiber, P.; Li, Y.-F.; Hou, W.; Schmid, M.; Selloni, A.; Diebold, U. *Science* **2013**, *341* (6149), 988–991.

(8)   Grant, J. T.; Carrero, C. A.; Love, A. M.; Verel, R.; Hermans, I. *ACS Catal.* **2015**, *5* (10), 5787–5793.

(9)   Beuhler, R. J.; Rao, R. M.; Hrbek, J.; White, M. G. *J. Phys. Chem. B* **2001**, *105* (25), 5950–5956.

(10)   Weckhuysen, B. M.; Keller, D. E. *Catal. Today* **2003**, *78* (1–4), 25–46.

(11)   Kim, H. Y.; Lee, H. M.; Metiu, H. *J. Phys. Chem. C* **2010**, *114* (32), 13736–13738.

(12)   Kaichev, V. V.; Chesalov, Y. A.; Saraev, A. A.; Klyushin, A. Y.; Knop-Gericke, A.; Andrushkevich, T. V.; Bukhtiyarov, V. I. *J. Catal.* **2016**, *338*, 82–93.

(13)   Xu, Y.; Lu, J.; Zhong, M.; Wang, J. *J. Nat. Gas Chem.* **2009**, *18* (1), 88–93.

(14)   Vogt, E. T. C.; van Dillen, A. J.; Geus, J. W.; Janssen, F. J. J. G. *Catal. Today* **1988**, *2* (5), 569–579.

(15)   Bond, G. C.; Tahir, S. F. *Appl. Catal.* **1991**, *71* (1), 1–31.

(16)   Kristoffersen, H. H.; Metiu, H. *J. Phys. Chem. C* **2016**, 13610–13621.

(17)   Khaliullin, R. Z.; Bell, A. T. *J. Phys. Chem. B* **2002**, *106*, 7832–7838.

(18)   Burcham, L. J.; Briand, L. E.; Wachs, I. E. *Langmuir* **2001**, *17* (20), 6175–6184.

(19)   Wachs, I. E. *Catal. Today* **2005**, *100* (1-2), 79–94.

(20)   Martínez-Huerta, M. V.; Fierro, J. L. G.; Bañares, M. a. *Catal. Commun.* **2009**, *11* (1), 15–19.

(21)   Bañares, M. A.; Martínez-Huerta, M. V; Gao, X.; Fierro, J. L. G.; Wachs, I. E. *Catal. Today* **2000**, *61* (1–4), 295–301.

(22) Chary, K. V. R.; Kishan, G.; Bhaskar, T. *Chem. Commun.* **1999**, *15*, 1399–1400.

(23) Haller, G. L.; Resasco, D. E. *Adv. Catal.* **1989**, *36*, 173–235.

(24) Boudart, M.; Djega-Mariadassou, G. *Kinetics of Heterogeneous Catalytic Reactions*; Princeton University Press, 1984.

(25) Toebes, M. L.; Van Dillen, J. A.; De Jong, K. P. *J. Mol. Catal. A Chem.* **2001**, *173* (1-2), 75–98.

(26) Kantcheva, M. M.; Hadjiivanov, K. I.; Klissurski, D. G. *J. Catal.* **1992**, *134* (1), 299–310.

(27) Birky, T. W.; Kozlowski, J. T.; Davis, R. J. *J. Catal.* **2013**, *298*, 130–137.

(28) Kouva, S.; Honkala, K.; Lefferts, L.; Kanervo, J. *Catal. Sci. Technol.* **2015**, *5*, 3473–3490.

(29) Lin, H.; Long, J.; Gu, Q.; Zhang, W.; Ruan, R.; Li, Z.; Wang, X. *Phys. Chem. Chem. Phys.* **2012**, *14* (26), 9468–9474.

(30) Bronkema, J. L.; Bell, A. T. *J. Phys. Chem.* **2007**, 14530–14540.

(31) Pan, X.; Yang, M. Q.; Fu, X.; Zhang, N.; Xu, Y. J. *Nanoscale* **2013**, *5* (9), 3601–3614.

(32) Klissurski, D. G. *Chem. Soc. Rev.* **1996**, *25*, 61–69.

(33) Di Valentin, C.; Finazzi, E.; Pacchioni, G.; Selloni, A.; Livraghi, S.; Paganini, M. C.; Giamello, E. *Chem. Phys.* **2007**, *339* (1–3), 44–56.

(34) Di Valentin, C.; Pacchioni, G.; Selloni, A.; Livraghi, S.; Giamello, E. *J. Phys. Chem. B* **2005**, *109* (23), 11414–11419.

(35) Finazzi, E.; Valentin, C. Di; Uni, V.; Cozzi, V.; Selloni, A. **2007**, *2* (101), 9275–9282.

(36) Zhang, Z.; Wang, X.; Long, J.; Gu, Q.; Ding, Z.; Fu, X. *J. Catal.* **2010**, *276* (2), 201–214.

(37) Zhao, D.; Huang, X.; Tian, B.; Zhou, S.; Li, Y.; Du, Z. *Appl. Phys. Lett.* **2011**, *98* (16), 162107.

(38) Deo, G.; Wachs, I. E. *J. Catal.* **1994**, *146* (2), 323–334.

(39) Wachs, I. E. *Dalt. Trans.* **2013**, *42* (33), 11762–11769.

(40) Wachs, I. E.; Weckhuysen, B. M. *Appl. Catal. A Gen.* **1997**, *157* (1–2), 67–90.

(41) Tanaka, T.; Yamashita, H.; Tsuchitani, R.; Funabiki, T.; Yoshida, S. *J. Chem. Soc.*

Faraday Trans. 1 Phys. Chem. Condens. Phases **1988**, *84* (9), 2987–2999.

(42)   Keller, D. E.; Visser, T.; Soulimani, F.; Koningsberger, D. C.; Weckhuysen, B. M. *Vib. Spectrosc.* **2007**, *43* (1), 140–151.

(43)   Keller, D. E.; Koningsberger, D. C.; Weckhuysen, B. M. *J. Phys. Chem. B* **2006**, *110* (29), 14313–14325.

(44)   Norskov, J. K.; Bligaard, T.; Rossmeisl, J.; Christensen, C. H. *PNAS* **2011**, *103* (3), 937–943.

(45)   Vittadini, A.; Selloni, A. *J. Phys. Chem. B* **2004**, *108*, 7337–7343.

(46)   Shapovalov, V.; Fievez, T.; Bell, A. T. *J. Phys. Chem. C* **2012**, *116* (35), 18728–18735.

(47)   Argyle, M. D.; Chen, K.; Resini, C.; Krebs, C.; Bell, A. T.; Iglesia, E. *J. Phys. Chem. B* **2004**, *108* (7), 2345–2353.

(48)   Argyle, M. D.; Chen, K.; Resini, C.; Krebs, C.; Bell, A. T.; Iglesia, E. *Chem. Commun.* **2003**, *16*, 2082–2083.

(49)   Gao, X.; Bare, S. R.; Weckhuysen, B. M.; Wachs, I. E. *J. Phys. Chem. B* **1998**, *102* (52), 10842–10852.

(50)   Gao, X.; Bare, S. R.; Fierro, J. L. G.; Wachs, I. E. *J. Phys. Chem. B* **1999**, *103* (4), 618–629.

(51)   Burcham, L.; Deo, G.; Gao, X.; Wachs, I. *Top. Catal.* **2000**, *11-12* (1-4), 85–100.

(52)   Gao, X.; Bañares, M. A.; Wachs, I. E. *J. Catal.* **1999**, *188* (2), 325–331.

(53)   Gao, X.; Wachs, I. E. *J. Phys. Chem. B* **2000**, *104* (6), 1261–1268.

(54)   Weber, R. S. *J. Catal.* **1995**, *151* (2), 470–474.

(55)   Zhang, J.; Li, M.; Feng, Z.; Chen, J.; Li, C. *J. Phys. Chem. B* **2005**, *110* (2), 927–935.

(56)   Wu, Z.; Rondinone, A. J.; Ivanov, I. N.; Overbury, S. H. *J. Phys. Chem. C* **2011**, *115* (51), 25368–25378.

(57)   Weckhuysen, B. M.; Centrum, V.; Opper, V.; Interfasechemie, D.; Leu, K. U. V; Wachs, I. E. *J. Phys. Chem. C* **2000**, *112*, 7382–7387.

(58)   Christodoulakis, A.; Machli, M.; Lemonidou, A. A.; Boghosian, S. *J. Catal.* **2004**, *222* (2), 293–306.

(59)   Tsilomelekis, G.; Boghosian, S. *J. Phys. Chem. C* **2011**, *115* (5), 2146–2154.

(60)   Wu, Z.; Kim, H.-S.; Stair, P. C.; Rugmini, S.; Jackson, S. D. *J. Phys. Chem. B* **2005**, *109* (7), 2793–2800.

(61)   Carrero, C. A.; Keturakis, C. J.; Orrego, A.; Schomacker, R.; Wachs, I. E. *Dalt. Trans.* **2013**, *42* (35), 12644–12653.

(62)   Jehng, J.-M.; Deo, G.; Weckhuysen, B. M.; Wachs, I. E. *J. Mol. Catal. A Chem.* **1996**, *110* (1), 41–54.

(63)   Weckhuysen, B. M.; Jehng, J.-M.; Wachs, I. E. *J. Phys. Chem. B* **2000**, *104* (31), 7382–7387.

(64)   Zaera, F. *Chem. Soc. Rev.* **2014**, *43* (22), 7624–7663.

(65)   Burcham, L. J.; Badlani, M.; Wachs, I. E. *J. Catal.* **2001**, *203*, 104–121.

(66)   Baron, M.; Abbott, H.; Bondarchuk, O.; Stacchiola, D.; Uhl, A.; Shaikhutdinov, S.; Freund, H.-J.; Popa, C.; Ganduglia-Pirovano, M. V.; Sauer, J. *Angew. Chem. Int. Ed. Engl.* **2009**, *48* (43), 8006–8009.

(67)   Freund, H.-J. *Chem. Eur. J* **2010**, *16* (31), 9384–9397.

(68)   Schraml-Marth, M.; Wokaun, A.; Baiker, A. *J. Catal.* **1990**, *124* (1), 86–96.

(69)   Hadjiivanov, K. I.; Klissurski, D. G. *Chem. Soc. Rev.* **1996**, *25* (1), 61.

(70)   Feng, Z.; Lu, J.; Feng, H.; Stair, P. C.; Elam, J. W.; Bedzyk, M. J. *J. Phys. Chem. Lett.* **2012**, *4* (2), 285–291.

(71)   Wu, W.-C.; Chuang, C.-C.; Lin, J.-L. *J. Phys. Chem. B* **2000**, *104* (36), 8719–8724.

(72)   Yu, Z.; Chuang, S. S. C. *J. Catal.* **2007**, *246* (1), 118–126.

(73)   Kilos, B.; Bell, A. T.; Iglesia, E. *J. Phys. Chem. C* **2009**, *113* (7), 2830–2836.

(74)   Nair, H.; Baertsch, C. *J. Catal.* **2008**, *258* (1), 1–4.

(75)   Nielsen, U. G.; Topsøe, N. Y.; Brorson, M.; Skibsted, J.; Jakobsen, H. J. *J. Am. Chem. Soc.* **2004**, *126* (15), 4926–4933.

(76)   Eckert, H.; Wachs, I. E. *J. Phys. Chem.* **1989**, *93* (V), 6796–6805.

(77)   Hu, J. Z.; Xu, S.; Li, W.-Z.; Hu, M. Y.; Deng, X.; Dixon, D. A.; Vasiliu, M.; Craciun, R.; Wang, Y.; Bao, X.; Peden, C. H. F. *ACS Catal.* **2015**, *5* (7), 3945–3952.

(78)   Klug, C. a.; Kroeker, S.; Aguiar, P. M.; Zhou, M.; Stec, D. F.; Wachs, I. E. *Chem. Mater.* **2009**, *21* (18), 4127–4134.

(79)   Risse, T.; Hollmann, D.; Brückner, A. *Catalysis : Chapter 1: In situ electron paramagnetic resonance (EPR) – a unique tool for analysing structure and reaction behaviour of paramagnetic sites in model and real catalysts*; 2015.

(80)   Dinse, A.; Ozarowski, A.; Hess, C.; Schomäcker, R.; Dinse, K.-P. *J. Phys. Chem. C* **2008**, *112* (45), 17664–17671.

(81)   Dinse, A.; Carrero, C.; Ozarowski, A.; Schomäcker, R.; Schlögl, R.; Dinse, K.-P. *ChemCatChem* **2012**, *4* (5), 641–652.

(82)   Arnarson, L.; Rasmussen, S. B.; Falsig, H.; Lauritsen, J. V.; Moses, P. G. *J. Phys. Chem. C* **2015**, *119* (41), 23445–23452.

(83)   Rusiecka, M.; Grzybowska, B.; Ga̧sior, M. *Appl. Catal.* **1984**, *10* (2), 101–110.

(84)   Boukamp, B. *Solid State Ionics* **2004**, *169* (1-4), 65–73.

(85)   Harth, M.; Mitdank, R.; Habel, D.; Görke, O.; Tovar, M.; Winter, H.; Schubert, H. *Int. J. Mater. Res.* **2013**, *104* (7), 657–665.

(86)   Harth, M.; Mitdank, R.; Habel, D.; Görke, O.; Tovar, M.; Winter, H.; Schubert, H. *Int. J. Mater. Res.* **2013**, *104* (7), 657–665.

(87)   Besselmann, S.; Freitag, C.; Hinrichsen, O.; Muhler, M. *Phys. Chem. Chem. Phys.* **2001**, *3* (21), 4633–4638.

(88)   Janssen, F. *Thermochim. Acta* **1989**, *148*, 137–147.

(89)   Beck, B.; Harth, M.; Hamilton, N. G.; Carrero, C.; Uhlrich, J. J.; Trunschke, A.; Shaikhutdinov, S.; Schubert, H.; Freund, H.-J.; Schlögl, R.; Sauer, J.; Schomäcker, R. *J. Catal.* **2012**, *296* (0), 120–131.

(90)   Ferreira, M. .; Volpe, M. *J. Mol. Catal. A Chem.* **2002**, *184* (1-2), 349–360.

(91)   Chary, K. V. R.; Kishan, G.; Bhaskar, T.; Sivaraj, C. *J. Phys. Chem. B* **1998**, *102* (35), 6792–6798.

(92)   Went, G. T.; Leu, L.; Bell, A. T. *J. Catal.* **1992**, *134* (2), 479–491.

(93)   Mori, K.; Inomata, M.; Miyamoto, A.; Murakami, Y. *J. Phys. Chem.* **1983**, *87* (23), 4560–4561.

(94)   Carrero, C. A.; Schloegl, R.; Wachs, I. E.; Schomaecker, R. *ACS Catal.* **2014**, *4*, 3357–3380.

(95)   Liu, H.; Bayat, N.; Iglesia, E. *Angew. Chemie* **2003**, *115* (41), 5226–5229.

(96)   Jones, A. J.; Carr, R. T.; Zones, S. I.; Iglesia, E. *J. Catal.* **2014**, *312*, 58–68.

(97)   Baertsch, C. D.; Komala, K. T.; Chua, Y.-H.; Iglesia, E. *J. Catal.* **2002**, *205* (1), 44–57.

(98)   Macht, J.; Iglesia, E. *Phys. Chem. Chem. Phys.* **2008**, *10* (35), 5331–5343.

(99)   Deshlahra, P.; Carr, R. T.; Chai, S.-H.; Iglesia, E. *ACS Catal.* **2015**, *5* (2), 666–682.

(100)   Oyama, S. T.; Went, G. T.; Lewis, K. B.; Bell, A. T.; Somorjai, G. A. *J. Phys. Chem.* **1989**, *93* (18), 6786–6790.

(101)   Mars, P.; van Krevelen, D. W. *Chem. Eng. Sci.* **1954**, *8*, 41–59.

(102)   Herbschleb, C. T. Imaging Catalysts under Realistic Conditions, 2011.

(103)   Rozanska, X.; Fortrie, R.; Sauer, J. *J. Am. Chem. Soc.* **2014**, *136* (21), 7751–7761.

(104)   Nair, H.; Gatt, J. E.; Miller, J. T.; Baertsch, C. D. *J. Catal.* **2011**, *279* (1), 144–154.

(105)   Oyama, S. T.; Zhang, W. *J.Am.Chem.Soc.* **1996**, *118* (21), 7173.

(106)   Sadovskaya, E. M.; Goncharov, V. B.; Gulyaeva, Y. K.; Popova, G. Y.; Andrushkevich, T. V. *J. Mol. Catal. A Chem.* **2010**, *316* (1-2), 118–125.

(107)   Chen, K.; Khodakov, A.; Yang, J.; Bell, A. T.; Iglesia, E. **1999**, *333*, 325–333.

(108)   Chen, K.; Iglesia, E.; Bell, A. T. *J. Catal.* **2000**, *192* (1), 197–203.

(109)   Goodrow, A.; Bell, A. T. *J. Phys. Chem. C* **2008**, *112* (34), 13204–13214.

(110)   Li, Y.-F.; Aschauer, U.; Chen, J.; Selloni, A. *Acc. Chem. Res.* **2014**, *47*, 3361–3368.

(111)   Linh, N. H.; Nguyen, T. Q.; Diño, W. A.; Kasai, H. *Surf. Sci.* **2015**, *633*, 38–45.

Chapter 2

2 The effect of interstitial nitrogen in the activity of the VO$_x$/N-TiO$_2$ catalytic system for ethanol partial oxidation

This chapter is based on Dongmin Yun et al., *Journal of molecular catalysis: A chemical*, 390, 169-177, (2014)

Abstract

Interstitial nitrogen (N) doped titanium dioxide was prepared and used as support for vanadium oxide to test the nitrogen effect on vanadia-catalyzed partial oxidation processes. Ethanol partial oxidation catalytic studies and surface studies on the structure of the N doped support before and after vanadia loading indicate that nitrogen acts as a promoter of catalytic activity. Samples were characterized by X-ray diffraction, electron dispersive X-ray, and surface area measurements to evaluate their crystallinity, surface chemical composition and surface area. Diffuse reflectance UV-visible and Fourier transform infra-red spectroscopy, together with X-ray photoelectron spectroscopy were used to probe the effect of nitrogen on the vanadia-titanium dioxide interaction. The band gap edge energies obtained for the vanadium oxide species suggest that the size of the vanadia cluster is larger on the nitrogen doped catalysts compared to the ones observed in the N-free support, pointing to a weaker interaction between vanadia and TiO$_2$ when nitrogen is present. At the same time and *in situ* Fourier transform infra-red spectroscopy studies indicate that interstitial N exists in the catalyst surface in forms of hyponitrite or nitrite-like species. A model in which nitrogen affects vanadia dispersion and ethanol adsorption capacity is proposed to explain all these observations.

2.1 Introduction

Catalytic systems based on vanadium oxides are known to be highly active and selective for a number of industrially relevant chemical transformations[1–3]. Several supports have been used to improve mechanical strength, thermal stability and catalyst lifetime[3,4] and studies on these systems have shown that both catalytic activity and selectivity are fairly dependent on the physicochemical nature of the support. For instance, high catalytic activity can be achieved when TiO_2, Al_2O_3, and ZrO_2 are used to support vanadium oxides, contrasting those observed on SiO_2 and MgO supported systems[5–7]. It is widely recognized now that among these supports, TiO_2 leads to an enhancement of the catalytic properties of VO_x[2,4,8,9].

At the same time, the physicochemical properties of titania can be modified by introduction of nitrogen (N), carbon (C) or sulfur (S)[10–12] into its surface or lattice structure. Several studies have been reported on nitrogen doped TiO_2 (N-TiO_2), focusing in a particular on photo-catalytic degradation of a range of environmental pollutants[13,14]. These studies indicate that nitrogen doping can be classified as substitutional and/or interstitial. And that the specific type of nitrogen doping obtained is strongly dependent on the protocol used to incorporate nitrogen into titania. In terms of the effectiveness of doping in improving TiO_2 photocatalytic activity, Diwald et al. suggested that interstitial N on TiO_2 would exhibit higher activity than substitutional N on TiO_2 for photo-catalyst[15]; while Feng et al. reported a synergistic effect in which the combination of interstitial and substitutional N resulted in improved activity[16]. Recently, Zizhong et al. proposed that band-gap tuning of N doped TiO_2 can be used to optimize the photo-catalytic activity for selective oxidation of alcohols to aldehydes in aqueous solution[17].

In this contribution, we report the effect of N doping on TiO_2 as VO_x catalyst support using gas phase ethanol partial oxidation as probe reaction. Our results indicate that the activity of this catalytic system is dependent on the content of doped N in N-TiO_2/VO_x. Detailed spectroscopic characterization of these materials suggest that nitrogen species present in the surface of the doped titania support play an important role on promotion of the VO_x/TiO_2 catalytic system.

2.2 Experimental

2.2.1 Catalyst Preparation

The nitrogen doped titanium dioxide supports were prepared by an hydrothermal process using a protocol previously reported[18]. Titanium tetrachloride (TiCl$_4$, Sigma Aldrich) was injected (8 mL) using a syringe pump (0.13 mL·min^{-1}) into an aqueous solution containing polyethylene glycol (1g, Alfa Aesar) and urea cooled in an ice bath at 0 ℃. The resulting solution was transferred into a Teflon coated stainless steel autoclave and heated at 105 °C for 6 hours; after heating a white precipitate was obtained. The obtained solids were washed with de-ionized water using centrifugation and then dried in an oven overnight at 110 ℃. After this step samples were calcined at 500 °C for 10 hours in dry air. Samples with two different nominal loadings of N were prepared: T1N (synthesized with 1g urea (CH$_4$N$_2$O, Sigma Aldrich) and T2N (with 2g urea) respectively. A sample without nitrogen (0g, urea) was also prepared and used for reference.

Vanadium oxide was incorporated into the surface of these materials after calcination. To calculate the nominal loading of VO$_x$ to be incorporated a BET surface area analysis was conducted on the N-TiO$_2$ supports. Desired loadings of vanadia were calculated based on a nominal vanadium oxide surface density of 3 V atoms·nm^{-2} for all samples. Vanadium oxide at the nominal desired mass loading was then incorporated using chemical vapor deposition. For this purpose N-TiO$_2$ samples were placed in a 20 mm tubular quartz reactor (15 mm i.d.) and heated in helium (Praxair, UHP, 2.0 cm^3·min^{-1}) from ambient temperature to 200 °C at the rate of 6 °C·min^{-1} and then held at 200 °C for 30 min. After this step vanadium oxytriethoxide (VO(OEt)$_3$, Sigma-Aldrich, 95%) was vaporized for 1 h unto the flowing He current at ambient pressure and 200 °C using a micro syringe pump to deliver the vanadium precursor. The total volume of VO(OEt$_3$) injected was adjusted to achieve the desired nominal loading of vanadium oxide. After this step, the system was flushed in pure helium for an hour at 200 ℃. This was followed by calcination in dry air at 400 °C for 2 hours to obtain the final materials. The final amount of vanadia incorporated in the samples was quantified by a spectrophotometric method using a series of VO$_x$-TiO$_2$ reference materials of known vanadium content. UV-Vis

absorption values at 422 nm were obtained for these reference materials together with those of the CVD samples. Bare TiO_2 or N-doped support were used as reference to prevent any contribution from the O $\rightarrow$ Ti charge transfer band. The results indicated a 40-30% efficiency on vanadia deposition during chemical vaporization of vanadium oxytriethoxide.

2.2.2   Catalyst Characterization

The elemental composition of obtained N-TiO_2 supports was determined by X-ray photoelectron spectroscopy (XPS) conducted on a Kratos Axis Ultra spectrometer with a monochromatic Al Kα radiation as the exciting source (15 mA, 14 kV). The binding energies were calibrated by referencing the C1s peak as 284.8 eV to reduce sample charge effect. Energy dispersive X-ray (EDX) analysis was carried using a Hitachi Variable-Pressure Scanning Electron Microscope. X-ray diffractograms (XRD) were recorded on a Rigaku RINT 2500 instrument (Tokyo, Japan) using CuKα radiation (λ = 1.54Å), operated at 40 kV and 50 mA with a scan rate of 0.02 degrees per second over a 2θ range of 20° to 80°. BET surface area of synthesized samples was determined by a Micromeritics TriStar 3000. UV-Vis spectroscopy measurements were carried in diffuse reflectance mode (DRS, Harrick, Praying Mantis) on a Shimadzu UV-Vis 3600 spectrophotometer. The spectra were collected between 200 and 800 nm using barium sulfate ($BaSO_4$, Sigma Aldrich, 99%) as a reference for the case of the samples without vanadium. For the samples containing vanadium the bare (VO_x free) TiO_2 and nitrogen doped TiO_2 materials were used to obtain the spectral baseline before the VO_x containing samples were analyzed.

2.2.3   Ethanol Partial Oxidation

Before catalytic testing all samples were pressed into wafers, crushed and sieved to a pellet size between 425 – 600 μm. Steady-state partial oxidation of ethanol was

conducted in a continuous flow fixed bed quartz glass micro reactor (5 mm O.D.) oriented vertically in an electrically heated furnace at atmospheric pressure. Reactant and product concentrations were measured using an online gas chromatograph (Shimadzu gas chromatograph, GC-2014) containing a capillary column (BP-5, 30 m $\times$ 0.53 mm, 1.0 μm thickness) connected to a flame ionization detector. VO_x-coated catalyst samples were loaded into the glass reactor, held in the reactor's quartz frit and placed in the furnace. The catalyst was heated to 200 °C in 30 min under O_2/He mixture (5% O_2, Praxair, UHP) at a flow rate of 20 $cm^3 \cdot min^{-1}$. Absolute ethanol (Brampton, Ontario) was introduced into the reactor by vaporizing it into the flowing O_2/He mixture at 150 °C using a microsyringe pump. Reactant conversions were varied by changing the O_2/He flow rate (1.38 - 3.47 $cm^3 \cdot s^{-1}$) equivalent to weight hourly space velocity (657 – 1642 mol ethanol / mol V·h^{-1}) at constant ethanol partial pressures (0.23 kPa) and temperature (200 °C). The conversion was kept under 40% so that differential reaction conditions could be assumed. Conversion and selectivity to products were calculated on a carbon molar basis, expressed as a mol% ratio of ethanol transformed to ethanol fed, and a ratio of ethanol transformed to each product relative to the total ethanol transformed, respectively. The normalized rate of partial oxidation of ethanol was calculated according to eq. (2.1) :

$$ r_{\text{EtOH ox}} = \frac{\rho F}{60 \, MW \times mole \, of \, V} X_{\text{EtOH}} \qquad \text{eq.(2.1)} $$

Where $r_{\text{EtOH ox.}}$ is the rate of partial oxidation (sec^{-1}), F is the total volumetric flow (cm^3 $_{STP} \cdot min^{-1}$), ρ refers to the density of ethanol ($g \cdot cm^{-3}$), MW is the molecular weight of ethanol ($g \cdot mol^{-1}$), and X_{EtOH} is the ethanol conversion, the rates were normalized by the molar amount of vanadium present in the sample.

2.2.4　*In situ* DRIFTs study

In situ DRIFTs experiments were carried on a FTIR Vertex 70, Bruker, equipped with a MCT detector and a diffuse reflectance cell (Harrick Scientific Co., Praying Mantis) with an *in situ* reaction chamber. Samples (35 mg) were supported on a stainless steel screen mesh (4.7 mm Di.) inside the reaction chamber. The reaction chamber is equipped with

two ZnSe windows, (cut off at 600 cm^{-1}), water cooling and electrical heating systems. The temperatures of the samples were measured using a K-type thermocouple. The samples were heated to 300 °C under a 50 cm^3·min^{-1} flow of He (Praxair, UHP) flow for 1 hour at a rate of 10 °C·min^{-1} then cooled to 25 °C. The spectral baseline was recorded at these conditions. Absolute ethanol was stored in a glass bubbler at 0 °C and slowly introduced to IR cell using a 10 cm^3·min^{-1} flow of He. The flow of ethanol achieved under these conditions was 82.6 μmol·min^{-1}, as measured using gas chromatography. Ethanol flowed past through the IR cell directly to a gas chromatograph (Shimadzu gas chromatograph, GC-2014) containing a capillary column (BP-5, 30 m × 0.53 mm, 1.0 μm thickness) connected to a flame ionization detector. Once the ethanol concentration was set to equilibrium, IR spectra were obtained continuously with a 4 cm^{-1} resolution. This step was followed by purging of the gas phase ethanol inside the FTIR reaction chamber using a current of 50 cm^3·min^{-1} of He for 30 min; spectra were recorded during and after this stage as well. The entire optical path outside the *in situ* cell was purged with high purity N_2 during spectral acquisition.

2.2.5   Ethanol pulse adsorption experiments

The same reactor system used for the catalytic tests was modified to operate in pulse mode. In this case, a six-port valve was connected to the reactor inlet, outlet and a 100 μL gas sampling sample loop to switch the flow and inject a pulse of ethanol. The reactor system included a parallel ¼ in. stainless steel tube used for bypass. All reactor lines, the six port valve and bypass tube were heated using heating tape to avoid ethanol condensation. The feed was injected using a micro syringe pump, evaporated in the injection port and carried by He gas flow (50 cm^3·min^{-1}, Praxair) into the sampling valve to fill the loop while the reactor holding the sample (10 mg) was kept at 200 °C in a He stream. Then, by switching the six-port valve, a pulse of ethanol was send to the reactor and carried into a FID (SRI 110) detector for analysis. The lag time of ethanol from the point of injection to the time at which it reached the detector was set to less than 30 seconds to reduce sample dispersion. Before starting the pulse reaction experiment over the catalyst, ethanol pulses were sent repeated times through the bypass line to verify

stability of the FID signal. The FID signal response was calibrated by injecting known amounts of ethanol directly to the system.

2.3   Results and Discussion

2.3.1   Catalyst Characterization

Figure 2.1 shows the XRD patterns obtained for the different titania supports (TiO_2, T1N and T2N). Four strong diffraction peaks were observed at 22.5°, 27.6°, 36.3°, and 54.5° indicating the presence of crystalline anatase and rutile. Nitrogen associated peaks were not observed. The phase contents of the samples were estimated from their XRD patterns using eq.2.2[19]:

$$x_A = \frac{1}{1+1.26 \times \frac{I_R}{I_A}} \qquad \text{eq. (2.2)}$$

Where x_A is the fraction of anatase phase, I_R and I_A are the intensities of the anatase (101) and rutile (110) diffraction peak. The contents of anatase phase in TiO_2, T1N and T2N were estimated to be 0.65, 0.57, and 0.69, respectively indicating that the addition of urea did not affect the phase content of the obtained samples, this is consistent with previous reports[18,20]. These results are summarized in Table 2.1 together with BET surface area, EDX and XPS results obtained on these samples.
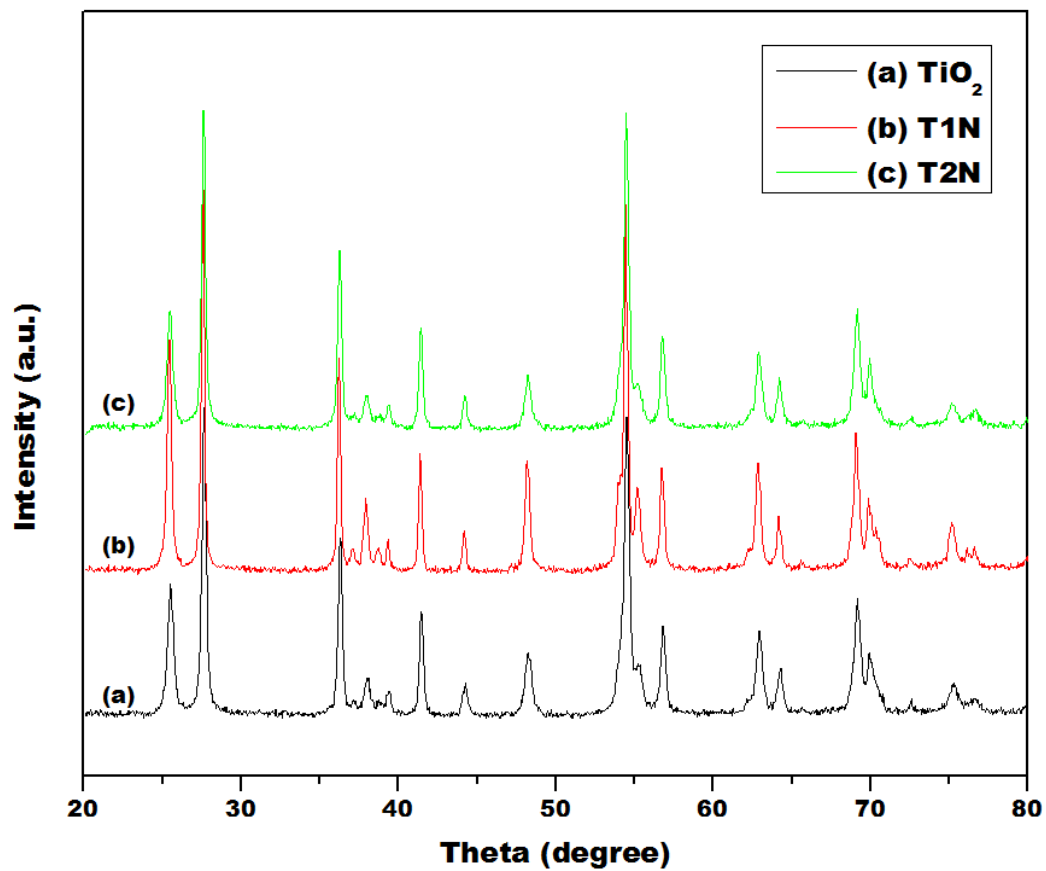
Figure 2.1. XRD patterns of synthesized (a) TiO₂, (b) T1N and (c) T2N materials.

Table 2.1. Textural properties of TiO$_2$, T1N, and T2N materials.

Catalyst	BET (m^2/g)	Crystallinity (x_A)	N Content wt % (EDX)	N Content at% (XPS)	O Content at% (XPS)	Ti Content at% (XPS)
TiO$_2$	24.3	Rutile/Anatase (0.65)	-	-	-	-
T1N	12.6	Rutile/Anatase (0.57)	3.3 ± 0.2	1.1	68.0	30.9
T2N	24.6	Rutile/Anatase (0.69)	7.5 ± 1.5	1.3	67.9	30.8

The XPS elemental analysis obtained on the T1N and T2N samples, shown in Table 2.1 are in agreement with those obtained by EDX analysis as both indicate a larger nitrogen content on the sample prepared using a larger amount of urea, although the differences are more pronounced in the bulk (EDX) than in the surface (EDX result indicating that the average surface nitrogen content for the T1N sample is 3.3% while for the T2N sample is 7.5%). The differences between the EDX and XPS results are likely due to the larger surface area of the T2N support. The high resolution XPS data and their fitting for the Ti2p, O1s, and N1s peaks are depicted in Figure 2.2 and Table 2.2, Figure 2.2 (a) and (d) show the Ti2p core level spectra for the T1N and T2N samples. Fitting of the Ti 2p$_{3/2}$ region for T1N and T2N indicates peak maxima at 458.5 and 458.7 eV respectively. The values obtained for pristine TiO$_2$ and TiN as reference (not shown) were 459.1 eV and 455.2 eV respectively. The slight shift in binding energy observed in the T1N and T2N samples is thus linked to the presence of nitrogen.

Table 2.2. Results for the fittings of the high resolution XPS spectra of the N-doped samples; (a) N1s core-level and (b) O1s and Ti 2p core-level. (N_a : absorbed nitrogen species, N_{I1} and N_{I2} : interstitial nitrogen, O_L : Lattice oxide, O_o: Non-lattice oxygen)

(a)	N_A (NO_x)			N_{I1} (N_2O_2)$^{2-}$			N_{I2} (NO_2)$^-$		
	B.E	FWHM	Area %	B.E	FWHM	Area %	B.E	FWHM	Area %
T1N	399.7	2.0	80.4	401.7	1.4	19.6	-	-	-
T2N	399.7	2.1	75.8	402.0	1.8	22.3	404.2	0.7	1.9

(b)	O_L (Ti-O-N)			O_o (Others)			Ti $2_P3/2$		
	B.E	FWHM	Area %	B.E	FWHM	Area %	B.E	FWHM	Area %
T1N	529.7	1.2	77.8	531.1	2.7	22.2	458.5	1.19	100
T2N	529.9	1.2	81.1	531.3	2.3	18.8	458.7	1.15	100
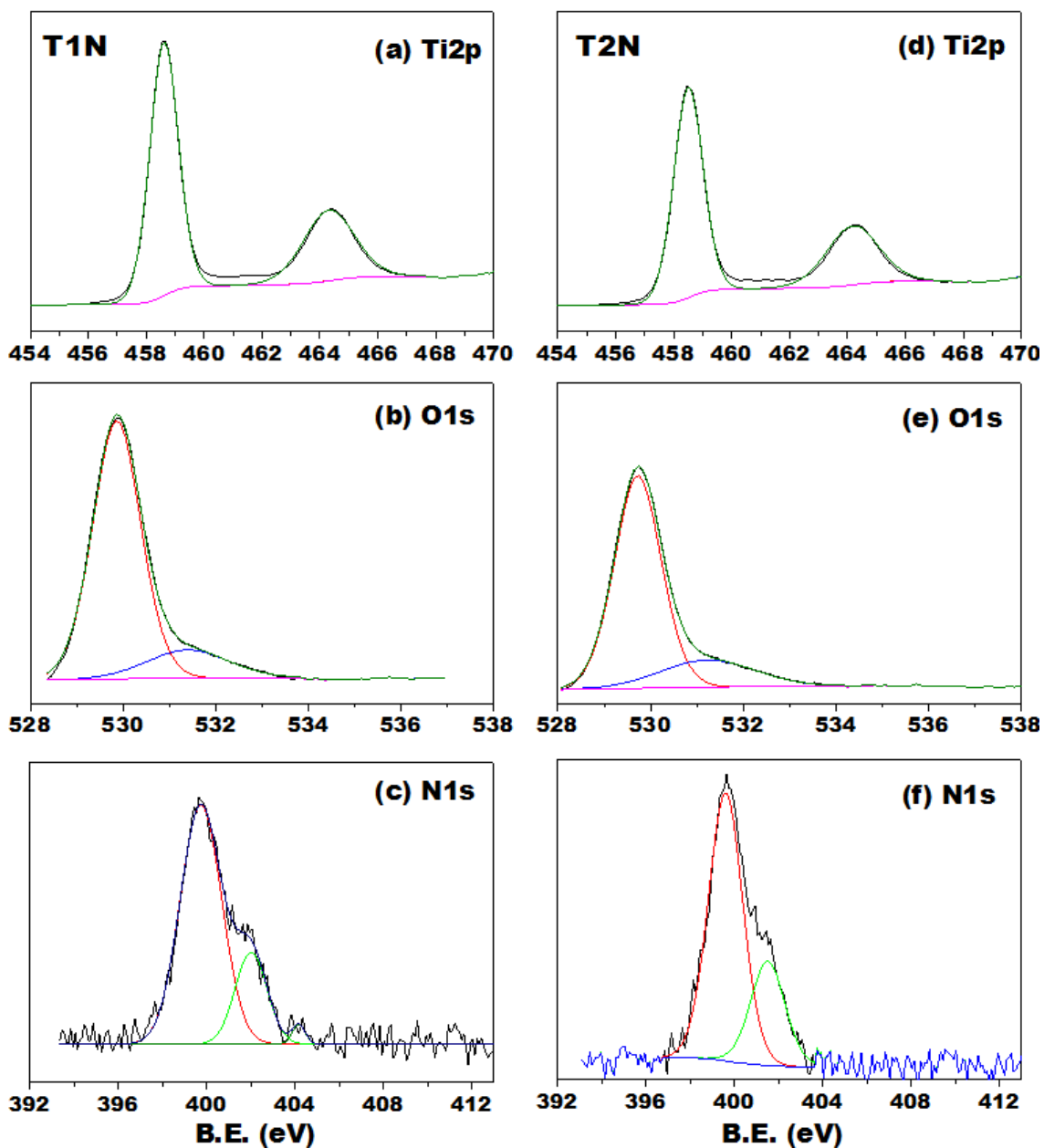
Figure 2.2. High resolution Ti2p, O1s and N1s XPS spectra obtained for T1N (a, b, c) and T2N (d, e, f).

The N1s high resolution spectra obtained for T1N and T2N yielded a broad peak with maximum around 400 eV. This peak can be fitted using two peaks at 402.0 and 399.7eV for the T1N sample and three peaks at 402.0, 399.7 and 404.2 eV for T2N respectively. The specific assignment of N1s-XPS features in nitrogen doped - TiO_2 materials is still

under debate[10,21–24]. In general, a peak around 396 eV is mostly assigned to nitrogen species incorporated into the TiO_2 lattice, called β substitutional nitrogen (Ti-N-Ti)[24]. The peaks at higher binding energies (from 400 eV to 402 eV) may be associated to adsorbed nitrogen species (NO_x) or to generic interstitial sites[21,25]. The presence of strongly adsorbed NO_x species that resulted from the decomposition and oxidation of the nitrogen precursor during the catalyst calcination is also plausible in our case[25]. In any case, the above XPS results indicate that the N species present in the T1N and T2N samples can be classified either as interstitial or adsorbed NO_x species. No significant peak was observed at 396 eV which potentially rules out the presence of β substitutional nitrogen. For the case of the O1s peaks, both T1N and T2N spectra of may be deconvoluted into two contributions, one arising from lattice oxide (O_L) at ~530 eV and other to surface oxide species (O_O) at ~531eV. Lattice oxide is linked to structural oxygen in TiO_2 while surface oxide species can be correlated with strongly chemisorbed water or terminal hydroxide ions[26,27]. The atomic ratio, as obtained from XPS, between lattice oxide and surface oxygen (O_L/O_O) is 4.3 for T1N and 3.5 for T2N. It should be noted that the relatively higher O_L/O_O ratio observed for the T2N sample suggests that this material has a relative large fraction of oxygen that is not part of the TiO_2 lattice. Combining this observation with the results obtained on the N1s high resolution spectra, and previous studies[10,28] we could propose that the peak at 402 eV observed on the N1s high resolution XPS spectra of both T1N and T2N samples results from the presence of surface N $^{+1}$ species[10,29,30]. The peak at 404 eV, which only appears on the N1s high resolution XPS spectra of the T2N sample, is attributed to N^{+3} species[11,29,31].

In order to get a further insight into the chemical state of surface nitrogen species identified by XPS, diffuse reflectance infrared Fourier transform spectroscopy (DRIFTs) measurements were carried on hydrated and dehydrated TiO_2, T1N and T2N samples. Dehydrated samples were obtained after *in situ* heating to 300 °C in He/O$_2$ atmosphere inside the DRIFTs reaction cell. Figure 2.3 shows the IR signals observed in the 2000 - 1000 cm^{-1} region. All hydrated samples showed a peak at 1635 cm^{-1} which arises from the bending vibration of surface hydroxyl groups and adsorbed water molecules [11,32,33]. The T1N sample shows distinct feature at 1442 cm^{-1} and the T2N sample at 1261 cm^{-1};

which can be attributed to ν(N-N) in solid hyponitrite-like structures, and ν(N-O) in nitrite-like systems respectively[11,31]. These observations are in agreement with the XPS results indicating that the surface structure of both T1N and T2N include hyponitrite-like species (N^{+1}) while the T2N sample showed features associated with nitrite-like surface species (N^{+3}).
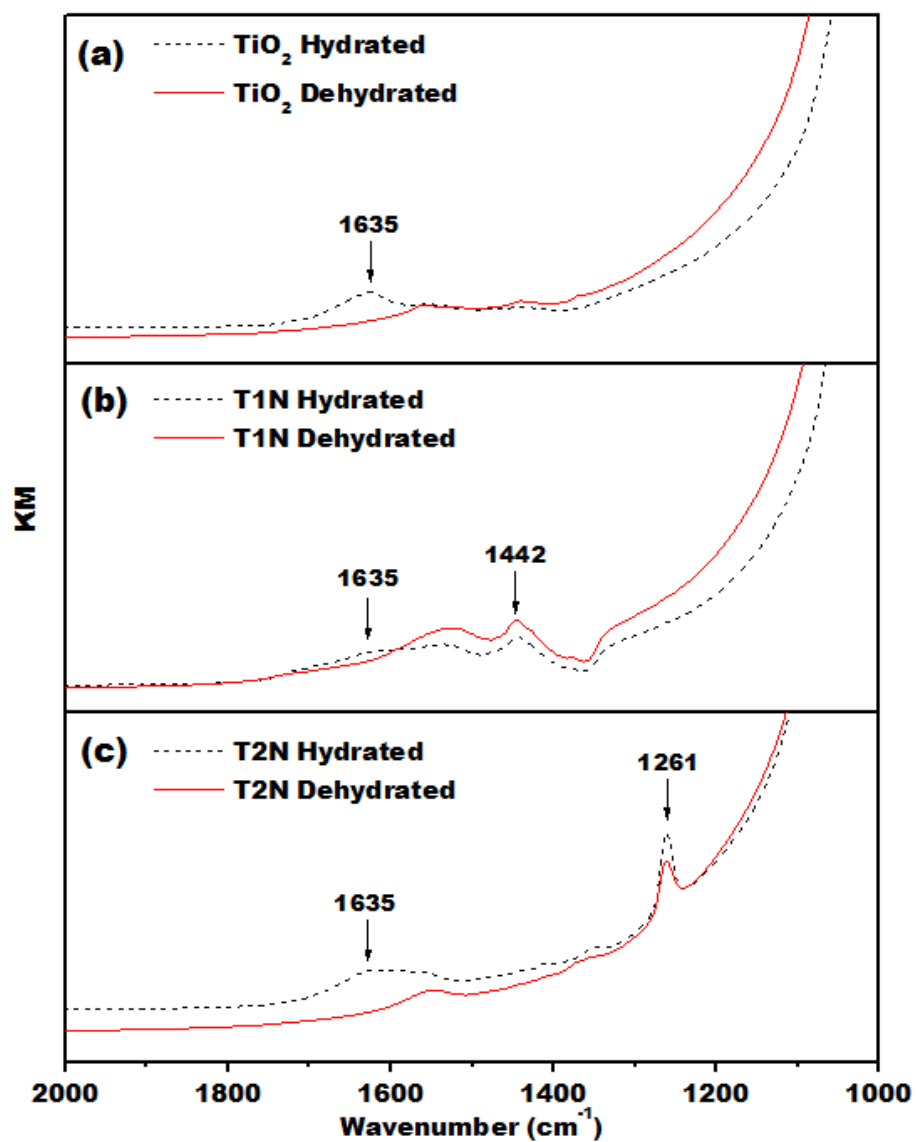
Figure 2.3. DRIFTs spectra of TiO₂, T1N and T2N before (dashed line) and after dehydration under He/O₂ at 300 °C.

The DRS UV-Vis spectra, measured in the range $300 - 600$ nm on the bare TiO_2, T1N and T2N supports is shown in Fig.2.4. Several methods have been proposed to estimate the band gap energy of titanium oxide compounds by using optical absorption spectroscopy. A general power law form has been suggested by Davis and Mott[34] which relates the absorption coefficient with the photon energy. The order of this power function is determined by the type of transition involved. In the case of titanium oxide particles a direct transition is assumed[35]. By plotting this new function versus the photon energy, the position of the absorption edge can then be determined by extrapolating the linear part of the rising curve to zero. The inset on Fig.2.4 shows this analysis, clearly indicating that for the nitrogen doped samples the band gap energy is shifted to lower values energies compared to that obtained on TiO_2. The band gap value considerably shifts for the case of the T1N sample, while for the case of the T2N the shift is not as pronounced[17]. This is consistent with previous reports in the literature[18]. Another interesting feature is that the spectra obtained on the T2N sample extended into the visible range of $400 - 550$ nm (black arrow in Fig.2.4).
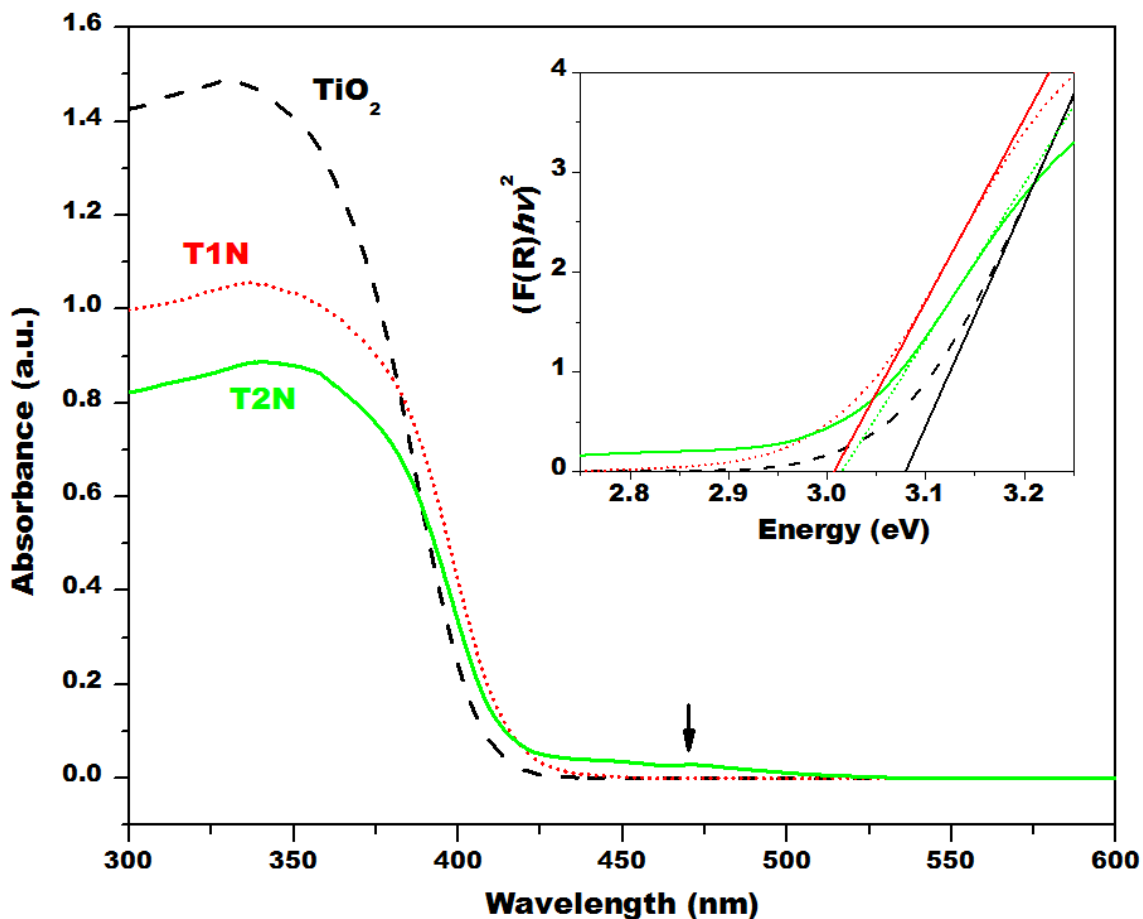
Figure 2.4. UV-Vis DRS spectra of TiO₂ (dashed line), T1N (dotted line), and T2N. Inset: ($\alpha h\nu$)^2 versus photon energy ($h\nu$).

The results of the analysis of the diffuse reflectance UV–vis spectra obtained for the supported VO$_x$ materials are shown in Table 2.3. For these sets of experiments the vanadium-free supports were used to obtain the spectral baseline, thus the data obtained reflects the vanadium oxide contributions resulting from a ligand to metal charge transfer band (LCT) transition[36–38]. To gain more quantitative insight on the average domain size of the species present on these samples, this UV data was evaluated using the direct allowed transition formalism in the Davis and Mott correlation[34]. The energy gap values obtained by this method are shown in Table 2.3. The results are compared to values reported on some reference samples of known domain size obtained by Gao and Wachs[39] in Table 2.4. The VO$_x$/TiO₂ sample exhibits a band gap energy value of 2.75. For the case

of N-doped samples, the VO_x edge energy increases with the addition of nitrogen. This in principle suggests that nitrogen leads to the formation of slightly more agglomerated polyvanadate species[39,40]. However this shift in band gap can be also attributed to a change on the vanadia cluster-support interaction that take places when nitrogen is present in the support.

Table 2.3. Band maxima and edge energies calculated for TiO₂V, T1NV, and T2NV samples.

Catalyst	Band Maxima (nm)	Eg (eV)
TiO₂V	424	2.75
T1NV	426	2.50
T2NV	428	2.57

Table 2.4. Average number of covalent V-O-V bonds present on different samples based on the correlation proposed in ref. 39.

Catalyst	Gap Energy	Average CVB number
V_2O_5	2.31	5
$Mg_3V_2O_8$	3.48	0
VO_x/TiO_2	2.75	3.1
$VO_x/T1N$	2.50	4.2
$VO_x/T2N$	2.57	3.9

2.3.2 Catalytic activity studies

2.3.2.1 Evaluation of catalytic activity for ethanol partial oxidation

The partial oxidation of ethanol to acetaldehyde was used to evaluate the catalytic activity of the VO_x coated samples. In a set of preliminary experiments performed in the same system with a blank reactor, no ethanol conversion was observed at 200 ºC at all weight hourly space velocities (WHSV) tested in this study. For the case of the VO_x coated catalysts, ethanol was converted to acetaldehyde and ethylene, though selectivity to ethylene was very low (below 0.5%). Combustion products (CO and CO_2) were not observed. The high selectivity to acetaldehyde under these conditions is an indication of the relatively high degree of dispersion of the VO_x moieties in these materials[1,41]. Figure 2.5 shows typical steady-state ethanol conversion and the selectivity to acetaldehyde as a function of time on stream using three different space velocities, indicating that with increasing SV the conversion of ethanol decreases and that the selectivity to acetaldehyde was not affected by the space velocity. Under our experimental conditions in all cases the observed selectivity to acetaldehyde was above 99% and we did not observe measurable differences in this selectivity among the different tested catalytic materials.
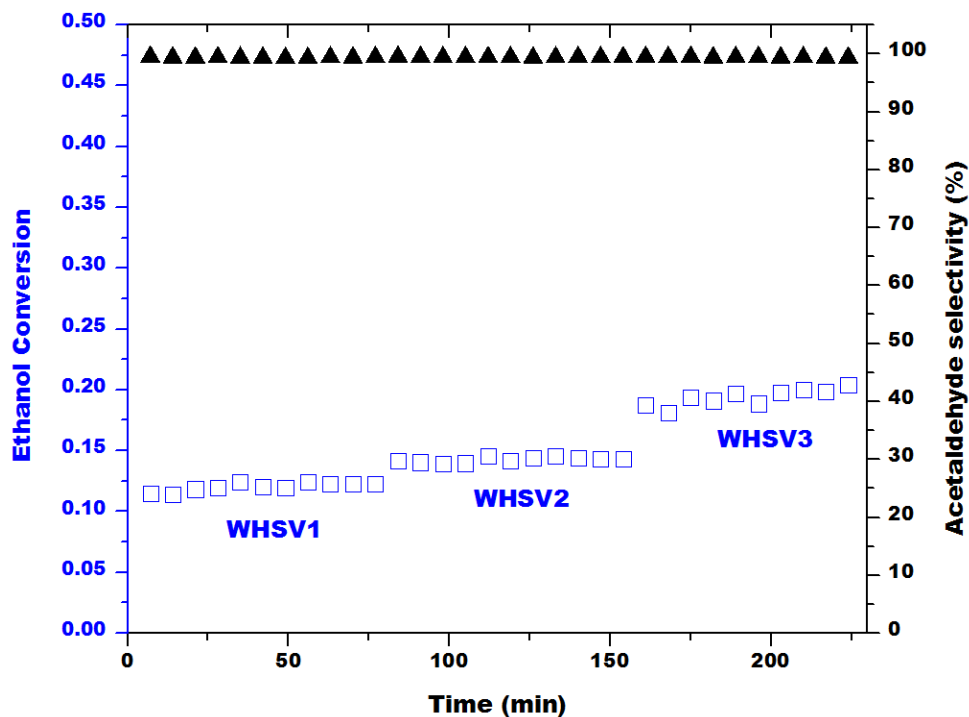
Figure 2.5. Typical catalytic activity data of TiO$_2$V at 200 °C for ethanol partial oxidation. Ethanol conversion on left axis (□) and its selectivity to acetaldehyde on right axis (▲) as a function of time at different weight hourly space velocity (WHSV); WHSV1 = 1642, WHSV 2 = 1314, WHSV3 = 657 mol ethanol / mol V·h^{-1}.

To carry meaningful comparisons between the three materials tested, we extrapolated the measured rates to zero reactant conversion (initial partial oxidation rate) and normalized them by the total V content in the catalyst. Table 2.5 shows the results of this calculation for the three catalytic materials tested together with two values reported in the literature for the same process over VO$_x$/TiO$_2$ systems at the same reaction temperature (T = 200°C). Both N-doped materials displayed higher catalytic activity that V over bare TiO$_2$ supports, notably the values obtained for our samples are within the same order of magnitude as those previously reported[42,43].

Table 2.5. Ethanol partial oxidation rates observed at 200 ºC. All values reported were obtained after extrapolating to zero conversion.

Catalyst	Nitrogen Content (wt.%)	Vanadium content (wt.%)	VO_x density (Atoms nm^{-2})	Calculated Turnover frequency at zero conversion (sec^{-1})
TiO$_2$V	-	0.6	3.1	0.21 ± 0.01
T1NV	7	0.4	3.6	0.48 ± 0.03
T2NV	14	0.6	2.7	0.26 ± 0.01
VO$_x$/TiO$_2$ [as reported in ref. 42]	-	3.0	6.0	0.80
VO$_x$/TiO$_2$ [as reported in ref. 43]	-	0.6	3.5	0.41

2.3.2.2 *In situ* infrared studies of ethanol adsorption

In situ infrared experiments of ethanol adsorption over the TiO_2 doped and undoped materials, with and without vanadium were carried in order to probe the effect of nitrogen doping in the catalyst's surface morphology. The spectroscopic features in the C-C and C-O stretching region were investigated (Fig.2.6). IR absorption bands were observed at 1146, 1124, 1117, 1107, 1095, 1072 and 1055 cm^{-1} for the undoped titania support. Similar peak assignments were obtained on both nitrogen-doped supports with most differences observed on peak position within the resolution used to collect the FTIR spectra (4 cm^{-1}) and peak ratio. Strong peaks corresponding to ν_{C-O} at 1055, 1117 and 1146 cm^{-1} were observed whereas the bands corresponding to ν_{C-C} appeared at 1074 and 1095 cm^{-1} (indicated dashed arrow in Fig.2.6)[32]. It has been previously reported that adsorption of ethanol on TiO_2 surfaces leads to the formation of monodentate (bands at 1118 and 1144 cm^{-1}) and bidentate (band at 1042 cm^{-1}) adsorbed species[32]. In our case, these three peaks appeared for all doped and undoped materials within the degree of resolution used to collect the spectra. Fig.2.6 shows the spectra obtained (Absorbance unit) in the range of 1600 – 1200 cm^{-1} for vanadium-free (TiO_2, T1N, and T2N) and vanadium-containing (TiO_2V, T1NV and T2NV) materials. The spectra obtained on gas phase ethanol (using KBr as baseline) is shown as reference as well (Fig.2.6a). In the 1600 – 1200 cm^{-1} free gas phase ethanol shows bands at 1452, 1406, 1394, 1383, 1250, and 1228 cm^{-1}. These bands are assigned to C-H bending (δ_{C-H}) modes (1280-1500 cm^{-1}) and O-H bending (δ_{O-H}) modes of ethanol (below 1260 cm^{-1})[32,33].
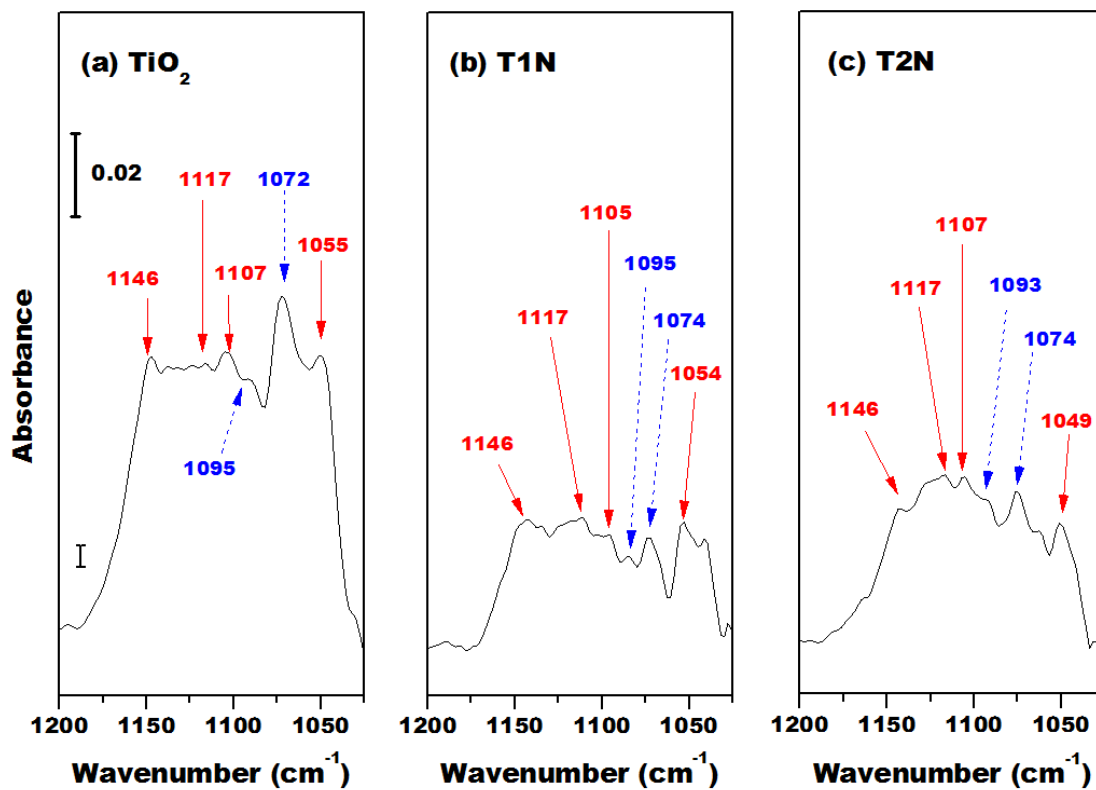
Figure 2.6. *In situ* **DRIFTs spectra of ethanol adsorbed over (a) TiO₂, (b) T1N, and (c) T2N, at 25°C in the 1200 -1000 cm⁻¹ region.**
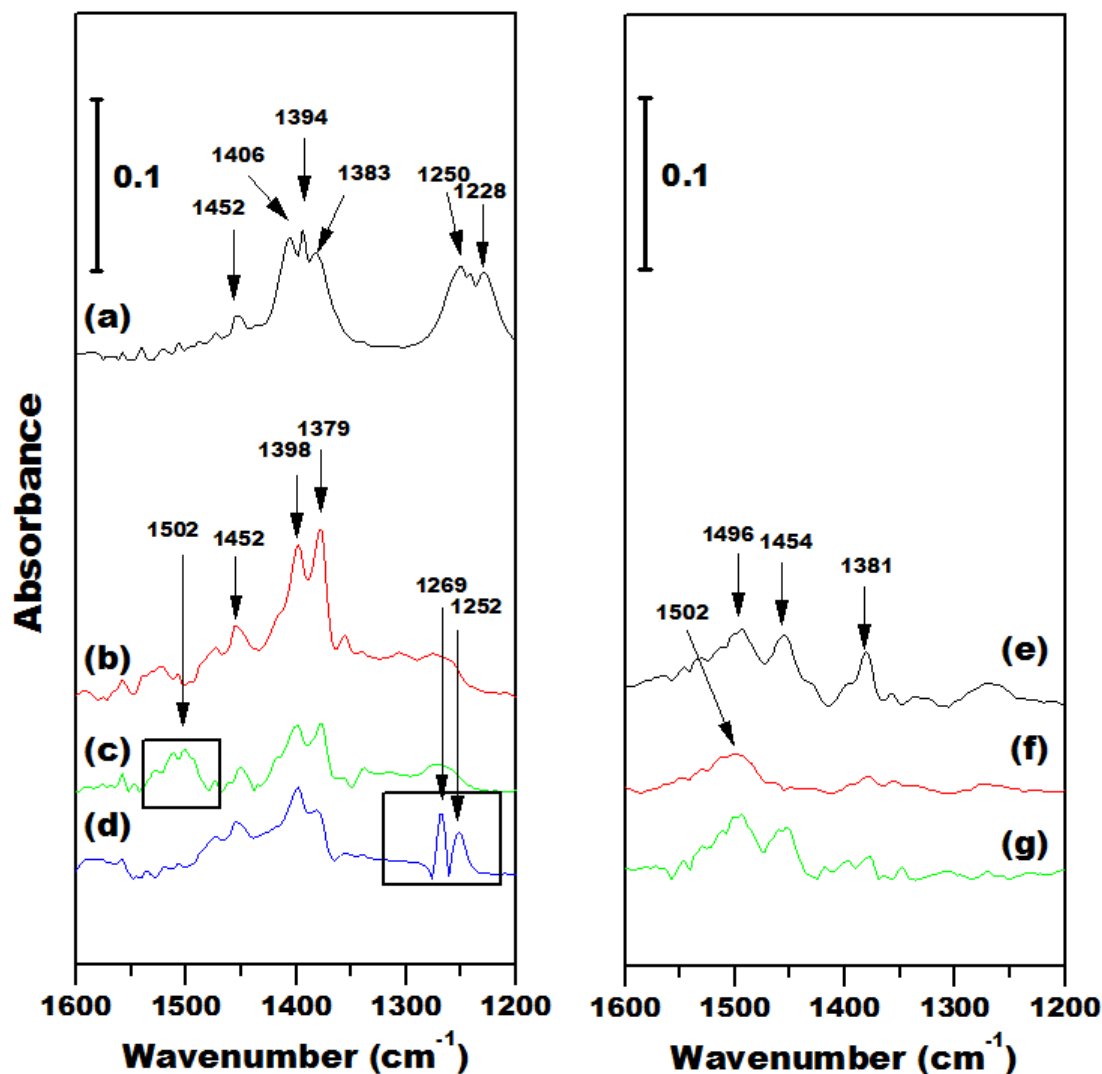
Figure 2.7. (Left) FTIR spectra of gas phase ethanol (a) and *in situ* DRIFTs spectra of ethanol adsorbed over (b) TiO$_2$, (c) T1N, and (d) T2N at 25°C in the region of 1600-1200 cm^{-1}. (Right) *in situ* DRIFTs spectra of ethanol adsorbed over (e) TiO$_2$V, (f) T1NV, and (g) T2NV at 25°C in the region of 1600-1200 cm^{-1}.

For the case of ethanol adsorbed on pristine TiO$_2$ (Fig.2.7b) the main IR bands are observed at 1398 and 1379 cm^{-1}. These peaks are attributed to the vibration of symmetric bending of CH$_2$ bonds in ethanol species (CH$_3$CH$_2$O(a)) adsorbed over TiO$_2$[32,33]. For the case of the nitrogen doped TiO$_2$ materials the main peaks appear at the same positions.

However in this case the peak intensities are quite weak (three to four times lower, Kubelka units). This suggests that the undoped TiO_2 support contains more sites for ethanol absorption than the N-doped supports. Two distinctive and relatively strong peaks are also observed in the N-doped TiO_2 samples at 1502 and 1269 cm^{-1} (Fig.2.7c and 2.7d).

Previous studies indicate that the absorption of ethanol over TiO_2 surface results in the production of water molecules, resulting from the reaction of ethanol with surface hydroxyl groups[32,33]. This process results in the appearance of the broad peak between 3000 - 3550 cm^{-1} linked to the formation of hydrogen bonded surface water $\nu(HO\cdots H)$ together with the disappearance of the sharp IR features in the range of 3800-3600 cm^{-1} attributed to isolated oxygen-hydrogen bonds stretching $\nu(OH)$ on the TiO_2 surface[44], which are consumed upon ethanol adsorption. These spectral changes are observed in the IR spectra of the undoped TiO_2 support (Fig.2.8). For the case of the N-doped samples the consumption of isolated hydroxyl moieties in the titania surface after ethanol adsorption is also observed (negative bands observed in the 3800 - 3550 cm^{-1} range) but as in the case the band is weaker and broader (rectangle shown in Fig.2.8b and 2.8c). These observations can be explained by proposing that, in agreement with the XPS observations (Fig.2.2), the surface structure of the T1N and T2N materials is partially covered with NO_x species resulting in a decrease on the number of surface hydroxyl species and thus limiting the formation of hydrogen bonded surface water that results from the reaction between surface hydroxyl groups and ethanol. Therefore proton abstraction from ethanol cannot take place on hydroxyl sites and instead ethanol adsorption yields different products such as $O-N-OCH_2CH_3$, resulting in the appearance of a relatively strong peat at 1502 cm^{-1} and peaks at 1269 cm^{-1}, attributed to the formation of surface nitro-like compounds, N-O (ν_{N-O}, see Fig.2.6c and 2.6d)[29,31].
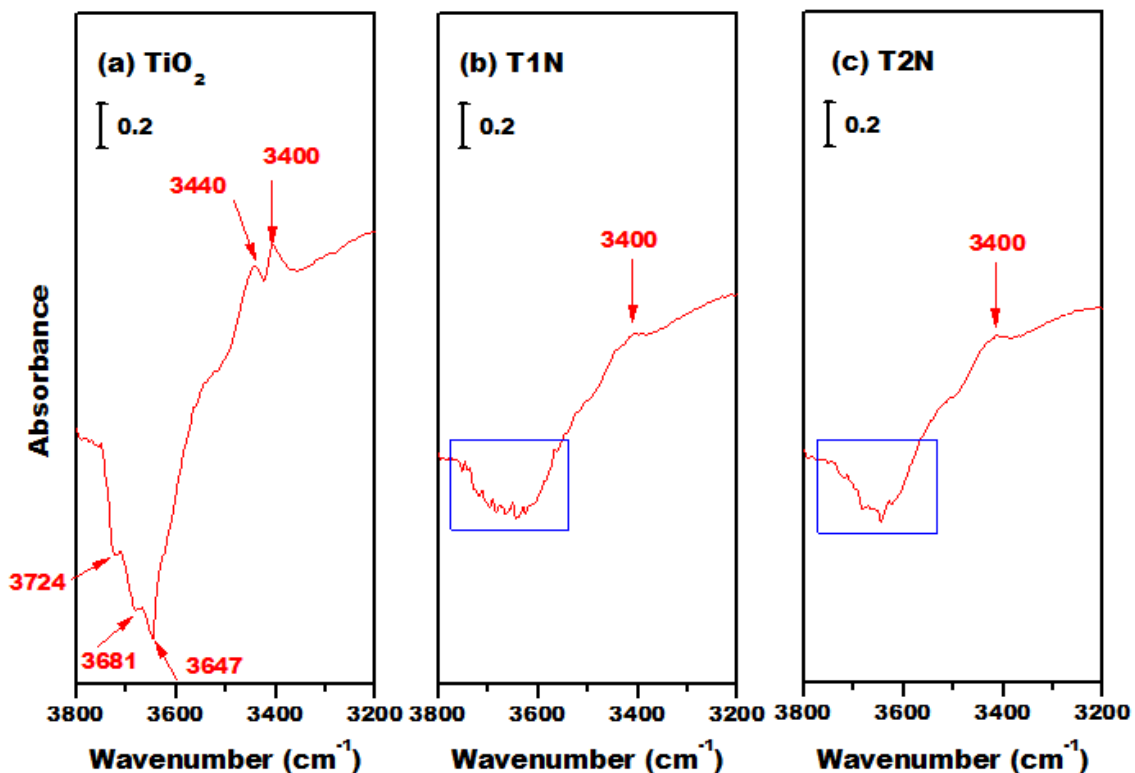
Figure 2.8. *In situ* **DRIFTs spectra of ethanol adsorbed over (a) TiO₂, (b) T1N, and (c) T2N, at 25°C in the 3800-3200 cm⁻¹ region.**

For the case of ethanol adsorbed over VO_x containing samples (Fig.2.7e, 2.7f, 2.7g) the intensity of the peaks between $1350 - 1400$ cm⁻¹ decreased significantly, compared to the ones observed on the VO_x-free samples. Interestingly, the peak at 1502 cm⁻¹, attributed to N-O stretching and observed on the T1N sample is still observed when vanadium is incorporated (T1NV sample). In contrast, T2NV did not display a peak at 1269 cm⁻¹ observed on the sample without vanadium (T2N). This observation could be rationalized by proposing that the N containing surface structures of T1N and T2N are different, and that ethanol adsorbing nitrogen sites in the T1N sample are not affected by VO_x deposition while the N containing sites on the T2N samples are covered after VO_x incorporation.

2.3.2.3   Pulse experiments on ethanol adsorption

To quantify the adsorption capacity of the materials tested, we carried pulse injections of ethanol at different temperatures: 25, 100 and 200°C over 10 mg of solid sample. Based on these results the overall amount of ethanol adsorbed on TiO_2, T1N and T2N were calculated. The calculation results together with those obtained at 100 and 200 °C are shown in Table 2.6. For the case of three supports (before VO_x incorporation) the results consistently show ethanol adsorption capacity is higher for the case of the TiO_2 material without nitrogen, while the two nitrogen doped supports show similar adsorption capacity. This is an interesting result since the BET data (Table 2.1) indicated that both TiO_2 and T2N samples have a surface area twice as large as that of the T1N sample. Nitrogen incorporation affects directly ethanol adsorption capacity, and the values observed at not proportionally linked to total available BET surface area. Therefore, results of the pulse experiments once again indicate that the incorporation of nitrogen on the titania affects the support surface structure. These observations are in agreement with the ethanol adsorption FTIR results presented in Fig.2.3 and XPS observations (Fig.2.2) which indicated the surface structure of the T1N and T2N materials is partially formed of NO_x species, resulting in a decrease on the number of surface hydroxyl species able to interact with ethanol.

Table 2.6. Calculated amount of ethanol adsorbed over samples as obtained from ethanol pulse adsorption experiments at different temperatures.

Samples	Temperature (°C)	Ethanol adsorbed (µg) per 1 mg sample
TiO_2	25	9.26
T1N	25	3.67
T2N	25	3.74
TiO_2	100	5.41
T1N	100	2.51
T2N	100	2.51
TiO_2	200	2.83
T1N	200	1.45
T2N	200	1.49
TiO_2V	200	0.04
T1NV	**200**	**0.66**
T2NV	200	0.42

We carried a similar suite of experiments on these samples after vanadium incorporation. The amount of ethanol adsorbed over these samples are also shown in Table 2.6. The quantity of ethanol adsorbed per milligram of material were 0.04, 0.66 and 0.42 $\mu g \cdot mg^{-1}$ for the VO_x/TiO_2, $VO_x/T1N$, and $VO_x/T2N$ respectively; when these values are normalized by surface area, values of 1.65, 52.54, and 17.05 $\mu g \cdot m^{-2}$ are obtained respectively. Compared to the values obtained on the vanadium free-support the overall

adsorption capacity decreases when vanadia is present. This result apparently contradicts the data presented in Figure 2.7 which showed more intense IR bands for adsorbed ethanol on the nitrogen free vanadia catalyst than for the nitrogen doped VO_x/TiO_2 samples. However we should emphasize that, as described in the methodology section, the FTIR spectra were obtained after ethanol adsorption at 25ºC, whereas the data presented in Table 2.6 indicates the amount of ethanol adsorbed over the vanadium containing catalyst at 200ºC. As the temperature difference is substantial both results are not comparable. We could attribute the observed differences at these two temperatures to the nitrogen doped material offering sites where strongly adsorbed ethanol species are formed which remain bonded to the catalyst surface at the higher temperatures used for the pulse experiments.

As for the reason for which the overall adsorption capacity at reaction conditions decreases when vanadia is present, we must take into consideration that vanadium deposition requires OH groups for anchoring into the TiO_2 surface[3]. And in our case, the resulting anchored species is a vanadia oligomer (with an average number of covalent V-O-V bonds of four, as presented in Table 2.4). Thus it is plausible to assume that the relative large footprint of the vanadium cluster, compared to that of ethanol, results on a blocking of sites that were available for ethanol adsorption before vanadia incorporation.

When comparing the results for the vanadia bearing materials, the results indicate that the doped $VO_x/T1N$ and $VO_x/T2N$ samples have a substantially higher capacity for ethanol adsorption than the undoped VO_x/TiO_2 sample. These values indicate once again that nitrogen plays a definitive role on the ethanol adsorption processes, suggesting that this positively affects catalytic activity as per the activity data presented in Table 2.5. We propose that the increase on the ethanol adsorption capacity on the N-doped vanadia catalyst is related to the creation of partially unsaturated sites on vanadium weakly anchored to the support, resulting from the replacement of oxygen by nitrogen in the surface. The FTIR data indicates the presence of hyponitrite species on the N-doped VO_x/TiO_2 catalyst surface (Fig.2.7) while the UV/Vis data confirmed the tendency of vanadia to agglomerate into larger domains when nitrogen is present (Table 2.4). If indeed the values observed for the band gap energies of the vanadia domains reflect that

larger vanadia clusters are formed when nitrogen is present in the surface we could suggest that this weaker interaction generates vanadia sites that are weakly anchored to the oxygen atoms of the support and thus able adsorb ethanol. Those sites would not be present in the case of the undoped catalyst. We acknowledge however this is a working hypothesis that would require exact identification of the type of site that is adsorbing ethanol in the catalyst surface. We plan to explore this scenario in subsequent contributions from our group, addressing the role of nitrogen in the cluster-support interaction between the vanadia species and the titania support.

2.4 Conclusion

Vanadia supported on interstitially N doped TiO_2 (N-TiO_2) were synthesized by hydrothermal methods. We have demonstrated that nitrogen promotes the catalytic activity of the TiO_2-VO_x system for the ethanol partial oxidation to acetaldehyde. The characterization of these materials indicates that nitrogen species are present in the surface support, and that their exact identity seems to depend on the amount of N doping. These NO_x surface species play a role on the catalytic activity of the material, and this effect seems to be associated with the ability of ethanol to adsorb on the catalyst surface and/or the degree of the vanadia cluster-support interaction.

References

(1)   Herrera, J. E.; Isimjan, T. T.; Abdullahi, I.; Ray, A.; Rohani, S. *Appl. Catal. A Gen.* **2012**, *417-418*, 13–18.

(2)   Wachs, I. E.; Weckhuysen, B. M. *Appl. Catal. A Gen.* **1997**, *157* (1–2), 67–90.

(3)   Bond, G. C.; Tahir, S. F. *Appl. Catal.* **1991**, *71* (1), 1–31.

(4)   Chary, K. V. R.; Kishan, G.; Bhaskar, T.; Sivaraj, C. *J. Phys. Chem. B* **1998**, *102* (35), 6792–6798.

(5)   Lakshmi, J. L.; Ihasz, N. J.; Miller, J. M. *J. Mol. Catal. A Chem.* **2001**, *165* (1–2), 199–209.

(6)   Kim, T.; Wachs, I. E. *J. Catal.* **2008**, *255* (2), 197–205.

(7)   Kilos, B.; Bell, A. T.; Iglesia, E. *J. Phys. Chem. C* **2009**, *113* (7), 2830–2836.

(8)   He, Y.; Rui, Z.; Ji, H. *Catal. Commun.* **2011**, *14* (1), 77–81.

(9)   Vogt, E. T. C.; van Dillen, A. J.; Geus, J. W.; Janssen, F. J. J. G. *Catal. Today* **1988**, *2* (5), 569–579.

(10)   Asahi, R.; Morikawa, T. *Chem. Phys.* **2007**, *339* (1–3), 57–63.

(11)   Sakthivel, S.; Janczarek, M.; Kisch, H. *J. Phys. Chem. B* **2004**, *108* (50), 19384–19387.

(12)   Chen, X.; Burda, C. *J. Am. Chem. Soc.* **2008**, *130* (15), 5018–5019.

(13)   Nolan, N. T.; Synnott, D. W.; Seery, M. K.; Hinder, S. J.; Van Wassenhoven, A.; Pillai, S. C. *J. Hazard. Mater.* **2012**, *211–212* (0), 88–94.

(14)   Li, H.; Yin, S.; Wang, Y.; Sato, T. *Environ. Sci. Technol.* **2012**, *46* (14), 7741–7745.

(15)   Diwald, O.; Thompson, T. L.; Zubkov, T.; Walck, S. D.; Yates, J. T. *J. Phys. Chem. B* **2004**, *108* (19), 6004–6008.

(16)   Peng, F.; Liu, Y.; Wang, H.; Yu, H.; Yang, J. *Chinese J. Chem. Phys.* **2010**, *23* (4), 437–441.

(17)   Zhang, Z.; Luo, Z.; Yang, Z.; Zhang, S.; Zhang, Y.; Zhou, Y.; Wang, X.; Fu, X. *RSC Adv.* **2013**, *3* (20), 7215–7218.

(18)   Hu, S.; Wang, A.; Li, X.; Löwe, H. *J. Phys. Chem. Solids* **2010**, *71* (3), 156–162.

(19)   Spurr, R. A.; Myers, H. *Anal. Chem.* **1957**, *29* (5), 760–762.

(20)   Sathish, M.; Viswanathan, B.; Viswanath, R. P.; Gopinath, C. S. *Chem. Mater.* **2005**, *17* (25), 6349–6353.

(21)   Di Valentin, C.; Finazzi, E.; Pacchioni, G.; Selloni, A.; Livraghi, S.; Paganini, M. C.; Giamello, E. *Chem. Phys.* **2007**, *339* (1–3), 44–56.

(22)   Chen, X.; Wang, X.; Hou, Y.; Huang, J.; Wu, L.; Fu, X. *J. Catal.* **2008**, *255* (1), 59–67.

(23)   Viswanathan, B.; Krishanmurthy, K. R. *Int. J. Photoenergy* **2012**, *2012*, 1–10.

(24)   Asahi, R.; Morikawa, T.; Ohwaki, T.; Aoki, K.; Taga, Y. *Science* **2001**, *293* (5528), 269–271.

(25)   Popa, M.; Macovei, D.; Indrea, E.; Mercioniu, I.; Popescu, I. C.; Danciu, V. *Microporous Mesoporous Mater.* **2010**, *132* (1–2), 80–86.

(26)   Yun, D.-M.; Cho, H.-H.; Jang, J.-W.; Park, J.-W. *Water Res.* **2013**, *47* (5), 1858–1866.

(27)   Erdem, B.; Hunsicker, R. A.; Simmons, G. W.; Sudol, E. D.; Dimonie, V. L.; El-Aasser, M. S. *Langmuir* **2001**, *17* (9), 2664–2669.

(28)   Pap, Z.; Baia, L.; Mogyorósi, K.; Dombi, A.; Oszkó, A.; Danciu, V. *Catal.*

Commun. **2012**, *17* (0), 1–7.

(29)   Hadjiivanov, K. I. *Catal. Rev.* **2000**, *42* (1-2), 71–144.

(30)   Jaiswal, R.; Patel, N.; Kothari, D. C.; Miotello, A. *Appl. Catal. B Environ.* **2012**, *126* (0), 47–54.

(31)   Navio, J. A.; Cerrillos, C.; Real, C. *Surf. Interface Anal.* **1996**, *24* (5), 355–359.

(32)   Wu, W.-C.; Chuang, C.-C.; Lin, J.-L. *J. Phys. Chem. B* **2000**, *104* (36), 8719–8724.

(33)   Yu, Z.; Chuang, S. S. C. *J. Catal.* **2007**, *246* (1), 118–126.

(34)   Davis, E. A.; Mott, N. F. *Philos. Mag.* **1970**, *22* (179), 903–922.

(35)   Madhusudan Reddy, K.; Manorama, S. V; Ramachandra Reddy, A. *Mater. Chem. Phys.* **2003**, *78* (1), 239–245.

(36)   Kwak, J. H.; Herrera, J. E.; Hu, J. Z.; Wang, Y.; Peden, C. H. F. *Appl. Catal. A Gen.* **2006**, *300* (2), 109–119.

(37)   So, H.; Pope, M. T. *Inorg. Chem.* **1972**, *11* (6), 1441–1443.

(38)   Iwamoto, M.; Furukawa, H.; Matsukami, K.; Takenaka, T.; Kagawa, S. *J. Am. Chem. Soc.* **1983**, *105* (11), 3719–3720.

(39)   Gao, X.; Wachs, I. E. *J. Phys. Chem. B* **2000**, *104* (6), 1261–1268.

(40)   Gao, X.; Bare, S. R.; Weckhuysen, B. M.; Wachs, I. E. *J. Phys. Chem. B* **1998**, *102* (52), 10842–10852.

(41)   Deo, G.; Wachs, I. E. *J. Catal.* **1994**, *146* (2), 323–334.

(42)   Chimentão, R. J.; Herrera, J. E.; Kwak, J. H.; Medina, F.; Wang, Y.; Peden, C. H. F. *Appl. Catal. A Gen.* **2007**, *332* (2), 263–272.

(43)   Beck, B.; Harth, M.; Hamilton, N. G.; Carrero, C.; Uhlrich, J. J.; Trunschke, A.; Shaikhutdinov, S.; Schubert, H.; Freund, H.-J.; Schlögl, R.; Sauer, J.; Schomäcker, R. *J. Catal.* **2012**, *296* (0), 120–131.

(44)   Hussein, G. A. M.; Sheppard, N.; Zaki, M. I.; Fahim, R. B. *J. Chem. Soc. Faraday Trans.* **1991**, *87* (16), 2661.

3 Electronic structure changes in the nitrogen doped VO$_x$/TiO$_2$ system during catalytic partial oxidation of ethanol

Abstract

The catalytic activity for ethanol partial oxidation of supported vanadium oxide catalysts prepared on N doped TiO$_2$ (VO$_x$/N-TiO$_2$) was correlated to the electronic structure of the vanadium clusters present in the catalyst surface. *In situ* Raman and UV-vis spectra together with ethanol temperature programmed desorption (TPD) profiles indicate that in all materials studied the average VO$_x$ cluster size is very similar, irrespective of the presence of nitrogen. However, the distribution of active sites and the reducibility of the VO$_x$ species are significantly affected by the presence of nitrogen in the support. The electronic structure of these materials was investigated using periodic density functional theoretical calculations. It was found that, compared to the nitrogen free materials, the electronic structure of reduced VO$_x$ is affected by the presence of N, as well as nitrogen position on the TiO$_2$ supports (interstitial vs. substitutional). Our analysis revealed that after vanadia reduction during ethanol oxidation, reduced VO$_x$ sites (V^{+4}) form, accompanied by the simultaneous reduction of adjacent Ti cations (Ti^{+3}). Calculated optical absorption spectra are also provided and matched with experimental spectroscopic results, confirming these observations.

3.1 Introduction

Redox heterogeneous catalyst are essential for industrial and environmental applications[1]. A fundamental understanding of the interactions between adsorbed chemical species and catalytically active surfaces is significantly important for evolving the science and progress in engineering applications of these systems[2,3]. Among redox catalysts, supported vanadium oxide (VO$_x$) is a versatile material due to its rich and diverse chemistry[1,3]. Processes such as partial oxidation, and oxidative dehydrogenation (ODH)

over vanadium oxide have been investigated at the atomic-structural level[4,5]. These oxidation reactions over VO_x domains involve Mars-van Krevelen redox cycles using lattice oxygen and reduced V^{+3} and V^{+4} centers as reactive intermediates[6–8]. The number of reduced sites directly determines the activity of the catalyst, so evaluation of the extent of reduction of the vanadia during turnovers has been used as descriptor of catalytic activity in the past[9,10].

At the same time, *in situ* vibrational spectroscopy such as Raman and infrared (IR) have often been used to probe the molecular structure of supported vanadium oxides[11–13]. A large amount of information can be obtained since Raman can detect vibrational modes of surface VO_x species. In addition, ultra-violet visible diffuse reflectance spectroscopy (UV-vis DRS) enables probing of reduced states of supported vanadia, which normally do not give rise to new detectable IR or Raman signals. Thus, *in situ* UV-vis studies for ceria, silica, and alumina-supported VO_x have been widely reported[9,12]. However, the application of UV-vis DRS to the study of vanadia supported on titania has comparably had less attention since the intense Ligand to metal charge transfer (LMCT) transition arising from the titania support overlaps with the vanadia signals[14,15].

We previously reported the superior catalytic properties of nitrogen doped TiO_2-supported VO_x for ethanol partial oxidation, and proposed a mechanism involving surface nitrogen affecting the dispersion of vanadia[16]. In this contribution we further examine the role of N with regard to the extent of reduction of vanadia species using a modified method for measuring the pre-edge energy (Eg') during ethanol partial oxidation over VO_x species. This method is based on previous work by probing changes in the pre-edge energy observed in the UV-visible spectra of VO_x species[9,10,17,18] after reduction. Theoretical calculations were also performed using a vanadia cluster on (101) surface terminated anatase slab with the aim to rationalize the reactivity trends observed in terms of changes of electronic structure of the active species.

3.2   Experimental

3.2.1   Catalyst Preparation

Nitrogen doped TiO_2 (N-TiO_2) supports with different amounts of nitrogen were prepared via a hydrothermal method previously reported, using $TiCl_4$ (Sigma-Aldrich, ACS grade) and urea (Sigma-Aldrich, ACS grade). This method results on the incorporation of mainly interstitial nitrogen into the titania matrix[16]. The prepared N-TiO_2 materials with different nitrogen loadings are denoted as TNx with x (x = 0, 1, 1.5, 2, and 4) depending on the weight concentration of urea (CH_4N_2O, Sigma Aldrich, ACS grade) used during synthesis. VO_x impregnation over these supports was carried out by incipient wetness impregnation, using aqueous vanadium pentoxide (V_2O_5, Sigma Aldrich, ACS grade) dissolved in 1M oxalic acid ($H_2C_2O_4$, Sigma Aldrich, ACS grade). After impregnation the catalyst were dried in the oven at 90 ºC overnight, and further calcined at 400 ºC for 2h in air (Praxair, UHP). The prepared N-TiO_2 supported VO_x are denoted as TN_xV (the surface vanadium density was kept constant at: 1.75 ± 0.25 V atoms·nm^{-2}).

3.2.2   Catalyst Characterization

The specific surface areas of the N-doped TiO_2 supports were measured by a seven point Brunauer-Emmett-Teller (BET) method using N_2 adsorption-desorption isotherms at 77 K (Micromeritics TriStar II 3020 Physisorption Analyzer) previous degassing at 90 ºC for 1 h and 200 ºC for 4 h under N_2 atmosphere. The amount of nitrogen incorporated in the supports was quantified using a previously reported spectrophotometric method using a bare TiO_2 and a series of N-TiO_2 reference materials of known N content (nitridized TiO_2)[19]. UV-Vis absorption values at 495 nm[20] were obtained for these reference materials.

The surface elemental composition of obtained TN supports and TNxV was determined by X-ray photoelectron spectroscopy (XPS) conducted on a Thermo Scientific K-Alpha using a monochromatic Al K_α radiation as the exciting source. The binding energies were calibrated by referencing the C1s peak as 284.3 eV. Raman spectra of the TNx supports

and TNxV catalyst were collected using a custom made Raman instrument equipped with an imaging spectrograph (SpectroPro-2500i, Acton Research Corporation) and an *in situ* reaction chamber (HVC-DRP, Harrick Scientific) and a liquid nitrogen cooled charge coupled device (CCD) detector (Acton). The 532 nm excitation line from a diode-pumped solid-state (DPSS) laser was used. The laser power at the sample position was 1.0 mW. The use of a 1200 lines/mm grating allows a spectral resolution of < 0.5 cm^{-1} to be achieved. Raman spectra of hydrated and dehydrated samples were recorded under controlled atmosphere. To obtain the spectra of the dehydrated samples the TNxV samples were heated in the reaction chamber in flowing 5% O_2 balanced with He (Praxair, 10 cm$^3 \cdot$min^{-1}) at 300 ℃ for 30 min to remove adsorbed moisture. Raman spectra were then taken at both 300 ^{o}C and after cooling down in the O_2/He mixture. Data collection was set 2 sec for the first spectral window (33 – 1270 cm^{-1}) and 30 sec for second one (720 – 1970 cm^{-1}). The Raman shift was calibrated by interpolation of the Rayleigh line and a silicon wafer signal (520 cm^{-1}).

3.2.3 *In situ* ultra-violet visible (UV-vis) experiments

Following previously reported methodology[14], an approximate for the number of average vanadium-oxygen-vanadium covalent bonds (CVB) on each sample were measured by diffuse reflectance UV-visible spectroscopy (Shidmadzu UV-Vis 3600) using and an *in situ* reaction chamber (HVC-DRP, Harrick Scientific) and a Harrick Praying Mantis. The spectra were collected between 200 and 800 nm using barium sulfate (BaSO$_4$, Sigma–Aldrich, 99%) as a reference for the case of the samples without vanadium. For the samples containing vanadium the bare (VO$_x$ free) TiO$_2$ and nitrogen doped TiO$_2$ materials were used to obtain the spectral baseline. This methodology enables us to get a preliminary descriptor for dispersion of the vanadium oxide species on the support.

The pre-edge energies (Eg') and the formation of reduced vanadium centers were monitored by a direct method based on changes in the pre-edge region of UV-visible spectra that takes place under reductive environments, as previously reported[9,10]. UV-vis spectra in the range of 250 – 1200 nm (1.03 – 4.96 eV) of the N-doped VO$_x$ catalysts

were measured during reduction by ethanol. Spectra were initially referenced to a Spectralon standard. About 30 mg of each catalyst powder were finely grounded and calcined *in situ* at 300 ºC in O_2 (Praxair, UHP, 10 $cm^3 \cdot min^{-1}$) balanced in He (Praxair, UHP, 45 $cm^3 \cdot min^{-1}$) for 1 hr. The system was then cooled down to room temperature in the O_2/He mixture and the spectrum acquired. This spectrum was used as baseline for the next step. After this stage the sample was heated again and ethanol was introduced in the chamber using a syringe pump (KDS200) via a heated injection (100 ºC, 0.017 $cm^3 \cdot min^{-1}$ C_2H_5OH/45 $cm^3 \cdot min^{-1}$ He) for one hour at different constant temperatures. After reduction of the catalysts for 1 hour, ethanol flow was stopped and the reaction chamber was cooled down under He flow to ambient temperature again and the spectra acquired. All diffuse reflectance spectra were obtained at ambient temperature in He atmosphere and converted into Kubelka-Munk units ($F(R_{\infty,rel})$). David and Mott's correlation was used to determine the pre-edge energy (E_g') by finding the intercept of a straight line in the low-energy rise of plots of $(F(R_\infty) \, hv)^2$ assuming a direct transition formalism against *hv*, where *hv* is the incident photon energy. The reduced centers were identified by the photon energy position at corresponding peak maxima following previously reported methodology[18].

3.2.4   Ethanol partial oxdiation

Before catalytic testing all samples were pressed into wafers, crushed and sieved to a pellet size between 425 – 600 μm. Steady-state partial oxidation of ethanol experiments were conducted in a continuous flow fixed bed quartz glass micro reactor (5 mm O.D.) oriented vertically in an electrically heated furnace at atmospheric pressure equipped with a digital temperature controller. Catalyst samples (10 mg) were supported on a quartz frit and a K-type thermocouple placed at the center of the catalyst bed. Chemical species in the feed and reactor effluent stream were measured using an online gas chromatograph (Shimadzu GC-2014) with a capillary column (BP-5, 30 m $\times$ 0.53 mm, 1.0 μm thickness) connected to a flame ionization detector.

The catalyst was pretreated at 200°C in 30 min under O_2/He mixture (5% O_2, Praxair, UHP) at a flow rate of 20 cm³·min⁻¹. Absolute ethanol (Brampton, Ontario) was introduced into the reactor by vaporizing it into the flowing O_2/He mixture at 150°C using a micro-syringe pump. Reactant conversions were varied by changing the O_2/He flow rate (0.8 – 1.6 cm³·s⁻¹) equivalent to weight hourly space velocity (657 – 1642 mol ethanol / mol V·h⁻¹) at constant ethanol partial pressures (0.23 kPa) and temperature (200 °C). The conversion was kept under 40% so that differential reaction conditions could be assumed. Conversion and selectivity to products were calculated on a carbon molar basis, expressed as a mol% ratio of ethanol transformed to ethanol fed, and a ratio of ethanol transformed to each product relative to the total ethanol transformed, respectively. The normalized rate of partial oxidation of ethanol was calculated according to eq. (3.1):

$$r_{EtOH} = \frac{\rho F}{60\, MW \times mole\ of\ V} X_{EtOH} \qquad\qquad eq.(3.1)$$

where r_{EtOH} is the rate of partial oxidation (sec⁻¹), F is the total volumetric flow (cm³·min⁻¹), ρ refers to the density of ethanol (g·cm⁻³), MW is the molecular weight of ethanol (g·mol⁻¹), and X_{EtOH} is the ethanol conversion, the rates were normalized by the molar amount of vanadium present in the sample.

3.2.5   Ethanol temperature programmed desorption

Ethanol temperature-programmed desorption (TPD) was performed in order to identify surface active sites. The ethanol-TPD experiments were carried out in a continuous flowing system under atmospheric pressure. For these experiments 0.2 g of catalyst were first treated under in the air (Praxair, UHP) flow of 15 ml·min⁻¹ for 2 hours at 300 °C. Then, the sample was cooled down to 25°C while purging in He (Praxair, UHP) feed flow rate of 15 mL·min⁻¹. Following this stage liquid distilled ethanol (without additional purification) was mixed with He (0.4 kPa ethanol partial pressure) to saturate samples by vaporizing it into the flowing He using a micro-syringe pump (KDS Scientific) for 1 hour. All the transfer lines were kept at 120 °C to prevent condensation of reactant, and products. To get rid of physically adsorbed ethanol, samples were flushed for 1 hour

under He flow at room temperature. Temperature programmed desorption was carried under He atmosphere using a ramp of 2 ºC·min^{-1} up to 250 ºC. The desorbed gases were analyzed using a by on-line GC-FID-MS (Agilent 6890A, 30m HP-Innowax column 0.25 μm thickness).

3.2.6   Computational details

Density functional theory calculations were performed within the generalized gradient approximation (GGA) and the periodic plan-wave approach, using the Perdew-Burke-Ernzerhof (PBE)[21] exchange-correlation functional and Vanderbilit ultra-soft pseudo-potentials[22]. The DFT+U correction is applied to both titanium and vanadium metal atoms in the support. We use U=2.3 eV on Ti and 2.0 eV on V d-states based on the suggestions made in the literature[23]. Plan-wave basis set cutoffs for the kinetic and density cutoff were 50 and 500 Ry, respectively. Plane-Wave Self-Consistent Field (PWscf code of the Quantum-Espresso package[24]), running on SHARCNET, was used to obtain geometric optimization, to calculate total and projected density of states (PDOS), and the density maps of electronic states. The k-point sampling of the Brillounin zone was limited to gamma. The Broyden-Fletcher-Goldfarb-Shanno (BFGS) algorithm was used for geometry optimization, with threshold values of 0.092 eV/Å and 6.8×10^{-4} eV for residual forces and energy variation, respectively.

Prior to geometry optimization of VO$_x$ supported surfaces, a clean anatase (101) surface was modeled with a periodically repeated slab. A 1×3 surface cell containing 72 atoms, with corresponding surface area of 10.24×11.36 Å^2, was modeled with a vacuum of 10 Å. The atoms in the bottom layer were fixed to their bulk positions during geometry optimization, in order to simulate the presence of the bulk underneath. Based on previous research regarding theoretical evaluation of the electronic structure of N doped TiO$_2$, the substitutional nitrogen doped surface was simulated by replacing a subsurface 3-fold oxygen in the slab with a nitrogen atom[25], as depicted in Fig.3.1b. In case of interstitial nitrogen doped surface, superficial N-O species was optimized for the most stable configuration, as depicted in Fig.3.1c. The chemical composition in the model slab thus

corresponds to $TiO_{2-x}N_x$ with x = 0.027. To represent a reduced isolated monomeric vanadia cluster adsorbed on the anatase (101) surface, a single VO cluster in this unit cell was built (See Fig.3.1). The VO_x supported surface corresponds to coverage of 1 V/nm^2, which is well below monolayer coverage (usually 7-8 V/nm^2).
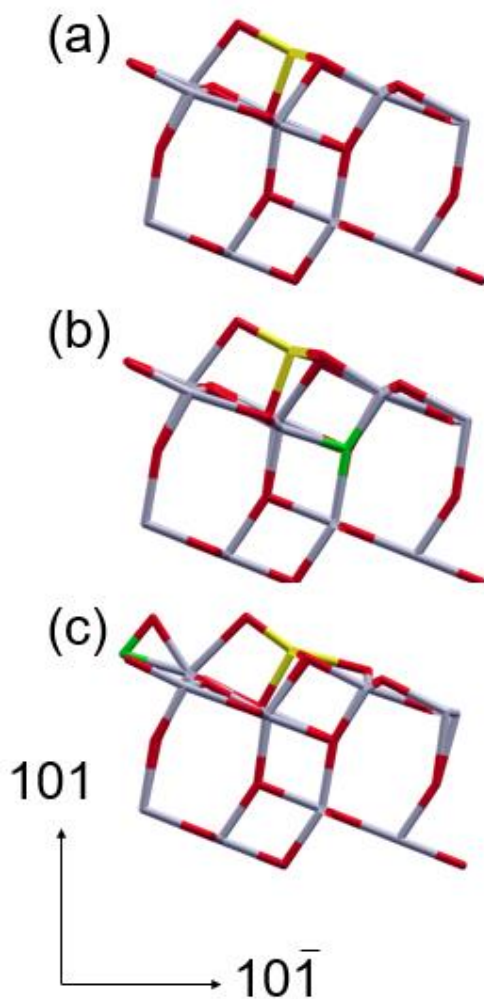
Figure 3.1. Stick models of proposed structures of a reduced tetrahedral vanadium oxide cluster supported on: (a) pristine anatase (101) surface, (b) substitutional N doped anatase (101) and (c) interstitial N doped anatase (101) as used for DFT. Ti, V, and O atoms are represented by red, grey and yellow, respectively. Doping N atoms are represented in green.

3.3 Results and Discussion

3.3.1   Catalyst Characterization

The XPS results obtained on the vanadium free supports are depicted in Fig.3.2 and Table 3.1. We focused on the data obtained on the O1s peak since the nitrogen signal was below detection limit due to the low nitrogen content on these materials. Based on previously reported results[1,26], we can state there exists two types of oxygen species; lattice oxygen (O_L at ~530 eV) and surface chemisorbed oxygen (O_o at ~ 531 eV). Lattice oxygen is linked to structural oxygen in the TiO_2 structure while chemisorbed oxygen is linked to strongly adsorbed water or terminal hydroxyl groups. Thus we fitted the obtained experimental data using these two species (Fig.3.2) and calculated the atomic ratio between lattice and chemisorbed oxygen (O_L/O_o). The obtained results are presented Table 3.1. A clear trend is observed, where the relative amount of lattice oxygen decreases as the amount of nitrogen in the support increases. Based on these results we propose that a part of nitrogen replaces lattice oxygen atoms in the titania support. The estimation of N content on the fresh catalyst indicated that less than 0.25 wt.% of doping N was present on catalysts, and as expected the nitrogen content increases with the amount of urea used during synthesis (Table 3.2).

Values obtained for BET surface area, calculated VO_x surface densities, and calculated edge energy (based on UV experiments) are shown in Table 3.2 as well. The edge energy values obtained were used to calculate the number of average V-O-V bonds present in the fully oxidized sample as an approximate value for evaluation of pentavalent vanadia dispersion. This calculation is referred to the regression plot from reference[27]: Average CVB number = -3.95 × Band gap (eV) + 14.03. The values reported in Table 3.2 indicate that only a slight change in surface area takes place upon nitrogen doping. The values obtained for edge energy (E_g) and the obtained CVBs number clearly indicate that our methodology successfully achieved a similar state of pentavalent vanadia dispersion on all probed supports.
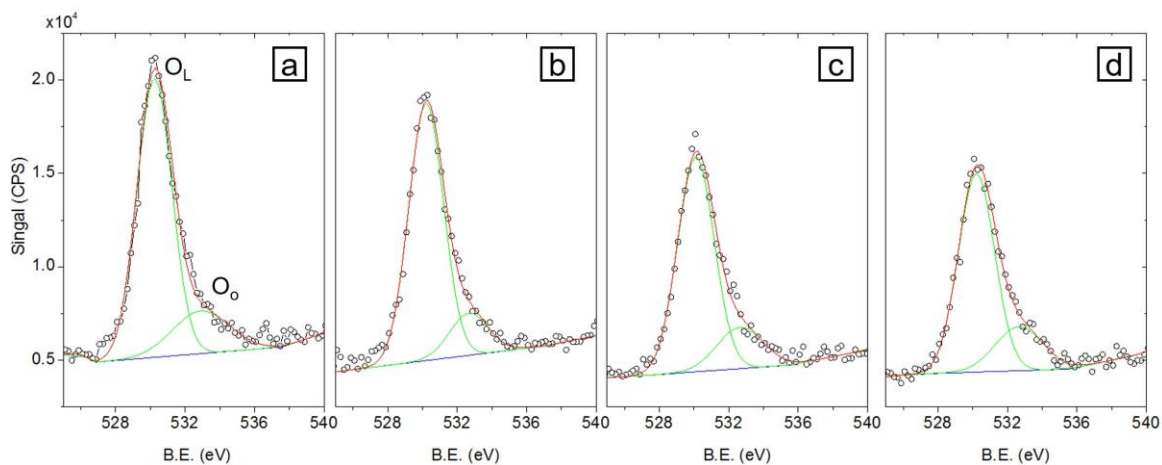
Figure 3.2. XPS spectra of O_{1s} obtained on fresh nitrogen doped catalyst: (a) TN1, (b) TN1.5, (C) TN2, and (d) TN4.

Table 3.1. Results for the O1s fittings of the high resolution O_{1s} XPS spectra of the N-doped samples (O_L: lattice oxide, O_o: chemisorbed oxygen).

	TN1		TN1.5		TN2		TN4	
	B.E.	Area %	B.E.	Area %	B.E.	Area %	B.E.	Area %
O_L	530.2	84.7	530.1	80.6	530.1	79.4	530.2	77.4
O_O	532.9	15.3	532.7	19.3	532.7	20.6	532.7	25.6
O_O/O_L	0.18		0.24		0.26		0.33	

Table 3.2. Sample parameters for fresh N-TiO₂-supported VOₓ samples.

Catalyst	Surface Area (m² g⁻¹)	N content (wt.%)	V contents as V₂O₅ (wt.%)	Edge Energy (eV)	CVB number	Surface density (V atoms nm⁻²)
TN0V	37.47 ± 0.38	0	1.12	2.73	3.21	1.98
TN1V	36.87 ± 0.40	0.05	1.12	2.74	3.16	2.02
TN1.5V	39.73 ± 0.40	0.09	1.12	2.74	3.16	1.87
TN2V	48.36 ± 0.37	0.10	1.12	2.74	3.16	1.54
TN4V	51.41 ± 0.41	0.25	1.12	2.74	3.16	1.45

3.3.2 Visible Raman spectra

Figure 3.3 shows the Raman spectra of pristine TiO_2 and a series of nitrogen doped TiO_2 supports. It is well known that the anatase phase of TiO_2 has six Raman bands at 144 cm^{-1} (E_g), 197 cm^{-1} (E_g), 399 cm^{-1} (B_{1g}), 519 cm^{-1} ($A_{1g}+B_{1g}$) and 639 cm^{-1} (E_g), while the rutile phase has four Raman bands at 143 cm^{-1} (B_{1g}), 447 cm^{-1} (E_g), 612 cm^{-1} (A_{1g}), and 826 cm^{-1} (B_{2g})[28]. A linear relationship between the integrated intensities of anatase (101) and rutile (110) XRD peaks and the area ratios of the Raman bands at 395 cm^{-1} (anatase) and 445 cm^{-1} (rutile) has been proposed[28]. Thus, Raman spectroscopy can be used to estimate the anatase and rutile contents in a TiO_2 sample. Based on this approximation, the anatase content on all samples was found to be in the range of 76-82% (weight). In agreement with previous reports[29,30], this result indicates that all synthesized N-doped TiO_2 materials consist of mostly anatase and that addition of nitrogen did not affect severely the phase content of the samples.
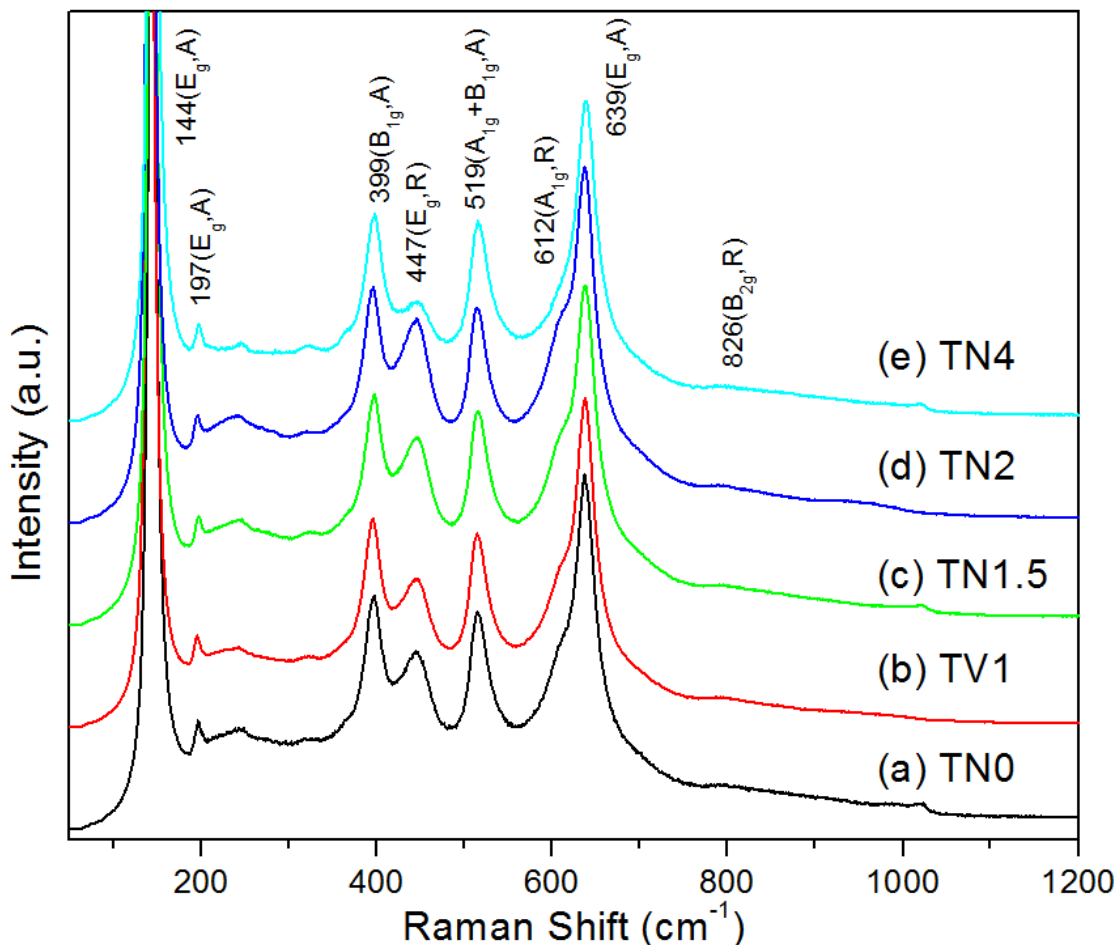
Figure 3.3. Visible Raman spectra of vanadium free nitrogen doped titanium dioxide supports (excitation line at 532 nm) (a) TN0, (b) TN1, (c) TN1.5, (d) TN2, and (e) TN4. R and A stand for anatase and rutile, respectively.

The interpretation of Raman spectra for supported VO_x phases has been extensively discussed[31]. Bulk V_2O_5 exhibits Raman peaks at 997, 700 and 485 cm^{-1}. The dominant peak at 997 cm^{-1} is associated with the symmetrical stretching mode of the terminal oxygen atom (V=O) in polymeric or bulk V_2O_5. A very important factor influencing the quality of the spectra and relative signal strength of this band is the level of sample hydration. For this reason, we obtained Raman spectra of the hydrated samples in flowing of He only at 25 ºC and those of the dehydrated samples were measured at 300 ºC in He/O$_2$ (5%) flow. Fig.3.4 shows typical Raman spectra obtained on dehydrated supported

VO_x in the 725 – 1200 cm^{-1} range, first, it is clear that a segregated V_2O_5 phase (994 cm^{-1}) is not present in this sample since peaks corresponding to bulk vanadium oxide are not observed. All the catalysts show a Raman band at ~1022 cm^{-1} attributed to the vanadyl (V=O) stretching as well as a weak broad band centered at 850 cm^{-1} and a shoulder at 980 cm^{-1} corresponding to either V-O-Ti bridging or V-O-V vibrations[31,32]. In agreement to previously reported work, these results indicate that there is a structural change in the supported VO_x phase upon dehydration[3]. The Raman spectra of all dehydrated samples show signals mostly characteristic for monomeric VO_4 species (1022 cm^{-1}) and bridging V-O-Ti moities. In addition, regardless of nitrogen content, all samples show the same position for the vanadyl band at 1022 cm^{-1} suggesting that the presence of nitrogen has no impact on the terminal V=O bond in the dehydrated samples. Thus we can conclude that most of the vanadia in the dehydrated sample exists mostly as a monomer, independently of the presence of nitrogen in the support.

On the other hand, the Raman signals for the hydrated samples differ from those of dehydrated samples. At ambient conditions, hydrophilic oxide surfaces are saturated with moisture and the surface VO_x species are solvated. The main Raman band for the hydrated undoped VO_x/TiO_2 catalyst is centered at ~984 cm^{-1} (Fig.3.5a). For the case of nitrogen doped samples the signal of the terminal V=O band appears at lower values. A possible reason for this shift toward lower wavenumbers can be explained in terms of the position of nitrogen in the support. Previous studies on the interstitial implantation of N in TiO_2 reported that interstitial nitrogen prefers to occupy positions on the surface layer of the support, leading to the formation of Ti-N-O-Ti moieties[30]. At the same time the solvated VO_x, has hydroxyl functional groups (V-OH) at ambient conditions. Thus we could attribute the observed shift in the Raman signal to a relative higher strength of the surface hydrogen bond (N···H) from VO_x/N-doped TiO_2 compared to that of surface O···H expected in pristine VO_x/TiO_2[33].
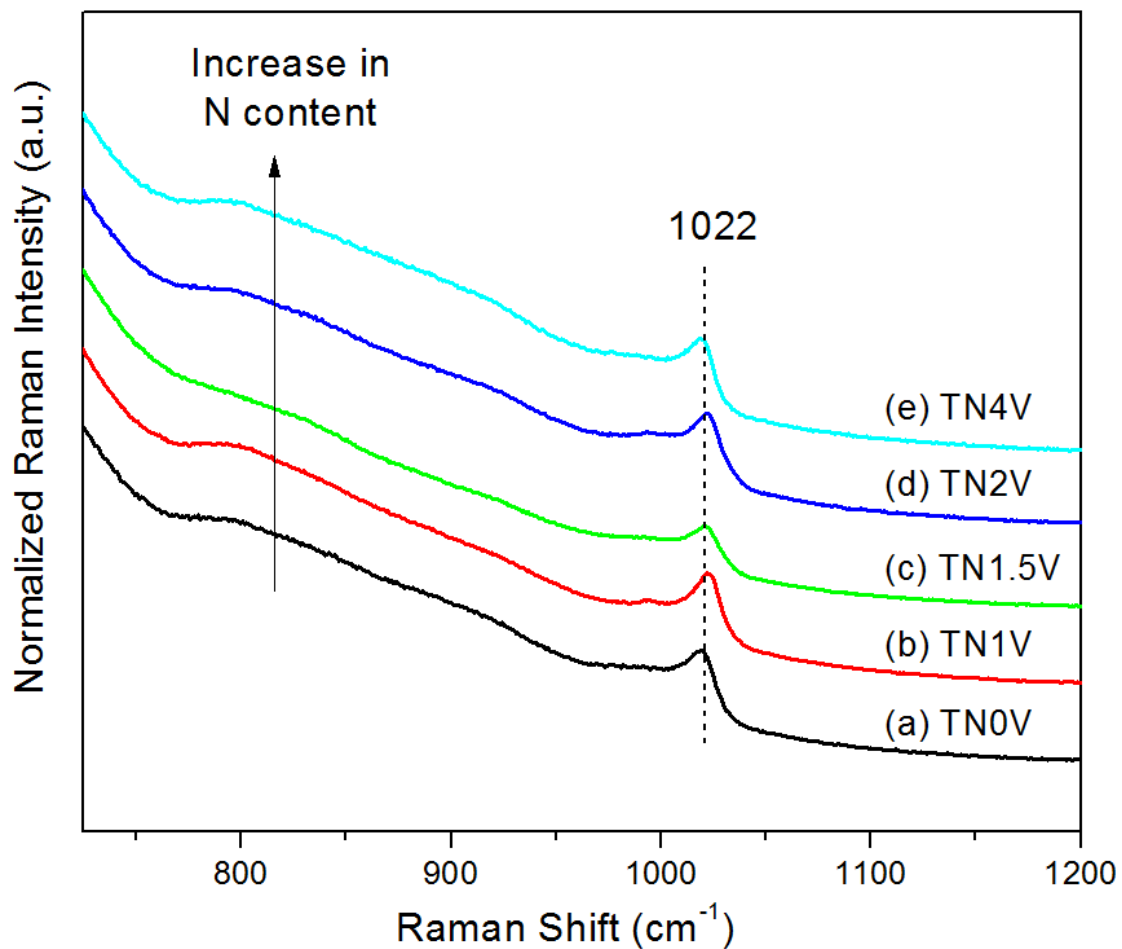
Figure 3.4. Normalized visible ($\lambda_{excitation}$ = 532 nm) Raman spectra of dehydrated VO$_x$/N-TiO$_2$ (300 ^{o}C) as a function of N content; (a) TN0V, (b) TN1V, (c) TN1.5V, (d) TN2V, and (e) TN4V.
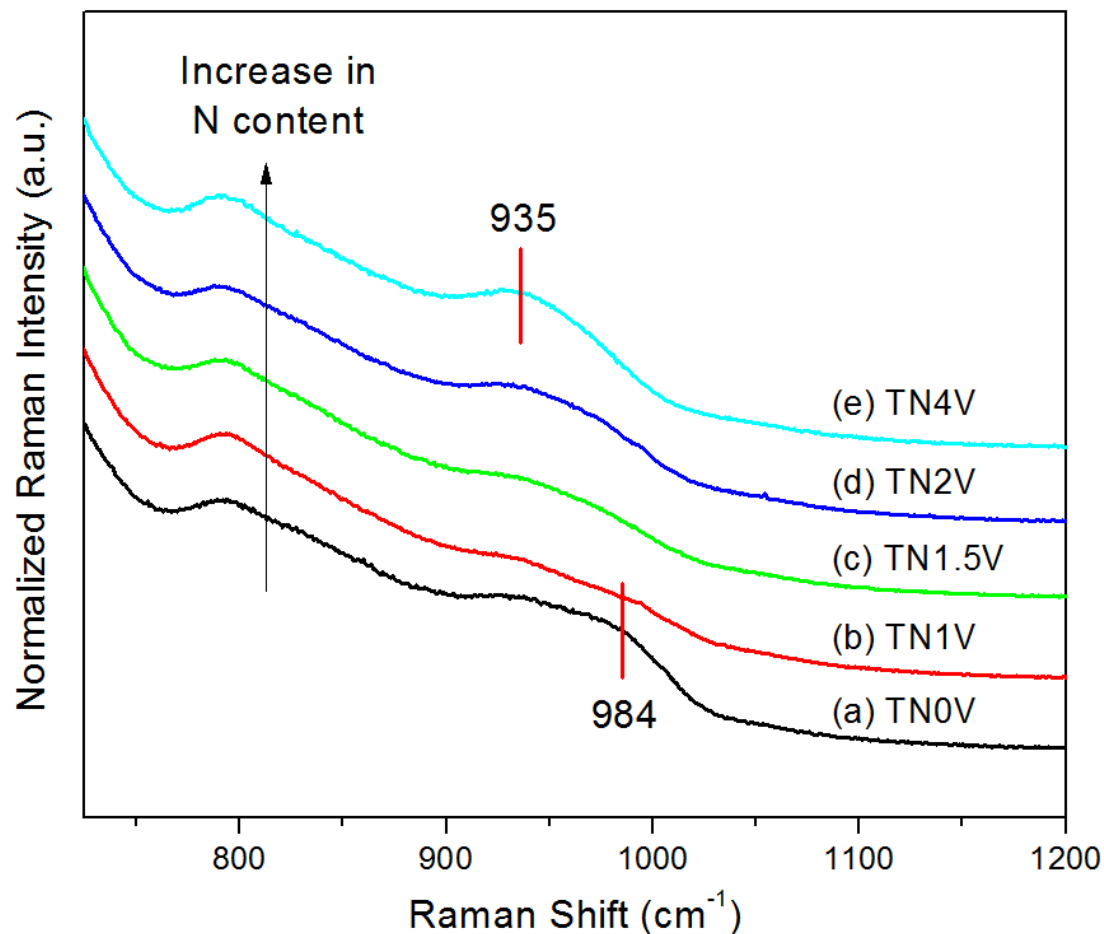
Figure 3.5. Normalized visible ($\lambda_{excitation}$ = 532 nm) Raman spectra of hydrated VO$_x$/N-TiO$_2$ as a function of N content; (a) TN0V, (b) TN1V, (c) TN1.5V, (d) TN2V, and (e) TN4V.

3.3.3   Reactivity

Partial oxidation of ethanol to acetaldehyde was used to evaluate catalytic activity. In a set of preliminary experiments performed in the same system with a blank reactor and vanadia free TiO$_2$, no ethanol conversion was observed at 200 ºC at all weight hourly space velocities (WHSV) tested in this study. For the case of the vanadium loaded samples, ethanol was converted to acetaldehyde and ethylene, though selectivity to ethylene was very low (below 0.5%). Combustion products (CO and CO$_2$) were not

observed. The high selectivity to acetaldehyde under these conditions is an indication of the relatively high degree of dispersion of the VO_x moieties in these catalysts[34]. Under our experimental conditions, in all cases the observed selectivity to acetaldehyde was above 99% and we did not observe measurable differences in this selectivity among the different tested catalytic materials. To carry meaningful comparisons between the catalysts tested, we extrapolated the measured rates to zero reactant conversion (initial partial oxidation rate) and normalized them by the total V content in the catalyst. Table 3.3 shows the results of this calculation for all catalytic materials tested at the reaction temperature (T = 200 ℃). All doped-N samples displayed higher activity than the nitrogen free catalyst (TN0V). Notably the values we obtained for apparent turnover frequencies are within the same order of magnitude as those previously reported by other researchers[34,35]. The table values also indicate a slight boost on catalyst activity as the nitrogen content on the catalyst increases to an optimum value (TN1.5V), after that point the catalytic activity decreases as nitrogen content keeps increasing. This observation will be discussed below in terms of the change of reducibility caused by N doping on the titania in the sections below.

Table 3.3. Ethanol partial oxidation rates observed at 200 ℃. All values reported were obtained after extrapolation to zero conversion.

Catalyst	Calculated turnover frequency at zero conversion (sec^{-1})
TN0V	0.137 ± 0.007
TN1V	0.164 ± 0.002
TN1.5V	0.274 ± 0.001
TN2V	0.159 ± 0.001
TN4V	0.140 ± 0.002

3.3.4   *In situ* diffuse reflectance UV-vis spectroscopy

Diffuse reflectance UV-*v*is spectroscopy can be used to probe the electronic structure of metal oxide domains. Indeed values obtained for edge energies from the UV-Vis spectra can be linked to metal oxide domain size since charge is more effectively delocalized when larger domains are supported on insulating oxides, resulting in lower values for observed edge energies[36]. On the other hand edge energies are weakly dependent on oxidation state, unless reduction processes significantly distort cation coordination symmetries[9,10]. For the case of titania-supported VO_x materials, the diffuse reflectance UV-vis spectra shows a broad band due to ligand-to metal charge transfer (LMCT) transitions of V^{+5} species. These bands originate from vanadate moieties in tetrahedral coordination. In the presence of polymeric species the spectra displays a red shift with peak tailing[18]. It has been also proposed that an absorption band in the range 1.55 - 2.48 eV (500 - 800 nm) originates from d-d transitions indicating the presence of V^{+4} moieties[12,37].

Using at starting point the work by Argyle and Iglesia[9,10] and the abundant literature in this respect we modified a methodology for measuring vanadia reduced centers generated under reductive conditions. This method is based on normalization of the observed changes in the UV-vis spectra and a rigorous calibration using a series of N free VO_x/TiO_2 samples reduced *in situ* at different temperatures. All spectra in this study were obtained at room temperature after the depicted treatment step. The relative absorbance values before and after unit base normalization against incident photon energy are shown in Fig.3.6b, for a nitrogen free sample reduced in ethanol at different temperatures. The pre-edge energy values (E_g') obtained after ethanol reduction at different temperatures and the energy value for maximum photon absorption after ethanol reduction at 200 ºC are presented in Table 3.4. A close inspection of the data presented for this sample reveals two characteristics. First, as expected, the pre-edge energy (E_g') values increase as the reduction temperature increases. The values for the peak maxima (reduced center) obtained after reduction at 200 ºC in ethanol (2.29 eV) fall within the value ascribed to d-d transitions. However, the exact identification of the d-d transitions features present on

the spectra of supported reduced vanadia is challenging since the oxidation state of reduced VO_x is highly dependent on the support. Dinse et al.[6–8] characterized the reduced sites of vanadia on various supports after reduction at high temperatures (500 ºC) and probed the oxidation state of vanadia using high frequency electron paramagnetic resonance (HF-EPR). Their results indicate that after reduction V^{+4} is the most abundant species when vanadia is supported on silica (SiO_2) and alumina (Al_2O_3). For the case of TiO_2 supported samples, V^{+4} sites were observed together with Ti^{+3}. In agreement with these observations, Eg' values previously reported for reduced VO_x supported on alumina appear at about $1.8 – 1.9$ eV (652 - 688 nm)[9,10], whereas the peaks for VO_x-TiO_2 in our experiments appear at $1.5 \sim 1.8$ eV for the direct band gap and $0.4 \sim 1.0$ eV due likely to the presence of Ti^{+3} species.
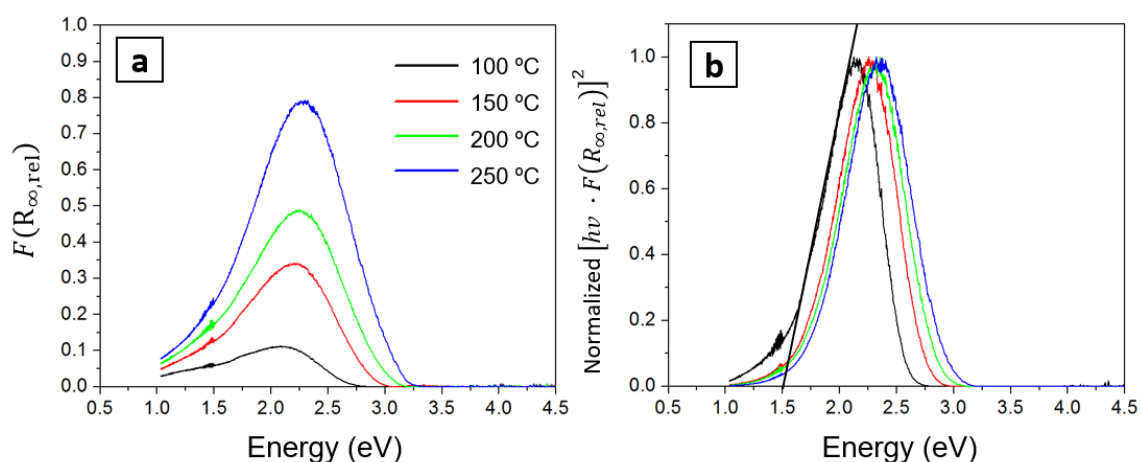
Figure 3.6. *In situ* **UV-vis spectra of TiO_2-supported VO_x (1.88 wt.% as V_2O_5) obtained after ethanol reduction at different temperatures for 1 h (a) and transformed plots assuming an allowed direct transition after unit base normalization using the spectra of the fully oxidized catalysts as reference ($R_{\infty,rel}$) (b).**

Table 3.4. Pre-edge energy (Eg') after reduction with ethanol at different temperature and position corresponding peak maxima at 200 ºC.

Catalyst	V contents as V_2O_5 (wt.%)	Pre-edge energy (Eg') at 100ºC (eV)	Eg' at 150ºC (eV)	Eg' at 200ºC (eV)	Eg' at 250ºC (eV)	Peak maxima at 200ºC (eV)
VO_x/TiO_2	1.88	1.51	1.63	1.69	1.72	2.29

Based on the results obtained on the nitrogen free samples, we measured and interpreted the Eg' values for supported VO_x catalysts on N doped TiO_2. Fig.3.7 depicts the UV-vis spectra for the pre-edge region obtained following the methodology outlined above for a series of nitrogen doped $VO_x/N-TiO_2$ catalyst reduced in ethanol at 200 ºC. Calculated Eg' and the peak maxima values observed for the reduced centers are summarized in Table 3.5. As discussed above, the peak originates due to a d-d transition, a blue shift indicates that the degree of reduction of vanadia increases with amount of nitrogen present in the support.
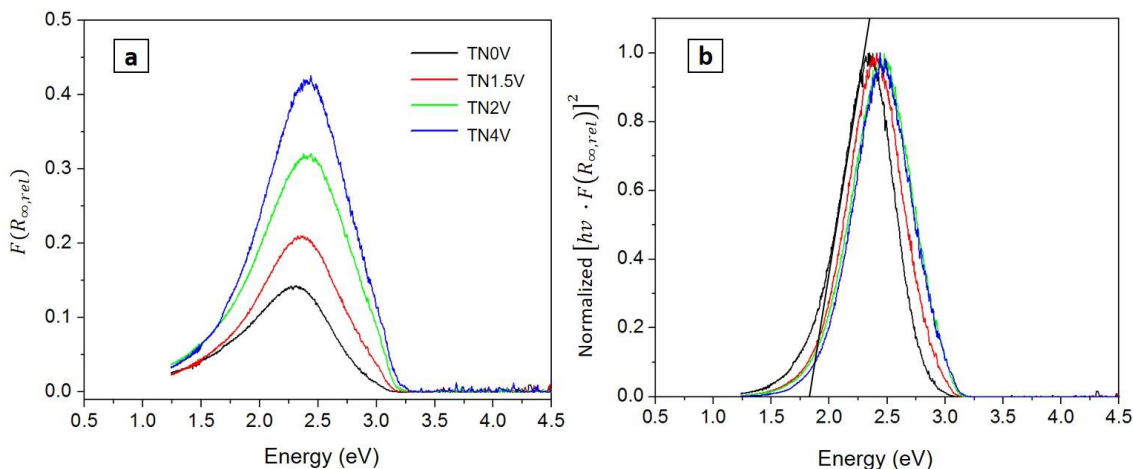
Figure 3.7. *In situ* **UV-vis spectra of TiO₂-supported VOₓ (1.52 wt.% as V₂O₅) nitrogen doped TiO₂-supported VOₓ as a function of N loading obtained at ambient temperature after ethanol reduction at 200ºC for 1 h (a) and transformed plots for allowed direct transitions after unity base normalization using the spectra of the fully oxidized catalysts as reference ($R_{\infty,rel}$) (b).**

Table 3.5. Pre-edge energy (E_g') and peak maxima in the pre-edge region after reduction in ethanol at 200ºC.

Catalyst	Eg' at 200ºC	Peak maxima at 200ºC
TN0V	1.83	2.37
TN1V	1.87	2.38
TN1.5V	1.89	2.41
TN2V	1.91	2.44
TN4V	1.96	2.48

3.3.5   Ethanol-temperature programmed desorption (Ethanol-TPD)

Figure 3.8 shows the temperature profile for acetaldehyde evolution over the $VO_x/N-TiO_2$ catalysts following ethanol adsorption. Ethanol-TPD profiles have been commonly measured by monitoring a primary peak in the mass spectrometer (m/z = 29 in case of acetaldehyde) in the effluent stream during desorption. However, dehydration of ethanol could also take place, depending on temperature, producing other products such as diethyle ether, which also has a significant mass fraction peak at 29 m/z resulting in overlapping with the acetaldehyde mass spectra[2]. To avoid this, we separated the effluent gases and analyzed them using gas chromatography. For all catalysts, acetaldehyde desorption profiles were observed below 200 ℃. The acetaldehyde evolution profiles show two main peaks, one at about 83 ℃ and another one at approximately 120 ℃. Figure 3.8 shows these profiles. A clear trend is observed; first, more acetaldehyde was released at lower temperature (peak 1) when the N content on the support increases compared to that at high temperature (peak 2). Assuming the TPD spectra is symmetric curves, this analysis based on the ratio between two deconvoluted peaks (area of peak 2/area of peak 1), which increased from 0.79 for N-free catalyst (TN0V) to 2.12 for TN4V.

Acetaldehyde is formed as a result of the reduction of vanadia by ethanol through an α-elimination mechanism. The amount of acetaldehyde released thus depends on the reducibility of the vanadia clusters present on the catalyst surface. It well established that the reducibility of vanadia depends on both the electronic structure of the support material, and the domain size of the vanadia cluster. On the other hand, the presence of two peaks on the TPD profile could suggest a distribution of sites with two different degrees of reducibility. And it could be proposed that this is an indication of a heterogeneous distribution of cluster sizes on these materials. However, the CVB number calculated from the UV-Vis spectra (Table 3.2) as well as the Raman results (Fig.3.5) clearly indicate that the average vanadia cluster size is very similar for all materials. Thus our results could be interpreted by proposing that the distribution of active sites and the reducibility of the VO_x species are significantly affected by the presence of nitrogen in the support.
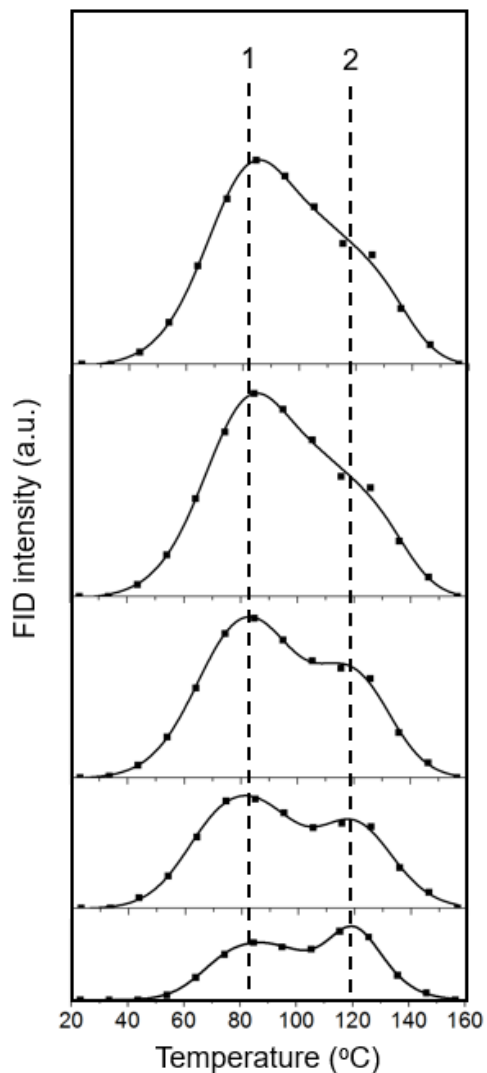
Figure 3.8. Acetaldehyde evolution during EtOH-TPD over nitrogen doped VOx/TiO2 as a function of N content; (a) TN0V, (b) TN1V, (c) TN1.5V, (d) TN2V, and (e) TN4V.

3.3.6 Electronic structure of the reduced VO_x

To understand the observed changes in catalytic activity and structure resulting from the introduction of nitrogen into the VO_x/TiO$_2$ system, we created a model for the reduced supported VO_x as an isolated monomer adsorbed on the (101) surface of nitrogen free and

two types of nitrogen doped TiO_2: interstitial nitrogen (N_i) and substitutional nitrogen (N_s) (Fig.3.9). Prior to discussing electronic changes that underline the N doping effects observed in the above subsections, the electronic structure of reduced VO_x on N-free anatase (101) slab in terms of its geometry and density of states (DOS) will be discussed.
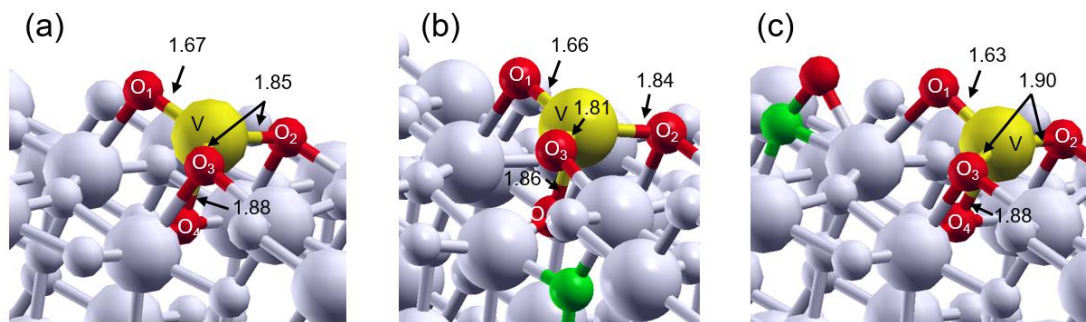
Figure 3.9. Geometries of the most stable configurations for: reduced VO_x on (a) N-free TiO_2, (b) substitutional N_s-TiO_2, and (c) interstitial N_i-TiO_2. Red, yellow, and green correspond to O, V, and N atoms, respectively. Grey are Ti and O atoms in the support not directly bonding the vanadium.

First, the reduced VO_x cluster is depicted as lacking the terminal vanadyl oxygen (V=O) commonly found in vanadium oxide (V) clusters. Four oxygen atoms are found to be responsible for the bonding of this reduced V center and were denoted to O_1, O_2, O_3, and O_4 in Fig.3.9, respectively. We compared the structure parameters (V-O distance) obtained from the relaxed reduced VO_x/N-free anatase (101) surface to those experimentally obtained by Silversmit et al. using extended X-ray adsorption fine structure spectroscopy (EXAFS) in order to confirm the accuracy of our model slab[38,39]. This comparison is shown in Table 3.6. We can see that our calculated structural parameters of N free model (Fig.3.9a) are consistent with this experimental study on the structure of reduced vanadia.

Table 3.6. Comparison of the V-O distances obtained in our calculation (right column) with previous experimental measurements of bond distances on reduced, monomeric VO_x/TiO_2 samples. The experimental values were obtained from an EXAFS fit by Silversmit et al. [38].

Key parameters	Experimental (Å) [1]	Key parameters	This study (Å)
V-O	1.64, 1.88 , 2.00, 2.45	V-O$_1$	1.67
		V-O$_2$	1.85
		V-O$_3$	1.88

[1] Ref. [38]

Figure 3.10 shows the calculated total density of states (TDOS) for the nitrogen free TiO_2 supported VO_x reduced cluster discussed above (a) and also the obtained TDOS on (b) interstitially N doped and (c) substitutionally N-doped reduced VO_x clusters. The projected density of state (PDOS) onto the vanadium as well as into the bridging oxygen atoms (O_1, O_2, and O_3) obtained for these 3 model slabs is presented in Fig.3.11. For both TDOS and PDOS the Fermi level is at 0 eV. Typically, for a clean TiO_2 surface the O-2p states completely fill the valence band, while the Ti-3d states are in the conduction band; the Fermi level positioned near the valence band. However, for the case of the N-free VO_x/TiO_2 slab, the Fermi level is located just below the conduction band meaning that the states between 0 eV and -0.5 eV are filled with electrons (* in Fig.3.10a). The projection onto the V 3d states provides evidence for a d-d transition we assigned as the pre-edge peak (Fig.3.5) during analysis of our UV-vis results. However, the projected DOS of the V-3d states occupies less than a half of the conduction band, therefore, reduced VO_x cannot be solely responsible for the observed transition. The obtained charge density plot of reduced VO_x over pristine anatase (101) at top of the valence band (highest electronic occupied state) is shown in Fig.3.12. The charge density is localized dominantly at the V cation center and is partially distributed to the titanium atoms nearby. Based on this analysis, we can propose that the transition observed in the optical spectra

originates not only from reduced V centers but also from partially reduced Ti atoms bonded to vanadium through bridging oxygens (V-O-Ti). In other words, the electronic density, which is introduced upon reduction of VO_x, is not evenly distributed over a large number of atoms and mostly results in a noticeable change on the electronic structure of the vanadium and those Ti atoms closest to it. Therefore, we conclude that the electronic d-d transition observed in the low energy region (1 - 2.5eV) on the *in situ* UV-vis spectroscopy experiments in this study is mechanistically related to partially filled V and Ti d-orbitals (V^{+4} and Ti^{+3}). The observation obtained from the calculated PDOS and charge density of the highest occupied state of the reduced VO_x/TiO_2 system are in excellent agreement with previous reports from *in situ* EPR[6,8] which identified both V^{+4} and Ti^{+3} present under reductive environments (section 3.3.4).
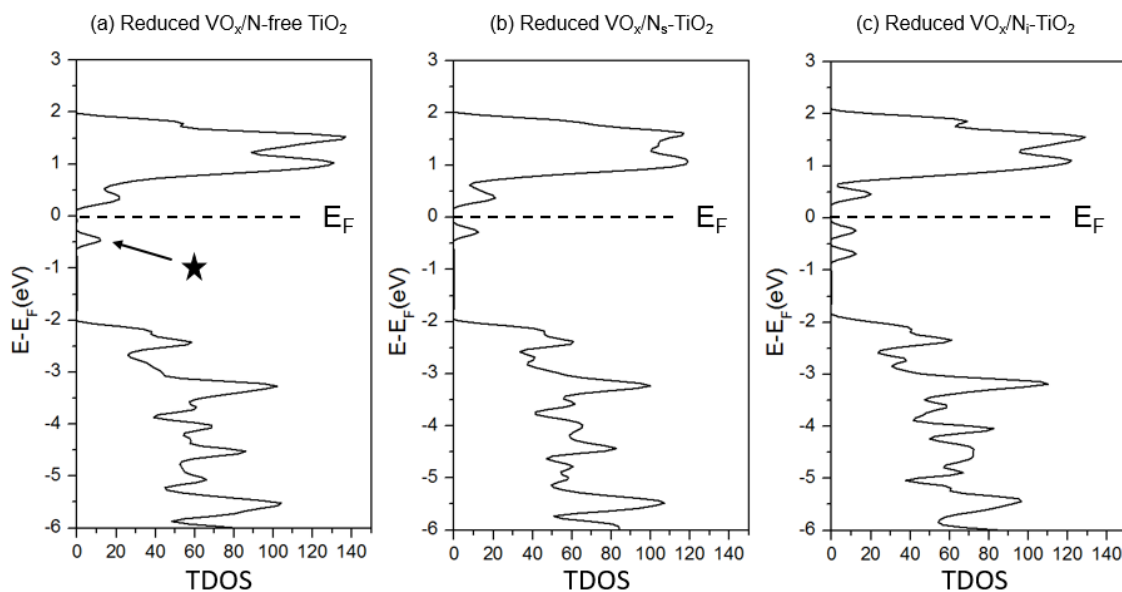
Figure 3.10. Total density of states of a reduced VO_x cluster supported on (a) nitrogen free anatase (101) surface, reduced VO_x on (b) N substitutional anatase (101) and (c) N interstitial anatase (101), as described in Fig.3.9.
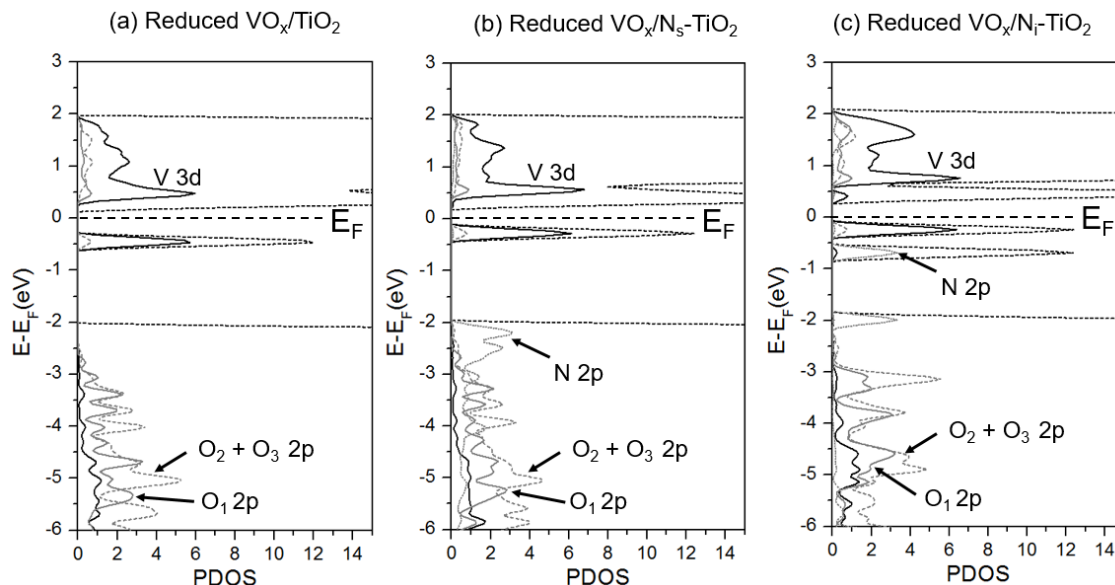
Figure 3.11. Calculated total (black dotted line) density of states of reduced VO_x clusters supported on (a) nitrogen free anatase (101) surface, (b) N substitutional anatase (101) and (c) N interstitial anatase (101). The projected DOS on the V 3d state (black solid line), 2-fold bridging oxygen (O_1, gray solid line), the sum of 3-fold bridging oxygen (O_2+O_3, gray dashed line) bound to the vanadium atom and doped nitrogen (N, gray dotted line) for each model are also presented. For the position of O_1, O_2, and O_3 see Fig. 3.9.

Based on the aforementioned considerations, we now focus on evaluating how the presence of N influence the electronic structure of reduced VO_x/TiO_2. To this aim we considered the most stable possible N positions within the first two TiO_2 layers for either substitutional (N_s) or interstitial (N_i) nitrogen. For the case of N_s doped anatase (101) structure, the location was assigned by replacing the subsurface three-coordinated bridging oxygen atom in the model slab for nitrogen (Fig.3.9b), since this location has been reported as the most thermodynamically stable for nitrogen substitution[25,30,40]. For the case of the substitutional nitrogen, the nitrogen atom prefers to occupy positions on the surface[41]. Thus, it is plausible to assume that in N_i doped anatase (101) the structure on the surface has been changed in some sites from Ti-O-Ti to Ti-N-O-Ti moities (Fig.3.9c).

A comparison between the values obtained for the total DOSs and projected DOS for some specific states for the case of reduced on N-free, N-interstitial and N-substitutional doped anatase is presented in Figures 3.10 and 3.11. First, as Fig 3.10 indicates, the presence of nitrogen considerably affects the conduction band, and in particular those states near the Fermi level. Indeed, substitution of one oxygen (Fig.3.10b) by nitrogen results in an increased bandwidth of the conduction band. In contrast, for the case of interstitial nitrogen this bandwidth is not severely affected. However in this case a new state is generated on the conduction band (-0.5 ~ -1.0 eV), which is likely linked to the N-2p state (see discussion below). These observations clearly indicate that the chemical behavior of interstitial N-doped materials is different from its substitutional counterpart. Moreover, it can be proposed, that in the reduced system, the electronic structure of the substitutional N_s atom has become similar to that of a lattice O atom, while for the case of interstitial nitrogen this is not the case. Indeed, previous studies on the electronic structure of vanadia free, N-doped anatase indicate that the presence of nitrogen results on the introduction of an unpaired N 2p orbital and the generation of an empty state where electrons can be trapped, which results from the removal of an oxygen atom[42]. On the other hand the obtained charge density (Fig.3.12) of reduced VO_x over N doped showed no obvious differences in the calculated charge density of the highest occupied state of the system, regardless of the presence of nitrogen.

To get a deeper insight into the electronic density for the reduced VO_x catalysts, we calculated Bader atomic charges, as listed in Table 3.7. The Bader charge analysis for atoms of interest further confirms the analysis presented above. The values obtained indicate that all oxygen atoms bound to V are similarly negatively charged, regardless of the presence of nitrogen. In contrast there are clear differences for the nitrogen charge that arise if nitrogen is in a substitutional (-1.301 |e|) or in an interstitial (-0.535 |e|) position. The more negative value in the Bader charge obtained for substitutional N confirms that in this case N gains more electrons, likely at the expense of nearby oxygen atoms. Moreover, when comparing the total density of states around the conduction band (-1.0 to -0.5 eV, Fig.3.11c), there is an increase on the number of available states for the case of interstitial nitrogen. This change is not observed for the case of substitutional N.

These observations drive us to conclude that, compared to substitutional nitrogen, surface interstitial N should have a larger influence on the electronic behavior of the catalytic system.
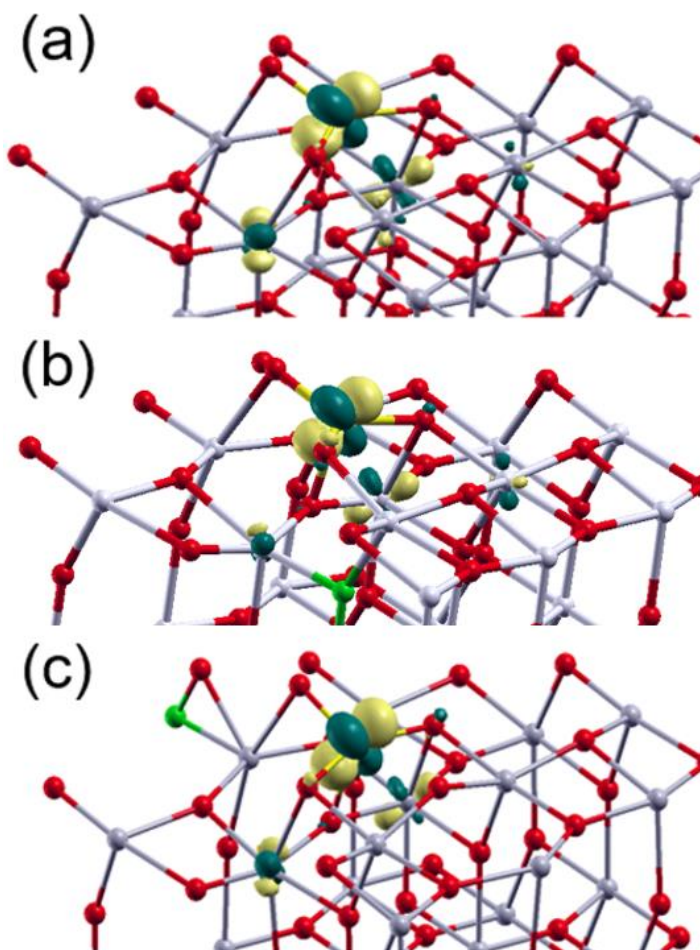
Figure 3.12. Charge density of the highest occupied state for the reduced VO$_x$ cluster supported on (a) pristine anatase (101) surface and (b) on substitutional N doped anatase (101) surface and (c) on interstitial N doped anatase (101) surface. Cyan and yellow orbital shapes correspond to the ± 0.01 isosurface. (Grey, red, and green represent are Ti, O, and N atoms, respectively).

Table 3.7. Bader charge analysis of proposed N-free and N-doped reduced catalyst models.

Structure	Reduced VO$_x$/N free anatase (101)	Reduced VO$_x$/N$_s$ doped anatase (101)	Reduced VO$_x$/N$_i$ doped anatase (101)
O1	-0.949	-0.928	-0.846
O2	-1.175	-1.172	-1.141
O3	-1.174	-1.166	-1.140
O4	-1.198	-1.191	-1.193
N	-	**-1.301**	**-0.535**
V	1.883	1.9133	1.933

Lastly, in Fig.3.13, we show the calculated optical absorption spectra of the three reduced modeled surfaces plus that one of an oxidized, nitrogen free VO$_x$ on anatase (101) obtained using time-dependent density functional theory (TDDFT) at DFT level. It is widely recognized that this approach is insufficient to give a correct band gap attributed to the incomplete cancellation of the self-interaction of pure exchange/correlation functional[41]. Fortunately, comparing the electronic structures at DFT and DFT+U levels of models of interest, both functional showed identical the delocalized energy states near Fermi level with the band gap difference. Thus, absorption spectra were calculated at DFT level and then, the photon energy, corresponding to x-axis in Fig.3.13 was corrected by multiplying a ratio factor of 1.4 (band gap of anatase 101 surface at DFT+U level / that at DFT level). The calculated absorption edge (E$_g$) value after the correction for oxidized VO$_x$/anatase (101) is 2.7 eV, similar to the experimental observation[27], shown as black solid line in Fig.3.13. Thus, the obtained trends are comparable. As the VO$_x$ is

reduced, the absorption spectra show a broad band appearing in the range of 0.25 – 2.5 eV, which corresponds to a d-d transition (V-3d $\rightarrow$ V-3d or Ti-3d $\rightarrow$ Ti-3d). It should be noted that, compared to N-free reduced VO_x/TiO_2, the d-d transition for the model obtained using interstitial nitrogen (N_i) shows a blue-shift of 0.2 eV while the value calculated for the model with substitutional nitrogen (N_s) showed a red-shift of 0.1 eV.

As discussed in section 3.3.4, we observed an analogous blue shift in the *in situ* UV-vis absorption spectra and proposed that there is an increase on the degree of reduction in the sample triggered by the presence of interstitial nitrogen in the support since as discussed before the nitrogen present in our samples is mainly occupying interstitial positions[30,43]. The result shown in Fig.3.13 thus further confirms the presence of nitrogen on catalyst increases reducibility of VO_x and the volcano-shape relationship in catalytic activity we observed can be led by the lower reoxidizability of reduced VO_x to a larger extent, anchored with a high N loading TiO_2 support.
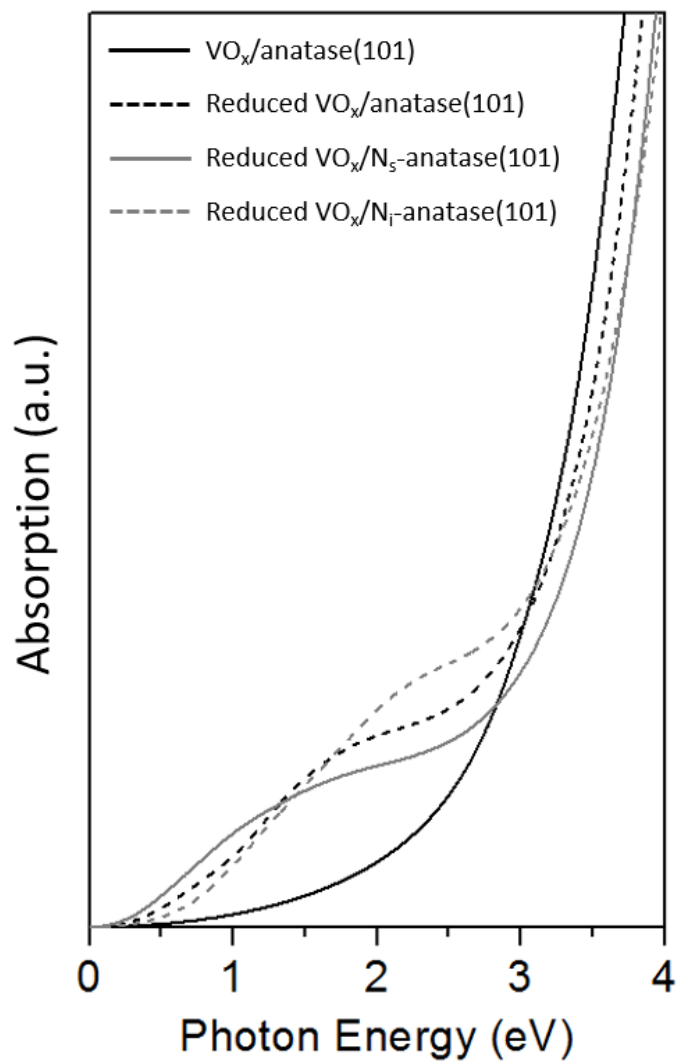
Figure 3.13. TDDFT calculation of the electronic spectra of oxidized VO$_x$ cluster supported on a pristine anatase (101) surface (black solid line) and of a reduced VO$_x$ cluster supported on pristine (black dashed line), substitutionally N doped (gray solid line) and interstitially N doped (gray dashed line) anatase (101) surface.

3.4 Conclusion

The results in this work demonstrate that the modification of the TiO_2 surface by nitrogen affects the activity of VO_x for redox catalysis. Catalyst synthesis and *in situ* Raman measurements enabled us to ensure that geometrical changes on the vanadia moieties are minimized. Optical spectroscopic measurements and theoretical calculations suggest that the degree of reduction of supported VO_x is larger in the presence of doping N on the titania support; thus under our experimental conditions, the presence of N results in a larger number of active sites for catalytic redox turnovers. The experimental trends obtained are further confirmed using computational calculations, enabling the identification of the origin of the observed d-d transition present on the reduced catalyst and rationalizing the blue shift on the electronic transition observed in the nitrogen doped catalysts in terms of an increase in the reducibility of vanadia caused by the presence of nitrogen.

References

(1)   Feng, Z.; Cheng, L.; Kim, C. Y.; Elam, J. W.; Zhang, Z.; Curtiss, L. a.; Zapol, P.; Bedzyk, M. J. *J. Phys. Chem. Lett.* **2012**, *3* (19), 2845–2850.

(2)   Beck, B.; Harth, M.; Hamilton, N. G.; Carrero, C.; Uhlrich, J. J.; Trunschke, A.; Shaikhutdinov, S.; Schubert, H.; Freund, H.-J.; Schlögl, R.; Sauer, J.; Schomäcker, R. *J. Catal.* **2012**, *296* (0), 120–131.

(3)   Wachs, I. E. *Dalt. Trans.* **2013**, *42* (33), 11762–11769.

(4)   Christodoulakis, A.; Machli, M.; Lemonidou, A. A.; Boghosian, S. *J. Catal.* **2004**, *222* (2), 293–306.

(5)   Kilos, B.; Bell, A. T.; Iglesia, E. *J. Phys. Chem. C* **2009**, *113* (7), 2830–2836.

(6)   Dinse, A.; Ozarowski, A.; Hess, C.; Schomäcker, R.; Dinse, K.-P. *J. Phys. Chem. C* **2008**, *112* (45), 17664–17671.

(7)   Dinse, A.; Schomäcker, R.; Bell, A. T. *Phys. Chem. Chem. Phys.* **2009**, *11* (29), 6119–6124.

(8)   Dinse, A.; Carrero, C.; Ozarowski, A.; Schomäcker, R.; Schlögl, R.; Dinse, K.-P. *ChemCatChem* **2012**, *4* (5), 641–652.

(9)   Argyle, M. D.; Chen, K.; Resini, C.; Krebs, C.; Bell, A. T.; Iglesia, E. *Chem. Commun.* **2003**, *16*, 2082–2083.

(10)   Argyle, M. D.; Chen, K.; Resini, C.; Krebs, C.; Bell, A. T.; Iglesia, E. *J. Phys. Chem. B* **2004**, *108* (7), 2345–2353.

(11)   Gao, X.; Bare, S. R.; Fierro, J. L. G.; Wachs, I. E. *J. Phys. Chem. B* **1999**, *103* (4), 618–629.

(12)   Burcham, L.; Deo, G.; Gao, X.; Wachs, I. *Top. Catal.* **2000**, *11-12* (1-4), 85–100.

(13)   Li, Y.; Wei, Z.; Gao, F.; Kovarik, L.; Peden, C. H. F.; Wang, Y. *J. Catal.* **2014**, *315* (0), 15–24.

(14)   Bañares, M. A.; Martínez-Huerta, M. V; Gao, X.; Fierro, J. L. G.; Wachs, I. E. *Catal. Today* **2000**, *61* (1–4), 295–301.

(15)   Gao, X.; Bañares, M. A.; Wachs, I. E. *J. Catal.* **1999**, *188* (2), 325–331.

(16)   Yun, D.; Zhao, Y.; Abdullahi, I.; Herrera, J. E. *J. Mol. Catal. A Chem.* **2014**, *390* (0), 169–177.

(17)   Gao, X.; Jehng, J.-M.; Wachs, I. E. *J. Catal.* **2002**, *209* (1), 43–50.

(18)   Malleswara Rao, T. V; Deo, G.; Jehng, J.-M.; Wachs, I. E. *Langmuir* **2004**, *20* (17), 7159–7165.

(19)   Zhang, Z.; Wang, X.; Long, J.; Gu, Q.; Ding, Z.; Fu, X. *J. Catal.* **2010**, *276* (2), 201–214.

(20)   Ansari, S. A.; Khan, M. M.; Ansari, M. O.; Cho, M. H. *New J. Chem.* **2016**, *40*, 3000–3009.

(21)   Perdew, J. P.; Burke, K.; Ernzerhof, M. *Phys. Rev. Lett.* **1996**, *77* (18), 3865–3868.

(22)   Vanderbilt, D. *Phys. Rev. B* **1990**, *41* (11), 7892–7895.

(23)   Lutfalla, S.; Shapovalov, V.; Bell, A. T. *J. Chem. Theory Comput.* **2011**, *7* (m), 2218–2223.

(24)   Giannozzi, P.; Baroni, S.; Bonini, N.; Calandra, M.; Car, R.; Cavazzoni, C.; Ceresoli, D.; Chiarotti, G. L.; Cococcioni, M.; Dabo, I.; Dal Corso, A.; de Gironcoli, S.; Fabris, S.; Fratesi, G.; Gebauer, R.; Gerstmann, U.; Gougoussis, C.; Kokalj, A.; Lazzeri, M.; Martin-Samos, L.; Marzari, N.; Mauri, F.; Mazzarello, R.; Paolini, S.; Pasquarello, A.; Paulatto, L.; Sbraccia, C.; Scandolo, S.; Sclauzero, G.; Seitsonen, A. P.; Smogunov, A.; Umari, P.; Wentzcovitch, R. M. *J. Phys. Condens. Matter* **2009**, *21* (39), 395502.

(25)   Chen, Q.; Tang, C.; Zheng, G. *Phys. B Condens. Matter* **2009**, *404* (8-11), 1074–1078.

(26)   Pap, Z.; Baia, L.; Mogyorósi, K.; Dombi, A.; Oszkó, A.; Danciu, V. *Catal. Commun.* **2012**, *17*, 1–7.

(27)   Gao, X.; Wachs, I. E. *J. Phys. Chem. B* **2000**, *104* (6), 1261–1268.

(28)   Zhang, J.; Li, M.; Feng, Z.; Chen, J.; Li, C. *J. Phys. Chem. B* **2005**, *110* (2), 927–935.

(29)   Hurum, D. C.; Agrios, a G.; Gray, K. a; Rajh, T.; Thurnauer, M. C. *J. Phys. Chem. B* **2003**, *107* (19), 4545–4549.

(30)   Di Valentin, C.; Pacchioni, G.; Selloni, A.; Livraghi, S.; Giamello, E. *J. Phys. Chem. B* **2005**, *109* (23), 11414–11419.

(31)   Wu, Z.; Kim, H.-S.; Stair, P. C.; Rugmini, S.; Jackson, S. D. *J. Phys. Chem. B* **2005**, *109* (7), 2793–2800.

(32)   Carrero, C. A.; Keturakis, C. J.; Orrego, A.; Schomacker, R.; Wachs, I. E. *Dalt. Trans.* **2013**, *42* (35), 12644–12653.

(33)   Emsley, J. *Chem. Soc. Rev.* **1980**, *9* (1), 91–124.

(34)   Herrera, J. E.; Isimjan, T. T.; Abdullahi, I.; Ray, A.; Rohani, S. *Appl. Catal. A Gen.* **2012**, *417-418*, 13–18.

(35)   Chimentão, R. J.; Herrera, J. E.; Kwak, J. H.; Medina, F.; Wang, Y.; Peden, C. H. F. *Appl. Catal. A Gen.* **2007**, *332* (2), 263–272.

(36)   Barton, D. G.; Shtein, M.; Wilson, R. D.; Soled, S. L.; Iglesia, E. *J. Phys. Chem. B* **1999**, *103* (4), 630–640.

(37)   Weckhuysen, B. M.; Keller, D. E. *Catal. Today* **2003**, *78* (1–4), 25–46.

(38)   Silversmit, G.; Van Bokhoven, J. a; Poelman, H.; Van Der Eerden, a. M. J.;

Marin, G. B.; Reyniers, M. F.; De Gryse, R. *Appl. Catal. A Gen.* **2005**, *285* (1-2), 151–162.

(39)   Silversmit, G.; van Bokhoven, J. a; Poelman, H.; van der Eerden, a; Marin, G. B.; Reyniers, M. F.; De Gryse, R. *Phys. Scr.* **2005**, *T115*, 798–801.

(40)   Finazzi, E.; Valentin, C. Di; Uni, V.; Cozzi, V.; Selloni, A. **2007**, *2* (101), 9275–9282.

(41)   Ortega, Y.; Hernández, N. C.; Menéndez-Proupin, E.; Graciani, J.; Sanz, J. F. *Phys. Chem. Chem. Phys.* **2011**, *13* (23), 11340.

(42)   Di Valentin, C.; Finazzi, E.; Pacchioni, G.; Selloni, A.; Livraghi, S.; Paganini, M. C.; Giamello, E. *Chem. Phys.* **2007**, *339* (1–3), 44–56.

(43)   Reyes-Garcia, E. A.; Sun, Y.; Reyes-Gil, K.; Raftery, D. *J. Phys. Chem. C* **2007**, *111* (6), 2738–2748.

Chapter 4

4 Electronic assessment of oxidized and reduced supported vanadium oxide (monomer, dimer, trimer and 1-d polymer): kinetic, *in situ* UV-vis spectroscopy and computational study

Abstract

The catalytic activity for ethanol partial oxidation of supported vanadia/titana (VO_x/TiO_2) catalysts was correlated to the electronic structure of the vanadium clusters present over the catalyst surface. *In situ* Raman spectroscopy and temperature programmed desorption (TPD) experiments indicate that the distribution of active VO_x species with different cluster sizes is very sensitive to vanadia loading: isolated VO_x predominantly existing at low VO_x contents while larger vanadia clusters coexist in the catalyst at higher VO_x loadings. *In situ* UV-vis spectroscopy revealed that a significant fraction of vanadium cluster remain reduced during catalysis, and thus do not participate in catalytic turnover, particularly for the case of samples prepared at higher vanadia loadings. The electronic structures of VO_x clusters of different sizes (monomer, dimer, trimer and one-dimensional polymer) were investigated using periodic density functional theoretical calculations. Results indicate the electronic structures of oxidized and reduced VO_x models were significantly affected by the VO_x cluster size. Our analysis revealed that the formation of the reduced VO_x sites (V^{+4}) during catalysis is concomitant to the reduction of adjacent Ti cations (Ti^{+3}). Theoretically calculated optical absorption spectra matched the experimental spectroscopic results, confirming these observations. Furthermore, the determination of defect formation enthalpies, reported previously as descriptors of catalytic activity for this system, predicted that the monomeric VO_x on TiO_2 predominantly takes part in catalytic turnovers.

4.1   Introduction

The superior catalytic performance of supported vanadia (VO_x) on TiO_2 has attracted the interest of researchers for decades[1]. Among all chemical processes that these material can catalyze, the partial oxidation of alcohols has been used a probe reaction in a relative large set of experimental and theoretical studies aimed at understanding kinetics and mechanism of this catalyzed redox process[1–4]. By analogy with other oxidation reactions, the alcohol oxidation process are suggested to take place via a Mars-van Krevelen redox cycle[5–8] in which the first step of the oxidation mechanism corresponds to dissociative adsorption of alcohol which lead to the formation of an alkoxy and a hydroxyl species on the catalyst site. This first step is quasi-equilibrated[6,9]. In addition, isotopic tracer studies using deuterium (D)-labeled ethanol (CH_3CH_2OH, CD_3CD_2OH, and CH_3CH_2OD) revealed that the rate limiting step, in which the hydrogen transfers from alkoxy species to lattice oxygen to produce aldehyde and second hydroxyl species, is irreversible[9,10]. This step results in the chemical reduction of vanadium centers and water formation resulting from hydroxyls recombination[11,12]. They sequentially are reoxidized by irreversibly dissociated O_2 (chemisorbed O_2), which is normally assumed to be the most abundant surface species[13]. Although there is a lack of experimental data for the elementary processes that take place after the rate limiting step[14], it is generally agreed that the formation of aldehydes from alcohol partial oxidation results in the formation of reduced vanadium centers and lattice oxygen vacancies that are generated on the surface when water desorbs as a result of surface hydroxyls recombination[14].

Furthermore, the catalytic activity for ethanol partial oxidation by supported VO_x is highly dependent on the size distribution of VO_x domains in the catalysts, generally displaying lower TOF values at higher surface coverage, which is attributed to the formation of larger sized vanadia domains[1]. Unfortunately, due to a lack of control on the exact vanadia cluster size the difference on reactivity of different VO_x structures is still subject of controversy and the exact determination of the active site is a topic of intense research[15–17]. Despite of these complexities, previous research reported that the reducibility of the vanadium (V^{+5}) oxide clusters is very sensitive to cluster size and structure[18,19] and polymeric vanadia species are harder to reduce than isolated VO_x

moities under propane oxidative dehydrogenation reaction conditions[10,20,21]. Additionally, Dinse et al., have reported the formation of Ti^{+3} species in the VO_x/TiO_2 system under reductive environments[22,23]. This observation highlights the role of the strong vanadia/support interaction in the VO_x/TiO_2 system.

In this contribution, we aim to provide a deeper insight into the correlations between the structure of different sized VO_x domains, their electronic structure, reducibility and catalytic activity. Electronic transitions in the solid catalyst observed during ethanol partial oxidation were measured using *in situ* UV-vis spectroscopy in order to evaluate the changes in reducibility of the VO_x species during catalysis. Computational calculations were conducted to investigate the electronic structure of the vanadia clusters present in the VO_x/TiO_2 system and to rationalize the electronic transitions observed in the UV-vis spectra during ethanol partial oxidation.

4.2   Methods

4.2.1   Catalyst Preparation

Nano-powdered TiO_2 were purchased and used without further purification (Sigma Aldrich, 99.7%, 21nm). VO_x impregnation over these supports was carried by incipient wetness impregnation, using aqueous vanadium pentoxide (V_2O_5, Sigma Aldrich, ACS grade) dissolved in 1M oxalic acid ($H_2C_2O_4$, Sigma Aldrich, ACS grade). After impregnation the catalyst were dried in the oven at 90ºC overnight, and further calcined at 400ºC for 2h in air (Praxair, UHP). The prepared TiO_2 supported VO_x are denoted as TV_X (x denotes the vanadium weight percent (wt.%) varying from 1 to 6 wt.%).

4.2.2   Catalyst Characterization

The specific surface areas of the VO_x/TiO_2 supports were measured by a seven point Brunauer-Emmett-Teller (BET) method using N_2 adsorption-desorption isotherms at 77K (Micromeritics TriStar II 3020 Physisorption Analyzer) previous degassing at 90 ºC for 1

h and 200 ºC for 4 h under N_2 atmosphere. Raman spectra of as-prepared TiO_2 supported VO_x catalyst were collected using a custom made Raman instrument equipped with an *in situ* reaction chamber (HVC-DRP, Harrick Scientific) and a liquid nitrogen cooled charge coupled device (CCD, SpectraPro 2500i). The 532 nm excitation line from a 1W diode-pumped solid-state (DPSS) laser was used. The laser power at the sample position was 1.0 mW. Raman spectra of hydrated and dehydrated samples were recorded under controlled atmosphere. To obtain the spectra of the dehydrated samples the TVx samples were heated in the reaction chamber in flowing 5% O_2 balanced with He (Praxair, 10 $cm^3 \cdot min^{-1}$) at 300 ºC for 30 min to remove adsorbed moisture. Raman spectra were then taken at both 300 ºC and after cooling down in the O_2/He mixture. Data collection was set 2 sec for the first spectral window (-33 – 1270 cm^{-1}) and 30 sec for second one (720 – 1970 cm^{-1}). The Raman shift was calibrated by interpolation of the Rayleigh line and a silicon wafer signal (520 cm^{-1}).

4.2.3   *In situ* ultra-violet visible (UV-vis) experiments

UV-vis spectra on each sample were measured by diffuse reflectance UV-vis spectroscopy (Shidmadzu UV-vis 3600) using and an *in situ* high temperature reaction chamber (HVC-DRP, Harrick Scientific) and a Harrick Praying Mantis™ diffuse reflection attachment (DRP-XXX). The spectra were collected between 250 and 1200 nm using as initially referenced to a Spectralon standard (DRP-SPR). About 30 mg of each catalyst powder were finely grounded and calcined *in situ* at 300 ºC in O_2 (Praxair, UHP, 10 $cm^3 \cdot min^{-1}$) balanced in He (Praxair, UHP, 45 $cm^3 \cdot min^{-1}$) for 1 hr. The system was then cooled down to room temperature in the O_2/He mixture and the spectrum was acquired. After this stage the sample was heated again and ethanol was introduced in the chamber using a syringe pump (KDS200) via an injection port heated at 100 ºC, (0.017 $cm^3 \cdot min^{-1}$ CH_3CH_2OH/45 $cm^3 \cdot min^{-1}$ 10%O_2/He) for one hour at 200 ºC. After reaction of the catalysts for 1 hour, the reaction chamber was cooled down to ambient temperature again and the spectra acquired. Lastly, the sample was reduced in flowing of only C_2H_5OH and He with O_2 cutoff for 1 hr at 200 ºC. All diffuse reflectance spectra were obtained at

ambient temperature and converted into Kubelka-Munk units, $F(R_\infty)$[24]. David and Mott's correlation was used to determine the edge energy (E_g) by finding the intercept of a straight line in the low-energy rise of plots of $(F(R_\infty) h\nu)^2$ for direct transition or $(F(R_\infty) h\nu)^{1/2}$ for indirect transition against $h\nu$, where $h\nu$ is the incident photon energy. The reduced centers were identified by the photon energy position at corresponding peak maxima following previously reported methodology[25].

4.2.4   Ethanol partial oxidation

Before catalytic testing all samples were pressed into wafers, crushed and sieved to a pellet size between $425 - 600$ μm. Steady-state partial oxidation of ethanol experiments were conducted in a continuous flow fixed bed quartz glass micro reactor (5 mm O.D.) oriented vertically in an electrically heated furnace at atmospheric pressure equipped with a digital temperature controller. Catalyst samples (10 mg) were supported on a quartz frit and a K-type thermocouple placed at the center of the catalyst bed. Chemical species in the feed and reactor effluent stream were measured using an online gas chromatograph (Shimadzu gas chromatograph, GC-2014) with a capillary column (BP-5, 30 m $\times$ 0.53 mm, 1.0 μm thickness) connected to a flame ionization detector.

The catalyst was pretreated at 200 °C in 30 min under O_2/He mixture (5% O_2, Praxair, UHP) at a flow rate of 20 cm^3·min^{-1}. Absolute ethanol (Brampton, Ontario) was introduced into the reactor by vaporizing it into the flowing O_2/He mixture at 150 ºC using a micro-syringe pump (KDS200). Reactant conversions were varied by changing the O_2/He flow rate ($0.8 - 1.6$ cm^3·s^{-1}) equivalent to weight hourly space velocity ($657 - 1642$ mol CH_3CH_2OH/(mol V-h)$^{-1}$) at constant temperature (200 ºC). The conversion was kept under 10% so that differential reaction conditions could be assumed. Conversion and selectivity to products were calculated on a carbon molar basis, expressed as a mol% ratio of ethanol transformed to ethanol fed, and a ratio of ethanol transformed to each product relative to the total ethanol transformed, respectively. The turnover rate of partial oxidation of ethanol was calculated according to equation below:

$$\frac{r}{V_T} = \frac{\rho F}{MW \times mole\ of\ V} X_{EtOH}$$

where $\frac{r}{V_T}$ is the turnover rate of partial oxidation (sec^{-1}), normalized by the molar amount of vanadium present in the catalyst (V_T, mol), F is the total volumetric flow (cm^3·sec^{-1}), ρ refers to the density of ethanol (g·cm^{-3}), MW is the molecular weight of ethanol (g·mol^{-1}), and X_{EtOH} is the ethanol conversion.

4.2.5   Ethanol temperature programmed desorption

Temperature-programmed desorption (TPD) was performed in order to identify surface active sites. The ethanol-TPD experiments were carried out in a continuous flowing system under atmospheric pressure. For these experiments 0.2 g of catalyst were first treated under in the air (Praxair, UHP) flow of 15 cm^3·min^{-1} for 2 hours at 300ºC. Then, the sample was cooled down to 25ºC while purging in He (Praxair, UHP) feed flow rate of 15 cm^3·min^{-1}. Following this stage liquid distilled ethanol (without additional purification) was mixed with He (0.4 kPa ethanol partial pressure) to saturate samples by vaporizing it into the flowing He using a micro-syringe pump (KDS Scientific) for 1 hour. All the transfer lines were kept at 120 ºC to prevent condensation of reactant, and products. To get rid of physically adsorbed ethanol, samples were flushed for 1 hour under He flow at room temperature. Temperature programmed desorption was carried under He atmosphere using a ramp of 2 ºC·min^{-1} up to 250 ºC. The desorbed gases were analyzed using a by on-line GC-FID-MS (Agilent 6890A, 30m HP-Innowax column × 25 *μm* thickness).

4.2.6   Computational details

Density functional theory calculations were performed within the generalized gradient approximation (GGA) and the periodic plan-wave approach, using the Perdew-Burke-Ernzerhof (PBE)[26] exchange-correlation functional and Vanderbilit ultra-soft pseudo-potentials[27]. The DFT+U correction is applied to both titanium and vanadium metal atoms in the support. We use *U*=2.3 eV on Ti and 2.0 eV on V d-states based on the

suggestions made in the literature[28]. Plan-wave basis set for the kinetic and density cutoff were 50 and 500 Ry, respectively. Plane-Wave Self-Consistent Field (PWscf) code of the Quantum-Espresso package[29], running on SHARCNET, was used to obtain geometric optimizations, to calculate total and projected density of states (PDOS), the density maps of electronic states, and the optical absorption spectra. The k-point sampling of the Brillounin zone was limited to gamma. The Broyden-Fletcher-Goldfarb-Shanno (BFGS) algorithm was used for geometry optimization, with threshold values of 0.092 eV/Å and 6.8×10^{-4} eV for residual forces and energy variation, respectively.

Prior to geometry optimization of vanadia TiO_2-supported clusters, a clean anatase (101) surface was modeled with a periodically repeated slab. A 1×3 surface cell containing 108 atoms, with corresponding surface area of 10.24×11.36 Å^2, was modeled with a vacuum of 15 Å for the support of monomeric, dimeric and one-dimensional polymeric VO_x. Similarly for the case of trimer, the surface with the area of 10.24×15.13 Å^2 was optimized. The atoms in the bottom layer were fixed to their bulk positions during geometry optimization, in order to simulate the presence of the bulk underneath.

Based on previous research regarding theoretical evaluation of the electronic structure of monomeric VO_x/TiO_2, one VO_3 cluster was deposited on top of the anatase (101) unit cell[30]. Dimeric, trimeric, and polymeric VO_x clusters were built by adding VO_2 and V_2O_3 clusters to a monomeric VO_3 cluster to form V_2O_5 and $[V_3O_6]_n$, respectively, along the (010) plane[31]. The vanadium density for monomeric, dimeric, trimer, and polymeric VO_x model correspond to a surface coverage of 0.8, 1.6, 1.9, and 2.4 V·nm^{-2} on the surface of titania, which is well below monolayer coverage (usually 8 V/nm^2). To represent a reduced isolated VO_x cluster adsorbed on the anatase (101) surface, two oxygens were removed: one a terminal O (V=O) and another a bridging oxygen (V-O-Ti) in the modeled unit cell.

4.3   Results and Discussion

4.3.1   Raman spectroscopy

A very important factor influencing the quality of the spectra and relative signal strength of the vanadyl (V=O) Raman bands is the level of sample hydration. For this reason, we obtained the Raman spectra of both the hydrated samples under ambient conditions (catalysts being exposed to ambient air at room temperature) and the dehydrated samples in flowing of He/O_2 at 300 ℃, respectively. Figure 4.1 shows typical Raman spectra obtained for the hydrated and dehydrated supported VO_x/TiO_2 samples (TV1.5, TV1.88, TV3.01, and TV6.02) in the 725 – 1200 cm^{-1} range. In case of the hydrated sample (Fig.4.1A), the characteristic vanadyl (V=O) stretching for isolated VO_x tetrahedra, normally appearing at 1024 cm^{-1}, was either not detected (TV1.52 and TV1.88 samples) or appeared as a very weak band (TV3.01 and TV6.02). This is likely due to the tendency of the vanadia cluster to hydrate at room conditions[32]. A band at 994 cm^{-1}, which is associated with the symmetrical stretching mode of the terminal oxygen atom (V=O) in polymeric or bulk V_2O_5[32,33] is also observed for the TV3.01 and TV6.02 samples. This observation indicates that vanadyl bonds in the isolated VO_x species (dominantly present in the samples with low vanadia content) are easily distorted due to moisture. This contrasts with the behavior observed at higher vanadia loadings (TV3.01 and TV6.02), which contains a relative higher proportion of polymeric vanadia, as previously reported[34,35].

Upon dehydration, the Raman spectra of the dehydrated VO_x/TiO_2, (measured at 200℃) differ from those obtained on the corresponding hydrated catalysts, in good agreement with previously reported work[36,37]. Regardless of VO_x loading, all the catalysts show a characteristic Raman band at ~1024 cm^{-1} attributed to the vanadyl (V=O) stretching for isolated vanada tetrahedra, as well as a weak broad band centered at 850 cm^{-1} and a shoulder at 980 cm^{-1} corresponding to either V-O-Ti bridging or V-O-V vibrations, respectively[38,39]. The Raman band at ~1024 cm^{-1} clearly grows in intensity as VO_x loading increases (Fig.4.1B), indicating that a larger number of isolated VO_x species are formed as the VO_x loading increases in the catalyst. At The same time, the intensity

Raman band at 994 cm^{-1}, which is associated with vanadyl (V=O) in polymeric or bulk V_2O_5, also increases in intensity as more vanadia is loaded on the TiO$_2$ surface. Thus, these observations suggests a distribution of VO$_x$ species with different sizes which is very sensitive to vanadia loading and that isolated and polymerized vanadia clusters coexist in the catalyst with bulk vanadia oxide species at high VO$_x$ loadings.
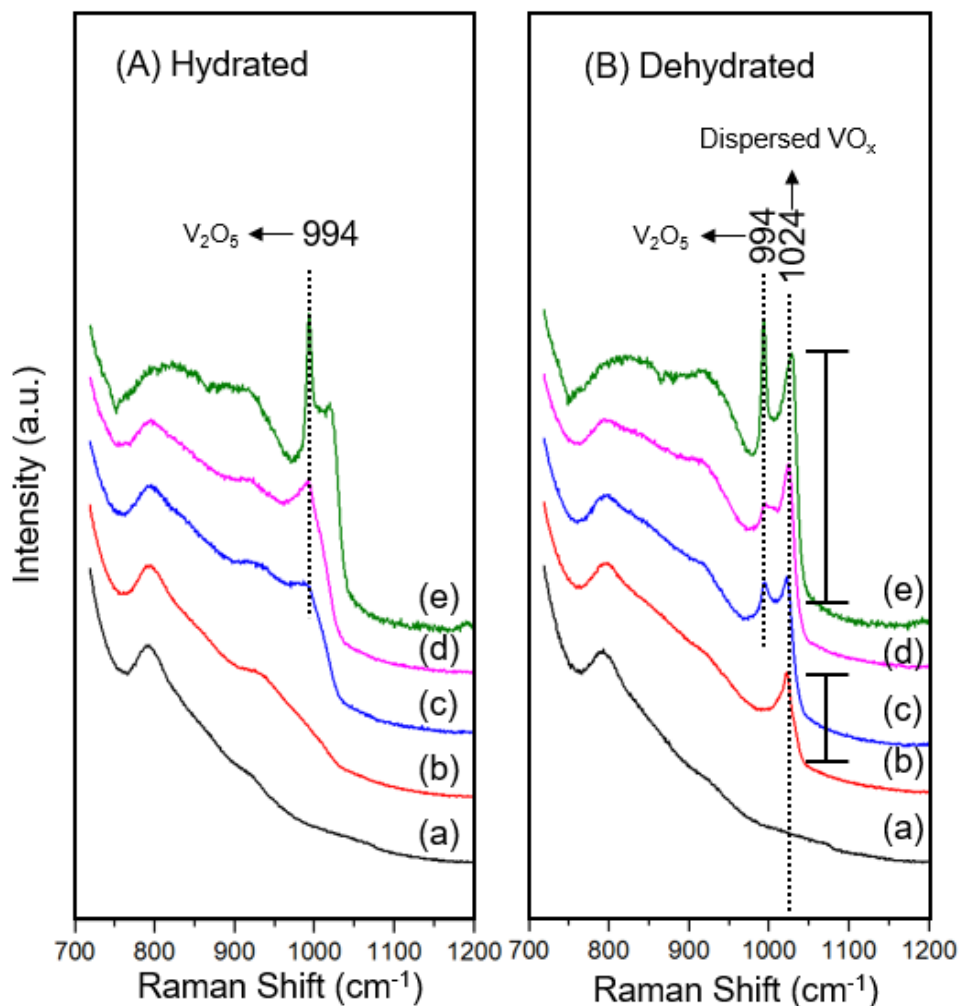
Figure 4.1. *In situ* **Raman spectra of a series of (A) hydrated supported VO$_x$/TiO$_2$ catalyst taken at 25 °C and (B) dehydrated VO$_x$/TiO$_2$ taken at 300 °C after calcination at 300 °C for 1 h in flowing of 5%O$_2$/He balanced. (a) pristine TiO$_2$, (b) TV1.52, (c) TV1.88, (d) TV3.01 and (e) TV6.02. (Raman conditions; λ=532nm, *w* =10mW, τ =30 s)**

4.3.2   Temperature programmed desorption of ethanol

Figure 4.2 shows the temperature profile for acetaldehyde evolution over the VO_x/TiO_2 catalysts following ethanol adsorption. Commonly ethanol-TPD profiles have been measured by singling out a primary mass peak (m/z = 29 in case of acetaldehyde) detected mass spectroscopy in order to keep the continuity of the desorption profile. However, dehydration of ethanol could also take place, depending on temperature, producing other products such as diethyl ether, which also has a primary mass fraction peak at 29 m/z resulting in overlapping with the acetaldehyde mass spectra. To avoid this problem, we first separated the desorbed gases in a chromatograph and carry the analysis using GC-FID system. Acetaldehyde evolution was not observed on experiments carried over the vanadia free bare titania support. For all catalysts, acetaldehyde desorption profiles can be observed below 200 ℃ and they consist of two overlapping peaks. Assuming TPD profiles appear symmetrically, the TPD data was deconvoluted using two peaks: one centered at about 80 ℃ and another one centered at approximately 120 ℃, as shown in Fig.4.2. A clear trend is observed: the relative amount of acetaldehyde released at higher temperatures increases when the VO_x content on the catalyst increases from TV1.52 (1.52 wt.% as V_2O_5) to TV6.02 (6.02wt.%). Acetaldehyde is formed as a result of the reduction of vanadia by ethanol through an α-elimination mechanism. The amount of acetaldehyde released thus depends on the reducibility of the vanadia clusters present on the catalyst surface. It is well established that the reducibility of vanadia depends on both the electronic structure of the support material, and the domain size of the vanadia cluster. The presence of two peaks on the TPD profile, thus suggests a distribution of vanadia sites with different reducibility. And assuming that cluster size and reducibility are linked, it could be proposed that these results are an indication of a heterogeneous distribution of vanadia cluster sizes on these materials. As previously indicated, the Raman results (Fig.4.1) clearly showed that the average vanadia cluster size changes as vanadia loading increases. Thus our results could be interpreted by proposing that the number of active sites for alcohol oxidation and the reducibility of the VO_x species are significantly affected by the VO_x content.
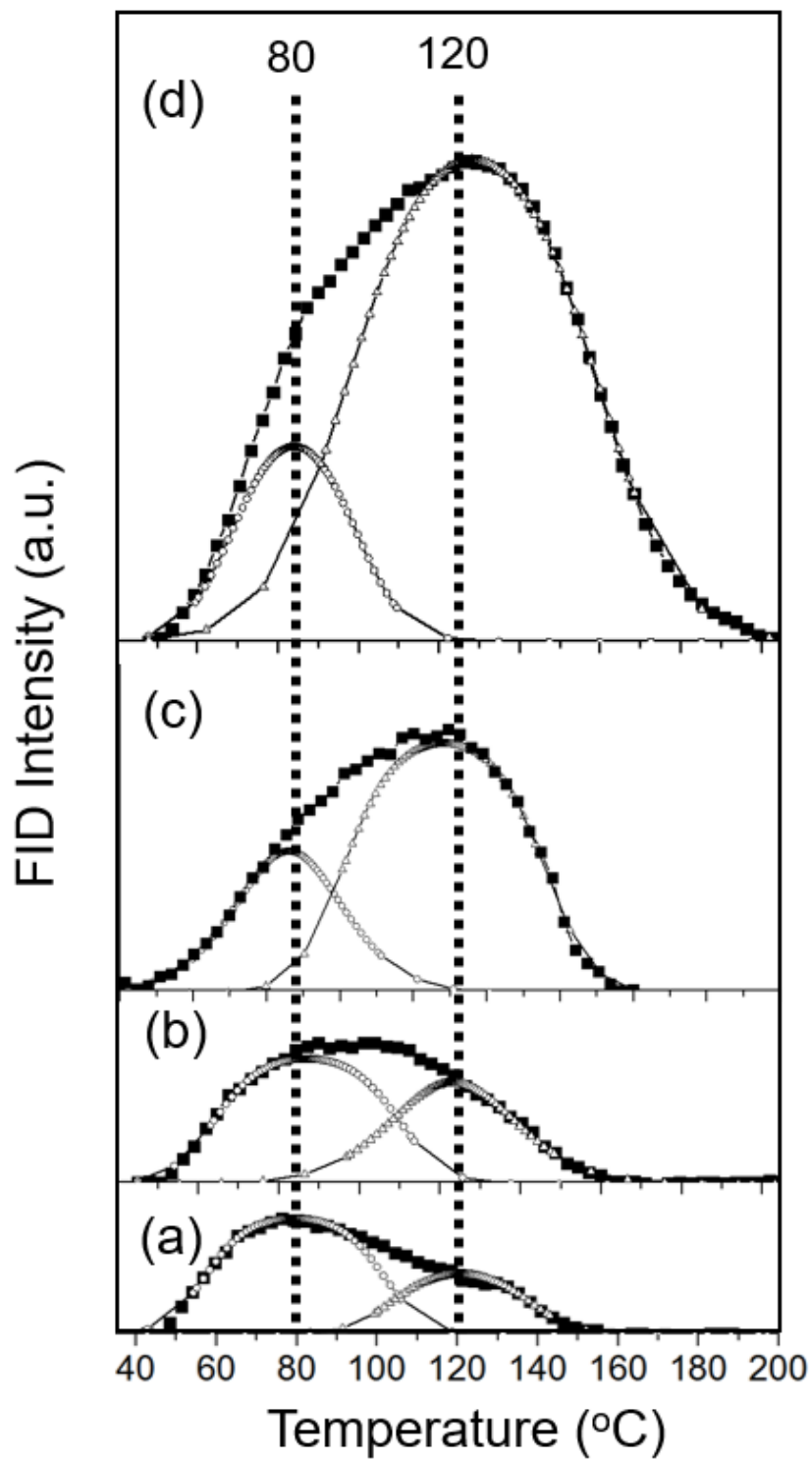
Figure 4.2. EtOH-TPD profiles (FID signal, acetaldehyde) of a series of VO$_x$/TiO$_2$; (a) TV1.52, (b)TV1.88, (c) TV3.01, and (d) TV6.02.

4.3.3 Catalytic activity and kinetic studies

Partial oxidation of ethanol to acetaldehyde was used to evaluate catalytic activity. In a set of preliminary experiments performed in the same system with a blank reactor and a vanadia free TiO_2, no ethanol conversion was observed at 200 ºC at all weight hourly space velocities (WHSV) tested in this study. Under our experimental conditions, in all cases the observed selectivity to acetaldehyde was above 99.5% and we did not observe measurable differences in this selectivity among the different tested catalysts. Combustion products (CO and CO_2) were not observed. The high selectivity to acetaldehyde under these conditions is an indication of the relatively high degree of dispersion of the VO_x moieties in these catalysts. To carry meaningful comparisons between the catalysts tested, we normalized partial oxidation rates by the total V content in the catalyst.

Fig.4.3 shows the effect of CH_3CH_2OH pressure (0.2-6.5 kPa CH_3CH_2OH at 200ºC) on the extrapolated apparent TOF values (calculated per total vanadium loading) at zero conversion during ethanol partial oxidation over several VO_x/TiO_2 catalysts with different VO_x loadings. For all catalysts tested, turnover rates increased linearly with ethanol partial pressure at the low CH_3CH_2OH partial pressure regime ($P_{CH_3CH_2OH}$< 1kPa) becoming independent of this variable at higher ethanol partial pressures ($P_{CH_3CH_2OH}$ > 3kPa). On the other hand, as the VO_x loading in the catalyst increases, turnover rates obtained at high CH_3CH_2OH partial pressure regimes gradually decreased. This behavior clearly indicates the ethanol partial oxidation over VO_x/TiO_2 catalysts follow a Langmuir-type rate equation (eq.4.1):

$$\frac{r}{*_T} = \frac{\alpha P_{CH_3CH_2OH}}{1 + \beta P_{CH_3CH_2OH}} \qquad\qquad eq.(4.1)$$

Previous work has attempted to derive the rate equation for alcohol partial oxidation over supported metal oxide catalysts (MoO_x, VO_x, RuO_x)[1,4,9,40]. In these studies, it is normally assumed that the step for O_2 dissociation on surface is irreversible, as verified by measuring isotopic $^{18}O_2$ exchange rates[6,41,42]. These reports also indicate that addition of

water to the reaction affected the reaction rates, presumably resulting from a high degree of coverage of alkoxyl species on the catalyst surface[9]. On the basis of these assumptions, the aforementioned studies have always proposed a zero-order dependence on oxygen partial pressure and turnover rates that follow either first-order[33] or zero-order[9] dependence on alcohol partial pressure, depending on the alcohol partial pressure regime. However, our data, obtained at a wider range of oxygen partial pressures, suggest that the turnover rates follows a Langmuir-type rate equation. Based on this data, we can propose elementary steps to derive a rate equation for partial oxidation of ethanol consistent with the experimental observations described on those aforementioned studies and the ones reported herewith.
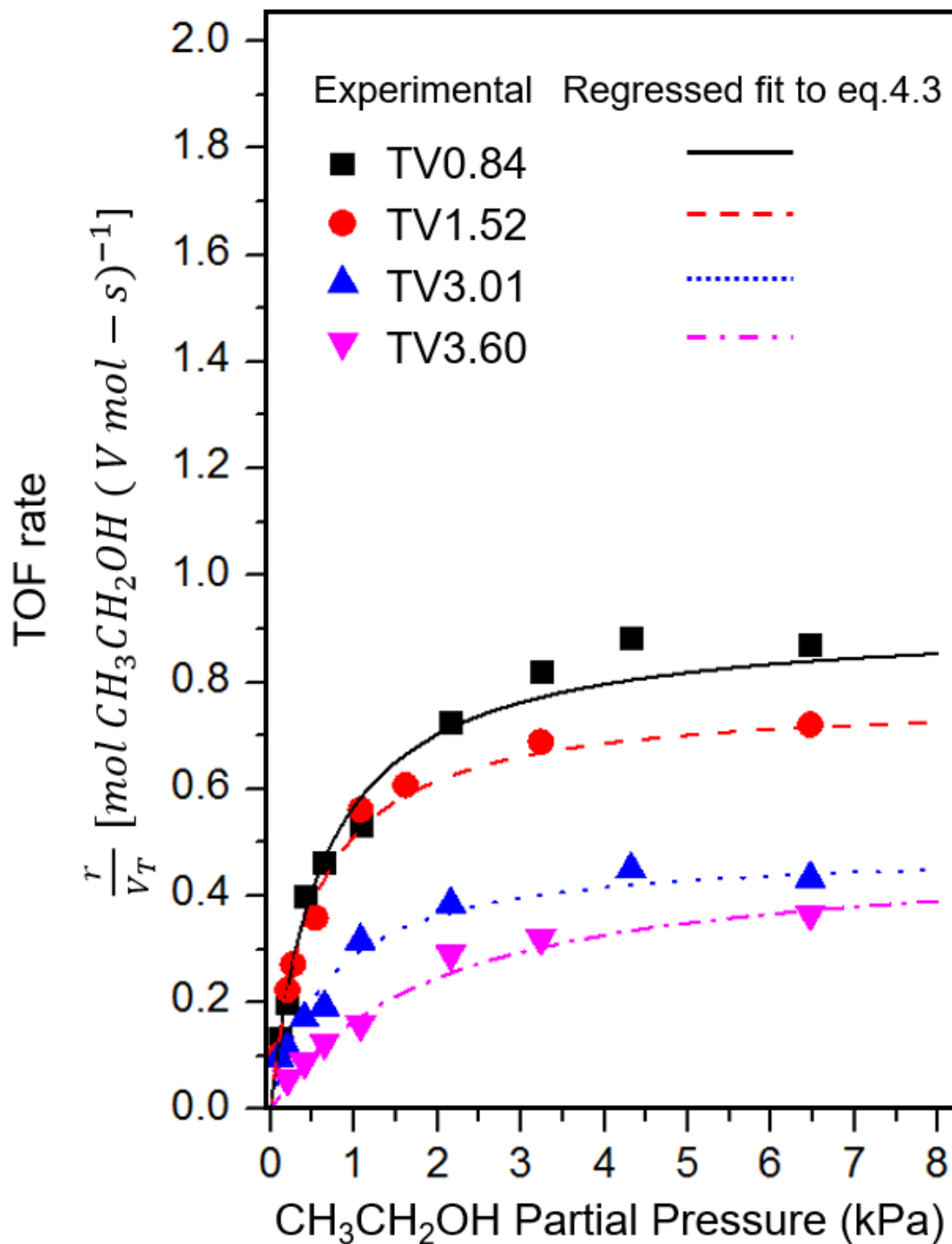
Figure 4.3. Measured TOF rate per V atom as a function of CH_3CH_2OH pressure on a series of VO_x/TiO_2; (a) TV1.52, (b)TV1.88, (c) TV3.01, and (d) TV3.6. (200 ºC, 5 kPa O_2). Calculated TOF rates were extrapolated to zero conversion with WHSVs (2, 1.6, and 1.2×10^3 cm³·(g-s)⁻¹). Regression curves were fitted in the form of eq.4.3.

The kinetics of the conversion of CH_3CH_2OH to CH_3CHO can be interpreted in terms of a sequence of elementary steps and simplified lumped steps based on Mars-van Krevelen redox cycles, shown in Table 4.1 and 4.2, respectively. The first step is the quasi-equilibrated dissociative adsorption of CH_3CH_2OH to form and adsorbed ethoxylate (*-CH_3CH_2O) at an oxidized V(+5) redox site (*) (Lumped step1). The next step involves surface reactions (Lumped step2) in which 1) the irreversible H atom abstraction from the alpha carbon atom takes place, leading to the generation of adsorbed acetaldehyde, which is the rate-limiting step[7,9,33], and 2) hydroxyl recombination takes place leading to the formation of adsorbed water, which is assumed to be fast. The following desorption of CH_3CHO step results in the reduction of the vanadium site (*r) and the generation of a lattice oxygen vacancy resulting from desorption of water. Finally, to complete the redox cycle, reoxidation of the reduced vanadium site (*r) either by an adsorbed O (O_{ad}) atom (*r+ O_{ad} → *) (which in turn is generated by irreversible chemisorption of O_2 onto surface vacant sites) or via the sequential irreversible dissociation of O_2 onto two adjacent reduced vanadium sites (*r + O_2 → * + O_m and *r + O_m → *, where O_m is mobile O atom). In former case, the vacancy sites differ from the reduced vanadium site. Although, the exact mechanistic details of this reoxidation step remain ambiguous, it has been reported that overall rate equation is independent of O_2 partial pressure at high oxygen partial pressures ($P_{O_2}/P_{CH_3CH_2OH} \gg 1$)[9,43].

Table 4.1. Proposed elementary reaction of ethanol partial oxidation on redox sites.

Entry	Elementary reaction
r_1	$CH_3CH_2OH(g) + * \leftrightarrow CH_3CH_2OH *$
r_2	$CH_3CH_2OH * + O * \leftrightarrow CH_3CH_2O * + OH *$
r_3	$CH_3CH_2O * + O * \leftrightarrow CH_3CHO *_r + OH *$
r_4	$CH_3CHO *_r \leftrightarrow CH_3CHO(g) + *_r$
r_5	$OH * + OH * \leftrightarrow H_2O * + O *$
r_6	$H_2O * \leftrightarrow H_2O(g) + *$
r_7	$O_2(g) + *_r \leftrightarrow * + O$
r_8	$O + *_r \leftrightarrow *$

Table 4.2. Lumped reaction steps of ethanol partial oxidation on redox sites.

Entry	Lumped reaction steps
Ethanol adsorption	$CH_3CH_2OH(g) + * \overset{K_1}{\leftrightarrow} CH_3CH_2O*/OH*$
Surface Reaction, rls	$CH_3CH_2O*/OH* \overset{k_2}{\rightarrow} CH_3CHO* + H_2O*$
Desorption	$CH_3CHO* \overset{k_3}{\rightarrow} CH_3CHO + *_r$
Reoxidation	$*_r + O_2 \overset{k_4}{\rightarrow} * + O$ *in sequence,* $*_r + O \overset{k_5}{\rightarrow} *$

A pseudo-steady-state analysis of proposed mechanical steps leads to a rate equation of the form (eq.4.2):

$$\frac{r}{V_T} = \frac{K_1 k_2 P_{CH_3CH_2OH}}{1 + K_1 P_{CH_3CH_2OH} + \dfrac{K_1 k_2 P_{CH_3CH_2OH}}{2k_4 P_{O_2}}} \qquad \text{eq.(4.2)}$$

    *   *-O CH₂CH₃   *r

in which the denominator terms corresponds the surface coverage ratio of a specific surface species present: a vanadia oxidized active site(*), a vanadia active site with ethanol adsorbed on it (*-O CH₂CH₃) and a vanadia reduced active site(*r). K_1 is the equilibrium constant for the reversible ethanol adsorption step, k_2 is the rate constant for the H-abstraction step that the adsorbed ethoxide species experience, and k_4 is the rate

constant for the vanadia reoxidation step. Previous reports indicate that the overall rate is independent of O_2 pressure at high O_2 partial pressures (5kPa, in our case) and that the surface concentration of reduced sites (*r) is very low compared to the concentration of oxidized sites (*r << * + *-E) [40,44]. Consequently, the rate equation can be simplified to:

$$\frac{r}{V_T} \cong \frac{K_1 k_2 P_{CH_3CH_2OH}}{1 + K_1 P_{CH_3CH_2OH}} \qquad \text{eq.(4.3)}$$

Therefore, the slope of the kinetic data shown in Fig.4.3 obtained at high oxygen partial pressures in the low ethanol partial pressure regime ($K_1 P_{CH_3CH_2OH}$<< 1kPa) provides the value of the first-order rate constant $K_1 k_2$ in eq.4.3 while at higher $P_{CH_3CH_2OH}$ values the rate becomes independent of CH_3CH_2OH pressure ($\frac{r}{V_T} \cong k_2$, zero order rate constant). By using the simplified rate equation in eq.4.3, the regression curves are fitted to ethanol partial oxidation turnover rates obtained over VO_x/TiO_2 catalysts with different loadings (Fig.4.3). At the same time, Fig.4.4 shows the values obtained for the first-order rate constant ($K_1 k_2$) and the zero-order rate constant (k_2) obtained using eq.4.3 and the data shown in Fig.4.4, as a function of different VO_x loadings. Both kinetic parameters show an identical trend: $K_1 k_2$ and k_2 values linearly decrease with increasing VO_x loadings, approaching zero as the vanadia content in the catalysts reaches that of a theoretical monolayer coverage (ML=1, red bar in Fig.4.4). The value obtained for the first order constant $K_1 k_2$ reflects the energy difference between the H-abstraction transition state ($E_{TS}^{\ddagger}$) and the reaction coordinate starting point ($E_* + E_{CH_2CH_3OH}$, oxidized vanadia active site plus gas phase ethanol), while k_2 reflects the energy barrier between the state corresponding to ethanol adsorption on the surface ($E_{CH_3CH_2OH*}$) and the H-abstraction transition state ($\Delta E_{TS}^{\ddagger}$):

$$K_1 k_2 = A_{K_1 k_2} e^{\frac{-(E_{TS}^{\ddagger} - E_* - E_{CH_2CH_3OH})}{RT}} \qquad \text{eq.(4.4)}$$

$$k_2 = A_{k_2} e^{\frac{-(E_{TS}^{\ddagger} - E_{CH_3CH_2OH*})}{RT}} \qquad \text{eq.(4.5)}$$

Where $A_{K_1 k_2}$ and A_{k_2} are the preexponential factors of these Arrhenius-type equations. The apparent activation energies for ethanol partial oxidation, obtained from these Arrhenius plots for the series of VO_x/TiO_2 catalysts with different loadings (TV0.8, TV1.6, TV3.6, and TV5.1) are independent of surface coverage ($75.5 \pm 7.2 \text{ kJ} \cdot \text{mol}^{-1}$), as shown in Fig.4.5. Thus, the different values obtained for the rate constants at different vanadium loadings are determined by the changes in the preexponential factor, which is turn linked to the number of effective collisions between the CH_3CH_2OH molecule and the vanadia active site. Therefore, the linear relationship observed (decreasing first ($K_1 k_2$) and zero order (k_2) rate constants with increasing VO_x coverage) in Fig.4.4 suggests the formation of a larger fraction of inactive VO_x sites as vanadia loading increases in the catalysts. This observation thus leads us to conclude that the higher k_2 and $K_1 k_2$ values observed at low vanadia loadings, compared to those observed at higher vanadia loadings, are due to a higher active site density (the number of active vanadia site per absolute vanadium loading) in catalysts at low vanadia loadings. This is consistent with the Raman observations depicted in section 4.3.1, where a relative larger fraction of isolated VO_x species was observed at lower VO_x coverages. In any case, this observations also indicates that not all VO_x clusters dispersed over the TiO_2 surface are actively participating in catalytic turnovers.
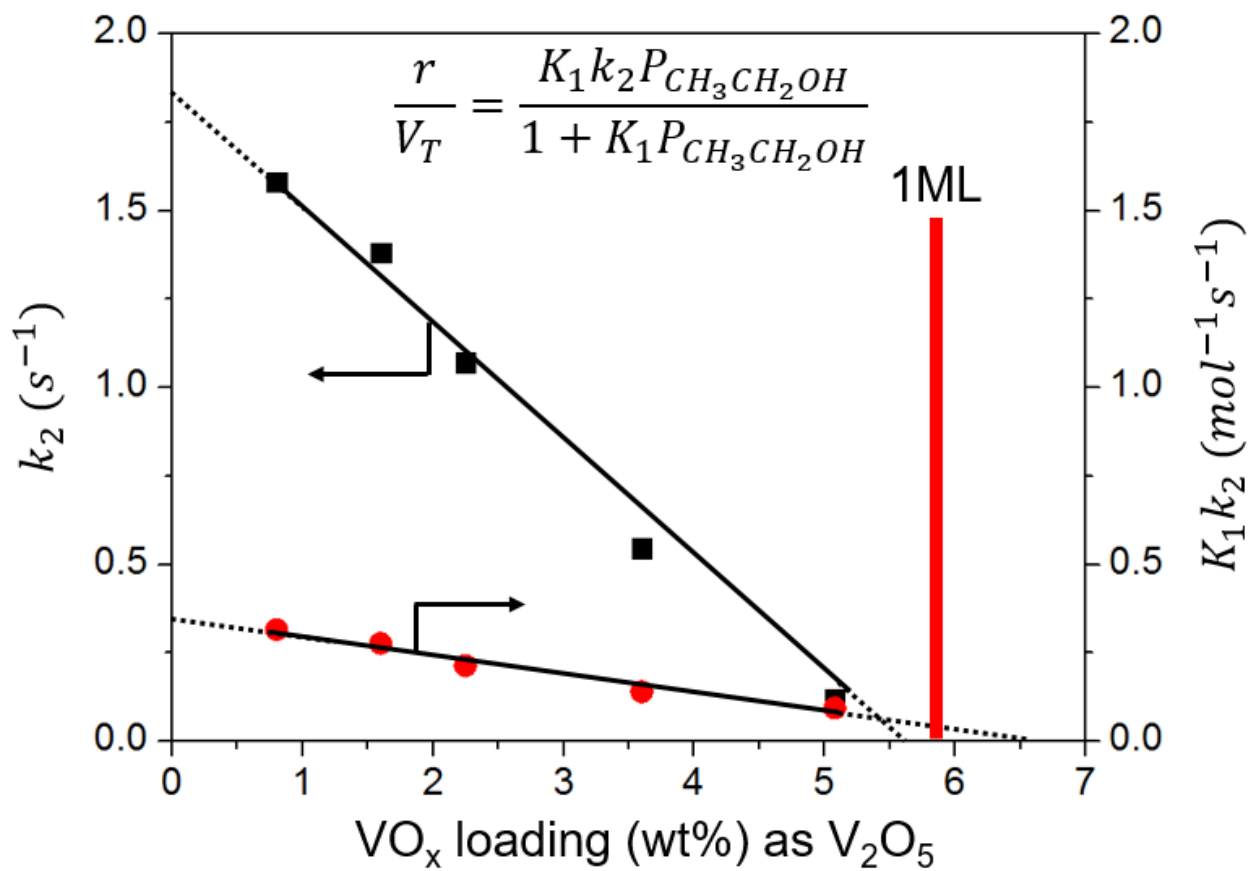
Figure 4.4. Measured first-order rate constant (K_1k_2) and zero-order rate constant (k_2) as a function of VO$_x$ loading at 200 °C (5kPa O$_2$). Red bar indicates VO$_x$ loading at monolayer, described in ref.[39].
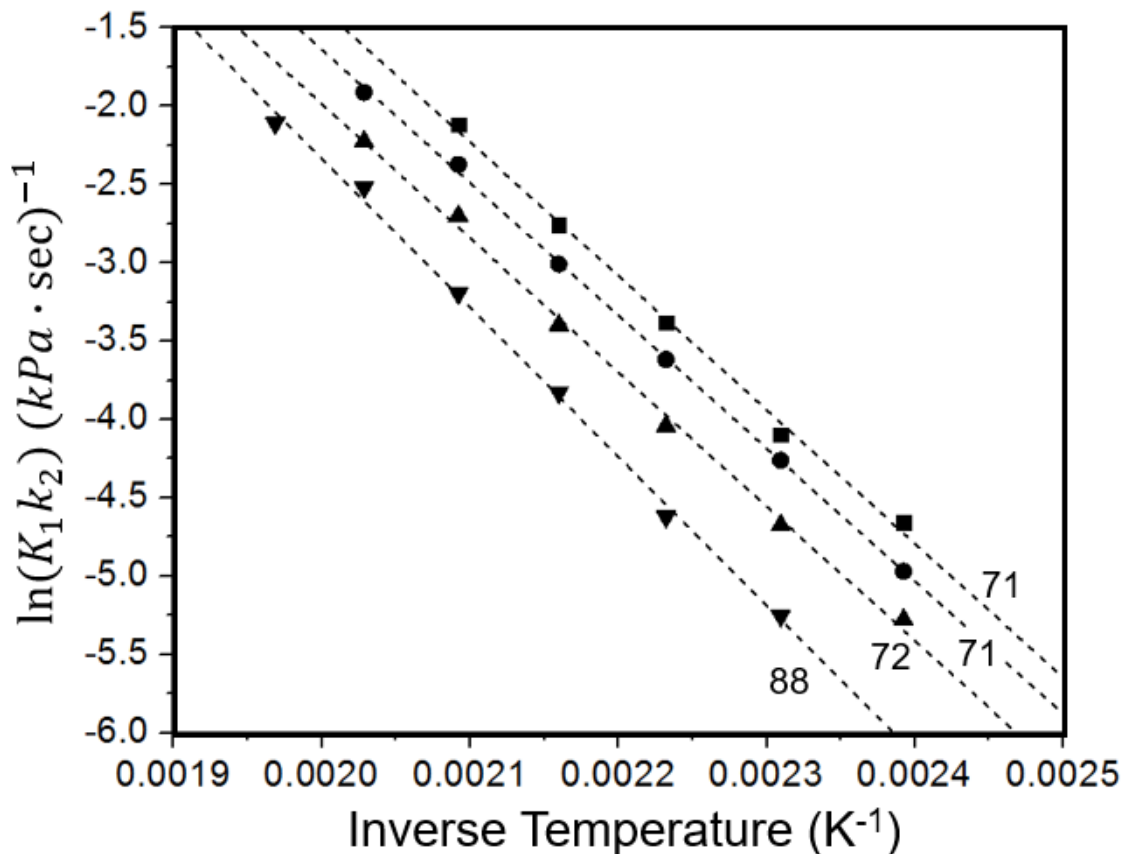
Figure 4.5. Arrhenius plot of first order rate constant ($K_1 k_2$) and activation energies in $kJ \cdot mol^{-1}$ for TV0.8 (■), TV1.6 (●), TV3.6 (▲), and TV5.1 (▼) with 1.34 kPa CH_3CH_3OH and WHSV = 1,479 (mol CH_3CH_3OH ·mol V^{-1}·h^{-1}) at global minimum. The rates were assumed to show first order dependence on CH_3CH_3OH partial pressure ($\frac{r}{V_T} \cong K_1 k_2 P_{CH_3CH_2OH}$).

4.3.4   *In situ* UV-vis spectroscopy analysis

The proposed catalytic model suggested that VO$_x$ species are predominantly oxidized (*) during ethanol partial oxidation since it is assumed that the reduced species go through fast reoxidation steps. However, the formation of the reduced species during catalytic reaction leads to the partial filling of d electronic states on the catalysts, and thus d-d electronic transitions can be monitored in the pre-edge energy region through optical

spectroscopy. We carried UV-vis spectral measurements in the range of 0.8 − 5 eV to probe the electronic behavior of supported VO_x species under both oxidative and reductive environments as well as during catalysis. Figure 4.6 shows the UV-vis DRS spectra obtained under oxidative conditions for the TV0.8, TV1.6 and TV3.6 catalysts obtained at 25 °C under a 10%O_2/He stream after an *in situ* calcination process carried out at 300 °C under flowing 10%O_2/He for 1 h in the spectroscopic cell. The black solid lines in Fig.4.6 show the acquired UV-vis DRS spectra of the oxidized VO_x/TiO_2 catalysts. In the fully oxidized state, only the ligand to metal charge transfer (LMCT, commonly reported as edge energy, E_g values) is observed. The edge energy values reflect the excitation of an electron from the highest occupied state (oxygen p-orbital in the valence band), to the lowest unoccupied state (empty d-orbital of the metal atom in the conduction band). The edge energy values obtained following previously reported methodology[25,45,46], experience a red shift with increasing vanadium loading: 3.0 eV for TV0.8 to 2.7 eV for TV3.6, (marked with *) in Fig.4.6. This has been previously reported and rationalized in terms of formation of polymerized species at higher vanadia loadings[47,46].
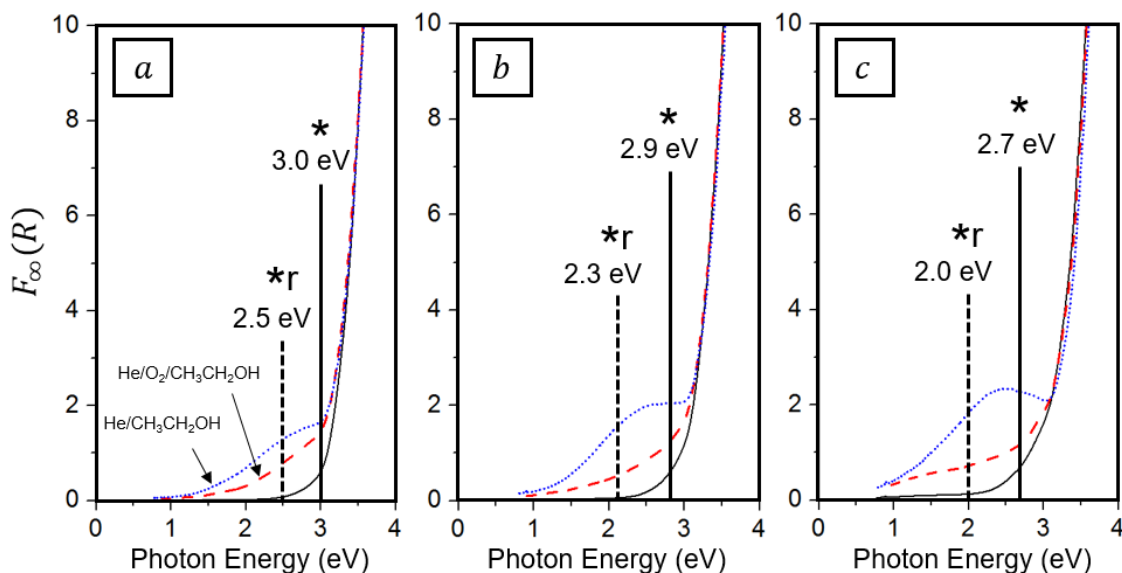
Figure 4.6. Optical absorption of a series of oxidized catalyst measured at ambient temperature. Catalysts at fully oxidized state (black line), after calcining at 300 ºC in flowing of (Black solid lines, 10%O$_2$/He) for 1 h, during catalytic reaction at 200 ºC (Red dash lines, 1 kPa CH$_3$CH$_2$OH/10%O$_2$/He), and after reduction by cutoff O$_2$ flow (Blue dot lines, 1 kPa CH$_3$CH$_2$OH/He) at 200ºC. (a) TV0.8, (b) TV1.6, and (c) TV3.6.

The introduction of CH$_3$CH$_2$OH into the He/O$_2$ stream, mimics catalytic conditions and led to the emergence of d-d transition bands in the pre-edge region, however, the observed spectral features are quite different depending of the vanadium loading in the catalyst. As the VO$_x$ coverage increases, the edge energy of the broad d-d electronic transition bands experience a red-shift: around 1eV for TN0.8 and lower than 0.8 eV for TN3.6. Their corresponding energies at pre-edge absorption maxima (arising from vanadia reduced centers, linked to d-d transitions) are 2.5 eV for TV0.8, 2.3 eV for TV1.6 and 2.0 eV for TV3.6 (*r in Fig.4.6).

To obtain the spectra under a reductive environment the flow of O_2 was cutoff, while the catalyst kept being exposed to CH_3CH_2OH in the He stream. Under these conditions the catalysts is completely reduced, and, their UV-vis spectra show identical values for the values of the edge energies and the energy of the reduced centers (*r, Fig.4.6 blue dotted line) as those obtained in the presence of both oxygen and ethanol together (Fig.4.6 red dashed line), although the intensity of the pre-edge feature is higher under reducing conditions (O_2 cut off). The identical energy values obtained during catalysis and under reductive conditions indicate that a significant number of VO_x species are catalytically inactive, permanently existing in a reduced state during ethanol partial oxidation, likely due to slow reoxidation rates caused by a higher reoxidation energy barrier[48]. The increased intensity observed after oxygen cutoff and complete reduction is, thus, caused by the formation of additional reduced species that were actively participating in catalytic turnover before oxygen was removed from the system.

A red shift in all these parameters is also observed in the spectra, regardless of environmental conditions, as the VO_x loading in the catalyst increases. This observed red-shift, suggests that the reduced VO_x species with larger domain sizes have a narrower band gap than those with smaller domain sizes. We can attempt to link this observation from *in situ* UV-vis spectroscopy to a decrease in the value of the kinetic constants obtained at higher vanadium loadings, as explained in section 4.3.3. It can be proposed that the changes observed in the values of the kinetic constants and the red shift observed in the UV-vis spectra of the reduced vanadia samples, occurring both at higher vanadium loadings, are linked to changes in vanadia reducibility. In the other words, species with larger domain size, formed at higher vanadium are more difficult to reduce under reaction conditions, and hence less active for partial oxidation of ethanol. However, the exact nature of the observed red-shift in the optical absorption spectra requires further investigation.

4.3.5 Geometries, Charges and Electronic structure of oxidized VO$_x$ species

In an attempt to understand the observed changes in catalytic activity, optical spectra, reducibility and their links to VO$_x$ electronic structure, we built and relaxed models that represent different configurations of oxidized VO$_x$ anchored on an anatase (101) slab. These included a vanadia monomer (Fig.4.7a), a dimer (Fig.4.7b), a trimer (Fig.4.7c) and an one-dimensional(1-D) vanadia polymer (Fig.4.7d). The anatase (101) surface was selected as vanadia support in our study since this surface is the most abundant reactive facet in anatase. The oxidized VO$_x$ is depicted as containing a terminal vanadyl oxygen (V=O), as previously reported[49,50]. Three different bond types involving oxygen atoms are defined in our model: terminal V=O, bridging V-O-Ti and bridging V-O-V. These are denoted as O^1, O^2, O^3, and O^4 assigned to terminal vanadyl, doubly-coordinated bridging oxygen in V-O-Ti, triply-coordinated bridging oxygen in V-O-Ti, and bridging oxygen in V-O-V, respectively. After model relaxation, the lengths of these bonds are compared. The values for average interatomic distances resulting from the computation are indicated in Fig.4.7. The monomeric VO$_x$ (Fig.4.7a) has one terminal V=O bond (O^1), and three bridging V-O-Ti bonds. One of the Ti-O-V bonds (O^3) is longer than the other two (O^2). The obtained value length of the vanadyl bond is 1.61 Å, in good agreement with previous research[30,51]. The interatomic distance of V-O^2 (doubly-coordinated bridging oxygen) is 1.75 Å and that of V-O^3 (triply-coordinated bridging oxygen) is 1.87 Å. Thus, the structure of the oxidized monomeric VO$_x$ is that of a slightly distorted tetrahedron.
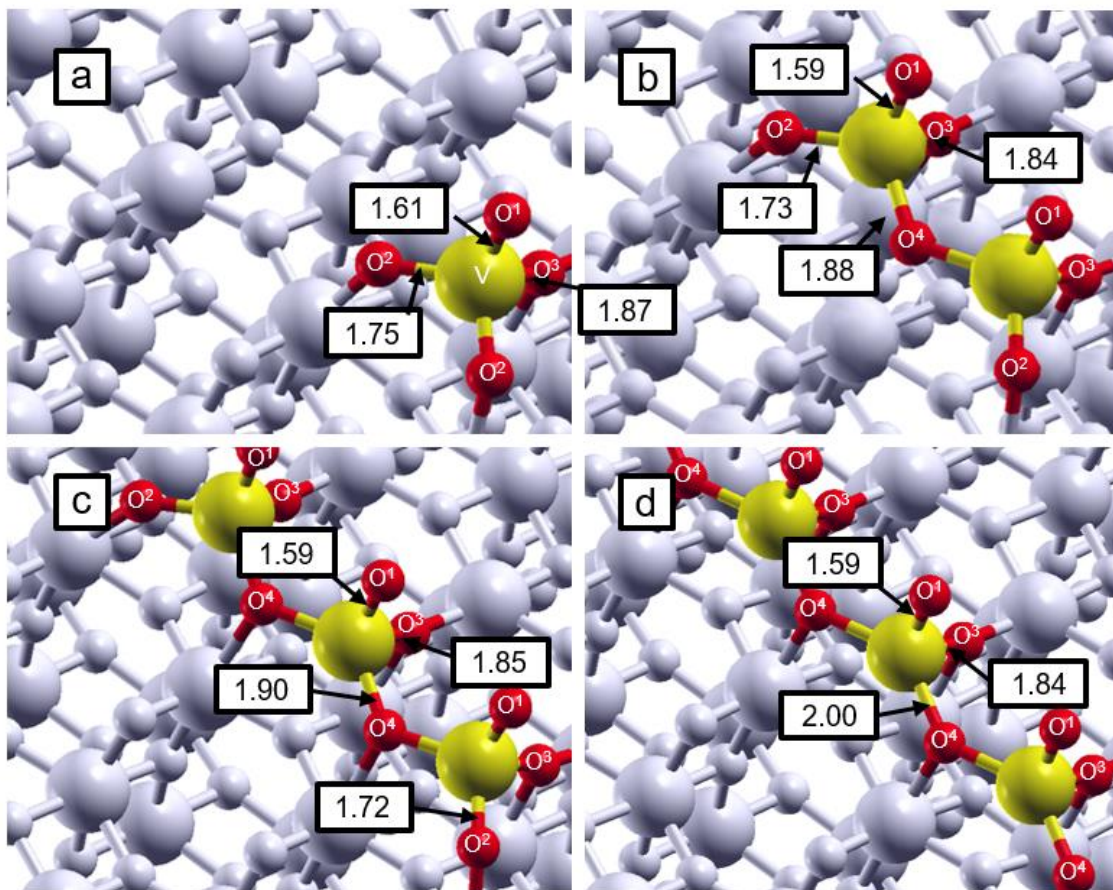
Figure 4.7. Structure of the oxidized supported VO$_x$ on anatase (101) surface. (a) monomer, (b) dimer, (c) trimer, and (d) 1-d polymer. Anatase support is represented by grey ball-stick model for readability. Numbers in each figure indicate interatomic distances in the unit of Å.

Similarly, the lengths of the oxygen bearing bonds for the other vanadia structures were calculated. As the number of V atoms increases in the vanadia cluster, a new V-O-V bond is formed (marked as O^4 in Fig.4.7b, 4.7c and 4.7d), whose O atoms are triply-coordinated for all cases (dimeric, trimeric, and polymeric VO$_x$). The interatomic distances of interest (i.e. V=O, V-O-Ti, and V-O-V) are similar among all these structures. Compared to that of monomeric VO$_x$, the V=O^1 bond length for the dimeric, trimeric, and polymeric VO$_x$ clusters are slightly shorter and nearly constant at ~1.59 Å for all these three structures. The interatomic distances for V-O^2 and V-O^3 in the bridging V-O-Ti bonds generally decrease as the vanadia cluster size increases. On the other hand,

the length of V-O[4] in the V-O-V bond increases for larger cluster sizes (1.88 Å for dimer and 2.00 Å for polymer).

To verify the validity of our model, we compared the values obtained for the structural parameters (V=O, V-O in V-O-Ti, and V-O in V-O-V bond distances) to those previously obtained experimentally by extended X-ray absorption fine structure spectroscopy (EXAFS) obtained for isolated vanadia tetrahedra supported on titanium dioxide[52,53]. This comparison is shown in Table 4.3. The values reported in Table 4.3 clearly indicate that our calculated structural parameters match well with experimental studies of the structure of VO_x/TiO_2 catalyst.

Table 4.3. Geometric parameters of modeled catalyst and EXAFS fit parameter values.

	Calculation				Experiment[4] (2.8wt.% VO_x/TiO_2)	
	V=O	V-O in V-O-Ti		V-O in V-O-V	V=O	V-O
	O[1]	O[2]	O[3]	O[4]		
Monomer	1.61[*] 1.61[1,2] 1.57[3]	1.75	1.87	-		1.78
Dimer	1.59	1.73	1.84	1.88	1.6	1.87
Trimer	1.59	1.72	1.85	1.90		1.95
Polymer	1.59		1.84	2.00		

* this study, [1] Ref.[51], [2] Ref.[30], [3] Ref.[49], [4] Ref.[53,54]

The Bader charge analysis (Table 4.4) indicate that all oxygen atoms bound to V are negatively charged and that positively charged vanadium centers are present on all modeled structures. This result was not unexpected. There are, however, subtle differences that predict a different chemical behavior for some of the vanadia clusters. The Bader charge values of the vanadium atoms are similar for monomeric, dimeric and trimeric vanadia clusters, but is slightly lower for polymeric VO_x. This suggests the vanadium atoms in polymeric VO_x have a relatively lower positive charge that those in the smaller vanadia clusters. Consequently, the Bader charge of O^1 in V=O, and O^2 in V-O-Ti gradually decrease as the vanadia cluster size increases. However the change in these values is more pronounced for the case of O^2 (V-O-Ti bond). This trend indicates that vanadia cluster size affects more the electronic charge of the doubly-coordinated bridging oxygen (O_2) atom than any other vanadia-associated moiety in the structure.

Table 4.4. Summary of Bader charge of vanadium (V) and oxygen atoms (O).

	V	O^1 in V=O	O^2 in V-O-Ti	O^3 in V-O-Ti	O^4 in V-O-V
Monomer	2.10	-0.70	-0.91	-1.13	-
Dimer	2.10	-0.69	-0.84	-1.15	-1.16
Trimer	2.11	-0.67	-0.73	-1.14	-1.16
Polymer	2.06	-0.67	-	-1.17	-1.16

For the case of multiple sites, average values are presented.

Figure 4.8 shows the calculated total density of states (TDOS) for the four proposed models. The projected density of states (PDOS) onto the vanadium as well as the terminal oxygen (O^1) and bridging oxygen atoms (O^2) are presented in Fig.4.8 as well. For the case of O_{2p} orbitals, only those of O_1 and O_2 atoms are only presented since the electronic density associated with the O_{2p} orbitals of the O^3 and O^4 atoms was found to be completely delocalized in the valence band (not shown). For both TDOS and the PDOS the Fermi level is at 0 eV. Typically, for the case of a pristine TiO_2 surface the O_{2p} states are responsible for filling the valence band (full) while the Ti_{3d} states (empty) are located in the conduction band. For this case the Fermi level is positioned near the valence band. When a monomeric vanadia moiety is anchored over the TiO_2 surface (Fig.4.8a), the V_{3d} orbital contributes to the conduction band and is localized away from the lower energy edge of the conduction band. As the vanadia cluster size increases to dimer and trimer, the PDOS for V_{3d} broadens toward lower energies. The Fermi level in turn is positioned on top of the valence band. On the other hand, for the case of polymeric vanadia the V_{3d} states are significantly broaden and they occupy states near the low energy edge of the conduction band. At the same time the Fermi level moves to the bottom of the conduction band. This behavior contrasts sharply with that of the other three modeled clusters. For the case of the monomer, dimer and trimer O_{2p} states, the energy of the 2p states of the O^2 atom are higher than those obtained for the O^1 2p states. This result will allow us to explain that observed UV-vis absorption features for oxidized VO_x/TiO_2 (discussed below in section 4.3.7), caused by ligand metal charge transfer (LMCT). Our calculation thus indicates that the electronic structure of these species is extremely sensitive to vanadia cluster size; indeed as Figure 8 shows, the band gap decreases with increasing vanadia domain size, because the energy of V_{3d} states descends toward the edge of the conduction band, as the VO_x cluster size increases and large domains VO_x are formed. The consequence of these changes on the position of the V_{3d} energy states on the optical absorption spectra will be discussed in the conduction band will be discussed in section 4.3.7.
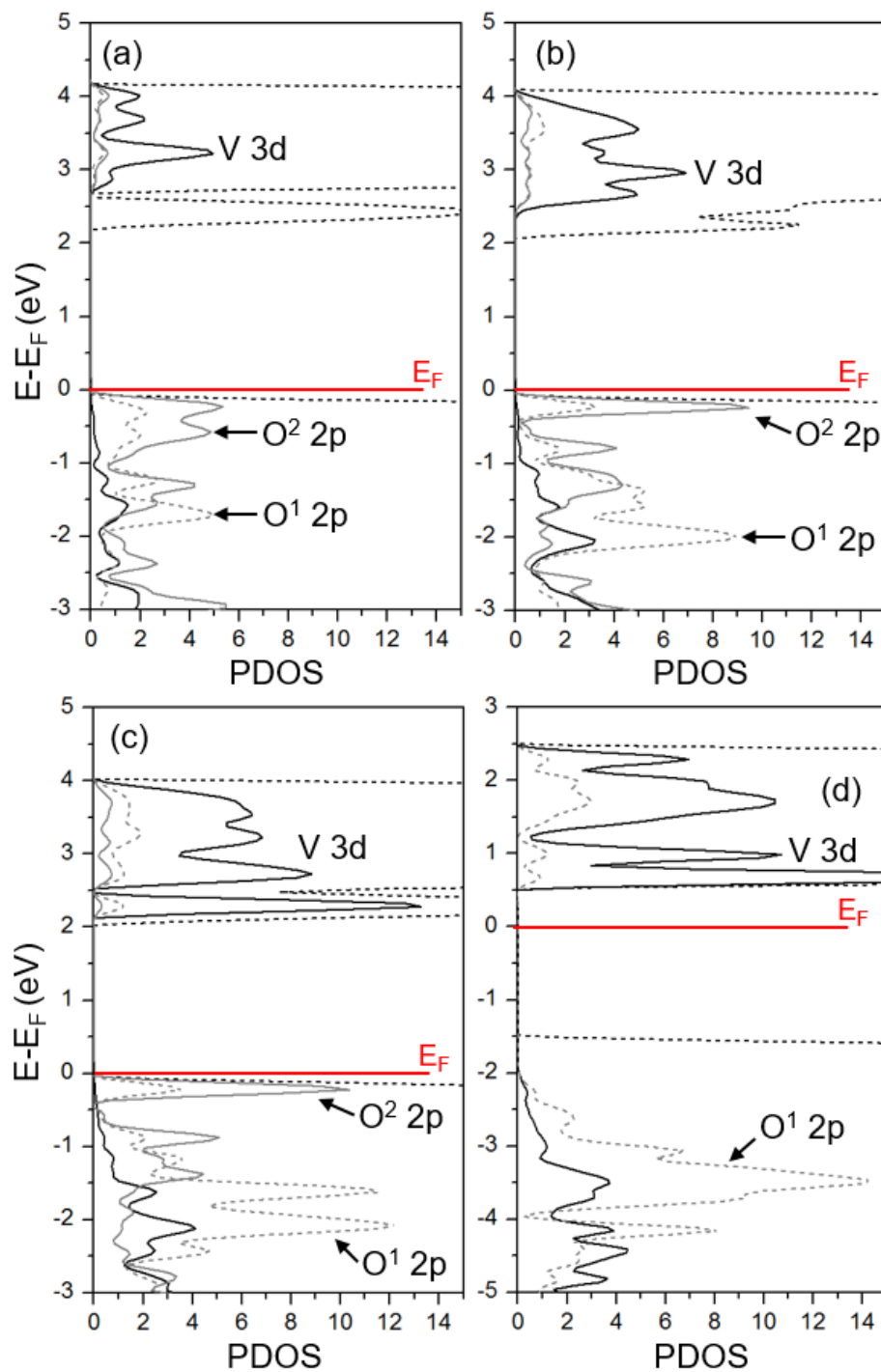
Figure 4.8. TDOS (dashed black) and PODSs of the vanadium (Solid black) and oxygen atoms (O^1:Dashed gray and O^2:solid gray). Energies are referenced to the calculated Fermi level (Red lines).

4.3.6 Geometries, Charges and Electronic structure of reduced VO$_x$ species

In our model, the reduced VO$_x$ cluster is depicted as lacking the terminal vanadyl oxygen (V=O) and one of the bridging oxygen (V-O-Ti) (Fig.4.9). In this case, three oxygen atoms are found to be responsible for the bonding of the reduced V center to the anatase (101) slab and are denoted to O^2, O^3, and O^5 in Fig.4.9. The interatomic distance of all bonds of interest (V-O^2, V-O^3 and V-O^5) generally increases as the vanadia cluster size increases, in particular, the length of V-O^3 increases by 0.15 Å, compared to those of the reduced monomer and polymer. This trend allowed us to predict that the vanadium charge in the polymeric structure can be less positive than that in the monomer since the oxygen atoms, surrounding the vanadium atom, are positioned at a longer distance in the polymeric vanadia structure than the monomeric one. Detailed information on charges will be discussed in the section below. Again, we compared the structure parameters (V-O distance) obtained after relaxation of these models to those experimentally reported by (EXAFS) in order to confirm the validity of our model. This comparison is shown in Table 4.5.

We can see that the calculated structural parameters in our model are consistent with the experimentally obtained values for the structure of reduced vanadia. Among the O atoms present, the behavior of O^5 is of particular relevance. This oxygen atom was originally linked to three Ti atoms in the oxidized VO$_x$ cluster. For the case of the reduced cluster, the O^5 still remains triple-coordinated, but now is bonded to two titanium atoms and one vanadium atom.

Figure 4.9. Structure of the reduced supported VO$_x$ on anatase (101) surface. (a) monomer, (b) dimer, (c) trimer, and (d) 1-d polymer. Anatase support is represented by grey ball-stick model for readability. Numbers in each figure indicate the distance of bonds in the unit of Å.

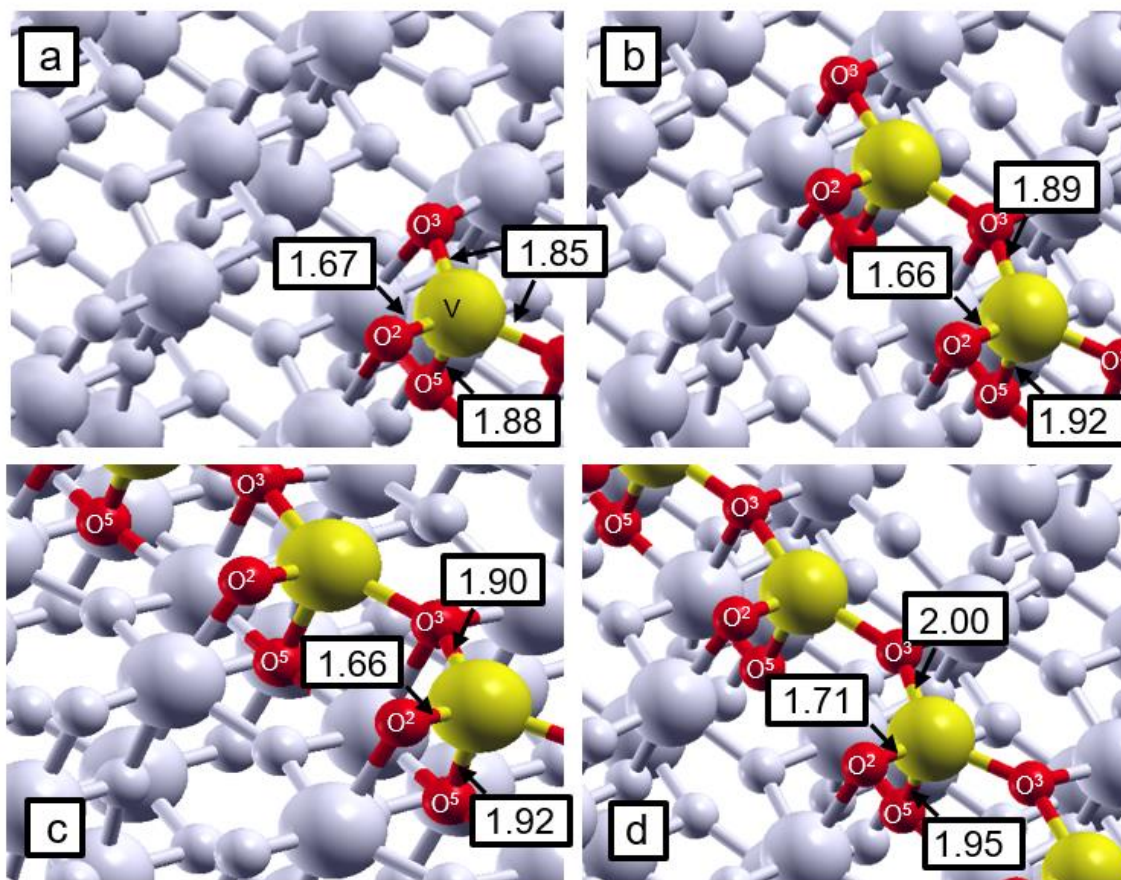**Table 4.5. Geometric parameters of modeled catalysts (reduced VO_x/TiO_2)**

	Calculation			Experiment[1] (2.8wt.% VO_x/TiO_2)
	$V-O^2$	$V-O^3$	$V-O^5$	V-O
Monomer	1.67	1.85	1.88	
				1.64
Dimer	1.66	1.89	1.92	
				1.88
Trimer	1.66	1.90	1.92	
				2.00
Polymer	1.71	2.00	1.95	

[1] Ref. [53,54]

Again, the Bader charge analysis for atoms of interest is presented in Table 4.6. As expected, the results indicate that all vanadium in the reduced clusters are less positively charged than those located in the oxidized structures. For instance, the Bader charge of oxidized monomer is found to be 2.10 |e|, but reduced one to be 1.93 |e|, a charge difference of 0.17|e|. The values for the charge of the oxygen atoms in the reduced clusters are mostly independent of cluster size, except for the case of O^3, where the Bader charge for the O^3 atom become more negative as the vanadium cluster becomes larger. In contrast, as predicted in the beginning of this section, the vanadium charges in the reduced polymeric vanadia are less positive than that in the reduced monomeric vanadia (1.93 |e| for the monomer vs. 1.80 |e| for the polymer). Remarkably, the difference on the V charge between oxidized (Table 4.4) and reduced structures (Table 4.6) increases as the V cluster sizes becomes larger by 0.17 |e| for monomeric VO_x, to 0.26 |e| for polymeric VO_x. The differences observed between oxidized and reduced vanadia structures suggests that, compared to the reduced monomeric VO_x, the reduced polymeric VO_x requires more electronic density to be fully oxidized. Therefore, the results obtained for the interatomic distances and the Bader charge analysis for a series of VO_x/TiO_2 models indicates that the reducibility of supported VO_x is linked to the size of the VO_x

cluster, in a good agreement with previous results obtained by H_2-Tempearature programmed reduction[37,55] and *in situ* spectroscopic techniques[20,21].

Table 4.6. Summary of Bader charge of V and O for reduced VO_x/TiO_2

	V	O^2	O^3	O^5
Monomer	1.93	-0.92	**-1.15**	-1.16
Dimer	1.85	-0.93	**-1.17**	-1.17
Trimer	1.84	-0.93	**-1.18**	-1.18
Polymer	1.80	-0.93	**-1.23**	-1.18

The calculated TDOS and PDOS onto the vanadium states is presented in Fig.4.10 for the reduced VO_x models; (a) monomer, (b) dimer, (c) trimer, and (d) 1-D polymer. For both TDOS and PDOS the Fermi level is set to 0 eV. As discussed above, the Fermi levels for the isolated oxidized VO_x model clusters (monomer, dimer, and trimer) tend to be positioned on top of the valence band (see Fig.4.8). However, the Fermi level of all reduced VO_x models lies just below the edge of the conduction band, clearly indicating that the states located near the high energy edge of the valence band are those of vanadium (highlighted with * in Fig.4.10a). The filling of these states is much more obvious as the vanadium cluster size increases. At the same time, the filled V_{3d} states are more localized toward the valence band for the case of the larger vanadium oxide clusters (-0.5 eV for monomer and -1.5 eV for the polymer).

Moreover, the projected DOS of V_{3d} occupies only half of the edge of the conduction band, suggesting that V_{3d} orbitals, in the reduced VO_x are not be solely responsible for the observed d-d transition, assigned as the edge peak in our UV-vis experimental results in section 4.3.4. To explore this possibility, the obtained charge density plot of the

reduced VO_x models at top of the valence band (highest occupied state) is shown in Fig.4.11. The charge density is localized dominantly at the V cation center and is partially distributed to the titanium atoms nearby. Based on this analysis, we can propose that the d-d transition observed in the optical spectra originates not only from reduced V centers but also from partially reduced Ti atoms bonded to V atom through bridging oxygens (V-O-Ti). In the other words, the electronic density, which is introduced upon reduction of VO_x, is not distributed over a large number of atoms and mostly results in a noticeable change on the electronic structure of the V atom and those Ti atoms close to the vanadium atom. Therefore, we conclude that the electronic d-d transition observed at low energy regions (0 - 2.5eV) in the *in situ* UV-Vis spectroscopy experiments in this study, is mechanistically related to filled V and Ti d-orbitals (V^{+4} and Ti^{+3}). Indeed, the calculated PDOS and charge density of highest occupied state are in excellent agreement with previously reported observations obtained by *in situ* EPR experiments[22,23] suggesting that both V^{+4} and Ti^{+3} are present on VO_x/TiO_2 materials subject to a reductive environment.

Figure 4.10. TDOS (black) and PODS of the vanadium (Red) for (a) monomer, (b) dimer, (c) trimer, and (d) 1D-polymer. Energies are referenced to the calculated Fermi level (Dashed line).

4.3.7   Geometries, Charges and Electronic structure of reduced VO_x species

In our model, the reduced VO_x cluster is depicted as lacking the terminal vanadyl oxygen (V=O) and one of the bridging oxygen (V-O-Ti) (Fig.4.9). In this case, three oxygen atoms are found to be responsible for the bonding of the reduced V center to the anatase (101) slab and are denoted to O^2, O^3, and O^5 in Fig.4.9. The interatomic distance of all bonds of interest (V-O^2, V-O^3 and V-O^5) generally increases as the vanadia cluster size increases, in particular, the length of V-O^3 increases by 0.15 Å, compared to those of the

reduced monomer and polymer. This trend allowed us to predict that the vanadium charge in the polymeric structure can be less positive than that in the monomer since the oxygen atoms, surrounding the vanadium atom, are positioned at a longer distance in the polymeric vanadia structure than the monomeric one. Detailed information on charges will be discussed in the section below. Again, we compared the structure parameters (V-O distance) obtained after relaxation of these models to those experimentally reported by (EXAFS) in order to confirm the validity of our model. This comparison is shown in Table 4.5.

We can see that the calculated structural parameters in our model are consistent with the experimentally obtained values for the structure of reduced vanadia. Among the O atoms present, the behavior of O^5 is of particular relevance. This oxygen atom was originally linked to three Ti atoms in the oxidized VO_x cluster. For the case of the reduced cluster, the O^5 still remains triple-coordinated, but now is bonded to two titanium atoms and one vanadium atom.

Again, the Bader charge analysis for atoms of interest is presented in Table 4.6. As expected, the results indicate that all vanadium in the reduced clusters are less positively charged than those located in the oxidized structures. For instance, the Bader charge of oxidized monomer is found to be 2.10 |e|, but reduced one to be 1.93 |e|, a charge difference of 0.17|e|. The values for the charge of the oxygen atoms in the reduced clusters are mostly independent of cluster size, except for the case of O^3, where the Bader charge for the O^3 atom become more negative as the vanadium cluster becomes larger. In contrast, as predicted in the beginning of this section, the vanadium charges in the reduced polymeric vanadia are less positive than that in the reduced monomeric vanadia (1.93 |e| for the monomer vs. 1.80 |e| for the polymer). Remarkably, the difference on the V charge between oxidized (Table 4.4) and reduced structures (Table 4.6) increases as the V cluster sizes becomes larger by 0.17 |e| for monomeric VO_x, to 0.26 |e| for polymeric VO_x. The differences observed between oxidized and reduced vanadia structures suggests that, compared to the reduced monomeric VO_x, the reduced polymeric VO_x requires more electronic density to be fully oxidized. Therefore, the results obtained

for the interatomic distances and the Bader charge analysis for a series of VO_x/TiO_2 models indicates that the reducibility of supported VO_x is linked to the size of the VO_x cluster, in a good agreement with previous results obtained by H_2-Tempearature programmed reduction[37,55] and *in situ* spectroscopic techniques[20,21].

The calculated TDOS and PDOS onto the vanadium states is presented in Fig.4.10 for the reduced VO_x models; (a) monomer, (b) dimer, (c) trimer, and (d) 1-D polymer. For both TDOS and PDOS the Fermi level is set to 0 eV. As discussed above, the Fermi levels for the isolated oxidized VO_x model clusters (monomer, dimer, and trimer) tend to be positioned on top of the valence band (see Fig.4.8). However, the Fermi level of all reduced VO_x models lies just below the edge of the conduction band, clearly indicating that the states located near the high energy edge of the valence band are those of vanadium (highlighted with * in Fig.4.10a). The filling of these states is much more obvious as the vanadium cluster size increases. At the same time, the filled V_{3d} states are more localized toward the valence band for the case of the larger vanadium oxide clusters (-0.5 eV for monomer and -1.5 eV for the polymer).

Moreover, the projected DOS of V_{3d} occupies only half of the edge of the conduction band, suggesting that V_{3d} orbitals, in the reduced VO_x are not be solely responsible for the observed d-d transition, assigned as the edge peak in our UV-vis experimental results in section 4.3.4. To explore this possibility, the obtained charge density plot of the reduced VO_x models at top of the valence band (highest occupied state) is shown in Fig.4.11. The charge density is localized dominantly at the V cation center and is partially distributed to the titanium atoms nearby. Based on this analysis, we can propose that the d-d transition observed in the optical spectra originates not only from reduced V centers but also from partially reduced Ti atoms bonded to V atom through bridging oxygens (V-O-Ti). In the other words, the electronic density, which is introduced upon reduction of VO_x, is not distributed over a large number of atoms and mostly results in a noticeable change on the electronic structure of the V atom and those Ti atoms close to the vanadium atom. Therefore, we conclude that the electronic d-d transition observed at low energy regions (0 - 2.5eV) in the *in situ* UV-Vis spectroscopy experiments in this

study, is mechanistically related to filled V and Ti d-orbitals (V^{+4} and Ti^{+3}). Indeed, the calculated PDOS and charge density of highest occupied state are in excellent agreement with previously reported observations obtained by *in situ* EPR experiments[22,23] suggesting that both V^{+4} and Ti^{+3} are present on VO_x/TiO_2 materials subject to a reductive environment.
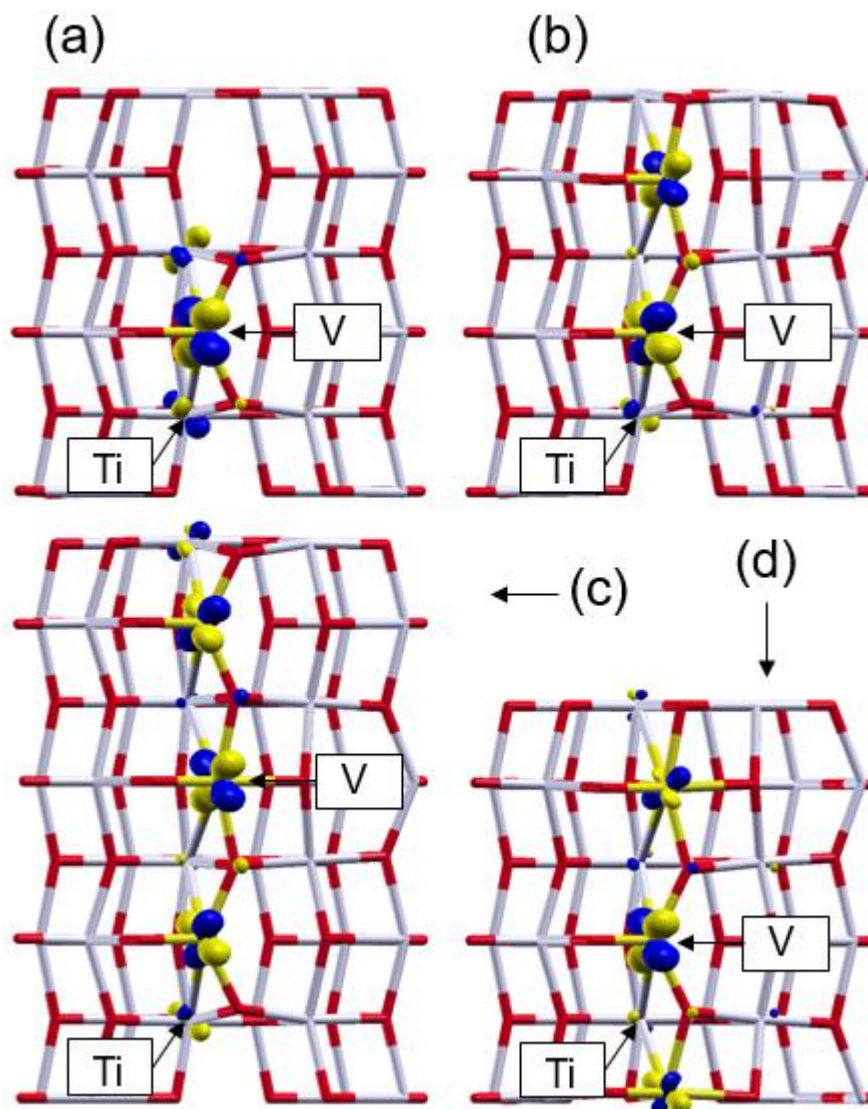

Figure 4.11. Charge density of the highest occupied state for the reduced VO_x cluster on anatase (101); (a) monomer, (b) dimer, (c) trimer, and (d) polymer. Blue and yellow orbital shapes correspond to the ± 0.01 iso-surface. (Grey, and red sticks represent Ti, and O, respectively)

4.3.8   Optical spectra for oxidized and reduced VO$_x$ models

We attempted to calculate the optical absorption spectra for both the oxidized and reduced VO$_x$ monomer, dimer and polymer models using a TDDFT protocol. The result of this calculation is shown in Fig.4.12. It is widely recognized that this approach is insufficient to attain a correct band gap, this deficiency is attributed to the incomplete cancellation of the self-interaction of pure exchange/correlation functional[56]. Fortunately, comparing the electronic structures at DFT and DFT+U levels for our models, both functionals showed identical delocalized energy states near the Fermi level with an observable band gap difference. Thus, the absorption spectra were calculated at DFT level and then, the photon energy, corresponding to x-axis in Fig.4.12 was corrected by multiplying a ratio factor of 1.4 (band gap of anatase 101 surface calculated using DFT+U level / band gap of anatase 101 surface calculated using DFT level). The calculated absorption edge (E$_g$) obtained for anatase (101) is ~ 3.0 eV (E$_g$ in Fig.4.12A), this value is consistent with the experimental band gap energy reported for pure TiO$_2$[57–59]. Prior to discussing the spectroscopic features that underline the domain size effect depicted in the sections above, we will discuss the optical absorption spectra of the oxidized and reduced monomeric VO$_x$. First, from the comparison between the spectra of monomeric oxidized VO$_x$ (black solid in Fig.4.12a) and pure TiO$_2$ (black dashed line in Fig.4.12a), we can observe an extra transition centered at 3.2 eV and extended to the band edge (marked as ★ in Fig.4.12a) for the case of the vanadia bearing model. We attribute this feature to electronic transitions from O$_{2p}$ to V$_{3d}$ states since the observed energy values correspond to the gap observed between the valence band and the projected V3d states (Fig.4.8a) for this model. At the same time, the spectra of the reduced vanadia monomer displays an extra broad absorption band centered at 2.0 eV (marked as *r in Fig.4.12b). This broad band is dominated by d-d transitions and its features are in a good agreement with our experimental data (Fig.4.6 in section 4.3.4).

Next, the spectroscopic features that underline the domain size effect are described by the comparison between optical absorption spectra obtained by *in situ* UV-vis spectroscopy in section 4.3.4 and the calculated absorption spectra for the oxidized and reduced vanadia models. Based on the observed experimental trends, we reported in section 4.3.4

(Figure 4.6) that the increase in domain size of the supported VO_x resulted in a red-shift of the energies at pre-edge maxima. Similarly, although the obtained TDDFT values are somewhat different, our calculations presented in Figure 4.12 are consistent with the experimentally observed red-shift, reporting values of 2.0 eV, 1.9 eV and 1.7 eV for monomeric, dimeric and polymeric vanadia respectively. The comparable trends, observed in our experimental and calculated results, consequently indicates that the broad band in absorption, appearing in the range of $0 - 2.5$ eV, corresponds to a d-d transition (V-3d → V-3d or Ti-3d → Ti-3d) and that the electronic energy gap of this d-d transition extremely sensitive to the degree of polymerization of the VO_x structure.
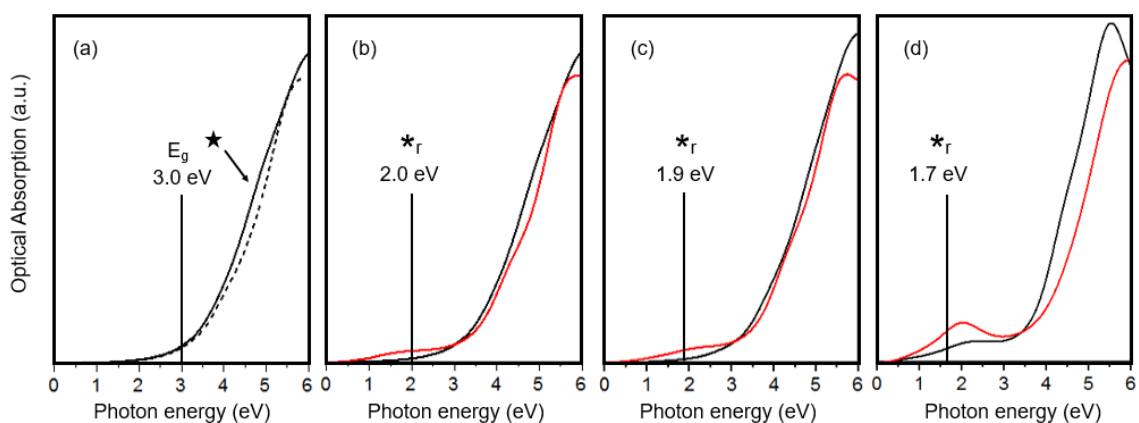
Figure 4.12. TDDFT calculation of electronic spectra of (a) VO_x free anatase (101) surface (Dashed line) and the oxidized monomeric VO_x on anatase (101) surface (Solid line). TDDFT calculation of electronic spectra of the oxidized VO_x cluster supported on pristine anatase (101) surface (Black solid lines) and the reduced VO_x cluster supported on pristine anatase (101) (Red solid lines): (b) monomer, (c) dimer, and (d) polymer. Symbols (E_g and *r) reflect the edge energy for VO_x free anatase (101) slab and energies at reduced peak maxima of the reduced VO_x/anatase (101) slabs, respectively.

4.3.9 The oxygen defect formation energy and catalytic consequence of vanadia size

Our results above indicate a clear link between reducibility and catalytic activity for the VO_x/TiO_2 system. In fact, the reducibility of VO_x, which is defined as the ability of the fully oxidized V^{+5} species to gain electrons, has been proposed as a descriptor for redox activity of vanadia catalysts[18,19]. More recently however, Schomäcker and coworkers[7] suggested that the reducibility of VO_x can be used as a relevant descriptor through the values for oxygen defect formation enthalpies of vanadia. Experimentally, the oxygen defect formation enthalpy for a VO_x/TiO_2 catalyst[7] was reported to be 44 kJ·mol^{-1}. Based on the relaxed structures and their calculated energies, presented in this study, the oxygen defect formation energies for the four oxidized structures modeled in this study were calculated. In our case, different number of oxygen atoms are removed, depending of the vanadia model cluster size, so the defect formation energy per O atom was compared. The defect formation enthalpy per oxygen atom is calculated as follows:

$$\mathrm{E}_{def} = \frac{1}{n}\left(E_{red} + \frac{n}{2}E_{O_2} - \mathrm{E}_{oxi}\right)$$

eq.(4.6)

Where E_{def} is the defect formation enthalpy per O atom (kJ·mol^{-1}). E_{red}, E_{oxi}, and E_{O_2} are the energies for the reduced VO_x/anatase (101) slab, the oxidized VO_x/anatase (101) slab, and gas phase oxygen, respectively. The value of n reflects the number of oxygen atoms from the oxidized VO_x/anatase (101) model slab removed to obtain the reduced vanadia cluster. Figure 4.13 compares oxygen defect formation energies per O atom for the monomer, dimer, trimer, and polymer. The defect formation energy per unit O atom shows the lowest enthalpy for monomeric VO_x (69 kJ·mol^{-1}). This value increases almost linearly as the number of vanadium atoms in the model cluster increase. Interestingly, the isolated trimeric and 1-D polymeric VO_x exhibit a high defect formation enthalpy (~400 kJ·mol^{-1}) with a difference of ~20 kJ·mol^{-1} between them. As previously reported, VO_x species with high reducibility tend to show a low value for defect formation enthalpy[7]. The trend observed in Figure 4.13 for the oxygen defect formation enthalpy for different VO_x species thus indicates that the reducibility of VO_x is

extremely sensitive to cluster size even under identical electronic environment (TiO_2 support in our case), as reported for the case of vanadia supported on ceria[60,61]. Our combined results thus suggest very well that dispersed isolated vanadia clusters, such as monomeric VO_x predominantly take part in catalytic turnovers and that some of the reduced species present during catalysis at high vanadia loadings do not participate in the ethanol partial oxidation redox cycle.
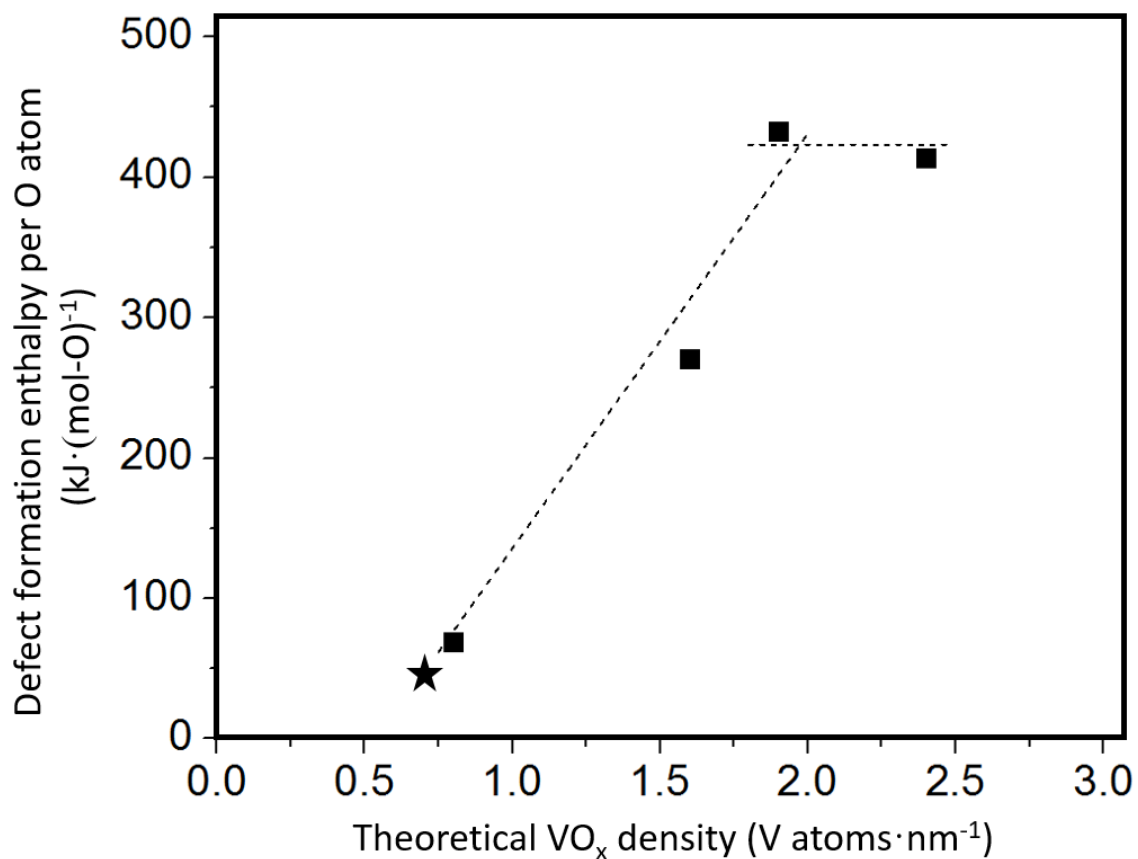

Figure 4.13. Defect formation enthalpy per O atom as a function of the theoretical VO_x density. ★ indicates experimental defect formation enthalpy for VO_x/TiO_2 (44 kJ·mol^{-1}), described in ref.[7]

4.4   Conclusion

The combination of experimental and theoretical work presented in this study revealed that monomeric vanadia active sites predominantly participate in the partial oxidation redox cycle. The heterogeneous distribution of supported VO_x over the TiO_2 surface was confirmed by *in situ* Raman spectroscopy and temperature programmed desorption. Kinetic analysis showed decreasing values for the first (K_1k_2) and zero (k_2) order rate constants at 200°C as VO_x loading in the catalysts increases. On the other hand, the apparent activation energy is independent of surface coverage (75.5 ± 7.2kJ/mol), however, the values on the experimental factor depend on vanadium loading; suggesting a larger density of active sites at low VO_x loadings. At the same time, the red-shift observed in the edge energy of both experimental and theoretical (TD-DFT) optical spectra indicates that the electronic structure of supported vanadia is sensitive to cluster domain size. The calculated oxygen defect formation enthalpy obtained for vanadia clusters of different size (monomer, dimer, trimer and 1-d polymer) indicates that vanadia monomer has the lowest oxygen defect formation energy, consistently indicating that ethanol partial oxidation turnovers take place mostly over monomeric vanadia clusters.

References

(1)   Deo, G.; Wachs, I. E. *J. Catal.* **1994**, *146* (2), 323–334.

(2)   Tesser, R.; Maradei, V.; Di Serio, M.; Santacesaria, E. *Ind. Eng. Chem. Res.* **2004**, *43* (7), 1623–1633.

(3)   Chen, K.; Bell, A. T.; Iglesia, E. *J. Phys. Chem. B* **2000**, *104* (6), 1292–1299.

(4)   Burcham, L. J.; Badlani, M.; Wachs, I. E. *J. Catal.* **2001**, *203*, 104–121.

(5)   Mars, P.; van Krevelen, D. W. *Chem. Eng. Sci.* **1954**, *8*, 41–59.

(6)   Chen, K.; Khodakov, A.; Yang, J.; Bell, A. T.; Iglesia, E. **1999**, *333*, 325–333.

(7)   Beck, B.; Harth, M.; Hamilton, N. G.; Carrero, C.; Uhlrich, J. J.; Trunschke, A.; Shaikhutdinov, S.; Schubert, H.; Freund, H.-J.; Schlögl, R.; Sauer, J.; Schomäcker, R. *J. Catal.* **2012**, *296* (0), 120–131.

(8)   Weckhuysen, B. M.; Keller, D. E. *Catal. Today* **2003**, *78* (1–4), 25–46.

(9)   Kilos, B.; Bell, A. T.; Iglesia, E. *J. Phys. Chem. C* **2009**, *113* (7), 2830–2836.

(10) Gao, X.; Jehng, J.-M.; Wachs, I. E. *J. Catal.* **2002**, *209* (1), 43–50.

(11) Dumesic, J. A.; Topsøe, N.-Y.; Topsøe, H.; Chen, Y.; Slabiak, T. *J. Catal.* **1996**, *163* (2), 409–417.

(12) Macht, J.; Iglesia, E. *Phys. Chem. Chem. Phys.* **2008**, *10* (35), 5331–5343.

(13) Sadovskaya, E. M.; Goncharov, V. B.; Gulyaeva, Y. K.; Popova, G. Y.; Andrushkevich, T. V. *J. Mol. Catal. A Chem.* **2010**, *316* (1-2), 118–125.

(14) Kim, H. Y.; Lee, H. M.; Pala, R. G. S.; Metiu, H. *J. Phys. Chem. C* **2009**, *113* (36), 16083–16093.

(15) Hu, J. Z.; Xu, S.; Li, W.-Z.; Hu, M. Y.; Deng, X.; Dixon, D. A.; Vasiliu, M.;

Craciun, R.; Wang, Y.; Bao, X.; Peden, C. H. F. *ACS Catal.* **2015**, *5* (7), 3945–3952.

(16)   Baertsch, C. D.; Soled, S. L.; Iglesia, E. *J. Phys. Chem. B* **2001**, *105* (7), 1320–1330.

(17)   Burcham, L. J.; Briand, L. E.; Wachs, I. E. *Langmuir* **2001**, *17* (20), 6175–6184.

(18)   Bañares, M. A.; Martínez-Huerta, M. V; Gao, X.; Fierro, J. L. G.; Wachs, I. E. *Catal. Today* **2000**, *61* (1–4), 295–301.

(19)   Chary, K. V. R.; Kishan, G.; Bhaskar, T. *Chem. Commun.* **1999**, *15*, 1399–1400.

(20)   Argyle, M. D.; Chen, K.; Resini, C.; Krebs, C.; Bell, A. T.; Iglesia, E. *J. Phys. Chem. B* **2004**, *108* (7), 2345–2353.

(21)   Argyle, M. D.; Chen, K.; Resini, C.; Krebs, C.; Bell, A. T.; Iglesia, E. *Chem. Commun.* **2003**, *16*, 2082–2083.

(22)   Dinse, A.; Carrero, C.; Ozarowski, A.; Schomäcker, R.; Schlögl, R.; Dinse, K.-P. *ChemCatChem* **2012**, *4* (5), 641–652.

(23)   Dinse, A.; Ozarowski, A.; Hess, C.; Schomäcker, R.; Dinse, K.-P. *J. Phys. Chem. C* **2008**, *112* (45), 17664–17671.

(24)   Nobbs, J. H. *Rev. Prog. Color. Relat. Top.* **1985**, *15* (1), 66–75.

(25)   Davis, E. A.; Mott, N. F. *Philos. Mag.* **1970**, *22* (179), 903–922.

(26)   Perdew, J. P.; Burke, K.; Ernzerhof, M. *Phys. Rev. Lett.* **1996**, *77* (18), 3865–3868.

(27)   Vanderbilt, D. *Phys. Rev. B* **1990**, *41* (11), 7892–7895.

(28)   Lutfalla, S.; Shapovalov, V.; Bell, A. T. *J. Chem. Theory Comput.* **2011**, *7*, 2218–2223.

(29)   Giannozzi, P.; Baroni, S.; Bonini, N.; Calandra, M.; Car, R.; Cavazzoni, C.;

Ceresoli, D.; Chiarotti, G. L.; Cococcioni, M.; Dabo, I.; Dal Corso, A.; de Gironcoli, S.; Fabris, S.; Fratesi, G.; Gebauer, R.; Gerstmann, U.; Gougoussis, C.; Kokalj, A.; Lazzeri, M.; Martin-Samos, L.; Marzari, N.; Mauri, F.; Mazzarello, R.; Paolini, S.; Pasquarello, A.; Paulatto, L.; Sbraccia, C.; Scandolo, S.; Sclauzero, G.; Seitsonen, A. P.; Smogunov, A.; Umari, P.; Wentzcovitch, R. M. *J. Phys. Condens. Matter* **2009**, *21* (39), 395502.

(30)   Shapovalov, V.; Fievez, T.; Bell, A. T. *J. Phys. Chem. C* **2012**, *116* (35), 18728–18735.

(31)   Vittadini, A.; Selloni, A. *J. Phys. Chem. B* **2004**, *108*, 7337–7343.

(32)   Wachs, I. E. *Dalt. Trans.* **2013**, *42* (33), 11762–11769.

(33)   Kim, T.; Wachs, I. E. *J. Catal.* **2008**, *255* (2), 197–205.

(34)   Wu, Z.; Rondinone, A. J.; Ivanov, I. N.; Overbury, S. H. *J. Phys. Chem. C* **2011**, *115* (51), 25368–25378.

(35)   Carrero, C. A.; Keturakis, C. J.; Orrego, A.; Schomacker, R.; Wachs, I. E. *Dalt. Trans.* **2013**, *42* (35), 12644–12653.

(36)   Burcham, L.; Deo, G.; Gao, X.; Wachs, I. *Top. Catal.* **2000**, *11-12* (1-4), 85–100.

(37)   Went, G. T.; Leu, L.; Bell, A. T. *J. Catal.* **1992**, *134* (2), 479–491.

(38)   Wu, Z.; Kim, H.-S.; Stair, P. C.; Rugmini, S.; Jackson, S. D. *J. Phys. Chem. B* **2005**, *109* (7), 2793–2800.

(39)   Carrero, C. A.; Schloegl, R.; Wachs, I. E.; Schomaecker, R. *ACS Catal.* **2014**, *4*, 3357–3380.

(40)   Nair, H.; Gatt, J. E.; Miller, J. T.; Baertsch, C. D. *J. Catal.* **2011**, *279* (1), 144–154.

(41)   Birky, T. W.; Kozlowski, J. T.; Davis, R. J. *J. Catal.* **2013**, *298*, 130–137.

(42)   Weckhuysen, B. M.; Centrum, V.; Opper, V.; Interfasechemie, D.; Leu, K. U. V;

Wachs, I. E. *J. Phys. Chem. C* **2000**, *112*, 7382–7387.

(43)   Klug, C. a.; Kroeker, S.; Aguiar, P. M.; Zhou, M.; Stec, D. F.; Wachs, I. E. *Chem. Mater.* **2009**, *21* (18), 4127–4134.

(44)   Deshlahra, P.; Iglesia, E. *J. Phys. Chem. C* **2014**, *118* (45), 26115–26129.

(45)   Bulánek, R.; Čapek, L.; Setnička, M.; Čičmanec, P. *J. Phys. Chem. C* **2011**, *115* (25), 12430–12438.

(46)   Gao, X.; Wachs, I. E. *J. Phys. Chem. B* **2000**, *104* (6), 1261–1268.

(47)   Yun, D.; Zhao, Y.; Abdullahi, I.; Herrera, J. E. *J. Mol. Catal. A Chem.* **2014**, *390* (0), 169–177.

(48)   Słoczyński, J. *Appl. Catal. A Gen.* **1996**, *146* (2), 401–423.

(49)   Goodrow, A.; Bell, A. T. *J. Phys. Chem. C* **2008**, *112* (34), 13204–13214.

(50)   Price, S. P.; Tong, X.; Ridge, C.; Neilson, H. L.; Buffon, J. W.; Robins, J.; Metiu, H.; Bowers, M. T.; Buratto, S. K. *J. Phys. Chem. A* **2014**, *2* (110), 8309–8313.

(51)   Du, Y.-J.; Li, Z. H.; Fan, K.-N. *Surf. Sci.* **2012**, *606* (11-12), 956–964.

(52)   Tanaka, T.; Yamashita, H.; Tsuchitani, R.; Funabiki, T.; Yoshida, S. *J. Chem. Soc. Faraday Trans. 1 Phys. Chem. Condens. Phases* **1988**, *84* (9), 2987–2999.

(53)   Silversmit, G.; Van Bokhoven, J. a.; Poelman, H.; Van Der Eerden, a. M. J.; Marin, G. B.; Reyniers, M. F.; De Gryse, R. *Appl. Catal. A Gen.* **2005**, *285* (1-2), 151–162.

(54)   Silversmit, G.; van Bokhoven, J. a; Poelman, H.; van der Eerden, a; Marin, G. B.; Reyniers, M. F.; De Gryse, R. *Phys. Scr.* **2005**, *T115*, 798–801.

(55)   Besselmann, S.; Freitag, C.; Hinrichsen, O.; Muhler, M. *Phys. Chem. Chem. Phys.* **2001**, *3* (21), 4633–4638.

(56) Ortega, Y.; Hernández, N. C.; Menéndez-Proupin, E.; Graciani, J.; Sanz, J. F. *Phys. Chem. Chem. Phys.* **2011**, *13* (23), 11340.

(57) Ong, W.-J.; Tan, L.-L.; Chai, S.-P.; Yong, S.-T.; Mohamed, A. R. *Nanoscale* **2014**, *6* (4), 1946–2008.

(58) Govind, N.; Lopata, K.; Rousseau, R.; Andersen, A.; Kowalski, K. *J. Phys. Chem. Lett.* **2011**, *2* (21), 2696–2701.

(59) Li, Y.-F.; Aschauer, U.; Chen, J.; Selloni, A. *Acc. Chem. Res.* **2014**, *47*, 3361–3368.

(60) Paier, J.; Penschke, C.; Sauer, J. *Chem. Rev.* **2013**, *113* (6), 3949–3985.

(61) Paier, J.; Kropp, T.; Penschke, C.; Sauer, J. *Faraday Discuss.* **2013**, *2* (162), 233–245.

169

body

Chapter 5

5 *In situ* redox active site titration of supported vanadia during ethanol partial oxidation catalysis: Structure refinement on the VO$_x$/TiO$_2$ catalytic system.

Abstract

An advanced titration method during ethanol partial oxidation with *tert*-butanol is proposed to quantify the number of active redox sites in supported vanadia-titania catalytic systems (VO$_x$/TiO$_2$). In agreement with previous reports, our results indicate that not all vanadia atoms participate in the catalytic redox cycle and therefore the use of total vanadium loadings to calculate turnover frequencies results in an underestimation of actual turnover frequency values. The kinetically relevant rate constants for ethanol partial oxidation obtained on the basis on the number of active sites calculated by our method indicate that these rate constants are independent of vanadia loading. This in turn suggests that isolated vanadia species are the main active sites for ethanol partial oxidation.

5.1 Introduction

The description and rationalization of the kinetics and molecular mechanism of partial oxidation processes over redox metal oxide (V, Mo, Re, and others) catalysts have been the subject of intense study[1–4]. Among these, alcohol partial oxidation processes carried over supported vanadia (VO$_x$) are useful at probing reactions to help the understanding of redox catalysis. Thus, a large body of literature has been dedicated to the evaluation of the catalytic reactivity for alcohol partial oxidation[2,5,6] over vanadia. The results suggest that two aspects are key parameters to determine catalytic performance: the chemical identity of the support and the structure of the supported VO$_x$ clusters.

Attempts have been made to correlate the reactivity for alcohol partial oxidation and the identity of the vanadia support[7]. Sanderson electro negativity[8], the degree of reducibility of the supports, or the extent of the formation of lattice oxygen vacancies have been proposed as reactivity descriptors. In most cases however, the observed activation energy of aldehyde formation over VO_x supported on different metal oxides (TiO_2, ZrO_2, Nb_2O_5, Al_2O_3, and SiO_2) was found to be similar regardless of the chemical identity of the support (~85 ± 2 kJ/mol for the case of methanol oxidation)[6,7].

As mentioned above, the catalytic reactivity for alcohol partial oxidation over VO_x is also highly sensitive to the size distribution of the VO_x domains, generally displaying lower turnover frequency (TOF) values at higher vanadia surface coverages[9]. The intrinsic reactivity of monodispersed VO_x clusters is still a subject of controversy and the determination of the specific active sites has yet to be established. Despite these complexities, rigorously performed spectroscopic experiments have been carried out to understand the behavior of VO_x during catalysis. For example, Wachs and coworkers used high temperature alcohol chemisorption and *in situ* infrared techniques to determine the number of surface active sites in vanadia bearing materials[10]. Baertsch and collaborators developed an isothermal anaerobic titration method to quantify active redox sites on vanadium oxide supported on alumina[11]. More recently, Peden et al. identified isolated VO_x species (mono and dimeric) as being the primary source of primary actives site for methanol ODH[12].

Despite of these sound and extensive efforts, challenges on the identification and quantification of active sites in vanadia catalysts still remain. For instance, since the formation of an intact Lewis-bound surface alcohol species (M··O(H)R, M represents a metal atom) and a dissociated surface alkoxy species (-OR) occurs at the same time, the data obtained by chemisorption and infrared spectroscopy is convoluted[10]. Moreover, anaerobic titration of redox active sites overestimates the actual number of sites for the case of vanadia supported on reducible substrates, such as titania or zirconia since lattice oxygen support can get involved it the catalytic cycle[13].

In this contribution, we report a method for *in situ* selective titration of the redox active site responsible for ethanol partial oxidation over VO_x/TiO_2 *during* catalysis using *tert*-butanol as titrating agent. This methodology takes advantage of *tert*-butanol's ability to hinder the kinetically-relevant adsorption step that takes place during ethanol partial oxidation needed to start the redox catalytic cycle over vanadia, thus both ethanol and *tert*-butanol adsorption over vanadia are equilibrated. A different scenario compared to *tert*-butanol poisoning all redox active sites. This method is based on the inability of *tert*-butanol to undergo oxidation under typical ethanol partial oxidation conditions, preventing it to engage in the selective oxidation cycle. As a consequence, when considering redox catalysis over VO_x, *tert*-butanol acts a spectator since it lacks an alpha hydrogen and thus, the hydrogen elimination pathway necessary for oxidation cannot take place. Moreover, under our reaction conditions (at 200 ºC and WHSV : 623 mole ethanol·(mol V-h)$^{-1}$ at global minimum) the formation of ethylene is negligible since the Brøsnted acid sites present in the catalyst are not strong enough to catalyze the dehydration pathway[26].

5.2   Method

5.2.1   Catalyst Preparation

Nano-powdered TiO_2 were purchased and used without further purification (Sigma Aldrich, 99.7%, 21 nm). VO_x impregnation over these supports was carried by incipient wetness impregnation, using aqueous vanadium pentoxide (V_2O_5, Sigma Aldrich, ACS grade) dissolved in 1M oxalic acid ($H_2C_2O_4$, Sigma Aldrich, ACS grade) containing the desired amount of V. After impregnation the catalysts were dried in the oven at 90ºC overnight, and further calcined at 400 ºC for 2h in flowing air (Praxair, zero grade, 0.83 $cm^3 \cdot s^{-1}$).

5.2.2   Catalytic testing and titration of vanadia active sites

Before catalytic testing all samples were pressed into wafers, crushed and sieved to a pellet size between 120-250 μm. Steady-state partial oxidation of ethanol experiments

were conducted in a continuous flow fixed bed quartz glass micro reactor (5 mm I.D.) oriented vertically in an electrically heated furnace at atmospheric pressure equipped with a digital temperature controller (Whatlow series 97 and 96). Catalyst samples were supported on a quartz frit equipped with K-type thermocouples placed at the vertical center of the catalyst bed on both sides. The catalyst was pretreated using a 0.16 $^{o}C \cdot sec^{-1}$ temperature ramp to 200°C and held at this temperature for 30 min under a O_2/He mixture (5%O_2, Praxair, UHP, 2.68 $cm^3 \cdot s^{-1}$ before exposing the catalyst to the reactants. After this pretreatment step liquid absolute ethanol (Brampton, Ontario) was evaporated into the flowing 5%O_2/He influent stream at 120 ^{o}C using a liquid syringe pump (KDS scientific) with the flow adjusted to give the desired ethanol partial pressure (0.5-11 kPa). All gas transfer lines were kept above 120 ^{o}C to prevent condensation of reactants and products. Ethanol conversion rates over VO_x/TiO_2 catalysts were measured at 200°C. The flow of 5%O_2/He were adjusted by a mass flow controller (MKS instruments) during these experiments. The rates of ethanol partial oxidation are reported either as total V-atom turnover rates (moles of ethanol converted per total V atom content (V_T) per second) or titrated V atom turnover rates (moles of ethanol converted per active V atom ($V_{POE,T}$) per second), as described in the following sections. A subsequent series of experiments was implemented to titrate the redox active sites in the catalyst. For this purpose the partial ethanol pressures were kept constant (1-7 kPa) and *tert*-butanol (Aldrich, 99.8%) was separately introduced into the reactor by vaporizing it into the flowing O_2/He carrier at 120 ^{o}C using a micro-syringe pump (KDS Scientific) to the desired *tert*-butanol partial pressure (0.5-5 kPa). The ethanol and *tert*-butanol conversion was kept under 10% and 15%, respectively so that differential reaction conditions could be assumed. Rates of *tert*-butanol dehydration are reported either as total V-atom turnover rates (moles of ethanol converted per total V atom (V_T) per second) or titrated V atom turnover rates (moles of ethanol converted per active V atom ($V_{DH,T}$) per second), Chemical species in the feed and reactor effluent stream were measured using an online gas chromatograph (Shimadzu gas chromatograph, GC-2014) with a capillary column (HP-1, 30 m × 0.53 mm, 1.0 μm thickness) connected to a flame ionization detector. For the identification of the observed GC peaks, the effluent stream was diverted to the Mass spectrometer detector (Agilent, 5975C). The carbon mass balance was always higher than 98%.

5.2.3 Ethanol-*tert*-butanol temperature programmed desorption

Temperature-programmed desorption (TPD) was performed to probe the role of surface hydroxyls during catalysis. The ethanol-*tert*-butanol TPD experiments were carried out in a continuous flowing system at atmospheric pressure. For these experiments 0.2 g of catalyst were first treated in dry air (Praxair, UHP) flow of 0.25 $cm^3 \cdot s^{-1}$ for 2 hours at 300 ºC. Then, the sample was cooled down to 25ºC while purging in He (Praxair, UHP, feed flow rate 0.25 $cm^3 \cdot s^{-1}$). After this stage, using a micro-syringe pump (KDS Scientific), either pure ethanol, pure *tert*-butanol (Sigma, 99.8%) or a liquid mixture of the two alcohols with different volumetric ratios (1:3, 1:1, and 3:1 v/v%) was introduced in the influent He stream to carry competitive adsorption. All the transfer lines were kept at 120 ºC to prevent reactant and product condensation. Physically adsorbed ethanol and/or *tert*-butanol were removed by flushing under He flow at room temperature until alcohol was not observed in the effluent stream. Temperature programmed desorption was carried under He atmosphere using a ramp of 0.033 $ºC \cdot sec^{-1}$ up to 250 ºC. The desorbed gases were analyzed using a by on-line GC-FID-MS (Agilent 6890A, 5975C, 30 m HP-Innowax column $\times$ 25 *μm* thickness).

5.2.4 Computational Details

Density functional theory calculations were performed within the generalized gradient approximation (GGA) and the periodic plan-wave approach, using the Perdew-Burke-Ernzerhof (PBE) exchange-correlation functional[14] and Vanderbilit ultra-soft pseudo-potentials[15]. The DFT+U correction is applied to both titanium and vanadium metal atoms in the support. We use *U*=2.3 eV on Ti and 2.0 eV on V d-states based on the suggestions made in the literature[16]. Plan-wave basis set cutoffs for the kinetic and density cutoff were 50 and 500 Ry, respectively ensuring convergence. The Plane-Wave Self-Consistent Field (PWscf) code of the Quantum-Espresso package[17], running on SHARCNET, was used to obtain geometric optimizations and to calculate total energy. The k-point sampling of the Brillounin zone was limited to gamma. The Broyden-

Fletcher-Goldfarb-Shanno (BFGS) algorithm was used for geometry optimization, with threshold values of 0.092 eV/Å and 6.8×10^{-4} eV for residual forces and energy variation, respectively. Anatase (101) surface was chosen for simulation since this surface is the most abundant among the exposed anatase facets. Prior to geometry optimization of hydroxylated anatase (101) surfaces, a clean anatase (101) surface was modeled with a periodically repeated slab. A 1×3 surface cell containing 72 atoms, with corresponding surface area of 10.24×11.36 Å^2, was modeled with a vacuum of 10 Å. Gas-phase molecules were simulated in a 15 Å cubic box, which is large enough to ignore interaction between the gas molecules.

5.3   Results and Discussion

5.3.1   Acid sites (Brønsted and Lewis) present on the bare TiO$_2$ surface are catalytically inactive for tert-butanol dehydration in the presence of ethanol

5.3.1.1   Site requirements for isobutene formation on VO$_x$-free titania: kinetic experiment

A kinetic study was carried to prove a critical hypothesis of our titration method: under our experimental conditions (200 °C) and in the presence of ethanol, the surface hydroxyl groups (potential Brønsted acid sites) and the coordinately unsaturated Ti^{+4} (Lewis acid sites) present on the titania surface are catalytically inactive for the the formation of isobutene; i.e. they do not participate in the catalytic dehydration of *tert*-butanol. For this purpose, the vanadium free support was tested first in a *tert*-butanol only stream (1.4kPa *t*ert-butanol, 200 °C, 2.67 cm^3·s^{-1}, Fig.5.1a), followed by addition of ethanol to the reactant mixture (1.4 kPa *t*ert-butanol, 0.5 kPa ethanol, 200 °C, 2.67 cm^3·s^{-1}, Fig.5.1b). In the absence of ethanol a small fraction of *tert*-butanol (~1.5%) was converted to isobutene; however, this process stopped in the presence of ethanol. This observation strongly suggests that, *in the presence of ethanol*, the few acid sites, participating in the dehydration of *tert*-butanol, present on titania play the role of spectators for the case of the formation of isobutene.
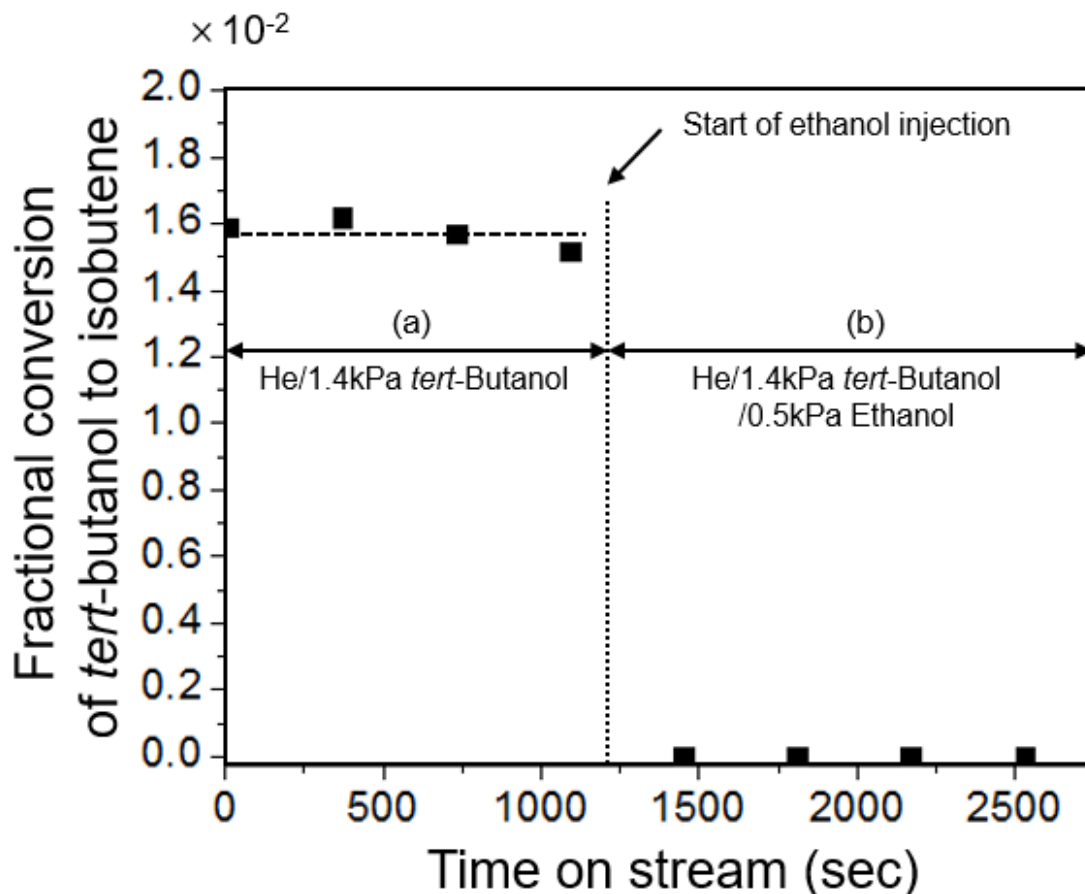
Figure 5.1. Fractional conversion at 200 °C of *tert*-butanol to isobutene (a) without ethanol (WHSV = 76 mol *tert*-butanol·(mol TiO₂-h)⁻¹), and (b) with ethanol in the stream over the VOₓ free titania support (WHSV = 76 mol *tert*-butanol·(mol TiO₂-h)⁻¹ and 31 mol ethanol·(mol TiO₂-h)⁻¹).

5.3.1.2 Ethanol and *tert*-butanol temperature programmed desorption (TPD)

Next, TPD experiments were also carried to establish another critical premise: under our experimental conditions, the adsorption processes taking place over the coexisting redox and acid sites on vanadia are equilibrated, in other words, adsorption of ethanol and *tert*-butanol takes place simultaneously on redox and acid active sites. Fig.5.2 shows the temperature programmed profile for acetaldehyde and isobutene evolution over a catalyst

(5.1wt.%VO_x/TiO_2) exposed to different volumetric ratios of ethanol to *tert*-butanol {1:0 v/v(a), 3:1 v/v(b), 2:2 v/v(c), 1:3 v/v(d), and 0:1 v/v(e)}. Acetaldehyde evolution was observed only for the case when ethanol was present (Fig.5.2e) in the influent stream during adsorption while isobutene was observed (Fig.5.2a) only when *tert*-butanol was used during adsorption treatment. For the cases where both ethanol and *tert*-butanol were introduced together, together with physisorbed ethanol and *tert*-butanol both, acetaldehyde and isobutene were observed as desorption products. Ethylene and diethyl ether were not observed since as mentioned above our catalyst lacks the strength of acid sites needed for dehydration product formation under the temperature regimes at which the TPD experiments were carried[18,19].

 A clear trend is observed: the amount of acetaldehyde, produced through ethanol partial oxidation decreased as the amount of *tert*-butanol in the mixture increased. The amount of acetaldehyde released, thus can be linked to the amount of VO_x redox active sites equilibrated with ethanol on the catalyst surface which will likely catalyze the partial oxidation pathway, thus our experimental observations suggest that the presence of *tert*-butanol prevents a significant amount of ethanol molecules from accessing VO_x redox sites.

The TPD experiments also support our previous observation on the passive role of the titania acid sites. As shown in Fig.5.2, the profile for isobutene evolution in the presence of ethanol appears as a symmetric peak centered at about 90°C (Right graphs in Fig.5.2). In the absence of ethanol, the same isobutene main desorption peak is observed but now displaying a broad shoulder at 125 °C (indicated with an arrow in Fig.5.2a). This broad shoulder in the 100-150 °C range is the result of isobutene formation over titania surface hydroxyls since *tert*-butanol TPD experiments carried over vanadia free titania showed a peak for isobutene formation that corresponds to this broad shoulder (data not shown). For the case when both ethanol and *tert*-butanol are present in the influent stream, no shoulder is observed in the isobutene desorption profile (Fig.5.2b, 5.2c, and 5.2d). Thus this observation clearly indicates that vanadia sites are responsible for isobutene formation and strongly suggest that the surface acid sites present on titania do not act as active sites and play the role of spectators for the case of the formation of isobutene in the

presence of ethanol. In the other words, ethanol completely prevents the accessibility of *tert*-butanol to surface hydroxyl groups present in the titania surface. This observation will be rationalized in terms of the significant difference on binding energy of C-O-Ti moieties between ethanol and *tert*-butanol in the computational analysis section below. Besides, the formation of isobutene decreases with increasing the ethanol/*tert*-butanol volumetric ratio in the influent stream from 1:3 v/v (Fig.5.2b) to 3:1 v/v (Fig.5.2d). This trend indicates that the competitive adsorption of ethanol and *tert*-butanol on acid VO_x sites is equilibrated.
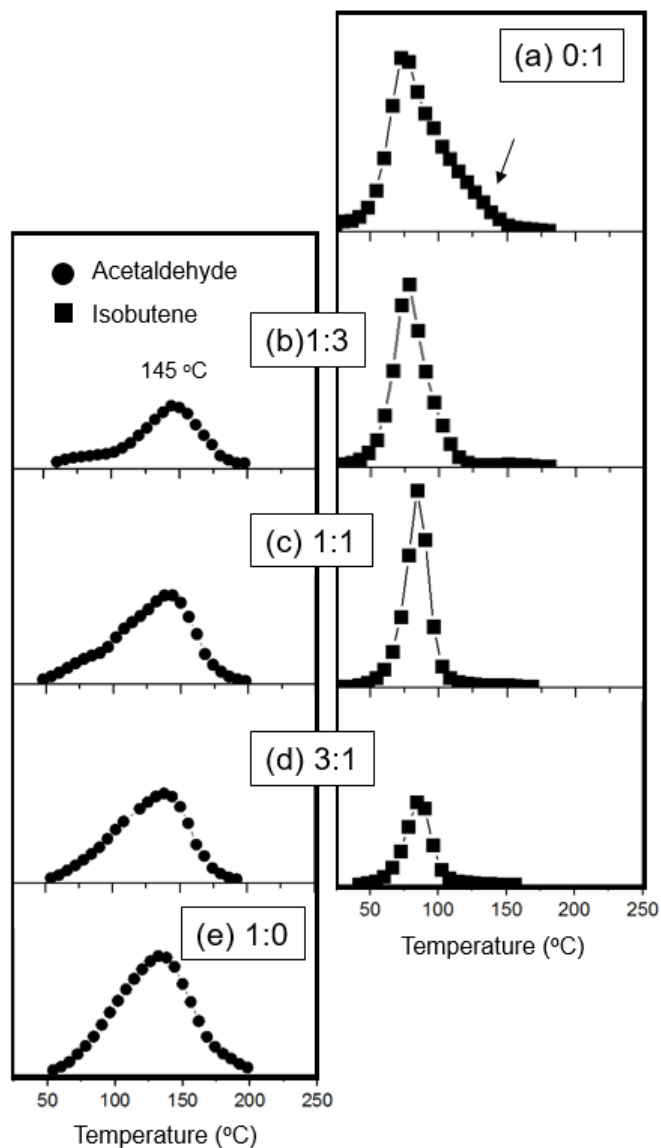
Figure 5.2. Formation of acetaldehyde over redox sites (left) and isobutene over acid sites (right) during TPD experiments carried on a 5.1wt.%VO$_x$/TiO$_2$ sample. Ratios shown in boxes indicate different volumetric compositions between ethanol and *tert*-butanol. Ratios shown in boxes indicate different volumetric compositions between EtOH and *tert*-BtOH.

5.3.1.3 Computational study: Reactivity of acid sites {terminal hydroxyl (Ti-O$_{2C}$H), and bridging hydroxyl (Ti-O$_{3C}$H) and coordinately unsaturated Ti$_{5C}$} groups on titania with ethanol and *tert*-butanol.

Given the complexity of this particular catalyst system, it is difficult to rule out the possibility that surface hydroxyl moieties present on the titania surface play a role in *tert*-butanol dehydration (DH). To explore this possibility, we used density functional theory (DFT) calculations. We carried out three simulations for each case (ethanol vs. *tert*-butanol). In one case we modeled adsorbed species on terminal titania hydroxyl (O$_{2C}$-H, twofold coordinated oxygen, see Scheme 5.1) species, in the second case the alcohol molecule was adsorbed to a bridging titania hydroxyl (O$_{3C}$-H, threefold coordinated oxygen), and in the third case the alcohol molecule was dissociatively adsorbed on top of the coordinately unsaturated Ti site (Ti$_{5C}$, five-fold coordinated titanium that represents Lewis acid site)[20]. We looked at the differences in adsorption energy when ethanol and *tert*-butanol react with either the O$_{2C}$-H or O$_{3C}$-H or Ti$_{5C}$ present on the TiO$_2$ surface by comparing the adsorption energies of both ethanol and *tert*-butanol over TiO$_2$. The adsorption energies (E$_{ads}$) indicated for Brønsted acid sites and Lewis acid site are calculated using the following equations, respectively

$$E_{ads} = E_{surf} + E_{mol} - E_{sys} - E_{H_2O} \qquad\qquad \text{eq.(5.1)}$$

$$E_{ads} = E_{surf} + E_{mol} - E_{sys} \qquad\qquad \text{eq.(5.2)}$$

where $E_{surf}, E_{mol}, E_{sys}, E_{H_2O}$ are the electronic energies of a bare anatase (101) surface bearing a hydroxyl group for eq.5.1 and without a hydroxyl for eq.5.2, the energy of the gas phase molecules (ethanol or *tert*-butanol), the energy of the combined system formed by the adsorbate and the adsorbent, and the energy of a water molecule (resulting from the formation of the alkoxylate over the TiO$_2$ surface), respectively. Negative values of *E$_{ads}$* correspond to more thermodynamically favorable adsorption configurations.

In the adsorption of ethanol or *tert*-butanol over hydroxylated TiO_2 surface, depicted in Scheme 5.1, the surface hydroxyl reacts with the adsorbed alcohol molecule to generate a surface bonded alkoxide and a water molecule. We optimized the initial and final structures for partially hydroxylated surfaces that include O_{2c}-H or O_{3c}-H and found that the adsorption configurations are significantly distinguishable depending on the alcohol adsorbate and the specific type of surface hydroxyl (terminal vs bridging) involved in the process. The adsorption energy (E_{ads}) for each configuration is indicated in Scheme 5.1. A negative value on the adsorption energy indicates a more thermodynamically favorable process. Thus, the calculated results show that for both ethanol and *tert*-butanol, the adsorption over terminal hydroxyl (O_{2c}-H) is a more thermodynamically favorable process than that over bridging hydroxyl (O_{3c}-H). In addition, the adsorption of ethanol over terminal hydroxyls O_{2c}-H (path a-E, -0.73 eV) is thermodynamically more favorable than that of *tert*-butanol over the same type of site (path a-B, -0.47 eV). At the same time, for both molecules, the reactions happening at the bridging O_{3c}-H site are close to thermoneutral {-0.12 eV for ethanol (path b-E) and +0.06 eV for *tert*-butanol (path b-B)}. This suggests that the bridging hydroxyl site could be ruled out as active site for the dehydration reaction of *tert*-butanol. This observation also can be supported also by differences in surface morphology, as it has been previously proposed that it is easier to adsorb on the O_{2c}-H sites than on the O_{3c}-H since the O_{2c}-H is less sterically hindered than the O_3C-H site[21]. Therefore, the calculated adsorption energies accounts for the low accessibility of *tert*-butanol to surface hydroxyl in the presence of ethanol. On the contrary, the adsorption of ethanol and *tert*-butanol at coordinately unsaturated Ti (Scheme 5.1c) site differs from what we observed from the surface hydroxyl cases. It is found that the adsorption of *tert*-butanol at this Ti site (path c-B, -0.60 eV) is also a less thermodynamically favorable process than that of ethanol over the identical site (path c-E, -0.65 eV). A narrow gap (0.05 eV) between these adsorption energies (-0.65 eV for path c-E and -0.60 eV for path c-B) implies that ethanol and *tert*-butanol adsorption at this site is competitive. However, it has been well documented that the number of the coordinately unsaturated Ti sties present in TiO_2 surface dramatically decreases upon the introduction of the supported VO_x[22,23]. Thus, when supported VO_x is accompanied with TiO_2, the dehydration of *tert*-butanol to isobutene, taking place at the coordinately

unsaturated Ti site (potential Lewis site) can be assumed to be negligible. All aforementioned results thus indicate that our initial hypothesis regarding the role of acid and redox sites in the reactivity of ethanol and *tert*-butanol are valid, thus using these hypothesis, in the next section we propose a kinetic model to rationalize our experimental observations on the catalytic activity of the VO_x/TiO_2 system.
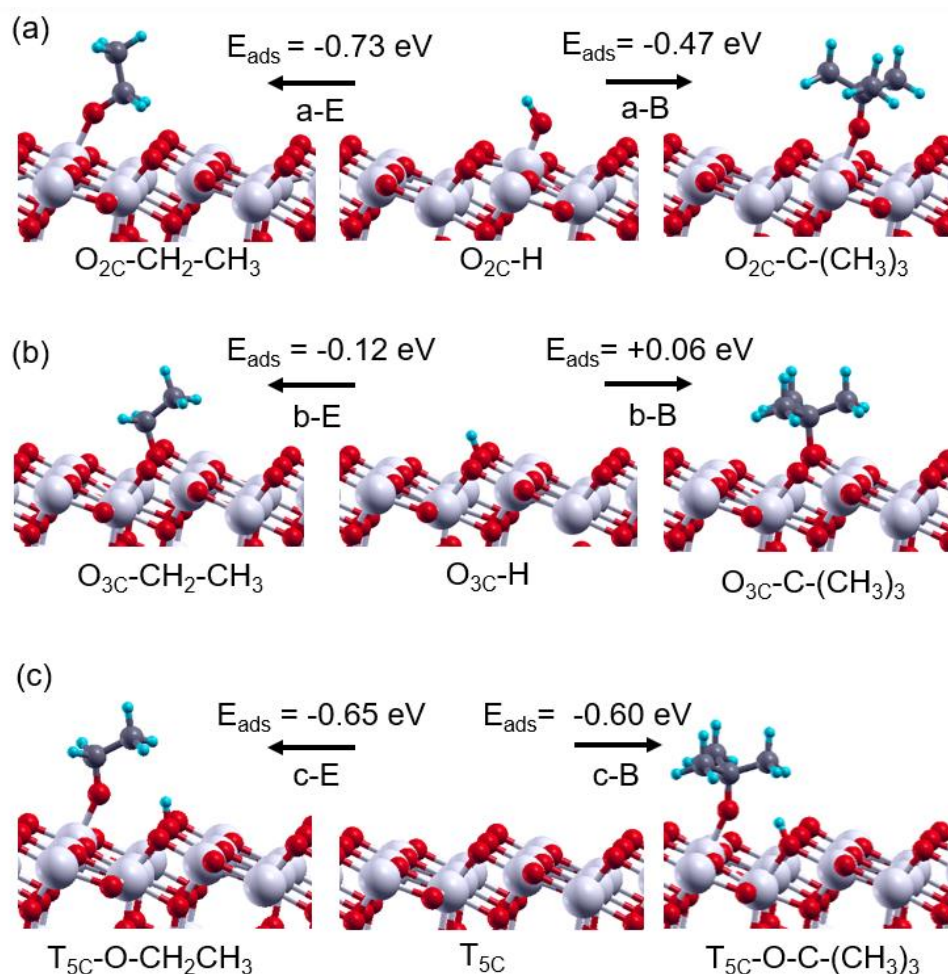
Scheme 5.1. Adsorption configurations of two different pathways {(a) terminal O_{2C} –H hydroxyl, (b) bridging O_{3c}-H hydroxyl, and (c) Ti_{5C}} for both ethanol and *tert*-butanol adsorption over partially hydroxylated anatase (101) (a) and (b) or coordinately unsaturated Ti (c) . The white, red, grey, and blue atoms represent Ti, O, C, and H, respectively.

5.3.2 Proposed catalytic cycles and kinetics
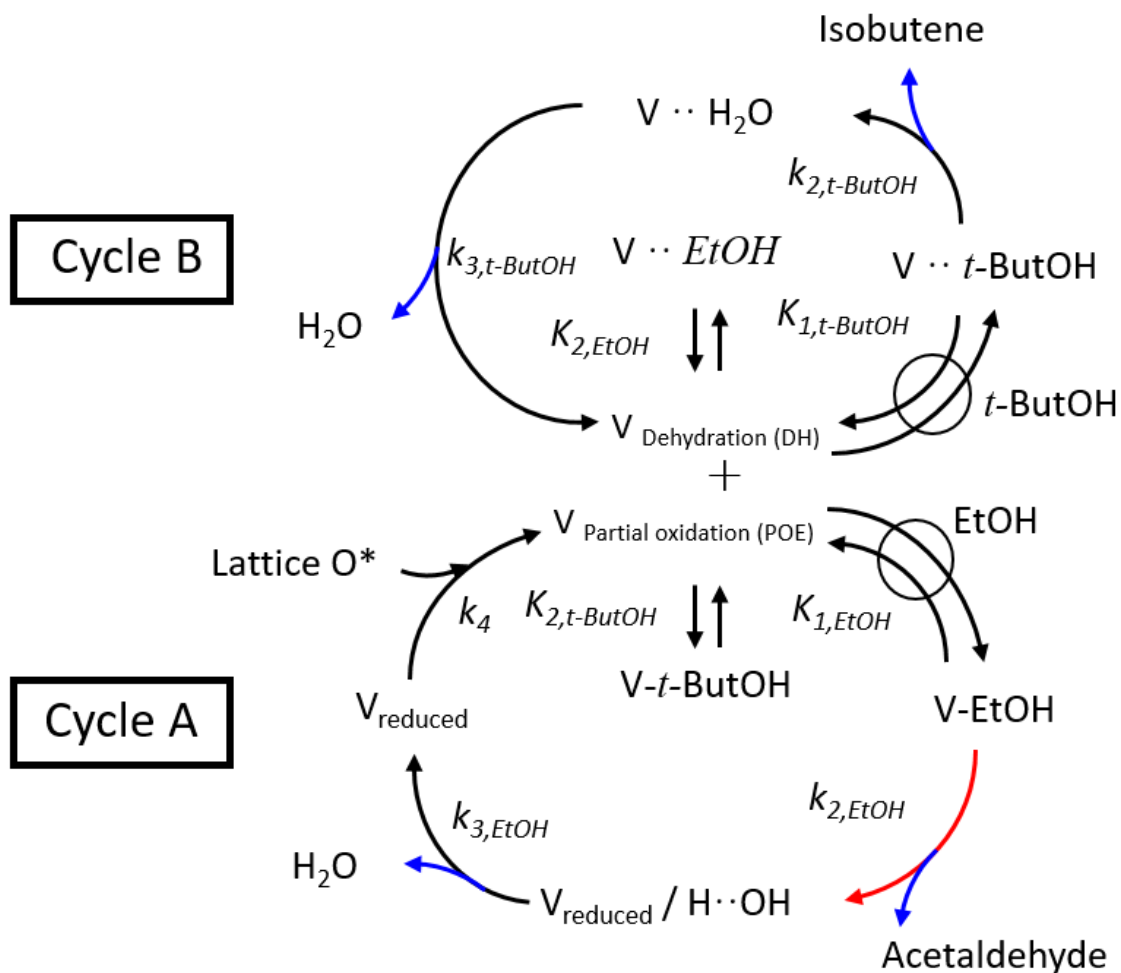
Scheme 5.2. A proposal for the catalytic cycles (A – ethanol partial oxidation and B – *tert*-butanol dehydration over supported VOₓ/TiO₂. Symbols, EtOH, and *t*-ButOH represent gaseous ethanol, *tert*-butanol, respectively.

5.3.2.1 Proposed kinetics for ethanol partial oxidation

Based on previously published work by Iglesia and colleagues[2,24], we developed a mechanism to describe both ethanol partial oxidation and *tert*-butanol dehydration taking place simultaneously over the VOₓ/TiO₂ catalysts surface. The mechanism and apparent overall kinetics of ethanol partial oxidation to acetaldehyde has been described in detail using different mechanistic assumptions. A Langmuir-Hinshelwood type rate is

applicable in which adsorption, surface reaction, and desorption processes are proposed as elementary steps[25–28]. Nevertheless, many of these studies report different dependences on ethanol partial pressure, having the overall rate following either first order dependence[5,29] or zero order dependence[2,6,28] on ethanol partial pressure on the basis of the experimental conditions used. Experimentally, ethanol partial oxidation rates show a linear dependence on ethanol partial pressure at low ethanol concentrations which gradually collapses into a zero order dependence at higher ethanol concentrations, again, in excellent agreement with a Langmuir type rate equation. Kinetically relevant rates are limited by the activation the alpha carbon-hydrogen bond ($C_a - H$), as revealed by isotopic experiments[2] carried using CH_2CH_5OH, CD_2CD_3OH and CH_2CH_3OD.

Based on a pseudo-steady state approximation of the elementary steps proposed in Cycle A in Scheme 5.2, the following turnover rate equation can be derived

$$\frac{r_{POE}}{V_T} = \frac{K_{1,EtOH}\, k_{2,EtOH} P_{EtOH}}{1 + K_{1,EtOH}\, P_{EtOH} + \frac{k_{2,EtOH}}{k_{3,EtOH}} K_{1,EtOH} P_{EtOH} + \frac{K_{1,EtOH} k_{2,EtOH} P_{EtOH}}{k_4 O^*}} \qquad \text{eq.(5.3)}$$

①　　　　②　　　　③　　　　④

where, $\frac{r_{POE}}{V_T}$ is the rate normalized per total number of vanadium atoms (V_T), $K_{1,EtOH}$ is the quasi-equilibrium constant for the ethanol adsorption step, $k_{2,EtOH}$ is the rate constant of the rate-limiting step for hydride -abstraction from adsorbed ethoxide species, $k_{3,EtOH}$ is the rate constant for water desorption resulting from hydroxyl recombination, and k_4 is the rate constant for the reoxidation of vanadia. The symbol (O^*) represents the concentration of lattice oxygen, involved in the reoxidation step. Each term in the denominator of eq.5.3 reflects the surface coverage ratio ($\theta_{species}$) of a specific surface species. The first term represents unoccupied oxidized vanadia sites (θ_{POE}). The second term in the denominator corresponds to vanadia sites bearing a surface ethoxide adsorbate (θ_{V-EtOH}). The third ($\theta_{V_{reduced}/H\cdots OH}$) and last denominator ($\theta_{V_{reduced}}$) term correspond to reduced vanadia sites, formed after acetaldehyde desorption or the following water desorption step, respectively.

Under our experimental conditions (low conversion < 10% and high WHSV: 623 mole ethanol·(mol V-h)$^{-1}$ at global minimum), a very fast surface hydroxyl recombination and reoxidation of the reduced sites can be assumed when the concentration of lattice oxygen is high enough ($P_{O^*} \gg P_{EtOH}$)[30,31]. Based on these assumptions, the rate becomes a weak function of O_2 pressure since the concentration of lattice oxygen can be described as a function of O_2 pressure[2]. Under these conditions, the fraction of $\theta_{V_{reduced}/H\cdot\cdot OH}$ and $\theta_{V_{reduced}}$ sites is much smaller than unity ($\theta_{V_{reduced}/H\cdot\cdot OH} + \theta_{V_{reduced}} \ll 1$)[2,25]. Therefore, a pseudo steady state analysis of elementary steps for then redox cycle presented in scheme 5.2 gives a simplified turnover rate equation:

$$\frac{r}{V_T} \cong \frac{K_{1,EtOH}\,k_{2,EtOH}P_{EtOH}}{1 + K_{1,EtOH}\,P_{EtOH}} \qquad \text{eq.(5.4)}$$

In order to obtain the kinetically relevant parameters ($K_{1,EtOH}$ and $k_{2,EtOH}$), initial ethanol partial oxidation rates at steady state conditions were measured at ethanol conversions below 10%. Fig.5.3 shows the obtained values for the first-order $(K_{1,EtOH}k_{2,EtOH})$ and zero-order rate constant ($k_{2,EtOH}$) as a function of VO_x loading in the catalyst. The values indicate that both parameters follow the same trend as the amount of vanadia in the catalyst changes. Measured values for $K_{1,EtOH}k_{2,EtOH}$ and $k_{2,EtOH}$ start at a higher value at low VO_x loadings, then linearly decrease with increasing VO_x loadings; reaching zero as the VO_x content in the catalyst approaches monolayer coverage (ML=1, red bar in Fig.5.3). This observed trend poses the question as to whether each VO_x moiety in the catalyst equally contributes to the ethanol partial oxidation reaction.
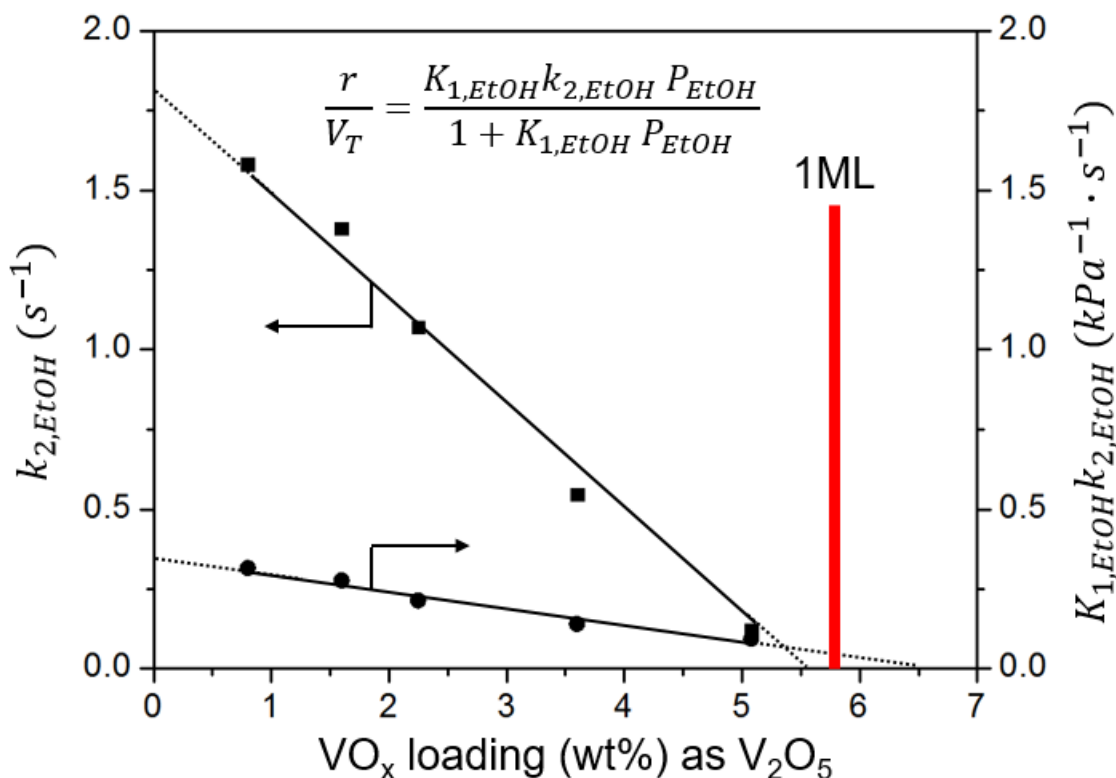
Figure 5.3. Measured first-order rate constant ($K_{1,EtOH}k_{2,EtOH}$) and zero-order rate constant ($k_{2,EtOH}$) as a function of VO$_x$ loading at 200ºC (5kPa O$_2$). Red bar indicates VO$_x$ loading at theoretical vanadia monolayer, described in ref.[32].

5.3.2.2 Simplified ethanol partial oxidation cycle with *tert*-butanol dehydration cycle

In order to quantify the active VO$_x$ sites for partial oxidation process, we investigated the ethanol partial oxidation rate response to *tert*-butanol presence, over the VO$_x$/TiO$_2$ system. The proposed catalytic cycle involving both ethanol partial oxidation and *tert*-butanol dehydration is presented in Scheme 5.2. The main assumption being that in the presence of ethanol the catalytic dehydration of *tert*-butanol takes place only on vanadia sites (denoted as V$_{DH}$) and not on Brønsted (surface hydroxyls) or Lewis acid sites (coordinately unsaturated Titanium sites) present in the titania support as discussed in

section 5.3.1. Moreover, when *tert*-butanol is added to the feed together with ethanol, it can adsorb on the redox site active for ethanol partial oxidation ($K_{2,t-ButOH}$).

Using this additional step, a pseudo-steady-state analysis of the proposed mechanistic steps for ethanol partial oxidation (cycle A) in the presence of *tert*-butanol results in a rate equation of the form:

$$\frac{r_{POE}}{V_{POE,T}} = \frac{K_{1,EtOH}\, k_{2,EtOH} P_{EtOH}}{1 + K_{1,EtOH}\, P_{EtOH} + \dfrac{k_{2,EtOH}}{k_{3,EtOH}} K_{1,EtOH} P_{EtOH} + \dfrac{k_{2,EtOH} K_{1,EtOH} P_{EtOH}}{k_4 O^*} + K_{2,t-ButOH} P_{t-ButOH}} \qquad \text{eq.(5.5)}$$

$$① \qquad ② \qquad\qquad ③ \qquad\qquad ④ \qquad\qquad ⑤$$

Again, the symbol (O^*) represents the concentration of lattice oxygen, involved in the reoxidation step. Each term in the denominator of eq.5.5 reflects the surface coverage ratio ($\theta_{species}$) of a specific surface species. The first term represents unoccupied oxidized vanadia sites (θ_{POE}). The second term in the denominator corresponds to vanadia sites bearing a surface ethoxide adsorbate formation (θ_{V-EtOH}). The third ($\theta_{V_{reduced}/H\cdot\cdot OH}$) and fourth denominator ($\theta_{V_{reduced}}$) terms correspond to reduced vanadia sites, formed after acetaldehyde desorption or the following water desorption step, respectively. The additional last term is the denominator representing vanadia sites equilibrated with *tert*-butanol ($\theta_{V-t-ButOH}$). The rate expression eq.5.5 can be further simplified using the same assumptions listed in section 5.3.2.1 (fast surface hydroxyl recombination and active site reoxidation) to obtain:

$$\frac{r_{POE}}{V_{POE,T}} \cong \frac{K_{1,EtOH}\, k_{2,EtOH} P_{EtOH}}{1 + K_{1,EtOH}\, P_{EtOH} + K_{2,t-ButOH} P_{t-ButOH}} \qquad \text{eq.(5.6)}$$

As explained above, we can then describe all vanadia active sites in the surface as either redox sites ($V_{POE,T}$) carrying ethanol partial oxidation and/or as acid sites ($V_{DH,T}$) used for dehydration of *tert*-butanol. We then can define the ratio of the number of active site only involved in ethanol partial oxidation ($V_{POE,T}$) to total accessible sites (V_T) as alpha (α),

therefore the fraction of active sites responsible for *tert*-butanol dehydration is equal to 1- α, thus:

$$V_T = V_{POE,T} + V_{DH,T} = \alpha V_T + (1 - \alpha)V_T \qquad \text{eq. (5.7)}$$

Using equations (5.6) and (5.7) we can define a linearized equation for the reciprocal partial oxidation rate as a function of *tert*-butanol partial pressure $(P_{t-ButOH})$. The resulting equation (eq.5.8) indicates that only the kinetically relevant parameters $(K_{1,EtOH}$ and $k_{2,EtOH})$ for ethanol partial oxidation are necessary to compute the fraction (α):

$$\frac{V_T}{r_{POE}} \cong \frac{1 + K_{1,EtOH}\, P_{EtOH}}{K_{1,EtOH}\, k_{2,EtOH} P_{EtOH}} \cdot \frac{1}{\alpha} + \frac{K_{2,t-ButOH}}{K_{1,EtOH}\, k_{2,EtOH}\, P_{EtOH}} \cdot \frac{1}{a} \cdot P_{t-ButOH} \qquad \text{eq.(5.8)}$$

5.3.2.3 The ratio (α) as a function of V loading and an answer to question: What is active Redox VO$_x$ species

In graph (A):

$$\frac{V_{POE}}{r_{POE}} \cong \frac{1 + K_{1,EtOH}\, P_{EtOH}}{K_{1,EtOH}\, k_{2,EtOH}\, P_{EtOH} \cdot \alpha} + \frac{K_{2,t-ButOH}}{K_{1,EtOH} k_{2,EtOH} P_{EtOH}} \cdot \frac{P_{t-ButOH}}{\alpha}$$

(a) 1.3 kPa (b) 2.2 kPa (c) 4.4 kPa

y-axis: Reciprocal of $\frac{r_{POE}}{V_{POE}} = \frac{r_{POE}}{\alpha \cdot V_T}$ (s^{-1})

x-axis: *tert*-Butanol partial pressure (kPa)

In graph (B):

$$\frac{r_{POE}}{V_T} \cong \frac{K_{1,EtOH} k_{2,EtOH} P_{EtOH}}{1 + K_{1,EtOH} P_{EtOH}}$$

$P_{O_2} = 5$ kPa

y-axis: $\frac{r_{POE}}{V_T}$ (s^{-1}); x-axis: Ethanol partial pressure (kPa)

In graph (C): $\alpha_{avg} = 0.46$; y-axis: α; x-axis: Ethanol partial pressure (kPa)

Figure 5.4. (A) Reciprocal ODH rate per mol V for ethanol (■ : 4.4 kPa,ethanol ● : 2.2 kPa ethanol, and ▲: 1.3 kPa ethanol) as a function of *tert*-butanol pressure (kPa) (200ºC, 5 kPa O₂) over 3.6wt.%VO$_x$/TiO₂. Dahsed lines in (A) represent linear extrapolated regressed fits to the form of eq.5.8 (B) Measured ethanol partial oxidation rate(■) per mol V as a function of ethanol partial pressure (kPa) (200ºC, 5 kPa O₂). Dashed curve in (B) represents regressed best-fits of the extrapolated rates to the form of eq.5.4. (C) Calculated α value as a function of ethanol partial pressure.

To identify the fraction of active sites responsible for redox catalysis it is essential to obtain the first order rate constant $(K_{1,EtOH}k_{2,EtOH})$ and the zero order rate constant $(k_{2,EtOH})$ for ethanol partial oxidation. For this purpose, ethanol partial oxidation turnover rates were measured on all VO_x/TiO_2 samples at 200 °C in the absence of *tert*-butanol $(0.8 - 5.08$ wt.% as V_2O_5 per gram catalyst, 5 kPa O_2) as a function of ethanol concentrations (1-11 kPa). Fig.5.4B shows representative Langmuir-type ethanol partial oxidation turnover rates as a function of ethanol partial pressure (kPa). As described above in section 5.3.2.1, ethanol partial oxidation follows a zero order dependence in ethanol at high ethanol partial pressure and first order dependence in ethanol at low ethanol partial pressure. We obtained first-order rate constant $(K_{1,EtOH}k_{2,EtOH})$ and zero-order rate constant $(K_{1,EtOH})$ values by regressing experimentally obtained rates to the form of eq.5.4. The reciprocal rates for ethanol partial oxidation were measured as a function of *tert*-butanol concentrations $(0.5 - 2.6$ kPa) at constant ethanol concentrations during steady-state reaction. At least three different ethanol partial pressures were used for comparison. The result of the reciprocal rates for three selected ethanol partial pressures (1.3, 2.2, and 4.4 kPa) is presented in Fig.5.4A. At given *tert*-butanol pressure, the reciprocal turnover rate value is higher at low ethanol partial pressure, suggesting the system retains its first-order dependence on ethanol concentration. Lastly, the calculated ratios (α) for different ethanol concentration are shown in Fig.5.4C by finding the y-intercepts of a linear fit of eq.5.8. The average ratio appears to be 0.46 ± 0.03, indicating that for the case of the 3.6wt.% VO_x/TiO_2 catalyst around half of the supported VO_x participates in the ethanol partial oxidation reaction while another half acts as acid catalysts for *tert*-butanol dehydration.

The identification of the surface species active for the ethanol partial oxidation reaction over VO_x/TiO_2 is still under debate. Some groups have reported that all types of vanadia species (monomeric, polymeric, and crystalline VO_x) present are catalytically active[33]. A counterview also exists[11,12]. Indeed, the positive correlation reported between experimental partial oxidation rates and the relative amount of isolated monomeric VO_x, species obtained experimentally using [51]V MAS NMR and peak deconvolution, supports

the view of monomeric vanadia as the main species responsible for catalysis. Our study aims to address this question. For this purpose we gathered a series of experimental kinetic data over a series of VO_x/TiO_2 catalysts with different vanadium loadings. Using the model developed above, eq.5.6 and eq.5.8, we obtained the ratio (α) of the number of active site (V_{ODH}) only involved in ethanol partial oxidation to total number of sites (V_T) and plotted this value as a function of VO_x loading in the catalysts. The results of these calculations are presented in Fig.5.5A. At low VO_x loadings, the calculated α value is close to one and decreases with increasing surface VO_x coverage in the catalyst, reaching a value of near 0.3 as we approach nominal vanadia monolayer coverage (1ML). In agreement with previously reported observations[12], this result strongly suggests that isolated VO_x species, predominantly present at low VO_x loadings, are the most catalytically active for redox processes. On the other hand, as vanadium loading increases in the catalyst, the fraction of active sites for dehydration increases. This is likely due to polymerization of the vanadium cluster taking place at higher loading, resulting in the generation of Lewis sites[34]. Indeed, Fig.5.5B shows the calculated partial oxidation first order rate constant ($K_{1,EtOH}k_{2,EtOH}$) normalized first by the total number of V atoms (V_T) present in the catalyst, and then normalized by the number of redox active V atoms ($V_{POE} = \alpha V_T$), as obtained from our proposed methodology. An inspection of the trend obtained when normalizing by the number of redox active V atoms (V_{POE}) clearly indicates that the calculated values for the first order rate constant ($K_{1,EtOH}k_{2,EtOH}$) are independent of VO_x loading. On the other hand a dependence on vanadia loading is obtained when the normalization is carried in terms of the total number of vanadium atoms (V_T) in the catalyst. This contrasting trend can be explained in terms of changes on the vanadia cluster reducibility and/or its ability to participate in the redox cycle. It is well established that, at different vanadia loadings, the size distribution of the vanadia clusters change, and thus their reducibility (often depicted as global descriptor for catalytic activity) changes as well[35–37]. If all vanadia clusters of different sizes with different reducibility were participating in the catalytic cycle, the first order constant normalized by the total number of V atoms (V_T) and the first order constant normalized by the number of active vanadium atoms (V_{POE}) calculated using our method should lead to an analogous trend that is dependent of vanadium loading. This will occur because at

higher vanadium loadings the average reducibility (and hence catalytic activity) of the ensemble of vanadium clusters decreases. However, the calculated values we obtained for the first order rate constant ($K_{1,EtOH} k_{2,EtOH}$) normalized by redox active V atoms (V_{POE}) are independent on vanadia loading, implicitly ruling out the hypothesis that all vanadia clusters are participating in catalytic turnovers, and confirming that isolated vanadia tetrahedral species dominantly participate in the redox cycle. This results thus confirms that the kinetic barrier is extremely sensitive to vanadia structure and supports the view of monomeric vanadia as the main species responsible for redox catalysis[12].
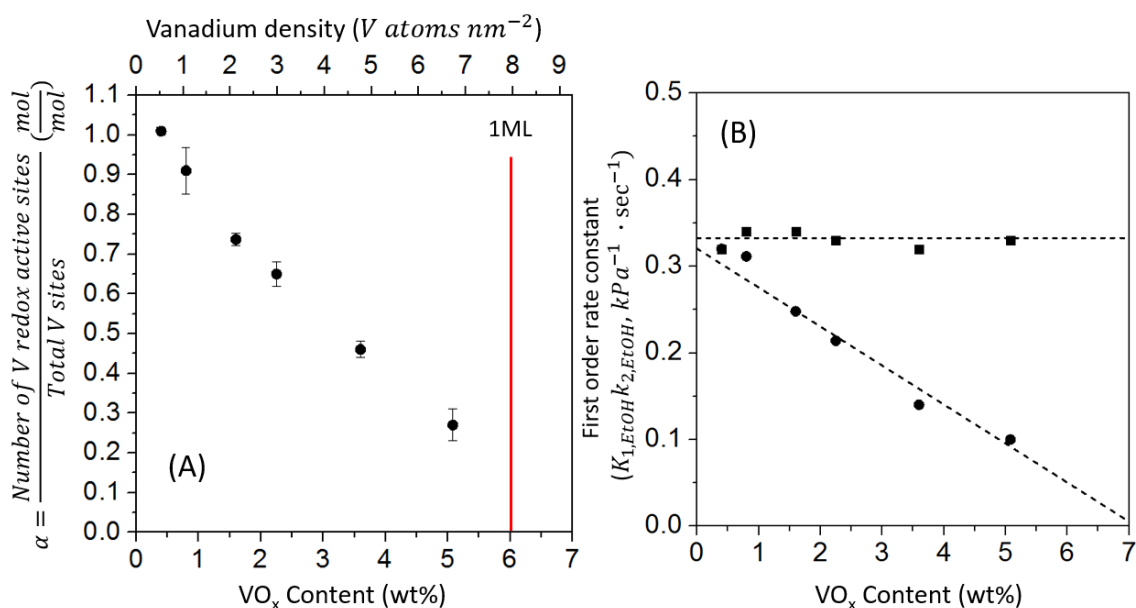
Figure 5.5. (A) The ratio (α) of the number of active site (V_{POE}) only involved in ethanol partial oxidation to total sites (V_T) as a function of VO$_x$ content. Vanadium density is also presented. (B) Calculated first order rate constant ($K_{1,EtOH} k_{2,EtOH}$) normalized by the number of total VO$_x$ content (V_T, ●) and by the number of titrated VO$_x$ active for POE (V_{POE}, ■) as a function of total VO$_x$ loading.

5.3.3   Kinetic dependencies related to *tert*-butanol-to-ethanol ratio
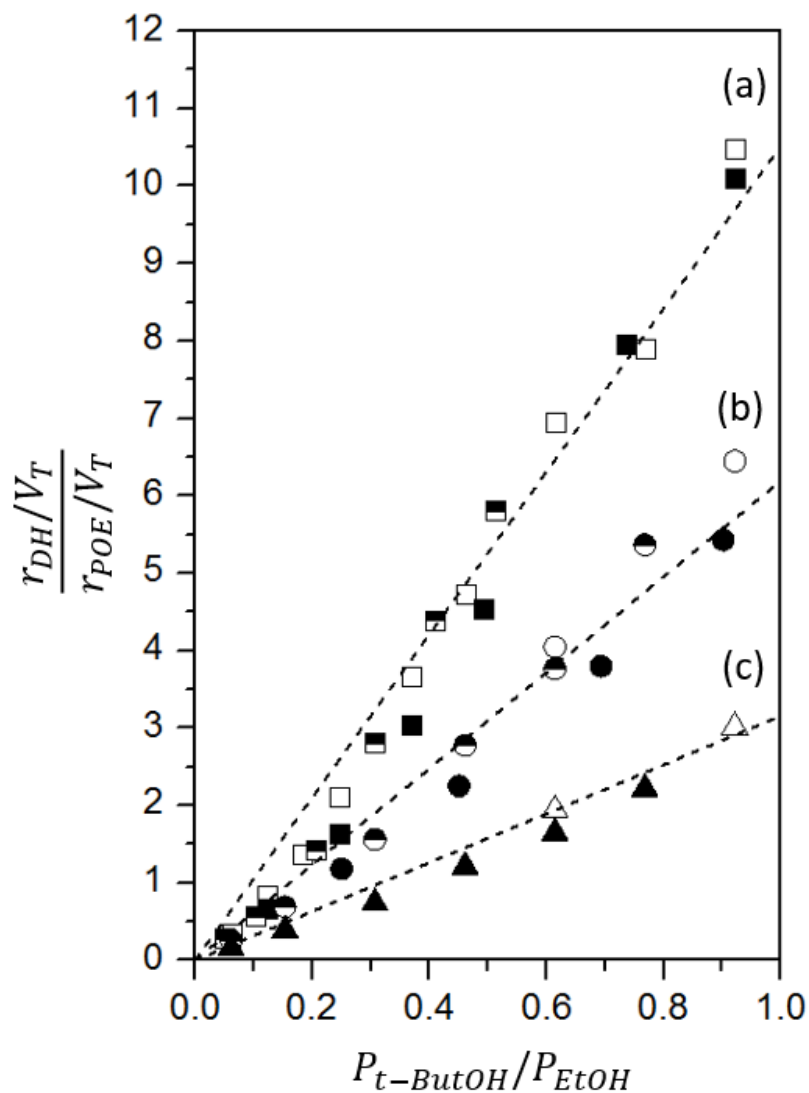
Figure 5.6. Ratio of the rate of *tert*-butanol DH (r_{DH}) to the rate of ethanol partial oxidation (r_{POE}) as a function of ratio of *tert*-butanol to ethanol partial pressure on (a) 3.6wt.%VO$_x$/TiO$_2$ with constant ethanol partial pressures (■: 2.2 kPa, □:4.4 kPa, and ▬ : 6.6 kPa), (b) 2.25wt.% VO$_x$/TiO$_2$ with constant ethanol partial pressures (● : 0.43 kPa, ○ :2.2 kPa, and ◓ :4.4 kPa) and (c) 0.84wt.% VO$_x$/TiO$_2$ with constant ethanol partial pressures (▲:2.2 kPa, and △ : 4.4 kPa)

Lastly, we plotted all kinetic data of ethanol partial oxidation and *tert*-butanol dehydration obtained in our work and plotted it as a single-value function of the ratio between ethanol partial pressure-to-*tert*-butanol partial pressures ($P_{t-ButOH}/P_{EtOH}$). In the previous section, different ethanol partial pressures and kinetic data obtained for the partial oxidation of ethanol in the presence of *tert*-butanol were used to obtain the ratio (α) of the number of active site (V_{POE}) involved in ethanol partial oxidation to total accessible sites in vanadia (V_T). In an analogous manner, the rate equation for *tert*-butanol dehydration in the presence of ethanol has to be derived first. The application of the pseudo-steady state assumption for all intermediates depicted in cycle B in Scheme 5.2 and assuming a reversible *tert*-butanol adsorption and the irreversible decomposition of adsorbed *tert*-butoxide as rate-liming as proposed by Iglesia and coworokers[38] leads to the following turnover rate equation for *tert*-butanol dehydration:

$$\frac{r_{DH}}{V_T} = \frac{K_{1,t-ButOH}\, k_{2,t-ButOH} P_{t-ButOH}}{1 + K_{1,t-ButOH}\, P_{t-ButOH} + \dfrac{k_{2,t-ButOH}}{k_{3,t-ButOH}} K_{1,t-ButOH} P_{t-ButOH} + K_{2,EtOH}\, P_{EtOH}} \qquad \text{eq.(5.9)}$$

$$\text{①} \qquad\qquad \text{②} \qquad\qquad\qquad \text{③} \qquad\qquad\qquad \text{④}$$

where, $\frac{r_{DH}}{V_T}$ is the rate normalized per total number of vanadium atoms present (V_T), $K_{1,t-ButOH}$ is the quasi-equilibrium constant for the no-dissociative adsorption step of *tert*-butanol over acid vanadia sites, $k_{2,t-ButOH,}$ is the rate constant of the rate-limiting step for *tert*-butanol dehydration to isobutene from no-dissociative adsorbed species[38], $k_{3,t-ButOH}$ is the rate constant for water desorption resulting from the recombination of two vicinal hydroxyl moieties generated in the surface after *tert*-butanol dehydration, and, $K_{2,EtOH}$ is the quasi-equilibrium constant for the competitive ethanol adsorption step. Again, each term in the denominator of eq.5.9 reflects the surface coverage ratio ($\theta_{species}$) of a specific surface species. The first term represents unoccupied acid vanadia sites (θ_{DH}). The second term in the denominator corresponds to acid vanadia sites bearing a surface *tert*-butoxy adsorbate ($\theta_{V\cdot\cdot t-ButOH}$). The third ($\theta_{V\cdot\cdot H_2O}$) denominator term corresponds to hydrated acid vanadia sites generated after hydroxyl recombination. The last term in the denominator represents acid vanadia sites covered by ethanol adsorbates ($\theta_{V\cdot\cdot EtOH}$). Similar to the ethanol partial oxidation redox cycle shown in section 5.3.2.1 the third term in the denominator is much smaller than the other terms ($\theta_{V\cdot\cdot H_2O} \ll$

$\theta_{DH}+\theta_{V\cdot\cdot t-ButOH}+\theta_{V\cdot\cdot EtOH}$), since vicinal surface hydroxyls recombine very fast. eq.5.9 then simplifies to:

$$\frac{r_{DH}}{V_T} \cong \frac{K_{1,t-ButOH}\,k_{2,t-ButOH}P_{t-ButOH}}{1+K_{1,t-ButOH}\,P_{t-ButOH}+K_{2,EtOH}\,P_{EtOH}} \qquad \text{eq.(5.10)}$$

Dividing this equation over the previously derived equation for partial oxidation of ethanol (eq.5.6) obtained from the elementary steps depicted in Scheme 5.2 and assuming conditions at low ethanol and *tert*-butanol partial pressures (i.e. for the denominator term in eq.5.6: $1 \gg K_{1,EtOH}\,P_{EtOH}+K_{2,t-ButOH,}P_{t-ButOH}$ for ethanol partial oxidation and for the denominator term in eq.5.10 $1 \gg K_{1,t-ButOH}\,P_{t-ButOH}+K_{2,EtOH}\,P_{EtOH}$ for tert-butanol dehydration) we can obtain the ratio of *tert*-butanol dehydration and ethanol partial oxidation turnover rates ($\frac{r_{DH}}{r_{POE}}$)

$$\frac{\frac{r_{DH}}{V_T}}{\frac{r_{POE}}{V_T}} \cong \frac{K_{1,t-ButOH,}k_{2,t-ButOH}}{K_{1,EtOH}k_{2,EtOH}} \cdot \frac{P_{t-ButOH}}{P_{EtOH}} \qquad \text{eq.(5.11)}$$

Using this equation, eq.5.7 and defining $k_{\frac{DH}{POE}}$ as a simplified grouped constant for $\frac{K_{1,t-ButOH,}k_{2,t-ButOH}}{K_{1,EtOH}k_{2,EtOH}}$, we can obtain:

$$\frac{r_{DH}}{r_{POE}} \cong \frac{1-\alpha}{\alpha} \cdot k_{\frac{DH}{POE}} \cdot \frac{P_{t-ButOH}}{P_{EtOH}} \qquad \text{eq.(5.12)}$$

Eq.5.12 thus predicts a linear dependence of the ratio of *tert*-butanol dehydration rate to ethanol partial oxidation rate on the ratio of *tert*-butanol-to-ethanol partial pressures, with a zero intercept that is independent on the vanadia loading, and the slope should converge to zero when all the vanadium sites participate in the redox reaction (α reaches a value of one). The results obtained plotting this relationship using the kinetic data obtained for three VO_x/TiO_2 catalysts {(a) 3.6wt.%VO_x/TiO_2, (b) 2.25wt.%VO_x/TiO_2 and (c) 0.84wt.%VO_x/TiO_2 at 200ºC} are shown in Fig.5.6. As predicted, a linear relationship obtained with zero intercept is obtained. The slope of the plots increases at higher VO_x loadings confirming the dependence of the distribution of acid and redox sites on the VO_x loading. Moreover, the plot indicates that the quantitative determination of the fraction of redox active sites for ethanol partial oxidation is independent of the range of operating $P_{t-ButOH}/P_{EtOH}$ ratios.

5.4 Conclusion

In this work, we have demonstrated the use of the dehydration of *tert*-butanol over vanadia as a method to quantify active redox sites during ethanol partial oxidation on the VO_x/TiO_2 system. Our results indicate that under our experimental conditions the surface hydroxyl species present on TiO_2 which could potentially act as acid catalysts for dehydration do not participate in catalysis. A relationship between the ratio of active vanadium oxide sites able to catalyze ethanol partial oxidation and reaction rates was obtained. Our results indicate as well that the normalized first order rate constant ($K_{1,EtOH}k_{2,EtOH}$) values obtained for the partial oxidation rate limiting step of ethanol partial oxidation are independent of VO_x catalyst loading and implicitly suggest that isolated VO_x species are the main species active site for ethanol partial oxidation, while larger VO_x clusters present at higher vanadia loading result in a relative increase of the amount of acid sites.

Acknowledgements

References

(1)   Oyama, S. T.; Zhang, W. *J.Am.Chem.Soc.* **1996**, *118* (21), 7173.

(2)   Kilos, B.; Bell, A. T.; Iglesia, E. *J. Phys. Chem. C* **2009**, *113* (7), 2830–2836.

(3)   Wachs, I. E. *Dalt. Trans.* **2013**, *42* (33), 11762–11769.

(4)   Döbler, J.; Pritzsche, M.; Sauer, J. *J. Am. Chem. Soc.* **2005**, *127* (31), 10861–10868.

(5)   Burcham, L. J.; Badlani, M.; Wachs, I. E. *J. Catal.* **2001**, *203*, 104–121.

(6)   Beck, B.; Harth, M.; Hamilton, N. G.; Carrero, C.; Uhlrich, J. J.; Trunschke, A.; Shaikhutdinov, S.; Schubert, H.; Freund, H.-J.; Schlögl, R.; Sauer, J.; Schomäcker, R. *J. Catal.* **2012**, *296* (0), 120–131.

(7)   Deo, G.; Wachs, I. E. *J. Catal.* **1994**, *146* (2), 323–334.

(8)   Wachs, I. E.; Weckhuysen, B. M. *Appl. Catal. A Gen.* **1997**, *157* (1–2), 67–90.

(9)   Rozanska, X.; Fortrie, R.; Sauer, J. *J. Am. Chem. Soc.* **2014**, *136* (21), 7751–7761.

(10)   Burcham, L. J.; Briand, L. E.; Wachs, I. E. *Langmuir* **2001**, *17* (20), 6175–6184.

(11)   Nair, H.; Baertsch, C. *J. Catal.* **2008**, *258* (1), 1–4.

(12)   Hu, J. Z.; Xu, S.; Li, W.-Z.; Hu, M. Y.; Deng, X.; Dixon, D. A.; Vasiliu, M.; Craciun, R.; Wang, Y.; Bao, X.; Peden, C. H. F. *ACS Catal.* **2015**, *5* (7), 3945–3952.

(13)   Suprun, W. Y.; Sabde, D. P.; Schädlich, H.-K.; Kubias, B.; Papp, H. *Appl. Catal. A Gen.* **2005**, *289* (1), 66–73.

(14)   Perdew, J. P.; Burke, K.; Ernzerhof, M. *Phys. Rev. Lett.* **1996**, *77* (18), 3865–3868.

(15)   Vanderbilt, D. *Phys. Rev. B* **1990**, *41* (11), 7892–7895.

(16)   Lutfalla, S.; Shapovalov, V.; Bell, A. T. *J. Chem. Theory Comput.* **2011**, *7*, 2218–2223.

(17)   Giannozzi, P.; Baroni, S.; Bonini, N.; Calandra, M.; Car, R.; Cavazzoni, C.; Ceresoli, D.; Chiarotti, G. L.; Cococcioni, M.; Dabo, I.; Dal Corso, A.; de Gironcoli, S.; Fabris, S.; Fratesi, G.; Gebauer, R.; Gerstmann, U.; Gougoussis, C.; Kokalj, A.; Lazzeri, M.; Martin-Samos, L.; Marzari, N.; Mauri, F.; Mazzarello, R.; Paolini, S.; Pasquarello, A.; Paulatto, L.; Sbraccia, C.; Scandolo, S.; Sclauzero, G.; Seitsonen, A. P.; Smogunov, A.; Umari, P.; Wentzcovitch, R. M. *J. Phys. Condens. Matter* **2009**, *21* (39), 395502.

(18)   Bahruji, H.; Bowker, M.; Brookes, C.; Davies, P. R.; Wawata, I. *Appl. Catal. A Gen.* **2013**, *454*, 66–73.

(19)   Bronkema, J. L.; Bell, A. T. *J. Phys. Chem.* **2007**, 14530–14540.

(20)   Vittadini, A.; Selloni, A.; Rotzinger, F. P.; Grätzel, M. *J. Phys. Chem. B* **2000**, *104* (6), 1300–1306.

(21)   Huang, W.-F.; Chen, H.-T.; Lin, M. C. *Comput. Theor. Chem.* **2012**, *993*, 45–52.

(22)   Wachs, I. E.; Deo, G.; Andreini, A.; Vuurman, M. A.; de Boer, M. *J. Catal.* **1996**, *160* (2), 322–325.

(23)   Mori, K.; Inomata, M.; Miyamoto, A.; Murakami, Y. *J. Phys. Chem.* **1983**, *87*

(23), 4560–4561.

(24)   Deshlahra, P.; Carr, R. T.; Chai, S.-H.; Iglesia, E. *ACS Catal.* **2015**, *5* (2), 666–682.

(25)   Deshlahra, P.; Iglesia, E. *J. Phys. Chem. C* **2014**, *118* (45), 26115–26129.

(26)   Suarez Negreira, A.; Wilcox, J. *J. Phys. Chem. C* **2013**, *117* (4), 1761–1772.

(27)   Jiang, B.-S.; Chang, R.; Lin, Y.-C. *Ind. Eng. Chem. Res.* **2013**, *52* (1), 37–42.

(28)   Nair, H.; Gatt, J. E.; Miller, J. T.; Baertsch, C. D. *J. Catal.* **2011**, *279* (1), 144–154.

(29)   Kim, T.; Wachs, I. E. *J. Catal.* **2008**, *255* (2), 197–205.

(30)   Kaichev, V. V.; Chesalov, Y. A.; Saraev, A. A.; Klyushin, A. Y.; Knop-Gericke, A.; Andrushkevich, T. V.; Bukhtiyarov, V. I. *J. Catal.* **2016**, *338*, 82–93.

(31)   Argyle, M. D.; Chen, K.; Resini, C.; Krebs, C.; Bell, A. T.; Iglesia, E. *J. Phys. Chem. B* **2004**, *108* (7), 2345–2353.

(32)   Carrero, C. A.; Schloegl, R.; Wachs, I. E.; Schomaecker, R. *ACS Catal.* **2014**, *4*, 3357–3380.

(33)   Carrero, C. A.; Keturakis, C. J.; Orrego, A.; Schomacker, R.; Wachs, I. E. *Dalt. Trans.* **2013**, *42* (35), 12644–12653.

(34)   Du, Y.-J.; Li, Z. H.; Fan, K.-N. *Surf. Sci.* **2012**, *606* (11-12), 956–964.

(35)   Bond, G. C.; Zurita, J. P.; Flamerz, S.; Gellings, P. J.; Bosch, H.; Van Ommen, J. G.; Kip, B. J. *Appl. Catal.* **1986**, *22* (2), 361–378.

(36)   Besselmann, S.; Freitag, C.; Hinrichsen, O.; Muhler, M. *Phys. Chem. Chem. Phys.* **2001**, *3* (21), 4633–4638.

(37)   Chary, K. V. R.; Kishan, G.; Bhaskar, T.; Sivaraj, C. *J. Phys. Chem. B* **1998**, *102* (35), 6792–6798.

(38)   Baertsch, C. D.; Komala, K. T.; Chua, Y.-H.; Iglesia, E. *J. Catal.* **2002**, *205* (1), 44–57.

Chapter 6

6   Conclusions and recommendations

6.1   General conclusions

This research was initiated as an attempt to understand the mechanism of catalytic activity promotion of supported vanadia on titania (VO_x/TiO_2) by nitrogen. Thus the resulting research work reported in this dissertation mainly focuses on addressing four aspects related to supported vanadia on titania (VO_x/TiO_2): 1) the geometric structure and size distribution of the vanadia clusters present on the surface of   nitrogen free VO_x/TiO_2 and nitrogen doped $VO_x/N\text{-}TiO_2$ catalysts, 2) the catalytic behavior of nitrogen doped $VO_x/N\text{-}TiO_2$ catalyst during ethanol partial oxidation, 3) the electronic structure of VO_x/TiO_2 and $VO_x/N\text{-}TiO_2$ catalyst and 4) the quantification of catalytic active redox sites of the VO_x/TiO_2 catalyst.

The use of *in situ* spectroscopies such as Raman, FTIR, and UV-vis provided detailed information on the geometric structure of VO_x/TiO_2 and $VO_x/N\text{-}TiO_2$ catalysts. Catalytic activity experiments of these materials for ethanol partial oxidation together with *in situ* techniques lead to the understanding of the behavior of supported VO_x species during the redox catalytic cycle. *In situ* UV-vis spectroscopy and computational simulations were implemented to look at the electronic structure of VO_x/TiO_2 and $VO_x/N\text{-}TiO_2$. Lastly, a novel *in situ* titration method was proposed to quantify the number of active sites involved in redox catalysis. Based on results from these detailed investigations, the main conclusions of the present dissertation can be summarized as follows:

- In agreement with results in the literature, the dispersion of vanadia is sensitive to vanadia loading. The results depicted in this dissertation indicate that for N free VO_x/TiO_2, vanadia exist mainly as isolated VO_x tetrahedra at low vanadia coverage, while polymerized VO_x and bulk V_2O_5 are present simultaneously at higher vanadia loadings. The presence of doped N influences the degree of dispersion and the average cluster size of the vanadia domains. Compared to N

free VO_x/TiO_2, a larger number of redox active sites are observed in the presence of nitrogen. On the other hand nitrogen presence leads to the formation of clusters with larger domain sizes.

- The strong interactions between titania and vanadium oxide were rationalized in terms of electronic structure changes. DFT calculations on the reduced VO_x/TiO_2 model indicates that the electronic d-d transition observed in the UV/Vis spectra of these materials originates not only from partially filled V (V^{+4}) but also from partially filled d-orbitals in titanium (Ti^{+3}) adjacent to the reduced V cations.

- The strong interactions from titania supports toward vanadia during catalytic activity was rationalized by exhibiting the charge density of reduced VO_x/TiO_2 model. The projection of charge density indicates that the electronic d-d transition is not solely responsible the d-d transition, resulted from the formation of reduced VO_x species during ethanol partial oxidation. Comprehensive investigations confirmed that the electronic d-d transition is attributed to partially filled V (V^{+4}) orbitals as well as Ti d-orbitals (Ti^{+3}) mechanistically adjacent to reduced V cation.

- The mechanism of promotion by nitrogen on these materials can be rationalized in terms of changes of the reducibility of the vanadia clusters. The reducibility of the VO_x species significantly increases by the presence of nitrogen in the support. It was observed that VO_x species present in the catalyst are more reducible when doping N is interstitially positioned in the support. This conclusion is based on the blue shift observed in UV-Vis spectra of the reduced VO_x samples, and in the computational simulations carried on the model reduced VO_x cluster anchored on anatase (101) and anatase (101) slabs doped with nitrogen.

- To complete the gaps in the literature on this system, an *in situ* titration method for redox active sites during ethanol partial oxidation over vanadium oxide dispersed on a reducible metal oxide support (TiO_2) was developed. The method

is based on the competitive adsorption of *tert*-butanol. Quantification of the redox active sites indicated that the first order rate constant for kinetically relevant step is independent of the level VO_x coverage in the catalyst (zero to monolayer). This result implicitly support literature results, suggesting that only isolated vanadia tetrahedral species are involved in catalytic turnovers during ethanol partial oxidation.

6.2 Recommendations and Future work

This dissertation work confirmed the role of doped N in titania toward the catalytic activity of VO_x in ethanol partial oxidation, we proved this role by comparing the change in electronic structure of reduced VO_x, driven by the presence of doped N. In order to confirm this electronic structure change directly, a further analysis of electronic structure by *in situ* photoemission spectroscopy should be conducted, in particular synchrotron ultraviolet photoemission spectroscopy (UPS). The use of ultraviolet radiation ($hv < 50eV$), will enable probing of the catalysts valence band thus it can confirm our current hypothesis on the mechanism of nitrogen promotion of catalytic activity.

In this work, we used the reducibility of the vanadia cluster as a descriptor for catalytic activity and used it to explain the promotion of catalytic activity that takes place in the presence of N. However, investigating reoxidizability of the VO_x species can give us a better understanding of the vanadia reoxidation step that takes place during ethanol partial oxidation catalytic turnovers. Measurement of the reoxidation enthalpies of a series of reduced $VO_x/N\text{-}TiO_2$ catalysts at reaction conditions using calorimetry techniques is suggested. The enthalpy values thus obtained can be correlated to the ability of the vanadia species to switch between different redox states and the influence of nitrogen on this enthalpy values can be assessed.

We carried computational studies on model anatase (101) surfaces. Several of the conclusions presented herewith were obtained by comparing experimental results to the results of these computational simulations. Even more accurate comparisons can be

achieved if vanadia clusters are experimentally grown in a controlled manner over a TiO$_2$ surface with well-defined facets. Therefore, the use of synthesized tetragonal bipyramidal nanocrystalline TiO$_2$ as support is recommended because its surface theoretically consists of only (101) facets. Then use of this material will allow for more control on the size distribution (and therefore reducibility) of the vanadia clusters.

Finally, we proposed a methodology for the quantification of redox sites in the VO$_x$/TiO$_2$ system, additionally experiments should be carried out using this methodology to evaluate the role of nitrogen on the number and availability of redox sites. Moreover the methodology should be further validated by using a series of VO$_x$/TiO$_2$ catalysts with a different number of acid sites. This can be achieved by cationic sodium poisoning of these materials during catalyst synthesis.

Appendices

Appendix A. Experimental setup

Appendix A presents experimental setups implemented for catalytic activity testing and spectroscopic *in situ* characterization over the course of this dissertation. The experimental setup mainly comprise of two systems: (a) main apparatus used for the catalytic activity tests and temperature programmed techniques, and (b) the *in situ* setup for spectroscopic analysis (FTIR, Raman, and UV-vis spectroscopies). Operating procedures are not discussed in this section as they were depicted in each chapters.

Figure A1 shows the experimental setup used for testing of catalytic activity, temperature programmed reduction (TPR) and temperature programmed oxidation (TPO). The electric resistance heater, denoted as 1, is positioned in the middle of the system. A fixed bed reactor is placed inside the heater, shared for the catalytic activity test, and temperature programmed analysis. A methanator and a moisture trap are denoted as 2 and 3, respectively. Nickel (Ni) based catalysts in the methanator converts the effluent gas produced during TPO analysis to CH_4 while a zeolitic material in used as moisture trap (ZSM-5) to adsorb water molecules produced during TPR experiments. All gas transfer lines from the valve at which gases are merged to the detectors are heated in order to prevent condensation. An injection port used to introduce liquid reactant (Ethanol or tert-Butanol) is positioned on the top of the reactor. Composition of the gas stream is controlled by either needle valves or mass flow controllers. In the case of mass flow controllers, they are electronically connected to a data acquisition system (National instruments USB-6009) and controlled by Labview software.
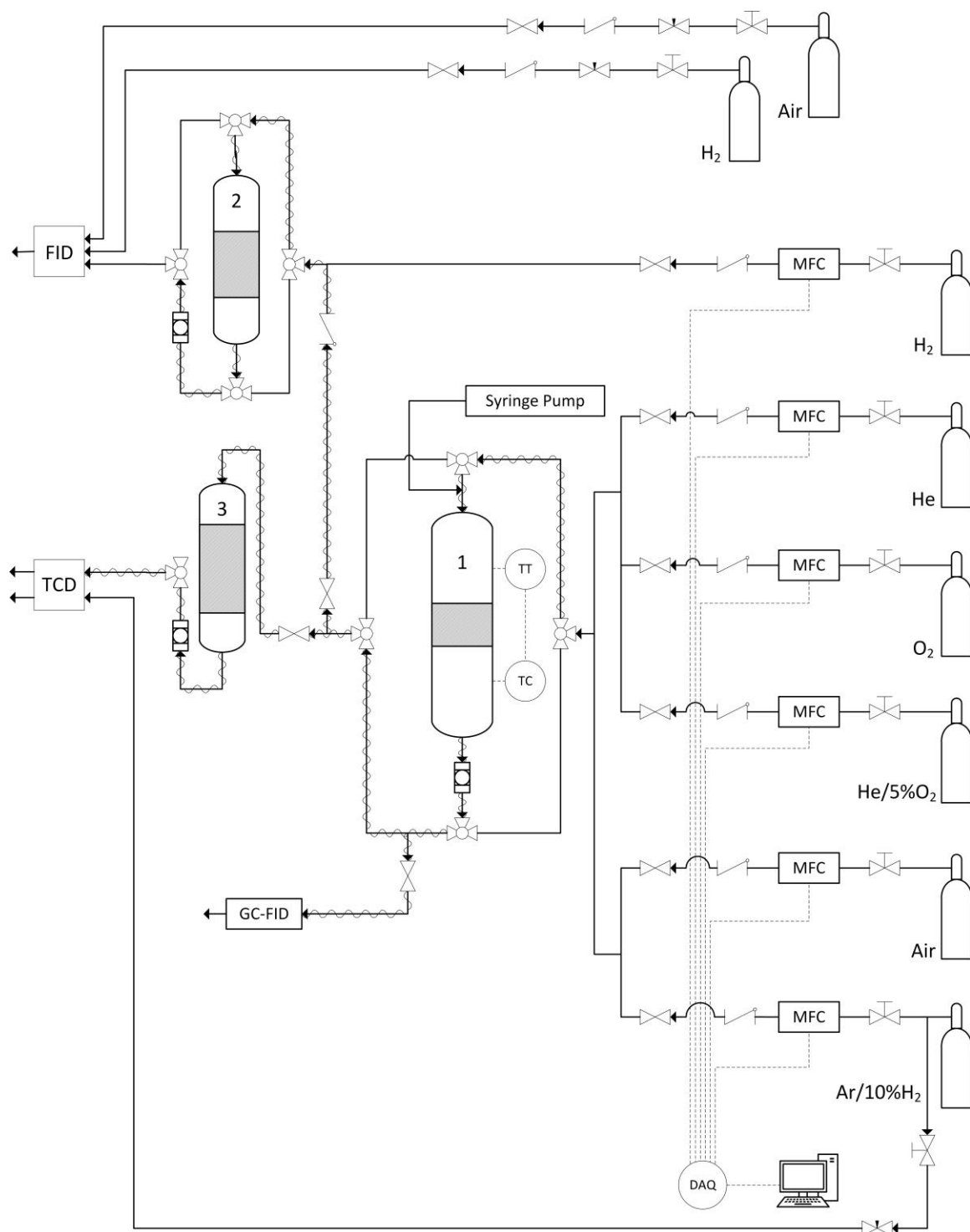
Figure A1. A process flow diagram of the experimental setup for the catalytic activity of ethanol partial oxidation, temperature programmed reduction (TPR), and temperature programmed oxidation (TPR).

Similarly, the experimental apparatus used for *in situ* spectroscopy is shown in Fig.A2. For *in situ* FTIR or UV-vis spectroscopy (marked by B), the reaction chamber (denoted as 1 in Fig.A2) with three windows dome (one glass observation and two ZnSe windows (denoted as 4) for infrared) is placed in the diffuse reflectance accessory. On the other hand, for *in situ* Raman spectroscopy experiments (marked by A), a reaction chamber equipped with a SiO_2 window (denoted a 5) is fixed on top of the optic table. Catalysts (denoted as 2) is packed in the cup-shaped holder in the middle of the reaction chamber and a heating cartridge (denoted as 3) is located below this sample holder. In addition to this, a 6 port switching valve (denoted as 6) with a fixed volume loop (denoted as 7) is occasionally installed when pulse experiments are carried. Analogously to the reactivity test, mass flow controllers control gas stream composition.
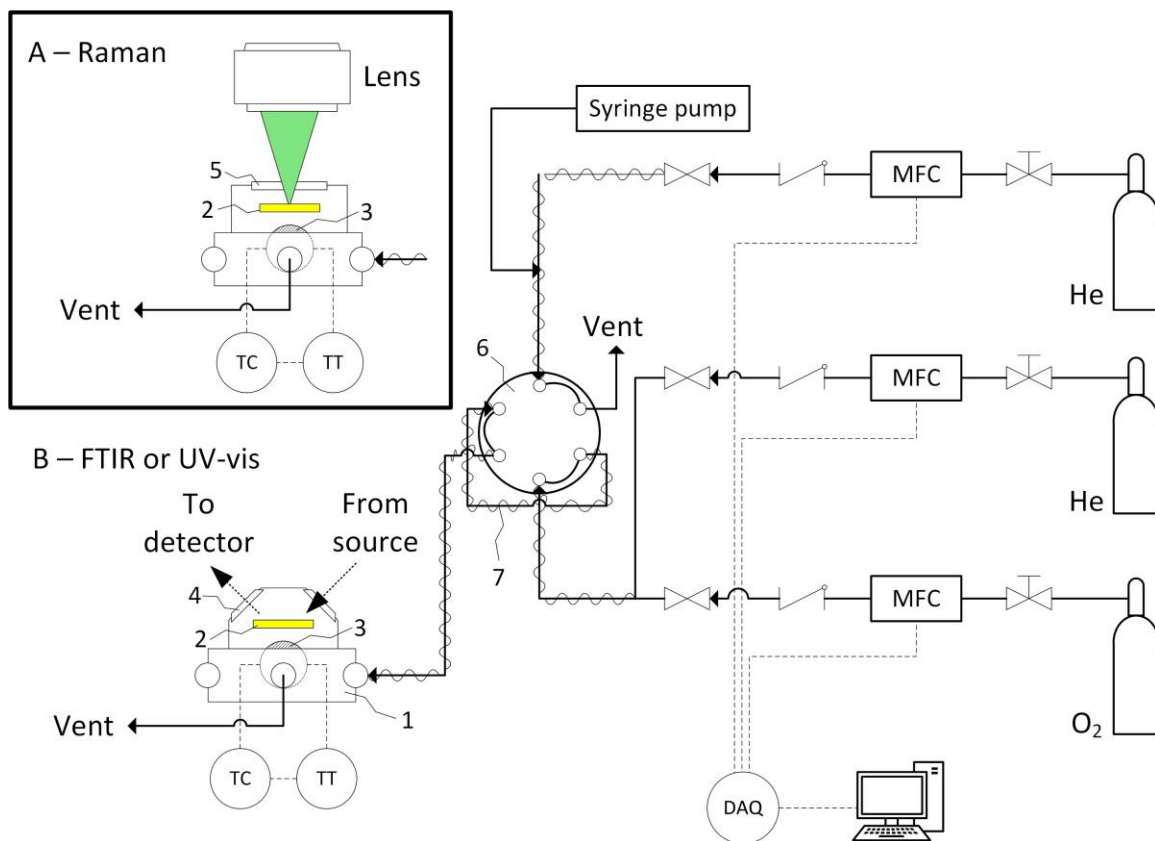
Figure A2. A process flow diagram of the *in situ* experimental apparatus equipped with A: Raman spectroscopy and B: UV-vis or FTIR spectroscopy.

Appendix B. Copyright permissions for figures

ELSEVIER LICENSE
TERMS AND CONDITIONS

Jun 09, 2016

This Agreement between Dongmin Yun ("You") and Elsevier ("Elsevier") consists of your license details and the terms and conditions provided by Elsevier and Copyright Clearance Center.

License Number	3885030061351
License date	Jun 09, 2016
Licensed Content Publisher	Elsevier
Licensed Content Publication	Journal of Molecular Catalysis A: Chemical
Licensed Content Title	The effect of interstitial nitrogen in the activity of the VOx/N-TiO2 catalytic system for ethanol partial oxidation
Licensed Content Author	Dongmin Yun,Yizhao Zhao,Inusa Abdullahi,José E. Herrera
Licensed Content Date	August 2014
Licensed Content Volume Number	390
Licensed Content Issue Number	n/a
Licensed Content Pages	9
Start Page	169
End Page	177
Type of Use	reuse in a thesis/dissertation
Portion	full article
Format	both print and electronic
Are you the author of this Elsevier article?	Yes
Will you be translating?	No
Order reference number	
Title of your thesis/dissertation	Fine tuning of the VOx-N-TiO2 catalytic system for chemical partial oxidation processes
Expected completion date	Aug 2016
Estimated size (number of pages)	200
Elsevier VAT number	GB 494 6272 12

Copyright Clearance Center

RightsLink®

Home | Account Info | Help | Live Chat

ACS Publications
Most Trusted. Most Cited. Most Read.

Title:	Periodic Density Functional Theory Studies of Vanadia—Titania Catalysts: Structure and Stability of the Oxidized Monolayer
Author:	Andrea Vittadini, Annabella Selloni
Publication:	The Journal of Physical Chemistry B
Publisher:	American Chemical Society
Date:	Jun 1, 2004

Copyright © 2004, American Chemical Society

Logged in as:
Dongmin Yun
Account #:
3001035622

LOGOUT

Copyright Clearance Center

RightsLink®

Home   Account Info   Help   Live Chat

Title:	The effect of electronegative difference on the electronic structure and visible light photocatalytic activity of N-doped anatase TiO2 by first-principles calculations	Logged in as: Dongmin Yun Account #: 3001035622
Author:	Dongqiu Zhao,Xiaowei Huang,Baoli Tian, et al.	LOGOUT
Publication:	Applied Physics Letters	
Volume/Issue	98/16	
Publisher:	AIP Publishing LLC	
Date:	Apr 22, 2011	
Page Count:	3	

Rights managed by AIP Publishing LLC.

Order Completed

Thank you for your order.

This Agreement between Dongmin Yun ("You") and AIP Publishing LLC ("AIP Publishing LLC") consists of your license details and the terms and conditions provided by AIP Publishing LLC and Copyright Clearance Center.

Your confirmation email will contain your order number for future reference.

Get the printable license.

License Number	3902691274752
License date	Jul 05, 2016
Licensed Content Publisher	AIP Publishing LLC
Licensed Content Publication	Applied Physics Letters
Licensed Content Title	The effect of electronegative difference on the electronic structure and visible light photocatalytic activity of N-doped anatase TiO2 by first-principles calculations
Licensed Content Author	Dongqiu Zhao,Xiaowei Huang,Baoli Tian, et al.
Licensed Content Date	Apr 22, 2011
Licensed Content Volume	98
Licensed Content Issue	16
Requestor type	Student
Format	Print and electronic
Portion	Figure/Table
Number of figures/tables	1

PERMISSION/LICENSE IS GRANTED FOR YOUR ORDER AT NO CHARGE

Copyright Clearance Center

RightsLink®

ACS Publications
Most Trusted. Most Cited. Most Read.

Title:	Extent of Reduction of Vanadium Oxides during Catalytic Oxidation of Alkanes Measured by in-Situ UV−Visible Spectroscopy
Author:	Morris D. Argyle, Kaidong Chen, Carlo Resini, et al
Publication:	The Journal of Physical Chemistry B
Publisher:	American Chemical Society
Date:	Feb 1, 2004

Copyright © 2004, American Chemical Society

PERMISSION/LICENSE IS GRANTED FOR YOUR ORDER AT NO CHARGE

Dalton Transactions

Title: Anomalous reactivity of supported V2O5 nanoparticles for propane oxidative dehydrogenation: influence of the vanadium oxide precursor

Author: Carlos A. Carrero,Christopher J. Keturakis,Andres Orrego,Reinhard Schomäcker,Israel E. Wachs

Publication: Dalton Transactions

Publisher: Royal Society of Chemistry

Date: May 8, 2013

Copyright © 2013, Royal Society of Chemistry

Review Order

Please review the order details and the associated terms and conditions.

No royalties will be charged for this reuse request although you are required to obtain a license and comply with the license terms and conditions. To obtain the license, click the Accept button below.

Licensed Content Publisher	Royal Society of Chemistry
Licensed Content Publication	Dalton Transactions
Licensed Content Title	Anomalous reactivity of supported V2O5 nanoparticles for propane oxidative dehydrogenation: influence of the vanadium oxide precursor
Licensed Content Author	Carlos A. Carrero,Christopher J. Keturakis,Andres Orrego,Reinhard Schomäcker,Israel E. Wachs
Licensed Content Date	May 8, 2013
Licensed Content Volume	42
Licensed Content Issue	35
Type of Use	Thesis/Dissertation
Requestor type	academic/educational
Portion	figures/tables/images
Number of figures/tables/images	1
Distribution quantity	10
Format	print and electronic
Will you be translating?	no
Order reference number	
Title of the thesis/dissertation	Fine tuning of the VOx-N-TiO2 catalytic system for chemical partial oxidation processes
Expected completion date	Aug 2016
Estimated size	200

ACS Publications
Most Trusted. Most Cited. Most Read.

Title: Bonding Geometry and Reactivity of Methoxy and Ethoxy Groups Adsorbed on Powdered TiO2

Author: Wen-Chun Wu, Chih-Chung Chuang, Jong-Liang Lin

Publication: The Journal of Physical Chemistry B

Publisher: American Chemical Society

Date: Sep 1, 2000

Copyright © 2000, American Chemical Society

PERMISSION/LICENSE IS GRANTED FOR YOUR ORDER AT NO CHARGE

Copyright Clearance Center

RightsLink®

JOURNAL OF CATALYSIS

Title:	Redox mechanism for selective oxidation of ethanol over monolayer V2O5/TiO2 catalysts
Author:	Vasily V. Kaichev,Yuriy A. Chesalov,Andrey A. Saraev,Alexander Yu. Klyushin,Axel Knop-Gericke,Tamara V. Andrushkevich,Valerii I. Bukhtiyarov
Publication:	Journal of Catalysis
Publisher:	Elsevier
Date:	June 2016

© 2016 Elsevier Inc. All rights reserved.

Logged in as:
Dongmin Yun
Account #:
3001035622

LOGOUT

Review Order

Please review the order details and the associated terms and conditions.

No royalties will be charged for this reuse request although you are required to obtain a license and comply with the license terms and conditions. To obtain the license, click the Accept button below.

Licensed Content Publisher	Elsevier
Licensed Content Publication	Journal of Catalysis
Licensed Content Title	Redox mechanism for selective oxidation of ethanol over monolayer V2O5/TiO2 catalysts
Licensed Content Author	Vasily V. Kaichev,Yuriy A. Chesalov,Andrey A. Saraev,Alexander Yu. Klyushin,Axel Knop-Gericke,Tamara V. Andrushkevich,Valerii I. Bukhtiyarov
Licensed Content Date	June 2016
Licensed Content Volume	338
Licensed Content Issue	n/a
Licensed Content Pages	12
Type of Use	reuse in a thesis/dissertation
Portion	figures/tables/illustrations
Number of figures/tables/illustrations	1
Format	both print and electronic
Are you the author of this Elsevier article?	No
Will you be translating?	No
Order reference number	
Original figure numbers	
Title of your thesis/dissertation	Fine tuning of the VOx-N-TiO2 catalytic system for chemical partial oxidation processes
Expected completion date	Aug 2016
Estimated size (number of pages)	200
Elsevier VAT number	GB 494 6272 12

ACS Publications
Most Trusted. Most Cited. Most Read.

Title: Structure and Reactivity of Vanadium Oxide Catalysts Supported on Anatase TiO2

Author: Komandur V. R. Chary, Gurram Kishan, Thallada Bhaskar, et al

Publication: The Journal of Physical Chemistry B

Publisher: American Chemical Society

Date: Aug 1, 1998

Copyright © 1998, American Chemical Society

Logged in as:
Dongmin Yun
Account #:
3001035622

LOGOUT

PERMISSION/LICENSE IS GRANTED FOR YOUR ORDER AT NO CHARGE

Title: Chemistry, spectroscopy and the role of supported vanadium oxides in heterogeneous catalysis

Author: Bert M. Weckhuysen, Daphne E. Keller

Publication: Catalysis Today

Publisher: Elsevier

Date: 28 February 2003

Order Completed

Thank you for your order.

This Agreement between Dongmin Yun ("You") and Elsevier ("Elsevier") consists of your license details and the terms and conditions provided by Elsevier and Copyright Clearance Center.

Your confirmation email will contain your order number for future reference.

Get the printable license.

License Number	3902701211545
License date	Jul 05, 2016
Licensed Content Publisher	Elsevier
Licensed Content Publication	Catalysis Today
Licensed Content Title	Chemistry, spectroscopy and the role of supported vanadium oxides in heterogeneous catalysis
Licensed Content Author	Bert M. Weckhuysen, Daphne E. Keller
Licensed Content Date	28 February 2003
Licensed Content Volume	78
Licensed Content Issue	1-4
Licensed Content Pages	22
Type of Use	reuse in a thesis/dissertation
Portion	figures/tables/illustrations
Number of figures/tables/illustrations	1
Format	both print and electronic
Are you the author of this Elsevier article?	No
Will you be translating?	No
Order reference number	
Original figure numbers	
Title of your thesis/dissertation	Fine tuning of the VOx-N-TiO2 catalytic system for chemical partial oxidation processes
Expected completion date	Aug 2016
Estimated size (number of pages)	200
Elsevier VAT number	GB 494 6272 12

Curriculum Vitae

Name	Dongmin Yun
Post-secondary Education and Degrees:	Hanyang University Seoul, South Korea 2004-2007 B.Sc
	Hanyang University Seoul, South Korea 2007-2011 M.Sc
	The University of Western Ontario London, Ontario, Canada 2012-2016 Ph.D

Publications

Dongmin Yun, Yizhao Zhao, Inusa Abdullahi, and José E. Herrera," The effect of interstitial nitrogen in the activity of the VO_x/N-TiO_2 catalytic system for ethanol partial oxidation", *Journal of Molecular Catalysis A: Chemical*, 390, 169-177 (2014)

Inusa Abdullahi, Taylor J. Davis, Dongmin Yun, José E. Herrera, "Partial oxidation of ethanol to acetaldehyde over surface-modified single-walled carbon nanotubes", *Applied Catalysis A: General*, 469(17), 8-17 (2014)

Dongmin Yun, Hyun-Hee Cho, Jun-Won Jang, Jae-Woo Park, "Nano zero-valent iron impregnated on titanium dioxide nanotube array film for both oxidation and reduction of methyl orange", *Water Research*, 47(5) 1858-1866 (2013)